GRATING COUPLED SURFACE PLASMON ENHANCED FLUORESCENCE SPECTROSCOPY

Dissertation zur Erlangung des Grades
„Doktor der Naturwissenschaften“

am Fachbereich
Chemie und Pharmazie der
Johannes Gutenberg - Universität Mainz

Andreas Heinz Nicol
geboren in Wiesbaden

Mainz, September 2005

Meinen Eltern gewidmet, die mich in guten
wie in schlechten Zeiten unterstützt haben.

Dedicated to my parents, who have
supported me at all times, both good and ill.

Contents

List of Figures

List of Tables

Chapter 1

Introduction

Over the last three decades the field of optical sensors capable of measuring surface reactions has vastly expanded. Among the methods that rose to prominence are: ellipsometry, fluorescence spectroscopy, Raman spectroscopy, waveguide spectroscopy and interferometry. In the nineteen seventies and eighties, sensors based on the phenomenon of surface plasmon resonance (SPR) have proven particularly suitable for real time thin film characterization [Poc78], gas detection [Nyl82], biomolecular interaction examination [Lie83] and to supplement electrochemical methods [Gor80]. Since then SPR has established itself as a widely employed analytical method for surface and materials science, in particular for biosensing. Consequently, SPR sensing technology has been commercialized in 1990 [BIA]. A number of review articles have been published bearing testimony to the value of the technique in fundamental research as well as in clinical studies [Boh97], [Sch97], [Fru98], [Hom99]. Combining SPR with fluorescence detection and dye labeled analytes placed within the enhanced electromagnetic field has led to surface plasmon fluorescence spectroscopy (SPFS), a technique that increases sensitivity even further [Att91], [Lie00b].

The majority of laboratory systems, as well as commercial products, relies on prism coupling as the method to achieve surface plasmon excitation by light. Alternatively, metal gratings can be employed to match photons for plasmon resonance. Grating systems have also reached maturity for the SPR market [HTS] lately. Whereas fluorescently labeled monolayer assemblies have been studied on gratings [Kno81], as well as with prism systems utilizing SPFS, the real time monitoring of binding reactions has to the author's knowledge not yet been successfully pursued in the combination of fluorescence detection and grating coupling. This is probably due to the fact that in grating coupling surface plasmon and fluorescence spectroscopy (GC-SPFS) the illumination source shines first on the solution before it hits the grating and excites plasmons at its surface. Thus the direct illumination of fluorophores in solution produces a background signal that is superimposed on the fluorescence generated by dye-labeled molecules immobilized on the sensor surface. Because it does not carry information related to recognition of the analyte by the sensor surface functionalization, bulk fluorescence emission is an unwanted signal contribution. This is especially of concern for time critical binding studies in which a quick distinction between a compatible and an inert analyte is demanded, while the sensor surface concentration of the analyte is still well below the equilibrium value.

This dilemma needs to be overcome in order to develop GC-SPFS to a commercially feasible stage. The effort is worthwhile, since grating devices promise more competitive products and offer interesting features. In prism systems, as well as grating based devices, the sensor surface must be manufactured as an expendable component. The metal film thickness in prism coupling has to be precisely maintained on the nanometer scale (e. g. 48 nm film thickness for gold excited at a wavelength of 632.8 nm) for every sample to allow for reproducible results. On the other hand, the requirement for the metal layer on a grating component is less stringent since the film only needs to be optically opaque. Any thickness beyond 100 nm is suitable for excitation at λ = 632.8 nm. Because the illumination does not pass through the metalized grating substrate, any kind of inexpensive polymer material suitable for injection molding is adequate. Substrate requirements are much stricter for prism coupling systems due to the demand for a highly transparent material. This is particularly true for designs in which the prism is part of the disposable element and is required to provide a high refractive index, as well as a certain optical shape fidelity. For these reasons, the savings in operating costs of a system based on grating coupling promise to surpass those for a device based on prism coupling. An additional benefit is the ability to engineer a convenient device geometry, since the choice of the grating constant determines the excitation as well as the detection angle.

1.1 Thesis overview

This thesis is comprised of a comprehensive study of the suitability of grating coupling for fluorescence based analyte detection. Fundamental properties of GC-SPFS are described, as well as issues related to device engineering. Several new experimental techniques are introduced and demonstrated in order to optimize performance in certain areas and improve upon capabilities in respect to conventional SPFS.

The following chapter gives the theoretical background of the research topic. It contains the electromagnetic theory necessary for the understanding of the surface plasmon resonance phenomenon. The optical excitation of surface plasmon modes is explained for both prism and grating coupling geometries. The mathematics used to calculate the excitation in these two schemes and to analyze data are also described in this chapter. It also contains the Langmuir theory describing adsorption processes. The basics of fluorescence and atomic force microscopy are covered as well.

Experimental methods and all information about sample preparation are given in the third chapter. It contains a description of the grating fabrication method and the surface functionalization protocol employed for deoxyribonucleic acid (DNA) immobilization experiments. The experimental set-up used in this work is introduced in this chapter, together with the different modes of measurement.

The fourth chapter focusses on sample characterization by several complementary methods. It describes the study of grating corrugations by atomic force microscopy and how the corrugation affects the efficiency of the coupling process. Optical characterization, by measuring reflectivity and diffraction, is also described in order to analyze the properties of adsorbed

dielectric layers. These measurements are accompanied by quantitative analysis based on calculations and a discussion of effects introduced by the flow cell. Many parameters influence the optical response of a grating and this chapter contains a comprehensive overview of these parameters on the reflection of light by a grating.

Chapter five presents fluorescence experiments of the strongly directional emission caused by back coupling of fluorophores to the grating. Studies of magnitude and geometry of the fluorescence emission pattern are presented for different grating constants and polarizations. The effect of bleaching on the interpretation of measurements is examined as well as the difference between the minimum of the reflected intensity and the maximum fluorescence excitation position.

The results from analyte binding experiments are contained in chapter six, focussing on the contribution of bulk fluorophores to the total signal. Affinity measurements with DNA are described and the factors determining the limit of detection of the technique are discussed. Experiments on the geometry of the bulk emission and its interaction with different excitation and detecting polarizations are covered as well in this chapter.

The seventh chapter demonstrates the suitability of replicated gratings for GC-SPFS. The cheap reproduction of disposable gratings by means of a hot embossing method is explained. Characterization of the resulting samples is presented with an emphasis on sample uniformity and reproducibility of the employed reproduction method.

Expansion of the experimental set-up to a system capable of imaging the full solid angle of the fluorescence emission is covered in chapter eight. Changes to the set-up, its capabilities and limitations are described. The reduced susceptibility of the system to bleaching and the resulting advantage for polarization sensitive detection are both demonstrated.

Chapter nine introduces an optical method to cancel the contribution of bulk fluorescence emission to the total signal. The detection scheme, involving the modulation of both polarization and intensity of the incident beam, is explained in detail, as well as the necessary changes to the experimental set-up. The method is demonstrated with DNA hybridization at high bulk concentrations and additionally with an entirely different sandwich-type assay.

The last chapter summarizes the most important experimental findings and provides an outlook and suggestions for future experiments.

Chapter 2

Theoretical background

This chapter outlines the theoretical treatment of surface plamons within the framework of Maxwell's theory and the Drude model of metals. Prism coupling is explained using the dispersion relation of plasmons at a smooth metal/dielectric interface. Next, the slightly more complicated case of grating coupling is discussed. The transfer matrix formalism and its expanded form based on the Rayleigh approximation are used for calculations of prism and grating coupling and are subsequently introduced. Furthermore, basic concepts of fluorescence and the Langmuir model of adsorption are described. The chapter concludes with a brief explanation of the operating principles of atomic force microscopy.

2.1 Surface plasmons

Surface plasmons[1] are charge density oscillations of the free electrons of a metal propagating along the interface shared with a dielectric. The electrons respond collectively and in resonance to an excitation by a light wave or an incoming electron. The dynamic variation in surface charge density corresponds to an electromagnetic field at the surface as illustrated in figure 2.1. Therefore one can conceive surface plasmons as light waves restricted to the surface of a conductor. This field is an evanescent field, i. e. it extends exponentially in both media. Due to the resonant response of the oscillating electrons the field features a strong enhancement close to the surface. Changes to the dielectric environment of the metal surface strongly alter the resonance condition. This is the principle on which all SPR sensors are based. SPFS, on the other hand, makes use of the electromagnetic field enhancement by placing fluorophores in close proximity to the metal surface. Hence a higher fluorescence signal is achieved as compared to exciting the dye molecules directly with the same light source.

A little more than 100 years ago R. W. Wood first described his observation of anomalous diffraction on diffraction gratings [Woo02], a phenomenon later attributed to the excitation of surface waves by U. Fano [Fan41]. R. H. Ritchie postulated the existence of surface plasmons in

[1]The term "plasmon" derives from the assumption of electrons behaving like a charged gas (plasma) in the Drude model of metals, as explained in section 2.1.2. One can also excite longitudinal charge density fluctuations in metals, dubbed volume plasmons. Hence distinction by the supplemental "surface".

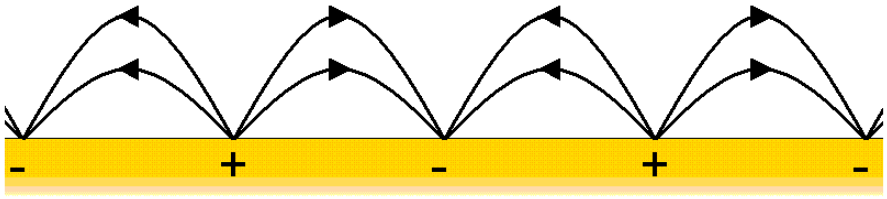

Figure 2.1: Electric field lines of a surface plasmon on a smooth surface. Surface plasmons are constituted of resonantly oscillating surface charges at a metal/dielectric interface and of the electromagnetic surface wave that originates from these surface charges. The field is present in both media, but for reasons of clarity it is here shown only in the dielectric, where it is strongest.

thin metal films penetrated by electrons [Rit57]. This was proven in the fifties by the electron energy loss experiments of C. J. Powell [Pow59]. A decade later both A. Otto [Ott68] and E. Kretschmann [Kre68] introduced different optical methods of surface plasmon excitation by utilizing attenuated total reflection (ATR) in a prism. The latter method is a very convenient one, for both the experimentalist as well as the commercial user, and since its contrivance the field has prospered and many properties of surface plasmons have been studied [Boa82], [Rae88], [Agr82].

2.1.1 Electromagnetic waves and matter

The fundamental equations governing electromagnetic phenomena are Maxwell's equations. In macroscopic media and without source terms they take the form [Jac98]

$$\begin{aligned} \mathrm{div}\mathbf{D} &= 0 \qquad & \mathrm{curl}\mathbf{E} + \frac{1}{c}\frac{\partial \mathbf{B}}{\partial t} &= 0 \\ \mathrm{div}\mathbf{B} &= 0 \qquad & \mathrm{curl}\mathbf{H} - \frac{1}{c}\frac{\partial \mathbf{D}}{\partial t} &= 0 \end{aligned} \tag{2.1.1}$$

with the electric field $\mathbf{E}$, the magnetic field $\mathbf{B}$, the electric displacement $\mathbf{D}$, the magnetic field strength $\mathbf{H}$ and the speed of light c. Assuming materials with linear polarization and magnetization responses in respect to the external fields, both the electric as well the the magnetic quantities are interconnected via the material equations

$$\begin{aligned} \mathbf{D} &= \varepsilon_0 \varepsilon(\omega)\mathbf{E} \\ \mathbf{B} &= \mu_0 \mu(\omega)\mathbf{H} \end{aligned} \tag{2.1.2}$$

introducing the electric permittivity of free space ε_0, the magnetic permeability of free space μ_0, the dielectric "constant"[2] $\varepsilon(\omega)$ and the relative permeability $\mu(\omega)$. In the following we will only consider homogenous and isotropic materials. This reduces $\varepsilon(\omega)$ and $\mu(\omega)$ to scalar quantities, while they are rank two tensors in the general treatment. They are still complex functions of

[2]Rather a function of ω as emphasized by the notation. But by convention $\varepsilon(\omega)$ is referred to as the dielectric constant.

the angular frequency ω of the exciting field. Under these circumstances Maxwell's equations can be solved by electric plane waves

$$\mathbf{E}(\mathbf{r},t) = \mathbf{E}_0 e^{i(\mathbf{k}\cdot\mathbf{r}-\omega t)} \tag{2.1.3}$$

with $\mathbf{r}$ denoting the point in space, t time, $\mathbf{E}_0$ the electric field amplitude and $\mathbf{k}$ the wavevector. Due to the transverse nature of light, $\mathbf{E}_0$ is always orthogonal to the direction of propagation, which is along $\mathbf{k}$. Alternatively, a magnetic plane wave of analogous design can be used to fully describe the solution since both fields are linked in this case to each other by purely algebraic relations:

$$\begin{aligned} \mathbf{H}(\mathbf{r},t) &= \frac{c}{\omega\mu_0\mu(\omega)}\,\mathbf{k}\times\mathbf{E}(\mathbf{r},t) \\ \mathbf{E}(\mathbf{r},t) &= -\frac{c}{\omega\varepsilon_0\varepsilon(\omega)}\,\mathbf{k}\times\mathbf{H}(\mathbf{r},t). \end{aligned} \tag{2.1.4}$$

$\mathbf{k}$ and ω are not independent of each other but rather satisfy the photonic dispersion relation:

$$\frac{\omega^2}{|\mathbf{k}|^2} = \frac{1}{\mu_0\mu(\omega)\varepsilon_0\varepsilon(\omega)}. \tag{2.1.5}$$

With the assumption of nonmagnetic media ($\mu(\omega) = 1$) from now on and with the identity

$$c^2 = \frac{1}{\mu_0\varepsilon_0} \tag{2.1.6}$$

the magnitude of $\mathbf{k}$ can be expressed in a way that is more convenient for the following considerations:

$$|\mathbf{k}| = \omega\sqrt{\mu_0\varepsilon_0\varepsilon(\omega)} = \frac{\omega}{c}\sqrt{\varepsilon(\omega)}. \tag{2.1.7}$$

2.1.2 Conductors and insulators

As introduced in equation (2.1.7) the complex dielectric function $\varepsilon(\omega) = \varepsilon'(\omega) + i\varepsilon''(\omega)$ governs the macroscopic response of a material to an external electromagnetic field. It is therefore important to have an understanding of $\varepsilon(\omega)$ for the materials employed in this work. They fall into two general categories that need to be distinguished: conductors (gold) and insulators (water, glasses, polymers, proteins, DNA).

In an insulator the electrons are strongly localized at the atomic sites. Only substantial electric fields will force mobility on them. Insulators typically show a small positive ε' and an almost vanishing ε'' for the visible and infra-red spectral ranges, as displayed for example by water in figure 2.2 (a). Metals, on the other hand, possess conduction electrons that can easily move to different lattice sites under the influence of an external electric field. This behavior at the microscopic level gives rise to many of their macroscopic characteristics like the typical metallic luster, ductility, conduction of heat and electric currents. Metals feature a negative ε' and a smaller, positive ε'' at visible and longer wavelengths.

The dielectric properties of metals can be described by the Drude model [Ash76]. It works well for a spectral range starting from the visible up to the microwave regime. Amazingly,

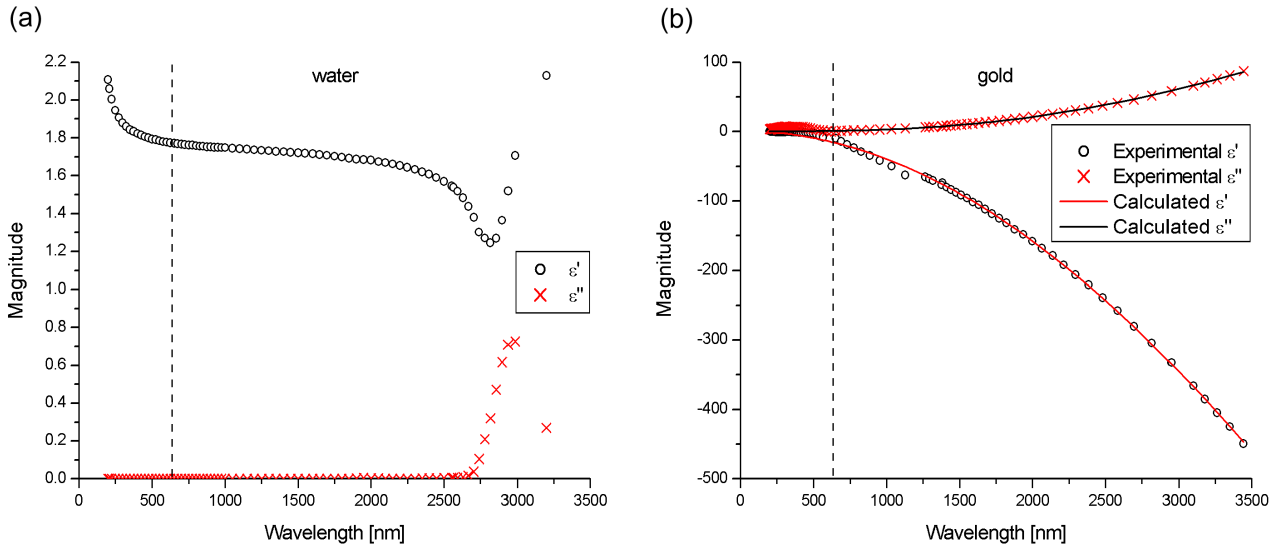

Figure 2.2: Dielectric functions of water and gold. (a) Both components of the dielectric function of water in the liquid phase are relatively constant in the visible and near infra-red part of the spectrum. The vertical line marks the HeNe laser wavelength of 632.8 nm. Transitions in the OH-stretching band are excited around and above 3000 nm [Ban95]. (b) Drude's theory of metals describes the dielectric function of metals well in the visible and near infra-red range, as shown in the graph for Au with ω_p between 1 and 1.2 x 10^{16} s^{-1} and τ at around 5 to 6 x 10^{-15} s. Drude's theory brakes down for frequencies approaching ω_p. This equals wavelengths in the ultraviolet range between 157 - 189 nm for these two fit curves. Dielectric data taken from literature [Har95].

Drude developed his theory of electrical and thermal conduction prior to the development of quantum theory [Dru00]. It is rather based on the successful kinetic theory of gases. Metals are essentially described as a gas of electrons governed by Newtonian mechanics. Their average velocity is determined by the thermal energy of the metal. They experience mutual collisions with each other after time intervals equal to the collision time τ. Other electron-electron interactions taking place between collisions are neglected. Ion-electron interactions, however, can not be fully ignored. This situation is summarized with the term "quasi-free" electron approximation. The response of the metal to an externally applied electric field is primarily determined by the acceleration imposed on the electrons. Within this framework the dielectric function of a metal as a function of the angular frequency ω of the external applied field is derived as:

$$\varepsilon(\omega) = 1 - \frac{\omega_p^2}{\omega^2 + i\frac{\omega}{\tau}}. \tag{2.1.8}$$

The plasma frequency ω_p is given by

$$\omega_p^2 = \frac{n_e e^2}{\varepsilon_0 m_e} \tag{2.1.9}$$

where n_e is the electron density, e the electron charge and m_e the effective electron mass. Equation (2.1.8) can be applied to frequencies lower than the plasma frequency. See figure 2.2 (b) for the dielectric data of gold taken from literature in comparison with curve fits of

the real and imaginary part of $\varepsilon(\omega)$ according to the Drude model. At ω approaching or exceeding ω_p the dielectric constant becomes mainly a negative quantity and the material becomes transparent. This is true for the alkali metals in the UV, but different in other metals in which other contributions to $\varepsilon(\omega)$ become significant that require a theoretical treatment based on quantum mechanics.

Alternatively, the optical properties of materials can be characterized by the complex refractive index $n(\omega)+i\kappa(\omega)$, with the real part n being the (ordinary) refractive index and the imaginary part κ being the absorption coefficient. This description is equivalent to the usage of the dielectric function and both properties are converted into each other via the following equations[3]:

$$\begin{aligned} (n+i\kappa)^2 &= \varepsilon' + i\varepsilon'' \\ \varepsilon' &= n^2 - \kappa^2 \\ \varepsilon'' &= 2n\kappa. \end{aligned} \tag{2.1.10}$$

2.1.3 Electromagnetic waves at interfaces

The reflection and the refraction of light have already been studied in ancient times. In 130 A. D. Claudius Ptolemy measured the angles of incidence and refraction for several media but was not able to find a mathematical framework to describe his results. Long before the formulation of the electromagnetic theory of light by J. C. Maxwell, R. W. van Snell discovered the law of refraction empirically in 1621. It was later reformulated by R. Descartes in terms of sines. P. de Fermat derived the law from his principle of least time, stating that light propagates from one point in space to another along a route that takes the least time.

Consider two materials, each occupying a half-space, which share a common, flat interface at z=0 as illustrated in figure 2.3. The electromagnetic response of each material i is described by the dielectric function ε_i (from which we can readily derive the refractive indices n_i using equation (2.1.11) for that material). For a plane electromagnetic wave with an angle of incidence α_i measured from the surface normal, we find the angle of transmission α_t via Snell's law of refraction:

$$\frac{n_1}{n_2} = \frac{\sin\alpha_t}{\sin\alpha_i}. \tag{2.1.11}$$

Reflection occurs at $\alpha_r = -\alpha_i$. For $n_2 < n_1$, α_t is always larger than α_i. If α_t equals 90°, no light is transmitted into medium two and the full intensity is reflected. This condition is called total internal reflection (TIR). The angle of incidence under which TIR occurs is called the critical angle θ_c. It is given by Snell's law when the numerator on the right side of equation (2.1.11) becomes unity:

$$\theta_c = \arcsin\left(\frac{n_2}{n_1}\right). \tag{2.1.12}$$

Since reflection and transmission constitute competing propagation channels, the question arises how the impinging intensity is split up quantitatively between the two. This problem has

[3]The ω-dependence is still implied but suppressed from now on for better readability.

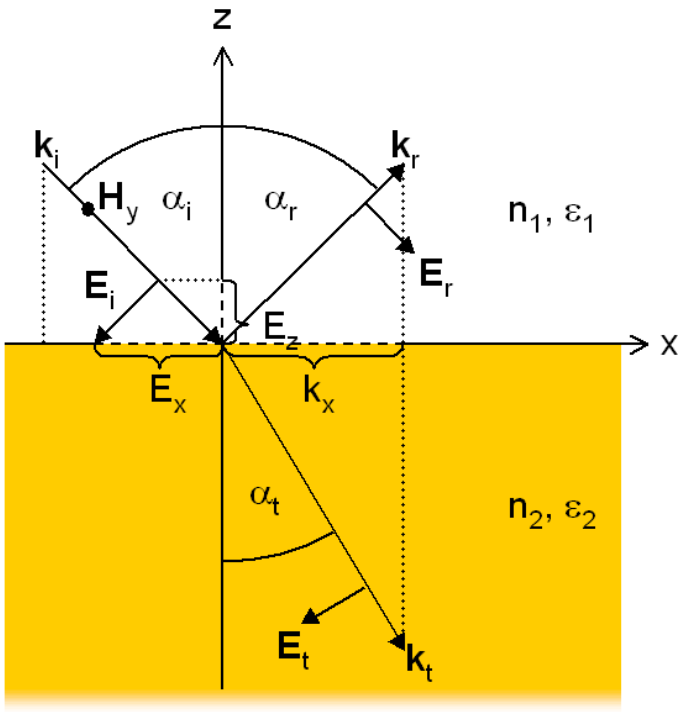

Figure 2.3: An electromagnetic wave at an interface. The incident wave $\mathbf{E}_i$ is split up at an interface into a reflected wave $\mathbf{E}_r$ and a transmitted wave $\mathbf{E}_t$. The angles are determined by Fermat's principle of least time, the field amplitudes by Fresnel's formulas.

been solved by Fresnel. His deduction [Bor99], [Hec01] is based on the continuity conditions for the tangential (interfacial) components of **E** and **H**. The different polarizations of the transversal field have to be distinguished since they behave differently at the interface. With its wavevector situated within the xz-plane, any arbitrary plane electric field can be decomposed into a component that is lying also within the xz-plane and a orthogonal component that runs parallel to the y-axis. The latter corresponds to an electric field of s-polarization (TE-mode). The in-plane component is of p-polarization (TM-mode). Fresnel's formulas express the ratio of the electric field amplitude of the reflected (or transmitted) wave divided by the incident wave amplitude for the two polarizations:

$$\begin{aligned}
r_s &= \frac{n_2 \cos\alpha_i - n_1 \cos\alpha_t}{n_2 \cos\alpha_i + n_1 \cos\alpha_t} && \text{reflection ratio for s-light} \\
t_s &= \frac{2n_1 \cos\alpha_i}{n_2 \cos\alpha_i + n_1 \cos\alpha_t} && \text{transmission ratio for s-light} \\
r_p &= \frac{n_2 \cos\alpha_t - n_1 \cos\alpha_i}{n_2 \cos\alpha_t + n_1 \cos\alpha_i} && \text{reflection ratio for p-light} \\
t_p &= \frac{2n_1 \cos\alpha_i}{n_2 \cos\alpha_t + n_1 \cos\alpha_i} && \text{transmission ratio for p-light.}
\end{aligned} \tag{2.1.13}$$

2.1.4 Surface plasmon solutions

Surface plasmon modes can be derived as solutions to Maxwell's equations (2.1.1) appearing as surface waves. We again consider the material interface of figure 2.3. Only a p-polarized electric field can induce surface charges due to its field component along the z-axis and therefore generate surface plasmons. Thus we will focus on the case of a p-polarized electric field. For both the electric and the magnetic field we make the harmonic ansatz

$$\begin{aligned} \mathbf{E}_1 &= \begin{pmatrix} E_{x_1} \\ 0 \\ E_{z_1} \end{pmatrix} \exp(i[k_{x_1}x + k_{z_1}z - \omega t]) \\ \mathbf{E}_2 &= \begin{pmatrix} E_{x_2} \\ 0 \\ E_{z_2} \end{pmatrix} \exp(i[k_{x_2}x - k_{z_2}z - \omega t]) \end{aligned} \tag{2.1.14}$$

where the indices 1 and 2 refer to quantities existing in either half-space 1 (z>0) or 2 (z<0) respectively. The k_{x_i} and k_{z_i} are the components of the respective total wavevector $\mathbf{k}_i$ decomposed along the x- and z-axis. Via equation (2.1.4) this results in a magnetic field that is oriented fully parallel to the y-axis:

$$\begin{aligned} \mathbf{H}_1 &= \begin{pmatrix} 0 \\ H_{y_1} \\ 0 \end{pmatrix} \exp(i[k_{x_1}x + k_{z_1}z - \omega t]) \\ \mathbf{H}_2 &= \begin{pmatrix} 0 \\ H_{y_2} \\ 0 \end{pmatrix} \exp(i[k_{x_2}x - k_{z_2}z - \omega t]). \end{aligned} \tag{2.1.15}$$

Because of the continuity condition for the components of **E** and **H** parallel to the interface we demand two identities:

$$\begin{aligned} E_{x_1} &= E_{x_2} \\ H_{y_1} &= H_{y_2}. \end{aligned} \tag{2.1.16}$$

From these follows the continuity of:

$$k_{x_1} = k_{x_2} =: k_x. \tag{2.1.17}$$

With these constraints equation (2.1.4) reduces to:

$$k_{z_1} H_{y_1} = \frac{\omega}{c}\varepsilon_1 E_{x_1} \tag{2.1.18}$$

$$k_{z_2} H_{y_2} = -\frac{\omega}{c}\varepsilon_2 E_{x_2}. \tag{2.1.19}$$

In the nontrivial case (i. e. nonvanishing fields) the division of equation (2.1.18) by equation (2.1.19) yields the relation:

$$\frac{k_{z_1}}{k_{z_2}} = -\frac{\varepsilon_1}{\varepsilon_2}. \tag{2.1.20}$$

As will be shown later, some of these four quantities can be complex numbers with small imaginary parts. If one ignores these small imaginary parts for a moment and assumes all quantities to be real numbers, relation (2.1.20) can only be met if one of the two materials has a positive dielectric number and the other one a negative ε. This restricts the existence of surface plasmon solutions to the common interface of a dielectric and a metal.

The k_{z_i} can be expressed via the magnitude of the wavevectors $\mathbf{k}_i$. Additionally, the latter can be replaced by the photonic dispersion relation (2.1.7):

$$k_{z_i}^2 = |\mathbf{k}_i|^2 - k_{x_i}^2 = \left(\frac{\omega}{c}\right)^2 \varepsilon_i - k_{x_i}^2 \qquad \text{with i=1, 2.} \tag{2.1.21}$$

Employing the square of equation (2.1.20) to connect both $k_{z_i}^2$ and at the same time dropping the subscript for x_i because of the continuity relation (2.1.17) leads us to

$$\left(\frac{\omega}{c}\right)^2 \varepsilon_1 - k_x^2 = \left(\frac{\varepsilon_1}{\varepsilon_2}\right)^2 \left[\left(\frac{\omega}{c}\right)^2 \varepsilon_2 - k_x^2\right] \tag{2.1.22}$$

from which we find the plasmonic dispersion relation:

$$k_x = \frac{\omega}{c}\sqrt{\frac{\varepsilon_1\varepsilon_2}{\varepsilon_1 + \varepsilon_2}}. \tag{2.1.23}$$

Considering an ideal metal/dielectric interface, $\varepsilon_1 = \varepsilon_d$ is a real number in case of the dielectric and $\varepsilon_2 = \varepsilon_m$ is complex for the metal with a negative real part and a smaller, positive imaginary part. Under the condition of $\varepsilon_m'' < |\varepsilon_m'|$, k_x also becomes a complex quantity. To satisfy equation (2.1.21), k_z is also required to be complex. The introduction of a imaginary component separates the phase term of the ansatz (2.1.14) into a harmonic and into an exponentially decaying part. For example in the case of a complex k_z:

$$\exp(i[\{k_z' + ik_z''\}z - \omega t]) = \exp(i[k_z' z - \omega t])\exp(-k_z'' z). \tag{2.1.24}$$

This describes the phase term of a wave decaying in magnitude along the z-axis with the decay length $1/k_z''$. All three plasmonic fields E_x, E_z and H_y show this evanescent characteristic. At the metal/dielectric interface the continuity condition dictates the transition behavior of the individual fields. Again H_y and E_x are continuous, whereas E_z is discontinuous. The same argument for the phase term holds true for a complex k_x and propagation along the metal/dielectric interface (x-axis). At a gold/air interface with $\varepsilon_{gold} = -12$+i1.3 and $\varepsilon_{air} = 1$ at an excitation of 632.8 nm the propagation length within the film is in the range of 10 μm. Hence surface plasmons are damped nonradiative surface waves.

2.1.5 Prism coupling

If we look again at the plasmonic dispersion relation (2.1.23) and briefly neglect the small imaginary component of the metal ($\varepsilon_m = \varepsilon_m'$), k_x of a surface plasmon will always exceed the wavevector of light in air unless ω approaches zero:

$$k_{surface\ plasmon} = \frac{\omega}{c}\sqrt{\frac{\varepsilon_m \varepsilon_d}{\varepsilon_m + \varepsilon_d}} \geq k_{photon,\ air} = \frac{\omega}{c}\sqrt{\varepsilon_d}. \tag{2.1.25}$$

This poses a dilemma for the surface plasmon excitation by light. For an interaction between photons and plasmons it is a fundamental requirement that the process adheres to the physical principles of both momentum as well as energy conservation. The inequality (2.1.25) as illustrated in figure 2.4 prevents this for "free" photons (impinging on the metal from vacuum or air).

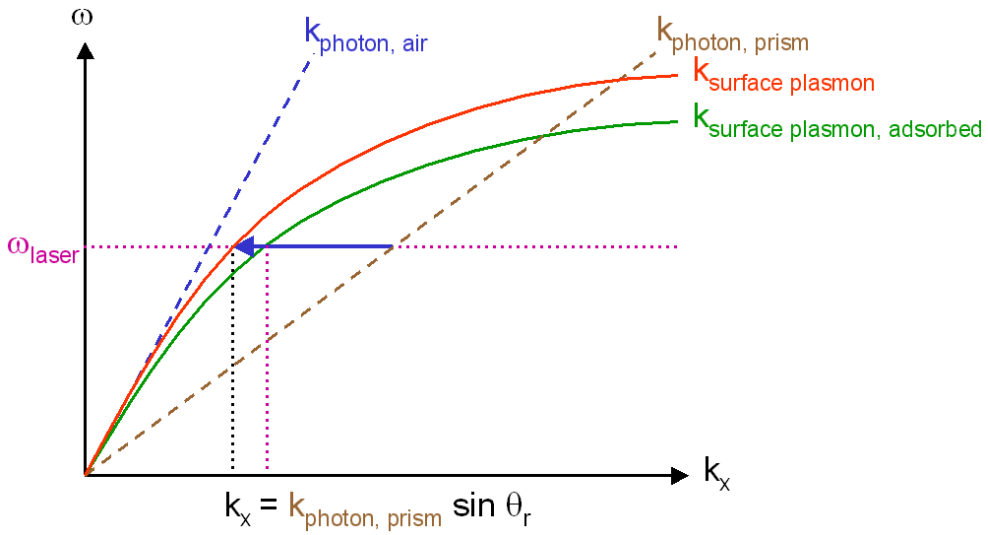

Figure 2.4: The plasmonic dispersion relation for prism coupling. The photonic (left dashed line) and plasmonic dispersion curves (upper solid curve) do not intersect apart from the origin. Introducing a higher refractive index dielectric lowers the slope of the free light line. By tuning the angle of incidence, the length of the photonic k_x can be reduced (see arrow) until it matches the plasmonic in-plane wavevector component and surface plasmon excitation becomes possible. Changing the dielectric environment, for example by adsorbing a material with a higher dielectric constant, will effect the plasmonic dispersion curve (lower solid curve) and thus result in a different resonance angle. The dispersion relation exists also in negative k-space for negative angles of course, because of the symmetry inherent to the problem.

The photonic dispersion relation line is given by the dashed line on the left. It only intersects with the plasmonic dispersion relation (upper solid line) at the origin. There is no other spot where both curves cross, i. e. where they feature the same energy $\hbar\omega$ as well as the same in-plane momentum $\hbar k_x$ at the same instance. Introducing a high refractive index dielectric in the upper half-space boosts the photonic wavevector according to equation (2.1.7) by a factor equal to the refractive index $n=\sqrt{\varepsilon}$ of the new material. This increase in n causes a reduction of the slope of the light line, as represented by the dashed line on the right. For a given laser color (frequency), the intersection of ω_{laser} with $k_{surface\ plasmon}$ or $k_{surface\ plasmon,\ adsorbed}$ gives the maximum in-plane component of the light wavevector. By rotating the interface by an angle θ[4], a factor of $\sin\theta$ can be applied to k_x, hence moving the intersection along the ω_{laser}-line to

[4]One has to distinguish between inner angles (within the prism) and outer angles (in air) because of refraction at the glass/air interface. The relation between both quantities is given by Snell's law. To avoid confusion only

the left as indicated by the arrow. If the intersection coincides with the plasmonic dispersion curve, energy and momentum of plasmon and photon match and surface plasmon excitation with light is possible. This scheme can explain the condition under which coupling occurs, but no information can be derived from it about the efficiency of the process or the magnitude of the resulting evanescent field.

Two configurations have been proposed to excite surface plasmons optically by employing a high refractive index prism. In the Otto configuration sketched in figure 2.5 (a) a laser beam is reflected off the base of a prism[5]. Adjacent to the base is a gap of low refractive index material with a thickness of the order of the employed laser wavelength. Located on the other side of the gap is a metal layer of optically infinite thickness. TIR takes place for angles equal to or larger than the critical angle. Under the TIR condition, the evanescent field at the prism base can tunnel across the dielectric spacer and excite surface plasmon modes on the metal/dielectric interface. The intensity of the reflected beam is monitored and the coupling condition appears as a minimum of the reflection intensity (see figure 2.5 (b)). The reflected intensity is usually scaled by the incident intensity. This normalized quantity is called the reflectivity R ($R := I_i/I_r$).

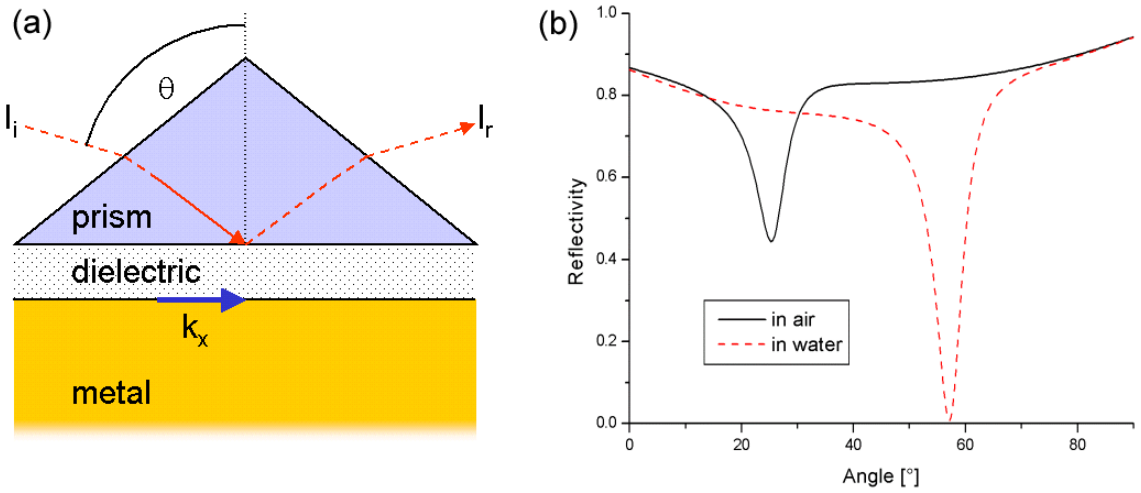

Figure 2.5: Prism coupling in the Otto configuration. (a) The p-polarized laser beam excites a surface plasmon in the dielectric gap (horizontal arrow). (b) The solid line of the simulation shows reflectivity data for illumination at $\lambda = 632.8$ nm as a function of the angle of incidence for a system built of a prism half-space (consisting of the high refractive index glass LaSFN9), 300 nm of air and infinitely thick gold with dielectric constants of 3.4, 1 and -12+i1.3 respectively. The coupling conditions are met at about 25.3° resulting in a significant decrease in the reflected intensity down to R = 0.44. The dashed line belongs to the same system with the air in the dielectric gap being replaced by water ($\varepsilon = 1.78$), yielding a very pronounced minimum of R = 0.01 at 57.2°. Clearly, by increasing the dielectric constant in the gap, the resonance angle increases. A gold thickness of 150 nm is already sufficiently opaque for the field not to sample the other side. For thinner gold, a second resonance dip can appear, for example in case of the sequence LaSFN9/water/gold/air (a type of Otto/Kretschmann-hybrid configuration).

outer angles are used in the graphs presented in this thesis.

[5]All prism coupling calculations, irrespective of the type of configuration, are based on the Winspall code (see section 2.1.7).

The tunnelling process is very sensitive to changes in the thickness of the gap and the thickness has to be chosen in accordance with the dielectric constant of the gap material in order to yield a high coupling efficiency. Thus the Otto configuration requires the ability to build this 3 component structure with precision. For the study of binding reactions and adsorption processes, access to the dielectric layer is necessary in order to exchange material and introduce dielectric contrast. This demands an extremely thin flow cell construction that can be disassembled and reassembled. This combined with the fact that the Otto configuration is very susceptible to thickness variations of the spacer layer introduced by dust particles etc. explains why the method is rather uncommon today.

The Kretschmann configuration is the prevalent method today to couple light to surface plasmons because of its relative simplicity and robustness. As illustrated in figure 2.6 (a), a laser beam is reflected off the base of a high refractive index prism and the reflected intensity is measured. Metal and low refractive index dielectric layers swap roles compared to the previous method but with the advantage that the dielectric phase is readily accessible in the Kretschmann configuration. A thin metal layer is located on the prism base, for example 48 nm thickness for the combination of a gold film and a HeNe laser, followed by a bulk dielectric. The metal layer thickness needs to be precisely controlled in order to obtain the most efficient coupling to the excitation. It is instructive to consider the two extreme cases shown in figure 2.6 (b): if the metal layer is too thick and opaque to the electromagnetic field, it will not reach the interface on the opposite side. This system is essentially a mirror. Its reflectivity is high but below one because of bulk absorption. If the layer is too thin, the interaction with the electrons can not fully develop, too much intensity will pass through the metal and propagate freely as a transmitted or a reflected wave. In this case, the refractive index contrast between prism and medium determines the reflectivity curve. The reflectivity is almost vanishing for angles smaller than the critical angle. It rises sharply at the critical edge located at θ_c, the onset of TIR. To excite the surface plasmon resonance, the layer needs to be thicker than this, but still thin enough for the field to sample the dielectric half-space. For the appropriate metal film thickness the surface plasmon resonance can be excited and the characteristic dip in the reflectivity scan appears if the power of the electromagnetic wave is nearly fully channelled into the surface wave. The resonance curve shape retains features of the two extreme cases: the high reflectivity below the resonance angle is similar to the infinitely thick metal mirror and the small critical edge stems from the glass/medium refractive index jump.

For exciting fluorescence with an electromagnetic field, the intensity of the total electric field $|\mathbf{E}_{total}|^2 = |E_x|^2 + |E_z|^2$ is the relevant quantity[6]. Figure 2.7 shows the field intensity just

[6]The full field intensity $|\mathbf{E}_{total}|^2$ is not necessarily a direct measure of the fluorescence signal detected in a surface plasmon excitation scheme. This is even true for an isotropic orientational distribution of the fluorophores' transition dipole moments. The detection geometry and fluorophore properties have to be taken into account for rigorous modelling [Vas04]. For example E_z excites a dye molecule the strongest if the transition dipole moment is oriented normal to the metal/dielectric interface. This dipole will emit primarily parallel to the interface and unless the experimental set-up can collect light from this type of grazing emission it is lost. Additionally, it is important to consider the fact that certain dyes feature an absorption dipole that is not parallel to the emission dipole and the impact of this asymmetry on the emission and detection processes be relevant.

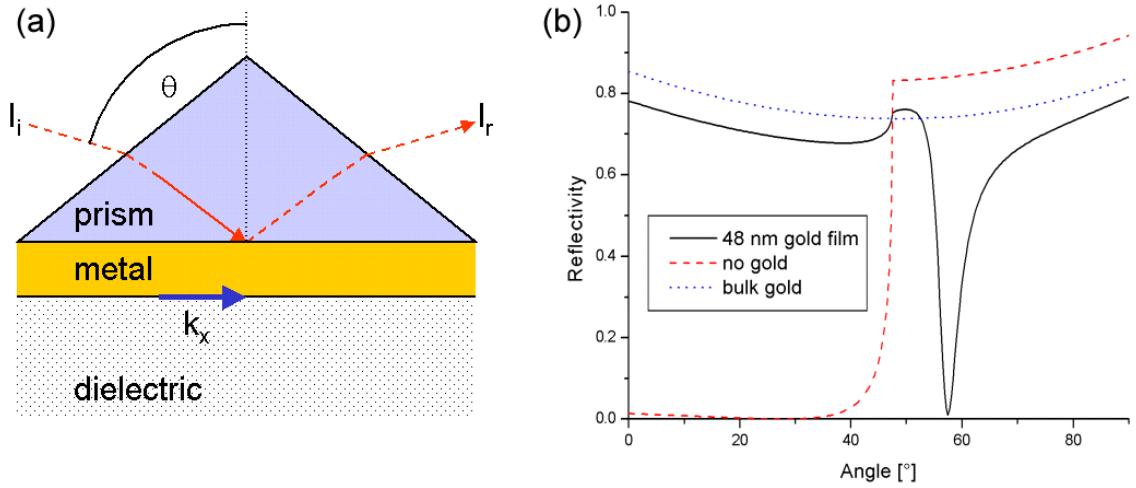

Figure 2.6: Prism coupling in the Kretschmann configuration. Metal and dielectric change positions compared to the Otto configuration. (a) The surface plasmon is excited by the p-polarized light source on the far side of the metal, indicated by the horizontal arrow. (b) The simulated data for $\lambda = 632.8$ nm on the right covers three situations: the dotted line represents bulk gold (thickness 150 nm or more), resulting in high reflectivity. The total absence of gold causes the dashed reflectivity curve, featuring TIR from the prism/dielectric interface for angles beyond $\theta_c = 46.35°$. If the optimum gold film thickness is picked (48 nm), the surface plasmon resonance can be excited appearing as a minimum (R=0.01) in the reflectivity scan at 57.39°. The critical edge at θ_c due to TIR and the high metallic reflectivity below the critical angle are still present in the curve. As in the case of the Otto configuration, increasing the dielectric constant of the dielectric half-space will increase the resonance angle. The simulated materials are a prism of LaSFN9 glass, gold and water with dielectric constants of 3.4, -12+i1.3 and 1.78 respectively.

above the gold surface calculated for the same system introduced in figure 2.6 in comparison with the reflectivity curve. The graph shows clearly that the reflectivity minimum and the intensity maximum aren't located at the same angle, a fact that has been experimentally proven previously [Lie00b]. In the case stated here, the intensity maximum is followed by the reflectivity minimum with an angular separation of about 0.4°. At first glance this might appear surprising since both extremal features relate to surface plasmon excitation. Having said this, there is still a fundamental difference in the nature of both extrema. The reflectivity minimum is found by mapping the far field intensity for various angles. The propagating electric field drops in magnitude if the resonant excitation funnels power from it into the surface plasmon mode. The presence of surface plasmons equals the presence of an evanescent field bound to the metal/dielectric interface. But the magnitude of the total electric field at the surface is a result of the superposition of the remaining, transmitted far field from the illuminating beam and the near field of the surface plasmon mode. Because of this it should be clear that both extrema are not necessarily located at the same position. So it is rather surprising to find a match of the two angles in special geometries, such as systems supporting long-range surface plasmon modes [Sar82].

Under the resonance condition the evanescent field leaking out into the dielectric experiences a strong enhancement. The fluorescence signal is harvested best by placing a dye in close

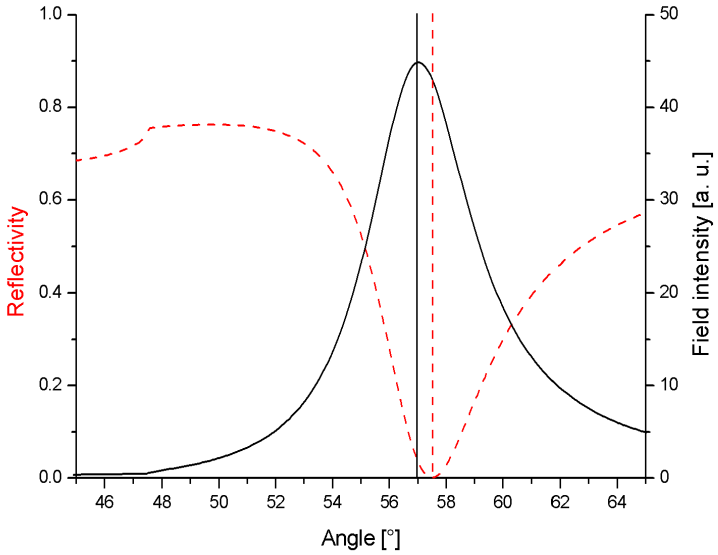

Figure 2.7: Reflectivity and field intensity for prism coupling. The dashed line represents a detail of the reflectivity curve of the system in Kretschmann configuration described in figure 2.6. The solid line shows the intensity of the total electric field in the dielectric half-space calculated 0.1 nm above the gold surface. The extremal features of both curves do not coincide because they relate to different processes. The reflectivity minimum (a far field quantity) is preceded by the field maximum (resulting from the superposition of the illuminating far field and the plasmonic near field) by about 0.4°.

proximity to the metal surface in order to exploit this gain in enhancement[7]. A calculation of the intensity distribution of $|\mathbf{E}_{total}|^2$ over the LaSFN9/gold/water multi-layer system at the resonance angle is plotted in figure 2.8. The values are normalized to the average intensity of the illuminating standing wave. At the surface the intensity enhancement exceeds a factor of 40. From there the intensity decays exponentially within the dielectric half-space with a decay length of about 150 nm (equaling 300 nm for the electric field itself). The maximum enhancement factor is determined by the damping of the metal. Silver features lower losses at the HeNe line and gives a field enhancement of up to a factor of 80 while exhibiting a narrower reflectivity minimum/intensity maximum at the same time. Gold is the preferred noble metal for this work because of its much higher adhesion stability in a saline buffer environment.

2.1.6 Grating coupling

Metallic gratings are utilized in many monochromators and spectrometers as the dispersive element [Loe97], [Pet80]. They can also be used to satisfy the energy and momentum matching conditions discussed in the previous section. The first observations of surface plasmons were reported on gratings, dubbed Wood's anomalies [Woo02]. A grating resembles a periodically

[7]On the other hand, placement too close to a metal surface is counterproductive, because of quenching of the excited fluorophore state. This subject is taken up in section 2.2.2

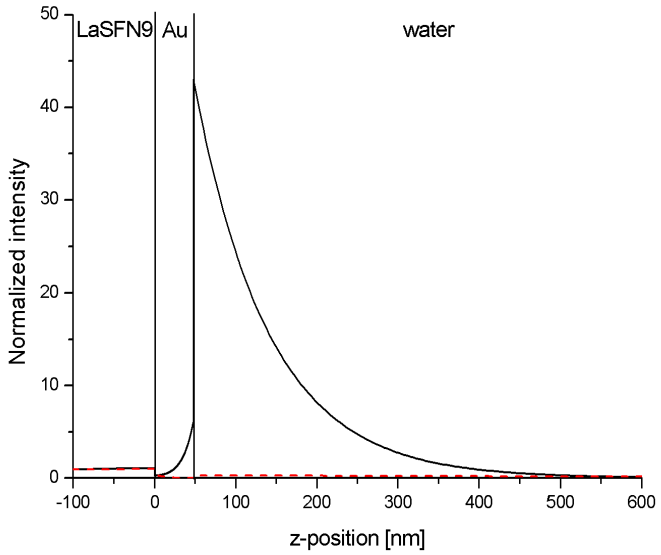

Figure 2.8: Enhancement in prism coupling. The electric field intensity was calculated for the LaSFN9/gold/water system. Illumination takes place from the left. The solid line shows the enhancement profile under the resonance condition ($\theta_r = 56.99°$). The barely visible dashed curve is calculated for illumination at the critical angle, the onset of surface plasmon excitation. Both curves are normalized to their respective intensity average in the LaSFN9 half-space.

corrugated surface modulation. The theoretically simplest grating is of sinusoidal shape[8]. It can be characterized by its periodicity or grating constant Λ and by its groove depth or rather by the amplitude a, being half of the groove depth (if one has a sinusoidal curve in mind). The periodic corrugation breaks the translational invariance of the metal surface. An incoming plane wave can interact with the grating grooves acting as an array of scattering centers. The total field can be constructed from the constructive interference of the individual scattered waves resulting in different diffraction orders. If the in-plane component of the wavevector of a given order matches the plasmonic dispersion relation, plasmons are excited.

For a grating constant Λ, we define the grating vector $\mathbf{G}$ with the magnitude:

$$|\mathbf{G}| = \frac{2\pi}{\Lambda}. \tag{2.1.26}$$

Its orientation is in the plane of the corrugated surface, perpendicular to the grating grooves, as can be seen in figure 2.9. Multiples m of the grating vector can be added to the wavevector of the reflected field (m=0) located in the xz-plane:

$$\mathbf{k}_{diffracted} = \mathbf{k}_{photon} + m\mathbf{G} = \begin{pmatrix} k_x \\ 0 \\ k_z \end{pmatrix} + \begin{pmatrix} m\frac{2\pi}{\Lambda} \\ 0 \\ 0 \end{pmatrix} \qquad \text{with m being an integer.} \tag{2.1.27}$$

[8]Gratings can have several grating constants and amplitudes that are not necessarily collinear and hence the grating can be two or even three-dimensional. This work focuses exclusively on one-dimensional gratings.

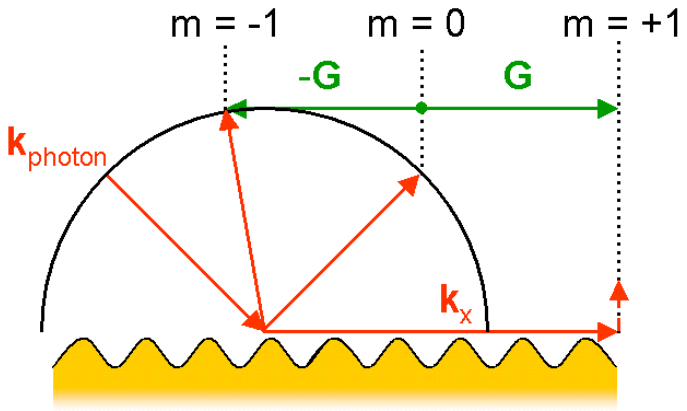

Figure 2.9: Diffraction by a grating. In this Ewald-like construction, multiples m of the grating vector **G** can be added to k_{photon}. Elastic scattering occurs if the vector sum lies on the circle. A combination with a magnitude exceeding the radius results in a solution bound to the surface with an evanescent component in the direction normal to the grating.

For a given wavevector, m indicates the diffraction order. Only those combinations can persist that conserve the magnitude of the wavevector $|\mathbf{k}_{diffracted}| = |\mathbf{k}_{photon}|$ (elastic scattering) and thus lie on a circle in reciprocal space[9] with a radius equal to this magnitude. Vector combinations that exceed the length of $\mathbf{k}_{photon}$ require an imaginary k_z because of the relation:

$$|\mathbf{k}_{diffracted}|^2 - \left(k_x + m\frac{2\pi}{\Lambda}\right)^2 = k_z^2 < 0. \tag{2.1.28}$$

For positive m and k_x, surface plasmon solutions exist that propagate along the x-axis and decay along the z-axis.

Because of the translational symmetry of the surface profile

$$\zeta(x) = \zeta(x + m\Lambda) \tag{2.1.29}$$

the dispersion relation is also periodic. This situation is similar to phonons in a periodic lattice. In prism coupling, only one pair of dispersion branches exists, starting at the origin and running in both directions. On a grating, a pair of new dispersion branches originates in reciprocal space at every multiple of the grating vector[10]. Consequently the surface plasmon dispersion relation exhibits the corresponding type of translational symmetry as the surface profile:

$$\omega(\mathbf{k}_x) = \omega(\mathbf{k}_x + m\mathbf{G}). \tag{2.1.30}$$

[9]This approach is similar to the Ewald construction in reciprocal space used in solid state physics to describe the elastic scattering of x-rays by a three-dimensional atomic lattice [Ash76]. While this concept is very pictorial and hence easy to understand, in the treatment of grating coupling this advantage is lost since imaginary components of the wavevector are present that can't be shown in real space drawings.

[10]The origin of an additional dispersion branches is solely determined by the grating vector. But its exact location and course are also a function of the profile shape and amplitude (see section 4.2.4.)

The dispersion branches either cross or form gaps at the border of the Brillouin zone (at $\pm\pi/\Lambda$) . The dispersion relation exhibits quite an intricate pattern. Figure 2.10 shows an exemplary section of this branched structure, gaps excluded. The signs of the branch labels refer to the direction of the branches (plus - right side, minus - left side). The number in the subscript denotes the diffraction order. The momentum matching principle is also valid for gratings. Coupling photons from the free light line to the 0^{th} order branch is impossible, because of the inequality 2.1.25 discussed above. But new branches of higher orders exist, criss-crossing the region between light line and ordinate, which enable coupling to surface plasmons. For a given frequency (dotted horizontal line), the maximum in-plane projection of the photonic wavevector is indicated by the intersection with the dashed light line. Rotating the grating by a certain angle θ scales k_x by $\sin\theta$ and the intersection can be shifted such, that it coincides with a point on the dispersion curve (denoted by the arrow), thus satisfying the coupling condition. An increase in the dielectric constant of the material on the grating decreases all the branches of the dispersion relation (not shown to reduce complexity) in the same manner like illustrated in figure 2.4. Focussing on the right half of the Brillouin zone for simplicity (from 0 to $+\pi/\Lambda$), adsorption results in an increase or decrease of the resonance angle, depending on whether a right (+) or left (-) branch direction is involved.

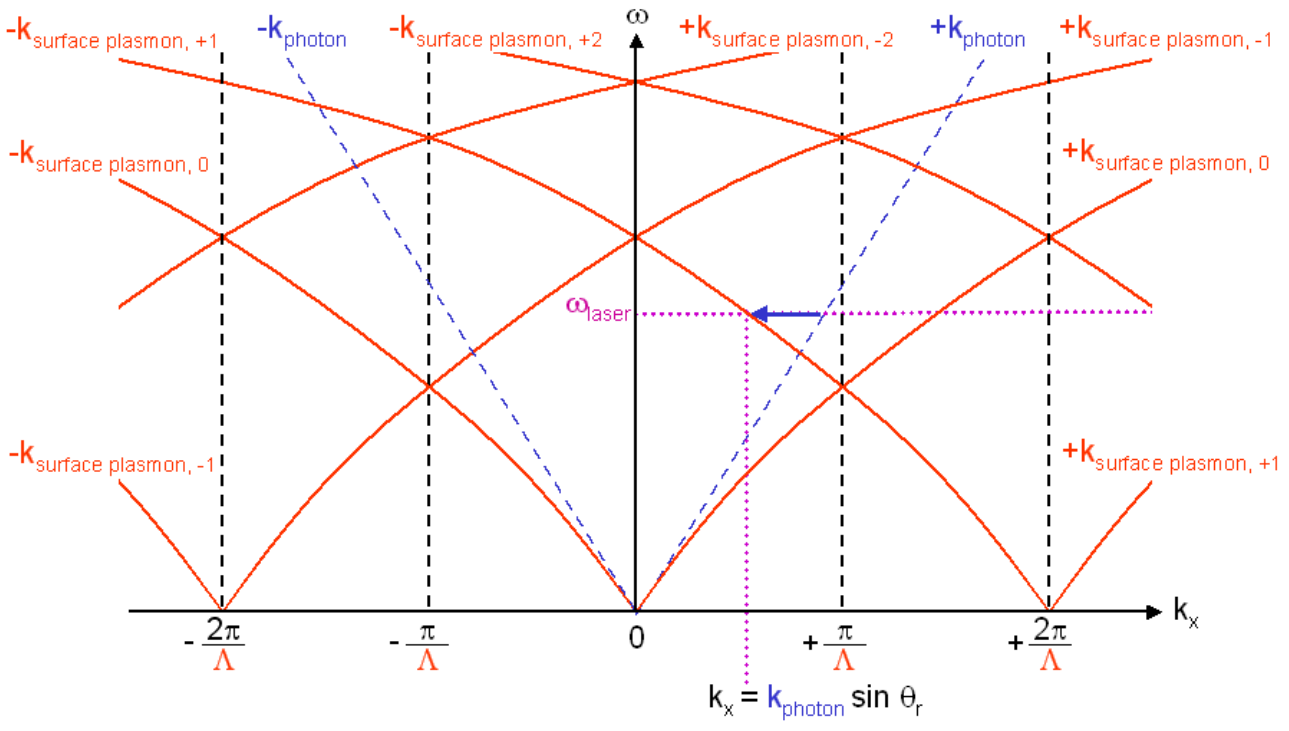

Figure 2.10: The plasmonic dispersion relation for grating coupling. The periodic corrugation of the surface results in a dispersion relation in reciprocal space that is also periodic. In order to excite surface plasmons optically, a light source with a frequency (dotted horizontal line) that intersects with one of the dispersion branches is necessary. If the dashed light line passes through that same intersection (indicated by the arrow) by rotating the grating, energy and momentum conservation are satisfied and the resonance can be excited.

The example chosen in figure 2.10 illustrates coupling to the negative half of the 1^{st} order

branch. An increase in the dielectric constant will result in a negative shift of the resonance angle in this case. Figure 2.11 shows exactly this kind of behavior for a simulated grating response[11]. Not only the resonance angle shift has changed its direction, but also the orientation of the edge in relation to the reflectivity minimum is reversed in comparison with prism coupling in the Kretschmann configuration. This (pseudo-)critical edge indicates the transition from a propagating to an evanescent wave. In grating coupling, the edge can generally appear on either side of the minimum, depending on the exact course of the dispersion branch involved in the coupling. In this example, the wave is evanescent on the left side of the edge (where the reflectivity minimum is located) and becomes a propagating one on its right. Knowledge of the exact location of the edge also allows to identify the diffraction order involved in the coupling process. The imaginary part of k_z becomes zero at the edge angle. It stays zero on the propagating side and is different from zero on the evanescent side. Plotting

$$\mathrm{Im}(k_z) = \sqrt{(\sqrt{\varepsilon_d}\, k_0)^2 - k_y^2 - (k_x + mG)^2} \tag{2.1.31}$$

as a function of m shows this transition clearly and yields m. Hence in the case of figure 2.11 it is understood that coupling to the 1^{st} diffraction order takes place.

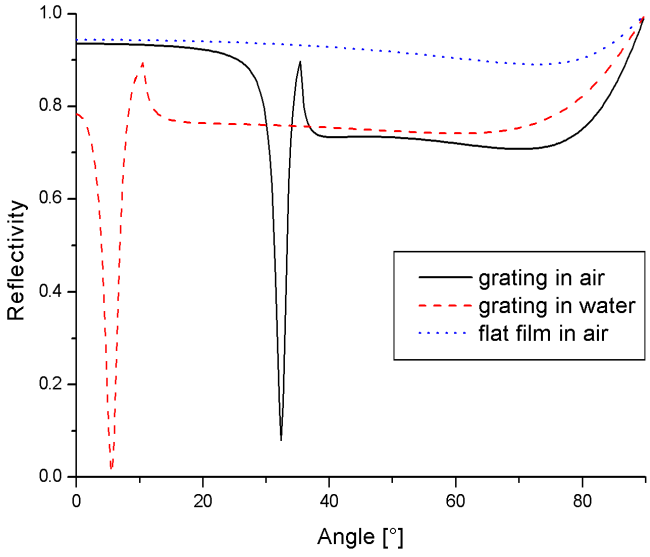

Figure 2.11: Reflectivity of a gold grating. The reflection response of an optically thick sinusoidal gold grating with a grating constant of 400 nm and 20 nm amplitude was calculated. The solid line shows the reflectivity of the grating in air for illumination at $\lambda = 632.8$ nm. The resonance dip occurs at 32.39° with R = 0.08 due to coupling to the 1^{st} diffraction order. The dotted line indicates an uncorrugated surface - a gold mirror. Replacing air with water yields the dashed curve. The resonance angle decreases in this case and reaches R = 0.01 at 5.58°. The same dielectric constants were used as in the previous simulations.

Similar to prism coupling, the reflectivity minimum and the intensity maximum of the total

[11] All calculations for grating coupling are performed under the Rayleigh approximation (refer to section 2.1.8).

electric field[12] do not coincide in grating coupling (see figure 2.12). The reason for this is the same as in the case of prism coupling. Like the edge, the intensity maximum can be situated to the left or to the right of the reflectivity minimum. But unlike for the edge there is no general rule. The position of I_{max} relative to R_{min} depends on the exact shape of the surface corrugation[13]. The magnitude of the angular separation between the two extremal angles depends also on the coupling order and can be as high as several degrees for higher order coupling. The field enhancement in this model system is plotted in figure 2.13. The intensity distribution reaches an enhancement factor of 40 and is characterized by a decay length of about 110 nm. The fundamental difference to prism coupling in the Kretschmann configuration lies in the excitation/detection geometry. Whereas the electromagnetic field tunnels through the gold film in the Kretschmann configuration, in grating coupling the plasmon is excited at the gold surface close to the light source. Thus the evanescent field interferes with the reflected beam and all of its diffracted components. This interference is the reason for the beat-like pattern in the intensity versus distance plot.

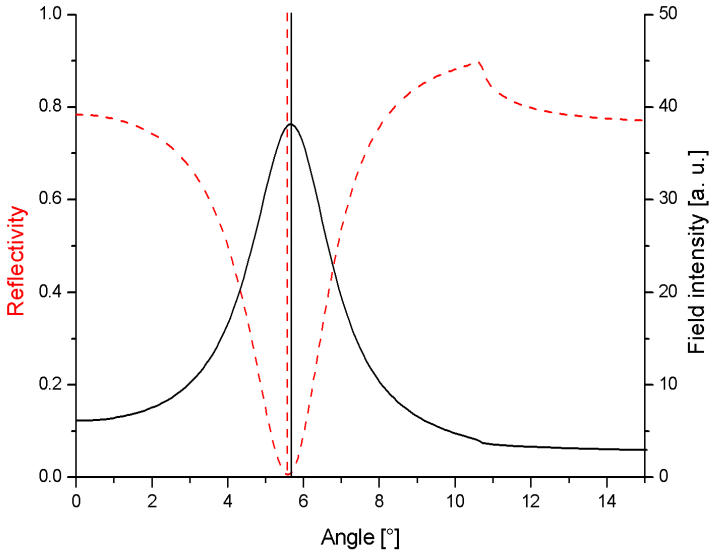

Figure 2.12: Reflectivity and field intensity for grating coupling. The angular separation between the minimum of the reflectivity (dashed line) and the maximum of the total electric field intensity (solid line) also exists in grating coupling. It amounts to 0.1° for the system detailed in figure 2.11. The fields are calculated at 0.1 nm above the weighted central line z=0 (refer to figure 2.17). The x-dependence of the fields is eliminated by averaging over a complete corrugation period.

Similar to the phononic dispersion relation of a crystalline solid, band gaps can appear between the branches of the plasmonic dispersion scheme. Both gaps in energy (i. e. frequency)

[12]Within the framework given in section 2.1.8 it consists of $|\mathbf{E}_{total}|^2 = \left|\sum_{l=-L}^{+L} E_x^{(l)}\right|^2 + \left|\sum_{l=-L}^{+L} E_z^{(l)}\right|^2$ where l indicates the diffraction order and L the order of the expansion providing sufficient convergence of the algorithm.

[13]Section 5.6 sheds more light on this issue and shows what profiles generate which sequence.

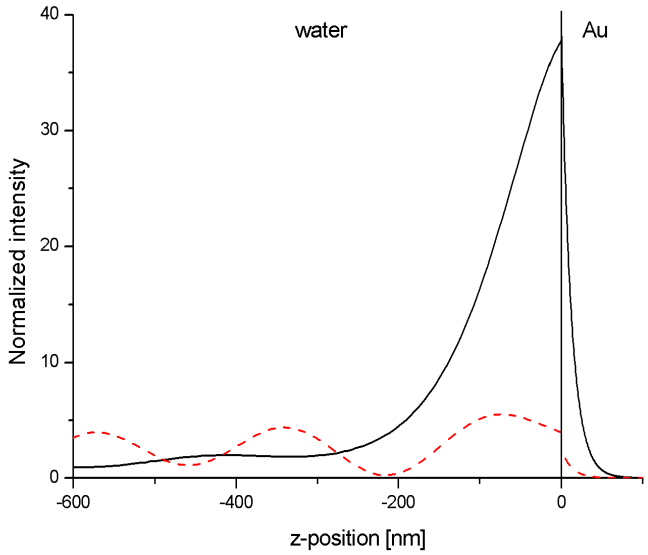

Figure 2.13: Enhancement in grating coupling. Under the resonance condition (solid line, $\theta_r = 5.58°$), the enhancement amounts to a factor of 40 in the water/gold grating system. Because of the superposition of incident, diffracted, refracted and evanescent fields a beat pattern develops in the left half-space. It is more pronounced off the resonance, for example at the edge (dashed line, $\theta = 10.63°$). Both curves are normalized to their respective far field intensity average in the water half-space and result from averaging the fields over the x-axis.

as well as in momentum have been reported [Hei87], [Rae88], [Cel88]. There is an ongoing discussion in the literature about the validity of the latter observation. Some authors claim the appearance of momentum gaps is an artifact and depends strongly on the method employed (scanning the frequency at constant angle versus maintaining the frequency and changing the angle) [Hal89], [Zai91], [Bar96]. Because of this ongoing controversy only a small introduction to energy gaps is given.

Energy band gaps can appear if the grating vector is equal to twice the surface plasmon wavevector. Two standing wave solutions are then possible as sketched in figure 2.14. Because of their different field and surface charge distributions the energy of the two states differs and hence their frequencies split to form an energy band gap like the one shown in figure 2.15. It has been recognized that the presence of second harmonic components in the surface profile is facilitating the gap formation [Fis94], [Bar96]. If an energy band gap is present there exists a frequency interval ranging from ω_- to ω_+, the stop gap, where no coupling between photons and plasmons is permitted. Photonic band gap materials are currently the subject of intensive and widespread study [JOS93], [JOM94]. By employing surface plasmons on structured metal films the design of photonic surfaces is possible by band gap engineering.

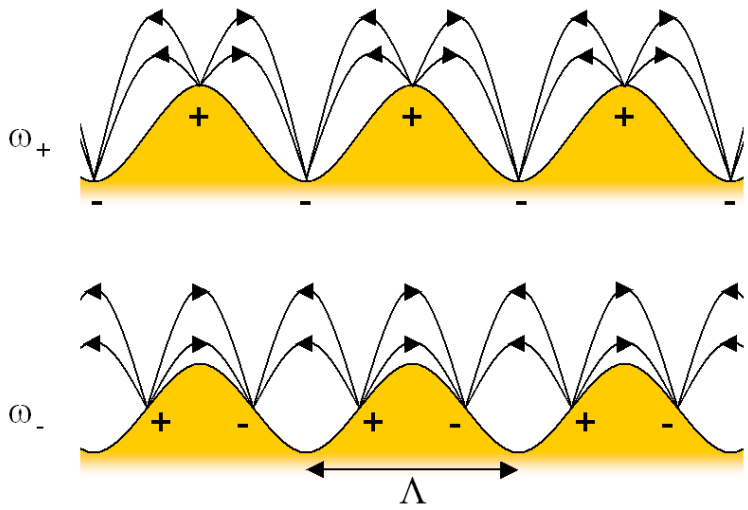

Figure 2.14: Electric field lines of a surface plasmon on a grating surface. For a surface plasmon with a momentum of half the grating vector two standing waves states are possible. They differ in energy and therefore frequency since their field and surface charge distributions are not the same. The solution ω_+ is of higher energy than ω_- because the field is more distorted. The field also extends into the metal with reduced density and thus strength, but this has been omitted for clarity.

2.1.7 Transfer matrix formalism

The reflectivity response of a flat multi-layer film can be calculated via two equivalent mathematical methods: the recursion procedure and the transfer matrix formalism. The former is based on the recursive calculation of the reflection coefficient starting from the last layer and progressing to the first one; a detailed explanation can be found elsewhere [Bec63]. The latter method is explained here, because it forms the basis for the algorithm of the program "Winspall" used in this work for quantitative analysis of prism coupling data and to calculate reflectivity curves, as well as field distributions. At the same time, it provides the basic principles on which the simulation code for grating coupling was built. The expansion of the program for layers with periodically modulated surfaces is covered in the following section.

Consider a system composed of N+1 consecutive layers, divided by N parallel, smooth interfaces like the one sketched in figure 2.16. Within the volume of each layer the electric field is the superposition of two components - the incident and the reflected wave propagating along the positive and the negative z-axis respectively. In a layer i, the electric field can therefore be expressed as

$$\mathbf{E}_i(x,z,t) = \mathbf{E}_i^+ \exp(i[k_x x + k_{z,i} z - \omega t]) + \mathbf{E}_i^- \exp(i[k_x x - k_{z,i} z - \omega t]) \tag{2.1.32}$$

with the following wavevector components:

$$\begin{aligned} k_x &= \frac{\omega}{c}\sqrt{\varepsilon_0}\sin\theta \\ k_{z,i} &= \sqrt{\left(\frac{\omega}{c}\right)^2 \varepsilon_i - k_x^2}. \end{aligned} \tag{2.1.33}$$

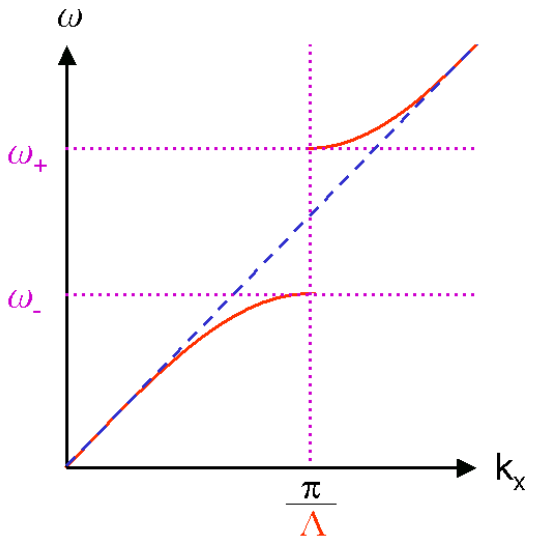

Figure 2.15: The formation of energy band gaps. The different energies related to the two standing wave solutions ω_+ and ω_- of figure 2.14 remove the degeneracy at the Brillouin zone boundary. Instead of dispersion branch intersections, an undulating band structure develops.

The wave impinging on the interface i is hence denoted $\mathbf{E}_i^+$, the reflected wave accordingly $\mathbf{E}_i^-$ and the transmitted wave $\mathbf{E}_{i+1}^+$. For s-polarization as well as for p-polarization it is sufficient for the problem to focus on a single component of the electric field since Maxwell's equations will readily yield the remaining components and also the magnetic field, as described in section 2.1.1. Expanding the annotation by an additional index for the polarization, the quantity $\mathbf{E}_{i,p}^{\pm}$ describes the E_x component in the case of p-polarization and $\mathbf{E}_{i,s}^{\pm}$ the E_y component for s-polarization. In this framework, the propagation of the electric field within the layer i along the z-axis of thickness d_i can be expressed in terms of two matrix multiplications

$$\begin{pmatrix} E_i^+(z_i) \\ E_i^-(z_i) \end{pmatrix}_{p,s} = \begin{pmatrix} \exp(-ik_{z,i}d_i) & 0 \\ 0 & \exp(ik_{z,i}d_i) \end{pmatrix} \begin{pmatrix} E_i^+(z_i+d_i) \\ E_i^-(z_i+d_i) \end{pmatrix}_{p,s} = \mathbf{\Phi}_i \begin{pmatrix} E_i^+(z_i+d_i) \\ E_i^-(z_i+d_i) \end{pmatrix}_{p,s} \tag{2.1.34}$$

with the propagation matrix $\mathbf{\Phi}_i$. Furthermore, the propagation from layer i through the interface to layer i+1 can also be shaped into a matrix equation. Continuity is required for the tangential component of the electric field and for the normal component of the electric displacement. The introduction of

$$\begin{aligned} \kappa^p &:= \frac{\varepsilon_{i+1}k_{z,i}}{\varepsilon_i k_{z,i+1}} \\ \kappa^s &:= \frac{k_{z,i}}{k_{z,i+1}} \end{aligned} \tag{2.1.35}$$

enforces this in a second set of matrix equations:

$$\begin{pmatrix} E_i^+ \\ E_i^- \end{pmatrix}_{p,s} = \frac{1}{2} \begin{pmatrix} 1+\kappa^{p,s} & 1-\kappa^{p,s} \\ 1-\kappa^{p,s} & 1+\kappa^{p,s} \end{pmatrix} \begin{pmatrix} E_{i+1}^+ \\ E_{i+1}^- \end{pmatrix}_{p,s} = \mathbf{Q}_{i,i+1}^{p,s} \begin{pmatrix} E_{i+1}^+ \\ E_{i+1}^- \end{pmatrix}_{p,s}. \tag{2.1.36}$$

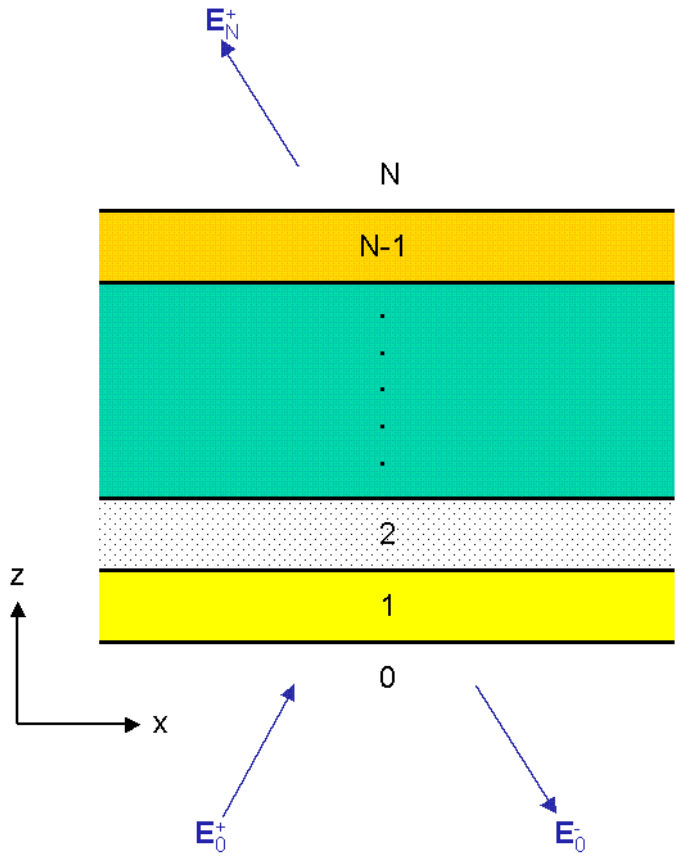

Figure 2.16: A model multi-layer system. The multi-layer stack is composed of N+1 layers, with each layer i having a dielectric constant ε_i and thickness d_i.

Calculating the transition of the electric field through the full stack of layers equates to applying all layer propagators $\mathbf{\Phi}_i$ and all interfacial propagators $\mathbf{Q}^{p,s}_{i,i+1}$ multiplied in the corresponding order. This product matrix is called the transfer matrix $\mathbf{T}^{p,s}$ of the multi-layer system:

$$\mathbf{T}^{p,s} = \mathbf{Q}^{p,s}_{0,1}\,\mathbf{\Phi}_1\,\mathbf{Q}^{p,s}_{1,2}\,\mathbf{\Phi}_2 \cdots \mathbf{\Phi}_{N-1}\,\mathbf{Q}^{p,s}_{N-1,N}. \tag{2.1.37}$$

It gives the relation between the fields in the two outer layers 0 and N. Normalizing all electric fields to the magnitude of E^+_N this relation takes the form:

$$\begin{pmatrix} E^+_0 \\ E^-_0 \end{pmatrix}_{p,s} = \mathbf{T}^{p,s}(\omega, k_x) \begin{pmatrix} 1 \\ 0 \end{pmatrix}. \tag{2.1.38}$$

E^-_N equals 0 since there is no further boundary beyond interface N to cause a reflection. The reflectivity R and transmission T can then be expressed in the matrix elements T_{ij} of the transfer matrix:

$$\begin{aligned} R &= \frac{\left|E^-_0(z_0)\right|^2}{\left|E^+_0(z_0)\right|^2} = \left(\frac{T_{21}}{T_{11}}\right)^2 \\ T &= \frac{\left|E^-_N(z_N)\right|^2}{\left|E^+_0(z_0)\right|^2} = \left(\frac{1}{T_{11}}\right)^2. \end{aligned} \tag{2.1.39}$$

2.1.8 Rayleigh approximation

Several authors have addressed the reflection of light on multi-layer systems with periodically modulated surfaces and several mathematical methods have been developed [Bar96], [Pet80]. Most commonly used among them are the Rayleigh approximation and the Chandezon technique. Chandezon's approach introduces a coordinate transformation in order to flatten the grating and the related boundary conditions. Accordingly, the problem is described with an analog curved set of Maxwell's equations) [Cha82]. In this work, the program `Wingitter`, based on the Rayleigh method, has been used to simulate the reflectivity of gratings, calculate the field distributions and analyze experimental data. It will be outlined here. Additional information about the algorithm can be found in the literature [Pop89], [Mar82], [Tio77]. A substantial advantage of this method is its rapid convergence at high numerical stability. However, it can only be applied to shallow gratings with an aspect ratio (amplitude divided by grating constant) below 0.1 [Pet66]. The program is an expansion of the transfer matrix algorithm described in the previous section for corrugated geometries under the assumption of the Rayleigh approximation. The code was developed in our group and expanded further during this work in collaboration with the programmer [WOR].

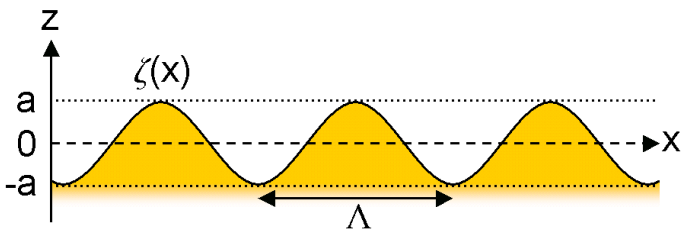

Figure 2.17: The Rayleigh approximation for periodically modulated surfaces. The Rayleigh approximation extends the application of the transfer matrix method to the region containing the corrugation ($-a \leq z \leq a$). All references to the height above the grating are based on the weighted central line z=0. This can be displaced from the middle of a and -a by an amount of $\frac{1}{\Lambda}\int_0^{\Lambda}\zeta(x)\,dx$ if the profile curve $\zeta(x)$ encloses more area in the z ¿ 0 half-space than in the z ¡ 0 region, or vice versa.

The grating surface profile $\zeta(x)$ exhibits the aforementioned translational symmetry

$$\zeta(x + m\Lambda) = \zeta(x) \tag{2.1.40}$$

with m being an integer and Λ the grating periodicity. Consequently, solutions to Maxwell's equations will also feature this symmetry property. An electric or magnetic field $\mathbf{F}$ satisfies the Floquet-Bloch theorem

$$\mathbf{F}(x + \Lambda, z) = \exp(ik_x\Lambda)\mathbf{F}(x, z), \tag{2.1.41}$$

again similar to the theory of solids, where the periodic potential of the lattice results in Schrödinger wave functions fulfilling this theorem [Ash76]. The Floquet-Bloch behavior determines the functional form of the electromagnetic fields. Assuming a harmonic time dependence in the shape of $\exp(-i\omega t)$ the fields can be expanded according to the so-called Raleigh expansion in the interval $0 < x \leq \Lambda$ into a superposition of plane and evanescent waves. The electric

field, for example, adopts the form

$$E_{x,i}(x,z) = \sum_{l=-\infty}^{+\infty} \left(E_{x,i}^{+(l)} \exp(i[k_x^{(l)} x + k_{z,i}^{(l)} z - \omega t]) + E_{x,i}^{-(l)} \exp(i[k_x^{(l)} x - k_{z,i}^{(l)} z - \omega t]) \right)$$

$$\text{with} \quad k_x^{(l)} = k_x + lG \quad \text{and} \quad k_{z,i}^{(l)} = \sqrt{\left(\frac{\omega}{c}\right)^2 \varepsilon_i - k_x^{(l)2}}. \tag{2.1.42}$$

This expansion is fully valid outside of the modulated region ($|z| > a$, see figure 2.17). The grating region ($-a \leq z \leq a$) itself is not homogenous because of the interdigitation of the two different media. Under the Rayleigh hypothesis, the expansion (2.1.42) is extended into the modulation zone[14]. The coefficient fields $\mathrm{E}_{x,i}^{\pm(l)}$ are then determined from the continuity conditions at the interface described by $\zeta(x)$. This can be done by expanding the transfer matrix formalism explained in the previous section.

The cartesian components of the fields can be expressed via $E_{x,i}^{\pm(l)}$ or $E_{y,i}^{\pm(l)}$ for p- or s-polarization respectively:

$$\text{p-polarization} \quad \begin{aligned} E_{z,i}^{\pm(l)} &= \mp \frac{k_x^{(l)}}{k_{z,i}^{(l)}} E_{x,i}^{\pm(l)} \\ H_{y,i}^{\pm(l)} &= \pm \frac{\omega \varepsilon_i}{c k_{z,i}^{(l)}} E_{x,i}^{\pm(l)} \end{aligned} \tag{2.1.43}$$

$$\text{s-polarization} \quad \begin{aligned} H_{x,i}^{\pm(l)} &= \mp \frac{c}{\omega} k_{z,i}^{(l)} E_{y,i}^{\pm(l)} \\ H_{z,i}^{\pm(l)} &= \mp \frac{c}{\omega} k_x^{(l)} E_{y,i}^{\pm(l)}. \end{aligned} \tag{2.1.44}$$

Similarly to the procedure given in equations (2.1.34) to (2.1.38), the electric fields in the 0^{th} and N^{th} layer can be set into relation by a transfer matrix equation for multi-layer systems with one or more layers periodically modulated and exhibiting the same surface profile $\zeta(x)$. For example, let the interface i/i+1 be modulated, the relation takes the form

$$\begin{pmatrix} \vdots \\ E_0^{+(l)} \\ E_0^{-(l)} \\ \vdots \\ E_0^{+(0)} \\ E_0^{-(0)} \\ \vdots \\ E_0^{+(-l)} \\ E_0^{-(-l)} \\ \vdots \end{pmatrix}_{p,s} = \mathbf{Q}_{0,1}^{p,s} \, \mathbf{\Phi}_1 \cdots \mathbf{\Phi}_i \, \mathbf{Q}_{i,i+1}^{p,s}(\{\zeta(x)\}) \mathbf{\Phi}_{i+1} \cdots \mathbf{\Phi}_{N-1} \, \mathbf{Q}_{N-1,N}^{p,s} \begin{pmatrix} \vdots \\ E_N^{+(l)} \\ E_N^{-(l)} \\ \vdots \\ E_N^{+(0)} \\ E_N^{-(0)} \\ \vdots \\ E_N^{+(-l)} \\ E_N^{-(-l)} \\ \vdots \end{pmatrix}_{p,s} \tag{2.1.45}$$

[14]The validity of this hypothesis, its limitations and its merits have been discussed thoroughly in the literature [Bun92], [Pau90]

$$\text{with} \quad \mathbf{\Phi}_j = \begin{pmatrix} \ddots & & & & & \\ & \mathbf{\Phi}_j^{(l)} & & & & \\ & & \ddots & & & \\ & & & \mathbf{\Phi}_j^{(0)} & & \\ & & & & \ddots & \\ & & & & & \mathbf{\Phi}_j^{(-l)} \\ & & & & & & \ddots \end{pmatrix} \tag{2.1.46}$$

$$\text{and} \quad \mathbf{Q}_{j,j+1}^{p,s} = \begin{pmatrix} \ddots & & & & & \\ & \mathbf{Q}_{j,j+1}^{(l)p,s} & & & & \\ & & \ddots & & & \\ & & & \mathbf{Q}_{j,j+1}^{(0)p,s} & & \\ & & & & \ddots & \\ & & & & & \mathbf{Q}_{j,j+1}^{(-l)p,s} \\ & & & & & & \ddots \end{pmatrix} \tag{2.1.47}$$

for j≠i. The $\mathbf{\Phi}_j$ and the $\mathbf{Q}_{j,j+1}^{p,s}$ are 2(2L+1) x 2(2L+1) matrices with the grating Fourier order l running from -L to L. The $\mathbf{\Phi}_j^{(l)}$ and $\mathbf{Q}_{j,j+1}^{(l)p,s}$ are 2 x 2 matrices and resemble (for j≠i) the layer propagators and the interfacial propagators for smooth surfaces analogous to equations (2.1.34) and (2.1.36) with the wavevectors $\mathrm{k}_{z,j}^{(l)}$.

All relevant information about the profile $\zeta(x)$ of the modulated interface i/i+1 is contained in the interfacial propagator $\mathbf{Q}_{i,i+1}^{p,s}(\{\zeta(x)\})$. It can be determined from the continuity conditions at the modulated interface. The surface normal $\mathbf{n}$ given by $\mathrm{grad}(z-\zeta(x))$. The operator for differentiation along the surface normal can be expressed by the cartesian differential operators:

$$\frac{\partial}{\partial n} = \left(1+[\zeta'(x)]^2\right)^{-1/2}\left[\frac{\partial}{\partial z} - \zeta'(x)\frac{\partial}{\partial x}\right] \quad \text{with} \quad \zeta'(x) = \frac{\partial \zeta}{\partial x}. \tag{2.1.48}$$

This allows us to find the tangential components of the electric field amplitudes $E_i^{\pm(l)}$. The continuity conditions at the modulated interface can then be brought into the shape of:

$$\sum_l \mathbf{M}_{i+1}^{p,s} \begin{pmatrix} E_{i+1}^{+(l)} \\ E_{i+1}^{-(l)} \end{pmatrix}_{p,s} = \sum_l \mathbf{M}_i^{p,s} \begin{pmatrix} E_i^{+(l)} \\ E_i^{-(l)} \end{pmatrix}_{p,s}. \tag{2.1.49}$$

In case of p-polarization the relevant fields are $E_i^{\pm(l)} = E_{x,i}^{\pm(l)}$ yielding

$$\mathbf{M}_i^p = \exp(ilGx) \begin{pmatrix} (1-\kappa_i^{(l)})\delta_i^+ & (1+\kappa_i^{(l)})\delta_i^- \\ \varepsilon_i(\zeta'+\kappa_i^{(l)})\delta_i^+ & \varepsilon_i(\zeta'-\kappa_i^{(l)})\delta_i^- \end{pmatrix} \tag{2.1.50}$$

$$\text{with} \quad \delta_i^{\pm} = \exp(\pm i k_{i+1}^{(l)}\zeta) \quad \text{and} \quad \kappa_i^{(l)} = \frac{k_x^{(l)}}{k_{z,i+1}^{(l)}}\zeta' \tag{2.1.51}$$

For s-polarization with $E_i^{\pm(l)} = E_{y,i}^{\pm(l)}$ this results in

$$\mathbf{M}_i^s = \exp(ilGx) \begin{pmatrix} \frac{\omega}{c}k_x^{(l)}\delta_i^+ & \frac{\omega}{c}k_x^{(l)}\delta_i^- \\ -\frac{\omega}{c}k_{z,i}^{(l)}\delta_i^+ & \frac{\omega}{c}k_{z,i}^{(l)}\delta_i^- \end{pmatrix} \tag{2.1.52}$$

Numerical evaluation of the matrix equation (2.1.49) can only be done approximately for a finite number of Fourier components. In order to find the interfacial propagator $\mathbf{Q}_{i,i+1}^{p,s}(\{\zeta(x)\})$, the equation has to be integrated over one period of $\zeta(x)$, normalized and finally inverted. The numerical fidelity of the result depends on the depth L of the Rayleigh expansion and the number of supports used to map $\zeta(x)$.

2.2 Fluorescence

Molecules which absorb radiation in the ultra-violet, the visible range or the near infrared may re-emit light at longer wavelengths. This phenomenon is called fluorescence. Molecules exhibiting it are named fluorophores and are for example polyaromatic hydrocarbons or heterocycles. Fluorescence based detection methods are widely used in the fields of biology, chemistry and medicine and include fluorescence microscopy [Wan96], fluorescence correlation spectroscopy [Hes02], fluorescence recovery after photo bleaching (FRAP) [Joh96], flow cytometry [Giv01] and green fluorescent protein (GFP) expression studies [Tsi98]. One reason for this is the extraordinary sensitivity that can be achieved with fluorescent probes, even down to the single molecule level [Pla97]. The typical long time scale of 10 ns of the fluorescence cycle allows the study of a range of molecular processes that can occur during this period and alter the photophysical parameters of the fluorescence emission. Fluorescence based techniques have also become successful in the life sciences due to the fact that fluorophores are already present in many biological molecules (amino acids like tryptophan and tyrosine in proteins, GFP, cofactors like NADH, riboflavin, etc.) or synthetic dyes can readily be introduced via coupling chemistries acting on proteins, nucleotide bases, membrane lipids, antibodies and much more.

Fluorescently labeled probes are particularly suited for the detection of analyte binding events and many techniques are established that monitor different spectral characteristics of fluorophores. Among them are fluorescence polarization [McG78], fluorescence quenching [Lin97], fluorescence enhancement [Smi77] and fluorescence resonant energy transfer (FRET) [Ull76]. Fluorescence detection is central to this work, as dye-labeled nucleic acids were employed, and therefore, an outline of fluorescence is given here.

2.2.1 Principles of fluorescence

The Jablonski energy level diagram given in figure 2.18 illustrates the absorption and emission of light in a molecule. There are three electronic singlet states S_0 to S_2 representing the ground and the first two excited states. For each of these, there exist several vibrational energy states 0, 1, 2 and so on. The population for each state is given by the Boltzmann distribution and thus only states belonging to S_0 are populated at room temperature. Transitions between these states are indicated by solid vertical arrows and occur quasi instantaneously (in 10^{-15} s). According to the Franck-Condon principle, this is not enough time for the nuclei to respond and move, so the same energy diagram can be used for both absorption and emission.

Upon absorption, the fluorophore is excited to some vibrational level of the first or second

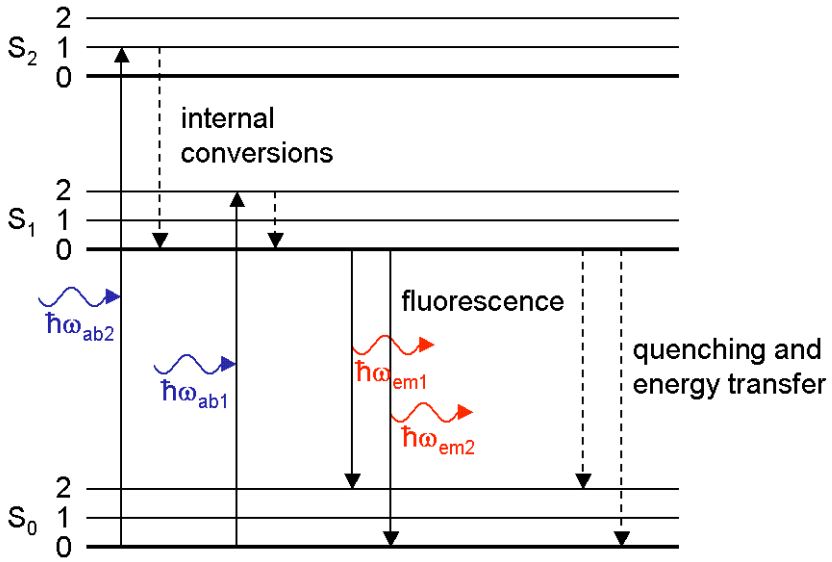

Figure 2.18: Jablonski energy level diagram for fluorescence. The diagram illustrates the transitions taking place within a fluorophore. Absorption of a photon excites the molecule to one of several possible higher electronic states. Rapid internal conversion causes relaxation to S_1 irrespective of the previous state without emission (dashed arrows). From there the final transition occurs via radiating a fluorescence photon. Quenching and energy transfer are competing radiationless processes that allow return to the electronic ground state.

excited electronic state, according to the energy $\hbar\omega_{ab}$ of the absorbed photon. Generally, it will relax to the thermally equilibrated lowest vibrational level of S_1, without emitting radiation by internal conversion, because of the collisions taking place between molecules in condensed phases (dashed arrows). This conversion takes place in 10^{-12} s. Since the final, radiative transition to S_0 takes place in 10^{-8} s, the internal conversion is usually finished before the fluorescence emission takes place. As in the case of absorption, the decay to the electronic ground state can reach an excited vibrational state and result in the emission of photons of different energies $\hbar\omega_{em}$. This creates spectra rather than crisp lines for both processes. Since electronic excitation does not greatly change the structure of the vibrational energy levels, both spectra are very similar and appear as a pair of mirror images. They are separated in energy, because of the energy loss due to internal conversion and because of the final radiative decay, that may lead to an excited vibrational state instead of the ground state. This difference in energy is called the Stoke's shift. The emission spectrum is generally independent of the excitation wavelength since all radiative relaxation happens from the lowest vibrational level of S_1 because of the dissipation that results from the internal conversion.

The energy loss constituted by the Stoke's shift allows us to distinguish between the two species of photons. Their difference in energy translates to different wavelengths. Using the appropriate filter in front of a detector eliminates the excitation light. Ideally, the detector will only record a signal in the presence of a fluorophore.

2.2.2 Quenching

Besides the spontaneous, radiative decay from S_1 to the ground state, there are also other processes that can cause the relaxation of the fluorophore without emission. These can be divided in decay channels that stay nonradiative or become radiative again in the end. FRET is an example for such a radiative process. The energy of the excited electronic state of the original fluorophore (donor) is resonantly transferred to another appropriate fluorophore (acceptor) in close proximity and this second dye molecule emits at another fluorescence wavelength. Those processes that ultimately do not cause emission are subsumed under the term quenching. They contain a variety of different decay channels, for example the excitation of surface plasmon modes or lossy waves [Bar98]. As mentioned before in the case of internal conversion, collisions between molecules can de-excite a fluorophore. Collisional quenching is described by the Stern-Volmer theory [Lak99]. A very efficient collisional quencher is oxygen. Excited states can also undergo reactions that prohibit emission, like charge transfer complex formation. At the same time, excited dyes are easily prone to chemical attack, destroying the system of conjugated double bonds.

In respect to the evanescent field excitation mechanism used in this work, it is very important to examine the behavior of fluorophores in the vicinity of metals. In order to take advantage of the enhanced evanescent field of a surface plasmon, the dye must be placed close to a metallic surface. Metals can also act as generic quenchers. The excited state of the fluorophore can couple to the broad band of electronic states in bulk metal and relax by essentially heating up the metal slightly. Such a decay will not generate a fluorescence photon. For immobilization assays employing the evanescent field as the source of excitation, one inevitably needs to have an understanding of the quenching process.

Classically, the metal/dye interaction is treated similarly to the dipole/dipole interaction governing FRET. This situation is described by the Förster model [Lak99]. For the interaction of two point-like dipoles the energy transfer efficiency depends on the separation d as in d^{-6}. The situation is different in case of an infinitely extended metallic plane. Integration over the plane compensates by a factor of d^2. The overall relation of the emission efficiency η_{em} is given by [Kuh70]:

$$\eta_{em}(d) = \frac{I(d)}{I_\infty} = \left[1 + \left(\frac{d_F}{d}\right)^4\right]^{-1} . \tag{2.2.1}$$

At infinity the dye will not interact with the metal and emit the intensity I_∞. At a finite distance d the emission intensity is I(d). At the Förster radius d_F, the emission intensity reaches 0.5. The curve (see figure 2.19) is characterized by d_F, which depends on the dyes involved. Typically, d_F is about 5 nm. In order to have efficient fluorescence emission, the surface has to be modified in a way that provides a separation of more than one Förster radius between the fluorophores and the metal. In experimental schemes where the enhanced surface plasmon field excites the fluorophores, the distance dependence of the evanescent field has to be considered. The field intensity drops exponentially for an increased distance from the metal surface. The complete fluorescence process samples the distance dependence of both quenching by the metal as well as the evanescent field excitation. An optimal distance exists where the fluorescence

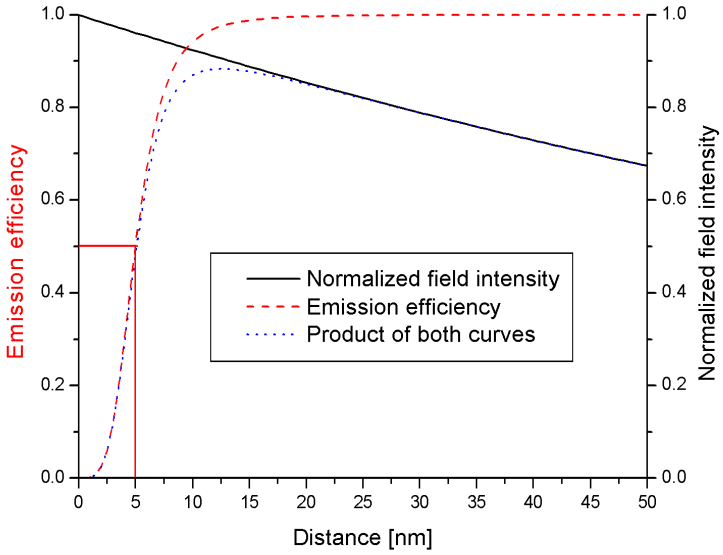

Figure 2.19: Fluorophore emission in proximity to a metal surface. The distance dependence of the mission efficiency of a fluorophore close to a metal surface is shown by the dashed curve. In close proximity to the metal virtually all emission is quenched. With a Förster radius of 5 nm for the dye, half the fluorescence intensity is lost at 5 nm distance. A dye/metal separation of several Förster radii is required for the efficient emission. In the case of SPFS the source of excitation is the evanescent field originating from the metal surface (dotted line). The product of both curves (solid curve) determines the optimal dye/metal separation which equates to about 13 nm for the Kretschmann geometry introduced in figure 2.6.

intensity reaches a maximum. This separation of the dye molecules is achieved by the surface architecture described in section 3.2. The same principle holds true for the reversed process where an excited fluorophore decays nonradiatively by exciting a surface plasmon mode in the metal [Bar98], a concept covered in chapter 5.

2.3 Langmuir model of adsorption

Surface interaction based sensors rely on the immobilization of an analyte from the liquid or the gaseous phase to the sensor surface. It is essential to have an understanding of the nature and dynamics of the surface/molecule interactions for both sensor and assay development. The kinetic parameters describing the immobilization are often the subject of a study themselves. The Langmuir model is one frequently employed way of describing adsorption processes [Atk02], [Lan18]. It is based on four fundamental assumptions:

- The flat, uniform substrate surface provides discrete binding sites for the molecules of interest.
- All binding sites are equivalent and independent of each other, irrespective of the occupation of the neighboring sites.

- Every binding site can only hold one molecule. Adsorption cannot proceed beyond monolayer coverage.

- The phase from which adsorption occurs occupies an infinite half-space and maintains a constant concentration of molecules.

Generally speaking, a dynamic equilibrium exists between the free and the immobilized molecules

$$A_{gas/liquid} + M_{surface} \underset{k_{off}}{\overset{k_{on}}{\rightleftharpoons}} AM_{surface} \tag{2.3.1}$$

with the two rate constants k_{on} and k_{off} for adsorption and desorption, respectively. The surface coverage Θ is a function of time t, these two rate constants and the initial concentration c_0 of the molecule A. In a pure desorption scenario the rate of change of Θ in time is proportional to the number of occupied sites:

$$\frac{\partial \Theta}{\partial t} = -k_{off}\Theta. \tag{2.3.2}$$

For adsorption, a second term consisting of the concentration, the adsorption rate constant and the vacant surface fraction $(1 - \Theta)$ is introduced:

$$\frac{\partial \Theta}{\partial t} = c_0 k_{on}(1 - \Theta) - k_{off}\Theta. \tag{2.3.3}$$

Integrating this equation with the boundary condition $\Theta(0) = 0$ yields:

$$\Theta(t) = \frac{c_0 k_{on}}{c_0 k_{on} + k_{off}} \left(1 - \exp[-(c_0 k_{on} + k_{off})t]\right). \tag{2.3.4}$$

Figure 2.20 (a) illustrates this function. Initially, the surface coverage increases until it reaches an equilibrium value Θ_e. This condition is met for a vanishing time derivative of Θ. Setting equation (2.3.3) equal to zero and solving for the surface coverage we find

$$\Theta_e = \frac{c_0 K_a}{1 + c_0 K_a} \tag{2.3.5}$$

with the association or affinity constant (also called the equilibrium constant) $K_a := k_{on}/k_{off}$. The inverse quantity $K_d := 1/K_a$ is known as the dissociation constant. In the absence of any unimmobilized molecule ($c_0 = 0$), equation (2.3.4) reduces to a pure desorption case:

$$\Theta(t) = \Theta_e \exp(-k_{off}t) \tag{2.3.6}$$

Experimentally this means the solution from which the molecules are resupplied and adsorb to the surface is exchanged with an infinite supply of buffer. In the figure this exchange has taken place after 3 s. For ideal dilution (c_0 stays zero in the solvent), the surface can be stripped again from all the molecules for $t \to \infty$. The corresponding desorption kinetic yields k_{off}. With this knowledge the remaining parameter k_{on} can be derived by fitting the adsorption curve. From the knowledge of these two parameters one can calculated the affinity constant. Alternatively, K_a can be determined from the Langmuir isotherm, i. e. plotting the equilibrium

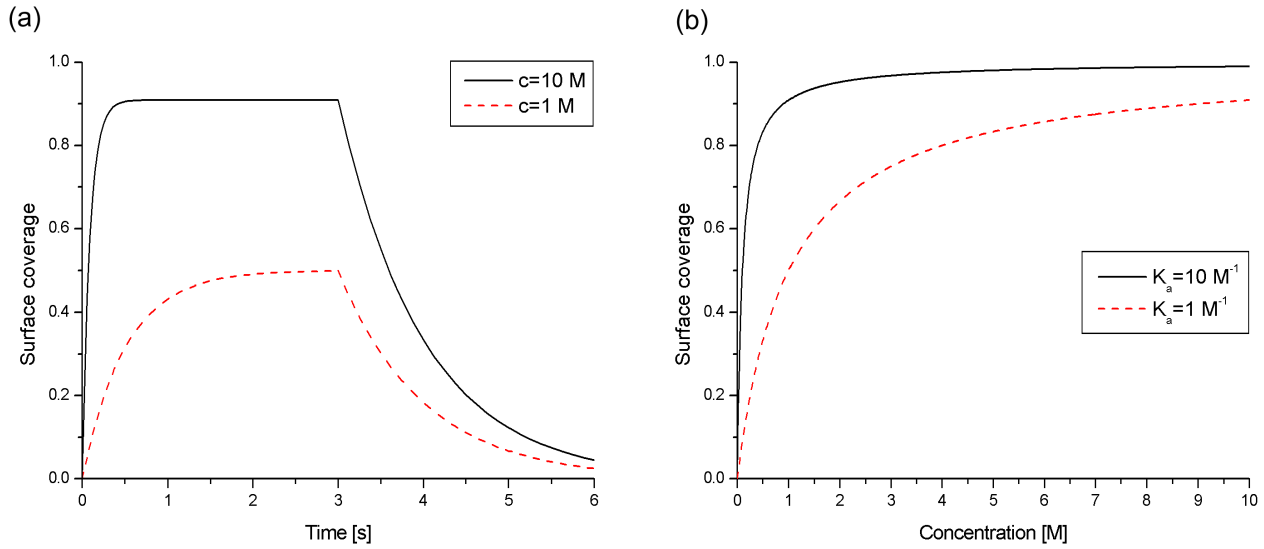

Figure 2.20: Examples of Langmuir kinetic curves and isotherms. (a) The curves in the graph are Langmuir kinetics calculated for the rate constants $k_{on} = 1/\mathrm{Ms}$ and $k_{off} = 1/\mathrm{s}$ (synonymous with $K_a = 1/\mathrm{M}$) and two different concentrations. Lower concentrations result in lower equilibrium surface coverage that is only reached after longer adsorption times. After removal of the adsorbate resupply by rinsing ($c_0 = 0$ after 3 s), desorption of the immobilized molecules takes place. (b) The graph shows Langmuir isotherms, indicating the relationship between the affinity constant and the equilibrium surface coverage for $t \rightarrow \infty$. Systems of higher affinity achieve a higher coverage at lower concentrations. All values are chosen for demonstration purposes only in order to introduce the characteristic curve shapes.

surface coverage versus the adsorbate concentration. This relationship is governed by equation (2.3.5) and illustrated in figure 2.20 (b).

The assumptions of the Langmuir model are based on an idealized experimental situation. Under certain conditions these are not met and the limitations of the model become relevant. One example is mass transport. The presence of the sensor surface with its attached molecular binding architecture introduces a non-stirred layer of solution in its close proximity. If diffusion of the adsorbing species from the mobile phase into the non-stirred phase is slower than the binding interaction, the resulting kinetics will by limited by mass transport. Rate constants determined from a diffusion limited experiment will turn out smaller than values obtained from an unimpeded situation. Mass transport is relevant in a given experiment, if the rate constants decrease for a reduction in flow rate or lower analyte concentrations [Nag00].

2.4 Atomic force microscopy

In grating coupling the shape of the corrugation of the metal surface determines the crucial parameters influencing the plasmon excitation such as the resonance angle and the coupling efficiency. Atomic force microscopy (AFM) is a suitable method to resolve and study the periodic structure of gratings and has been employed in this work for that purpose. Competing methods

capable of sufficient spatial resolution include scanning tunnelling and electron microscopies. The advantage of AFM lies in the absence of any special preparational requirements (like electric connections or vacuum conditions) and in the capability of imaging both conductive as well as insulating substrate topographies.

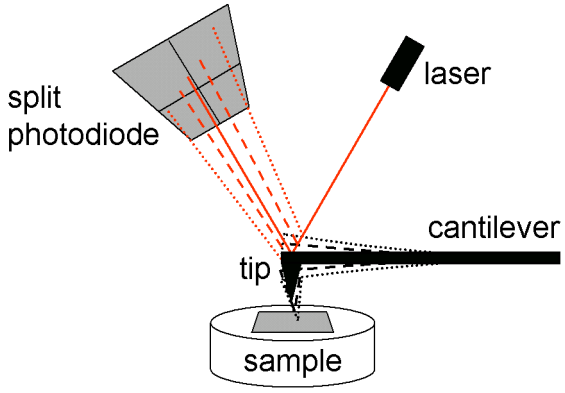

Figure 2.21: Schematic of AFM operation. A laser shines on the back of the tip. The position of the reflected beam is detected with a position sensitive photodiode. Upon presence of a force between tip and sample, the cantilever bends and the reflection spot moves. In tapping mode AFM, the cantilever is brought to resonant vibration and deviations from the free oscillation amplitude are monitored.

Atomic force microscopy, also known as scanning force microscopy, was developed in 1986 by Binnig, Quate and Gerber [Bin86]. It is an instrument that is utilized today on a routine basis for the characterization of surface features below optical resolution. Therefore, only a quick introduction to the technique shall be given here; further information is readily available elsewhere [Sar91], [Wie94]. The sample is scanned by a microfabricated tip mounted on the end of a cantilever spring. A laser beam is focused on the opposite side of the cantilever and its reflection is monitored with a split photodiode as illustrated in figure 2.21. In response to a force between the tip and the sample the cantilever bends. As it flexes, the reflected laser spot moves and the intensities measured on the four segments of the split photodiode change. The movement of the tip can be found from linear combinations of the photocurrents. Applying Hooke's law for small displacements, the forces acting on the tip can be obtained. With scanners built from piezo-electric ceramics, sub-Angstrom resolution can be achieved.

There are several modes of operation for AFM: images are usually taken in contact, non-contact or tapping mode. The latter was used in this work. In tapping mode, the cantilever is driven to vibrate at its resonance frequency. The height is adjusted in a way that the tip is in contact with the surface during the lower segment of its oscillation trajectory. Contacting the sample will reduce the amplitude of the vibration. The tip height is regulated in tapping mode in a way to achieve a constant vibrational amplitude, smaller than the value of the free vibration, while scanning the surface. This type of operation provides high lateral resolution. Lateral forces are avoided and contact time between sample and tip is low. Hence damage to the sample from scraping, friction and long contact times is avoided at the cost of slightly lower scan speeds compared to contact AFM.

Chapter 3

Experimental

The experimental techniques common to all the following chapters are outlined here. First the grating fabrication method is explained, including photolithographic and reactive ion beam etching process steps. The surface functionalization necessary to turn a gold surface into a biologically compatible and molecularly specific sensor surface are described next, together with a background on the individual molecular species employed. The experimental set-up used for SPR and SPFS measurements is explained and its different measurement modes are detailed. The chapter concludes with a description of the flow cell design used in immobilization experiments.

3.1 Grating fabrication

Historically, diffraction gratings have been manufactured mechanically. For certain applications, this is still done today. The grating grooves are ruled by diamonds in glass substrates by vibration damped machines in a process that is very sensitive to environmental factors like changes in temperature and atmospheric pressure [Pal02]. The ruling cycle can last from one day to six weeks.

Alternatively, gratings with grating constants and amplitudes suitable for plasmon coupling can be manufactured via photolithography in a clean room over the course of two days according to the steps illustrated in figure 3.1. Initially, the grating structure is holographically formed in a photoresist film. The pattern is then transferred into the substrate material by ion milling. Adding a gold film of suitable thickness on top of the corrugated surface completes the coupling grating. During a binding experiment, the gold will be irreversibly (for all practical purposes) contaminated due to the surface functionalization chemistry. Since the gold can easily be removed again from the glass without substrate attrition, new evaporation of gold allows multiple usage of a single grating. Every specimen used in this thesis is listed in appendix A together with its coupling efficiency and grating constant for reference.

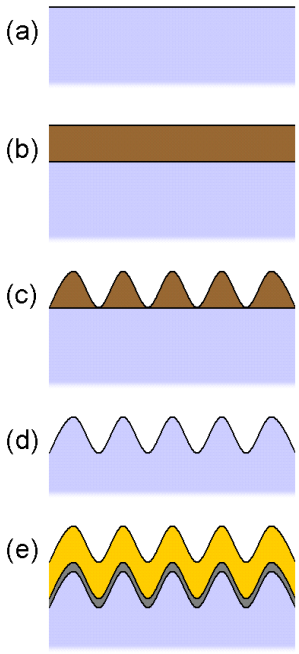

Figure 3.1: The different steps of grating fabrication: (a) cleaning of the substrate, (b) deposition of a photoresist film by spin coating, (c) writing of the grating profile with an interference pattern, (d) transfer of the surface relief into the glass by reactive ion beam etching, (e) chromium and gold evaporation. Grating substrates with a corrugated glass surface can be stripped from the metal layers, cleaned and coated again.

3.1.1 Substrate cleaning

Glass substrates (BK-7 microscope slides, Menzel-Gläser [MEN]) were carefully wiped clean from any visible dust or stains with a soft tissue and thereafter underwent this cleaning procedure:

- 10 x rinsing in purified water (18.2 MΩ cm, produced with Milli-Q plus 185, Millipore [MIL])
- 15 minutes sonication in 2 % detergent (Hellmanex, Hellma [HEL]) at 30° C
- 15 x rinsing in purified water
- 5 minutes sonication in ethanol (HPLC grade, Fisher Scientific [FIS])
- drying under a flow of dry nitrogen

For optimal results, it is imperative to work with clean substrates as well as in a clean environment. Therefore all the following grating manufacture steps were performed in a clean room (class 100).

3.1.2 Photoresist deposition

Prior to spin coating the substrates with the photoresist, the glass surface was treated with a primer silane (Microposit UN 2924, Shipley, now a division of Rohm and Haas Electronic Materials [ROH]) to improve photoresist adhesion. The substrate surface was covered with the primer and left to interact for 30 s. Excess solution was then removed by spinning the sample for 1 minute at 3000 rounds per minute (rpm). The photoresist (ma-P 205, microresist [MIC]) was applied directly afterwards. To reduce viscosity, the photoresist was diluted with an equal volume of thinner (Microposit EC-solvent, Shipley, ditto). A film thickness of approximately 100 nm was adjusted by spinning the substrate at 3500 rpm for one minute. Remaining solvent was removed by heating the sample in a vacuum oven at 95° C for 30 minutes (soft baking).

3.1.3 Holographic grating manufacture

Photolithography combined with holographic exposure is a feasible method to manufacture gratings [Rud70], [Mai85]. In order to introduce a periodic illumination condition, the photoresist was exposed to an interference pattern generated with the set-up shown in figure 3.2. Black adhesive tape was glued flush (avoiding any bubbles) on the backside of the sample to prevent reflections from the backside to interfere. A mirror was clamped perpendicular to the sample surface and both were mounted on a rotary stage. The beam of a helium-cadmium laser (λ = 441.6 nm, 35 mW, 4270 NB helium-cadmium laser, LiCONiX, now a division of Melles Griot Inc. [MEL]) was passed through a beam expander and a spatial filter. The Gaussian intensity profile of the parallel beam was limited by an iris to the inner part of the beam waist where the intensity profile is nearly constant. One half of this uniform beam illuminated the photoresist directly; the other half struck the mirror first, where it was reflected and then hit the sample. According to the phase difference between these two beams they interfered either constructively or destructively on the substrate surface. Since the beams were expanded and illuminated an extended surface region, a range of phase differences was present, generating a sinusoidal interference pattern. This method produces semicircular gratings with a diameter of up to 2 cm. The periodicity Λ depends on the path length difference between the two beams, determined by the tilt angle α between the optical axis and the surface normal:

$$\Lambda = \frac{\lambda_{HeCd}}{2 \sin \alpha}. \tag{3.1.1}$$

Next is the development of the pattern. The chosen photoresist was of the positive variety. Thus exposure to the laser light induces a photochemical reaction in the photoresist that promotes solubility in the developer solution (ma-D 330, microresist [MIC]). The remaining unilluminated material remains insoluble. According to the sinusoidal intensity profile of the interference pattern, solubility was periodically introduced in the film. Immersion in the developer reagent translates the solubility contrast into a surface relief grating by solving the illuminated regions. Optimal illumination and development times depend strongly on the laser power. Both were typically in the order of 30 s, but had to be determined precisely again for each batch. Excess developer was removed by rinsing with purified water. The remaining

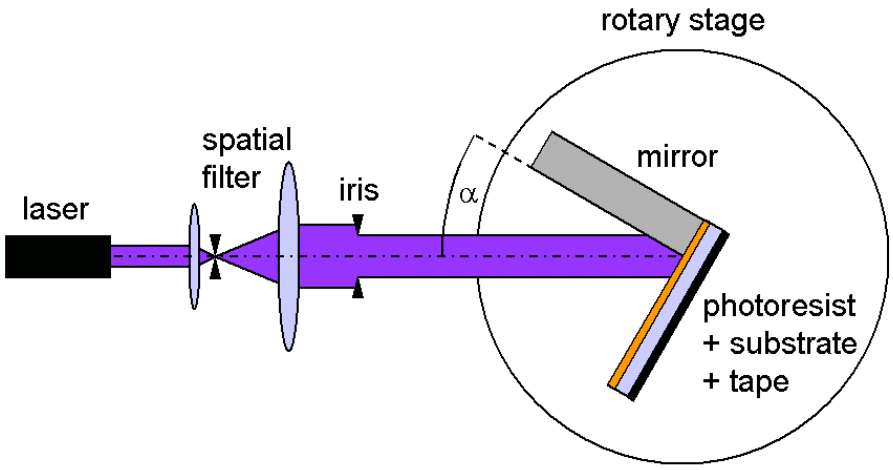

Figure 3.2: Holographic grating manufacture. Gratings were manufactured from a photoresist film by exposure to an interference pattern generated from the superposition of a HeCd laser beam and its reflection off a mirror.

photoresist regions were cured by heating the substrates at 110° C for 30 minutes in a vacuum oven (hard baking). This treatment activates a thermoinitiator in the material, facilitating cross-linking.

3.1.4 Grating transfer

Since the grating writing and development steps can result in products from a quality range that is not always as narrow as appreciated, it is well worth to invest a little more work in order to enable multiple use of a good specimen. For this reason, the surface relief grating written into the photoresist was transferred into the underlying glass by reactive ion beam etching (RIBE). Corrugations shaped in the soft photoresist can be evaporated with a noble metal and used for grating coupling once. Removal of the metal will destroy the grating. The transfer of the structure into the hard glass substrate yields gratings in a more durable form that can be used, cleaned and re-evaporated many times.

The working principle of the RIBE system (RR-I SQ76, Roth & Rau [ROT]) is sketched in figure 3.3 [Lie94], [Sug98]. Electrons are ejected from the cathode within the discharge chamber and are accelerated to and through the anode ring due to its higher potential. A dilute flow of O_2 and CF_4 is passed through the opposite part of the chamber. Upon collision with the gas molecules, the cathode beam strips them of electrons and ionizes them. Positive ions from this plasma are pulled in the direction of the screen grid at ground potential. Passing this grid, they are accelerated further by the negative potential of the acceleration grid that also serves as a focussing element. The ions hit the sample perpendicularly as a parallel beam with a diameter of about 7 cm. To prevent charging of the probe, negative ions and electrons are injected by the plasma bridge neutralizer. The plasma etches into the sample in two ways: first, the pure bombardment of ions ablates the material. Additionally, radicals from the plasma chemically decompose both photoresist and glass. The composition of the reactive gases O_2 and CF_4 is

optimized to attack glass. One has to keep in mind that a difference in etching rates between photoresist and glass of about a ratio of 2:1 exists [Ron91], distorting the pattern transferred from the photoresist into the glass.

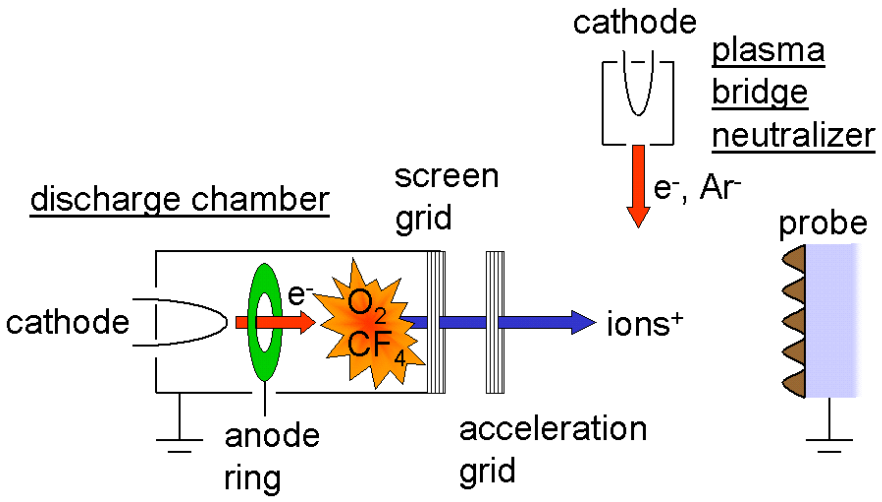

Figure 3.3: Schematic of reactive ion beam etching. The process allows to transfer the surface relief formed from photoresist into the glass substrate. An electron beam ionizes O_2 and CF_4 molecules to yield reactive ions that are suitable for etching into glass. These are accelerated towards the probe where material is removed either due to the particle bombardment or by chemical reaction with the ions.

The exact parameters used for operating the RIBE system are the following:

- Discharge voltage: 100 V
- Discharge current: 0.55 A
- Beam voltage: 600 V
- Beam current: 0.4 A
- Acceleration voltage: 200 V
- Acceleration current: 0.05 A
- Plasma bridge neutralizer voltage: 16 ± 4 V
- Plasma bridge neutralizer current: 0.53 A
- Probe current: 0.52 ± 0.05 A

To reduce the heat load on the sample, the total etching time was broken down into two 25 s periods with a 30 s cooling break in between. After the etching, any remaining photoresist was removed by exposing the substrate to a remover solution for 5 minutes (PRX-417, Shipley, now a division of Rohm and Haas Electronic Materials [ROH]).

3.1.5 Metal evaporation and removal

A thermal evaporation chamber (FL400, BOC Edwards [BOC]) equipped with a quartz crystal microbalance to monitor the film growth was used for evaporation. First a chromium layer of 2 nm was evaporated (0.2 nm/s evaporation rate, 1.5 x 10^{-6} mbar pressure) on the corrugated glass surface, followed by 150 nm of gold (both metals of 99.99 % purity, Leybold Optics [LEY]) at the same rate. Fresh samples were stored in sealed coloration vessels under dry nitrogen to protect them from contamination, for example by airborne thiols. The chromium layer promotes adhesion between the substrate and the successive gold film, especially useful when working with saline buffer solutions. At this thickness the gold film can be considered optically opaque and surface plasmons excited on the gold face will not sample the refractive index of the glass substrate on the opposite side.

After having performed binding experiments with a sample, the gold surface is contaminated with the chemicals (namely thiols) used to functionalize the surface that are unremovable in practical terms. In order to reuse a grating sample both metal layers can be stripped chemically and the sample can be coated again. A solution containing 0.24 M potassium iodine and 0.04 M iodine (both from Sigma-Aldrich [SIG]) will remove 100 nm of gold in 1 to 3 hours, depending on the age of the solution. The chromium layer was removed by immersing the sample in a 0.36 M solution of ammonium cerium(IV)nitrate (Sigma-Aldrich, ditto) for a couple of minutes. Stripped samples were cleaned according to the procedures detailed in section 3.1.1 excluding the sonication steps[1]. Finally, new metal layers were evaporated upon the substrates.

3.2 Surface functionalization

The purpose of the surface functionalization is twofold: to provide sensor specificity and optimal spacing. Biological molecules can show a variety of nonspecific interactions and will adsorb to surfaces in an uncontrolled fashion. Particularly for sensor surfaces, it is important to possess the right surface functionalization so specific binding becomes the dominant process and false response is suppressed. Additionally, in the case of fluorescence detection schemes utilizing surface plasmon excitation, it is necessary to engineer the optimal dye/metal separation with a spacer architecture, in order to prevent quenching of excited dyes by the metal film (see 2.2.2).

These two requirements were fulfilled with a self-assembling multi-layered architecture sketched in figure 3.4. First, a monolayer of two different thiols was applied to the corrugated gold surface. One thiol species was end-capped with a biotin group and used for subsequent binding steps. The other type served only as a lateral spacer. Next streptavidin was bound to the biotinylated thiols. Its remaining binding pockets were used to immobilize a biotin terminated DNA probe sequence. This concludes the DNA sensor build-up. Fluorescently labeled DNA target strands of complementary sequence can bind to the sensor surface by hybridization to the probe strand and will be located at the optimal distance for the trade-off between maximum

[1]There are warnings in the literature that sonication of corrugated substrates may harm the grating [Sch00]. Ultra sound was therefore not used during the cleaning of slides that already carry a grating profile.

electric field intensity and minimized quenching. This biological functionalization of the sensor surface constitutes a direct assay, i. e. the analyte molecule carries the fluorescent label itself. Dye and analyte concentration are identical in this case. Other formats like sandwich assays exist, in which the unlabeled analyte adsorbs to the surface first and a fluorescent molecule binds to the analyte in a second, separate reaction step. In a sandwich assay the concentrations of both have to be distinguished, which can lead to different results, especially in the context of bulk fluorescence contributions. Most of the experiments in this work are performed with the direct DNA assay described subsequently.

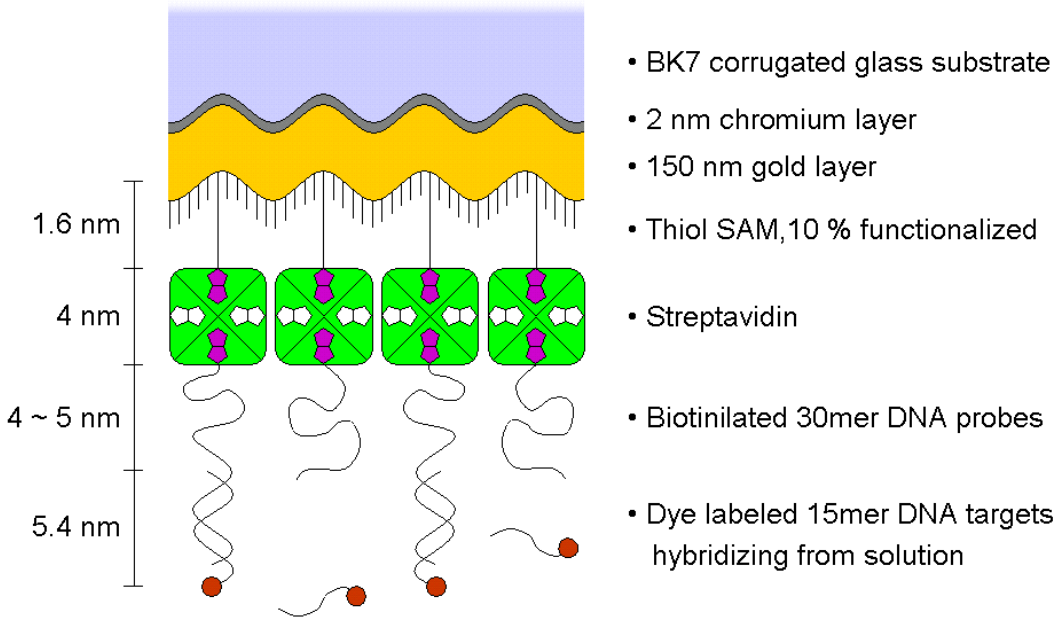

Figure 3.4: Biomodification of the sensor surface. The figure sketches the individual layers of the functionalization architecture with some artistic freedom. It is schematic and not to scale. In fact the gratings are of very small aspect ratio (grating constant between 475 and 515 nm versus a typical amplitude of 20 nm) and the subsequent layers are mimicking the underlying undulations.

3.2.1 Thiol SAM

Self-assembled monolayers (SAMs) are two-dimensional molecular assemblies of a surfactant that form spontaneously upon immersion of a substrate [Ulm91] into a solution. SAM formation is mainly driven by the chemisorption of the surfactant head group on the substrate. The stronger and more exothermic the interaction is, the more likely and faster the surfactant will occupy all available binding sites on the surface. Additionally, interactions between the surfactant tails, like van der Waals interaction between alkyl chains or the dipole/dipole interaction between polar groups, can promote film assembly. The most common surfactant/substrate combinations are alkanethiols on gold, silver and copper where the interaction is based on the covalent sulfur/metal bond. Other head group functionalities include alcohols on platinum and fatty acids on oxidic materials. SAMs of alkanethiols and gold are easily prepared and

relatively stable when compared to other monolayer formation techniques like the Langmuir-Blodgett method for example. For this reason they have been chosen in this work to tailor the dye/metal layer spacing by selecting an alkyl chain of desired length. Alkanethiol SAMs on gold have been extensively studied during the last two decades by many groups. Among the characterization methods used are ellipsometry [Bai89a], electrochemistry [Chi90], infra-red spectroscopy [Por87], electron diffraction [Str88] and scanning tunneling microscopy [Wid91].

In order to adjust the binding site density for the subsequent streptavidin layer, a mixed SAM was used. A 5 mM solution of the biotin functionalized thiol 12-mercapto(8-biotinamide-3,6-dioxaoctyl)dodecanamide (Roche Diagnostics [ROC], but discontinued) was mixed at a ratio of 1:9 with a 5 mM solution of the spacer thiol 11-mercapto-1-undecanol (Sigma-Aldrich [SIG]). The chemical structure of both molecules are shown in figures 3.5 and 3.6 respectively. This binary mixture was then diluted to achieve a total thiol concentration of 50 μM. In all cases the solvent was HPLC grade ethanol. This 1:9 ratio, favoring the spacer thiol, is reported to generate the optimal surface density of the biotin functionalized thiol to allow for maximum streptavidin monolayer surface coverage [Spi93], [Pis95], [Mit95]. At lower surface concentrations, fewer binding sites are available. Increasing the concentration beyond a certain point results into a reduced number of binding sites. Since the binding of biotin to streptavidin requires entry of a major part of the biotin molecule into the binding pocket of the protein, steric hindrance by closely packed neighboring biotin endcaps can reduce the streptavidin surface density.

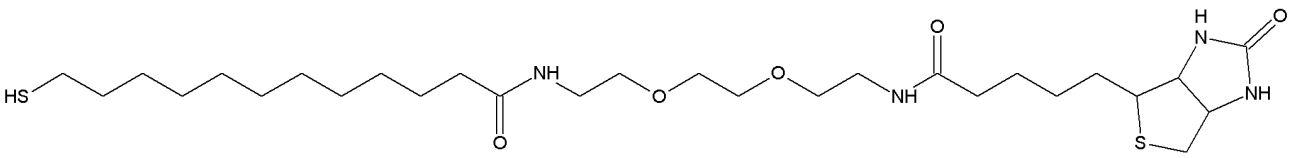

Figure 3.5: Biotinylated thiol: 12-mercapto(8-biotinamide-3,6-dioxaoctyl)dodecanamide, $M_g = 588.88$

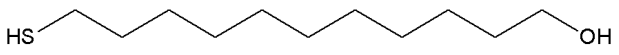

Figure 3.6: Spacer thiol: 11-mercapto-1-undecanol, $M_g = 204.38$

To form a SAM on the metal evaporated gratings, the corrugated side of the substrates were wetted with the 50 μM solution and left over night (t $\simeq$ 10 h) in a closed incubation cell. This results in a closely packed, ordered assembly of the thiol molecules on the gold with the alkyl chains being uniformly oriented at 30° relative to the surface normal. Analysis of this SAM indicates that the monolayer consists of a random distribution of the two thiol species without phase separation. Properties like the effective (optical) film thickness and hydrophobicity can be varied continuously by changing the mixing ratio [Bai89b], [Bai89c].

3.2.2 Streptavidin and biotin

The interaction between the protein streptavidin and the ligand biotin is exploited in many important biotechnological applications and diagnostic assays. One reason for the widespread use of the streptavidin/biotin system is the extraordinary high affinity of the interaction ($K_d \simeq 10^{-15} M$ [Gre75]). The related free energy of association is one of the largest known for noncovalent protein/ligand binding. Additionally, biotin can easily be chemically altered to allow for derivatisation of the molecule. Two different biotin derivatives are used in the functionalization assay described here to bind to streptavidin: a biotinylated thiol as part of the SAM and a biotinylated DNA sequence as the probe component of the sensor.

Streptavidin (SA) is a tetrameric protein with a molecular weight of 4 x 15 kDa isolated from the bacterium *Streptomyces avidinii*. One streptavidin molecule can bind four molecules of biotin. Two binding sites each are located on two opposing faces of the protein and are arranged in a tetrahedron. The capability of building molecular architectures from alternating streptavidin/biotin building blocks stems from this geometric property. In its crystalline form the protein has a size of 5.6 nm x 4.2 nm x 4.2 nm [Ebe90]. The structure has been mapped by X-ray crystallography [Hen89] yielding the conformation shown in figure 3.7 [Fre97]. In nature, streptavidin (and its counterpart avidin found in egg-white) serves to deplete the environment of biotin, also known as vitamin H. With its isoelectric point close to neutrality streptavidin exhibits less nonspecific binding than avidin. Nevertheless nonspecific binding of streptavidin on surfaces of gold and polystyrene has been reported resulting in thick protein layers [Wil90]. For building a robust and reproducible architecture it is preferable to immobilize both the streptavidin as well as the consecutive layer via the streptavidin/biotin interaction. In the biological context this interaction is pratically irreversible. The ligand biotin (see figure 3.8) reaches 1-2 nm into the host protein to form multiple hydrogen bonds and allow for additional van der Waals interactions. A further reason for the high affinity of the binding reaction is the structural change of parts of the protein surface to partially bury the ligand in the protein interior [Web89]. The carboxylic group protrudes from the binding site. Hence biotin derivates in which the carboxylic functionality has been exploited to couple to other small molecules can still be used to bind to streptavidin.

Streptavidin (Roche Diagnostics [ROC]) was immobilized from a 1 μM solution. The protein was dissolved in phosphate-buffered saline (PBS) buffer solution containing 0.137 M NaCl, 0.0027 M KCl and 0.01 M phosphate buffer with a pH of 7.4 at 25° C. In combination with the above stated functionalized binary thiol SAM a protein surface coverage of about 53% has been reported [Spi93], equalling a binding site density of $4.5 \times 10^4\, \mu m^{-2}$.

3.2.3 DNA

Deoxyribonucleic acid (DNA) is a linear biopolymer carrying the genetic instructions for the biological processes taking place in all cellular forms of life and some viruses [Alb02], [Lod04]. DNA is built from four different types of nucleotide subunits forming a four letter code that contains the information for protein expression. Via the molecular genetic processes

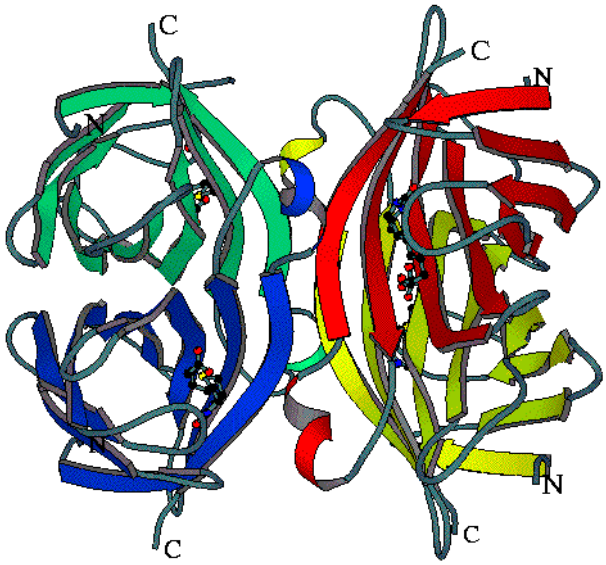

Figure 3.7: Streptavidin. The protein consists of four subunits, each capable of binding a single biotin molecule with very high affinity. Conformation according to [Fre97].

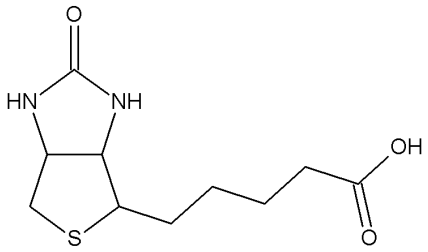

Figure 3.8: Biotin. Only the left part of the biotin molecule enters streptavidin and takes part in the interaction. The carboxylic functionality can therefore be used to attach other molecules.

of transcription and translation it is converted into the 20 letter amino acid language making up proteins. The building blocks of DNA consist of an organic base, a sugar (deoxyribose) and a phosphate group. The backbone is composed of an alternating deoxyribose-phosphate sequence illustrated in figure 3.9. A phosphate group connects to the 3' carbon and to the 5' carbon of adjacent sugar molecules. This chemical linkage is commonly called a phosphodiester bond. It creates an end-to-end chemical orientation similar to polypeptides. Because the synthesis of DNA in nature proceeds from the 5' end to the 3' end, polynucleotide sequences are commonly written in the same direction. The four bases are of two different types. Adenine and guanine are purines, cytosine and thymine are pyrimidines. The bases are attached to the 1' carbon atom of the sugar via the nitrogen atom at position 9 (in case of a purine) or position 1 (for a pyrimidine).

Native DNA consists of two polynucleotide strands with antiparallel orientation. The strands are held in formation by the interaction of opposing bases. Adenine (A) is paired with thymine

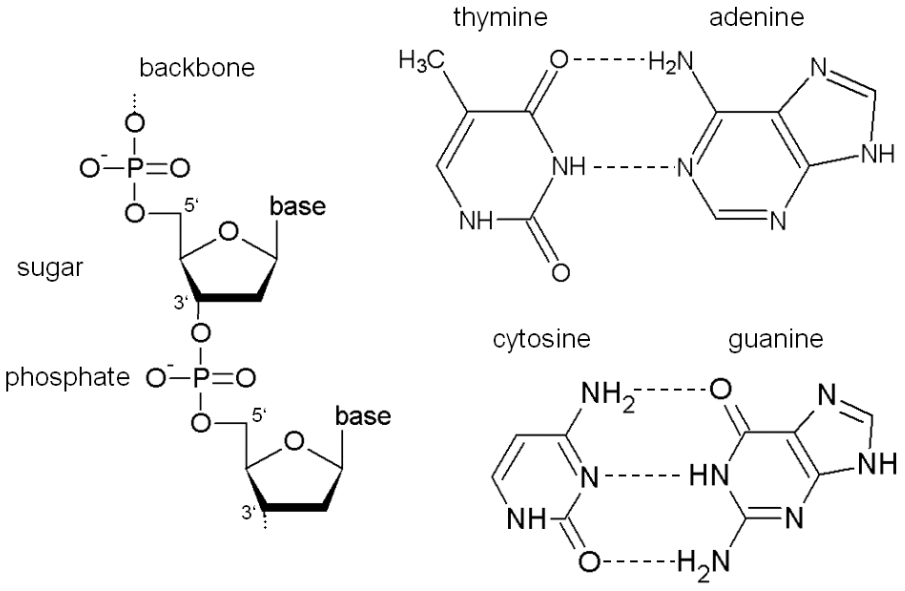

Figure 3.9: The structure of nucleic acids. The backbone of DNA is formed by an alternating copolymer of phosphate groups and sugars. One of the four possible bases is connected to every sugar. For two complimentary strands the one strand will provide a purine and the other one a pyrimidine. A pair of bases from these two classes develops a double or triple hydrogen bond (dashed lines), according to the exact type of base pair.

(T) through two hydrogen bonds also shown in figure 3.9. Three hydrogen bonds are responsible for pairing guanine (G) and cytosine (C). The two DNA strands are of complementary sequence, if the opposing number of every base is the right partner to allow for this double or triple hydrogen bonding respectively. The nucleotide (and thus base) sequence determines the primary structure of DNA. The secondary structure is that of a double helix. It is a consequence of the bond geometry dictated by the multitude of hydrogen bonds present in a double strand and the hydrophobic and van der Waals interaction between stacked adjacent base pairs. The radius of the helix is about 2 nm. Every base pair contributes approximately 0.34 nm to the total length. At pH = 7 the two phosphate groups of each base pair are deprotonated. DNA is therefore a polyelectrolyte with a substantial charge.

The association of two complementary single strands is also called hybridization. Internal factors like the length of a sequence, the ratio of G-C to A-T and base pair mismatches (combinations other than G-C or A-T) all affect the stability of the hybridized state. On the other, hand it can be influenced and even be dissociated by certain environmental influences like ionic strength of the solvent, temperature and pH. These parameters can easily be controlled in the lab environment. It is especially useful to be able to separate strands in order to regenerate and later reuse a sensor surface.

The sensor surface was built from a 30-mer DNA sequence (all DNA samples were purchased from MWG, [MWG]). It carried a biotin functionality at the 5' end (see figure 3.10) to allow immobilization on the underlying streptavidin layer and serve as the probe. The first 15 bases were all thymines providing separation from the protein layer to facilitate access to the second half of the probe strand. The remaining 15 bases represent the recognition sequence for

hybridization. There are two different types of dye-labeled target oligonucleotides: the zero mismatch (MM0) strand and an inert sequence (MM15). The inert strand is a MM10 sequence in respect to the probe oligonucleotide, since it allows five T-A base pairs to form. The melting temperature of MM10/probe and various "real"[2] MM15/probe duplexes (at 25° C, both strands present in a concentration of 500 nM in PBS buffer solution) is -273.1° C. Compared to the melting temperature of MM0/probe of 45.3° C, MM10 behaves like MM15 for all practical purposes. Both types of target strands are attached at the 5' end to one molecule of the cyanine dye Cy5 (refer to figure 3.11 for its chemical structure) that can well be excited by the HeNe laser line. The absorption and the emission spectra of the fluorophore are given in figure 3.12. All three oligonucleotides were solved in PBS buffer solution. The probe strand was typically immobilized on the surface from a 500 nM solution whereas target concentrations varied according to the particular experiment.

Probe	Biotin-5'-TTT TTT TTT TTT TTT TGT ACA TCA CAA CTA-3'
MM0 target	3'-ACA TGT AGT GTT GAT-5'-Cy5
MM15 target	3'-ATA CCG AAT CCG TGT-5'-Cy5

Figure 3.10: Sequences of probe and target strands. The probe strand forms the interaction site of the biosensor. The mismatch zero target is the sequence complementary to the probe. An inert target was also used to quantify background levels.

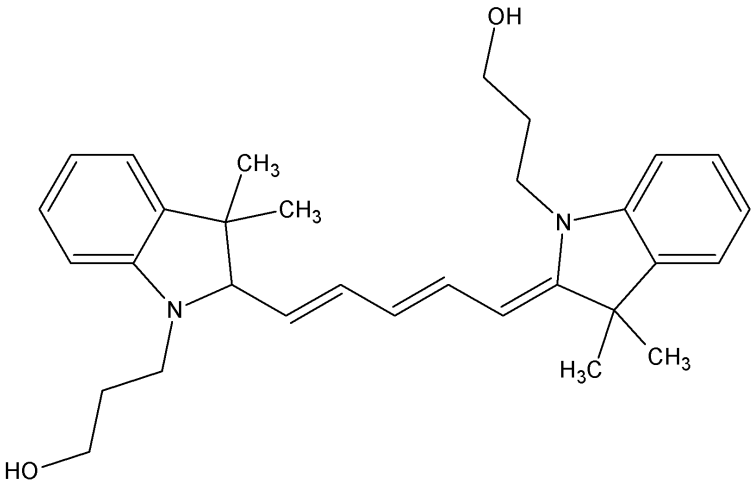

Figure 3.11: Cy5. The dye molecule can be attached to the phosphate group of a DNA strand via an ester bond to one of its hydroxylic functionalities.

[2]Many types of fully incompatible sequences are imaginable. Yet for strands of 15-fold mismatched bases the exact chemical composition has only a negligible influence on the melting temperature of the duplex.

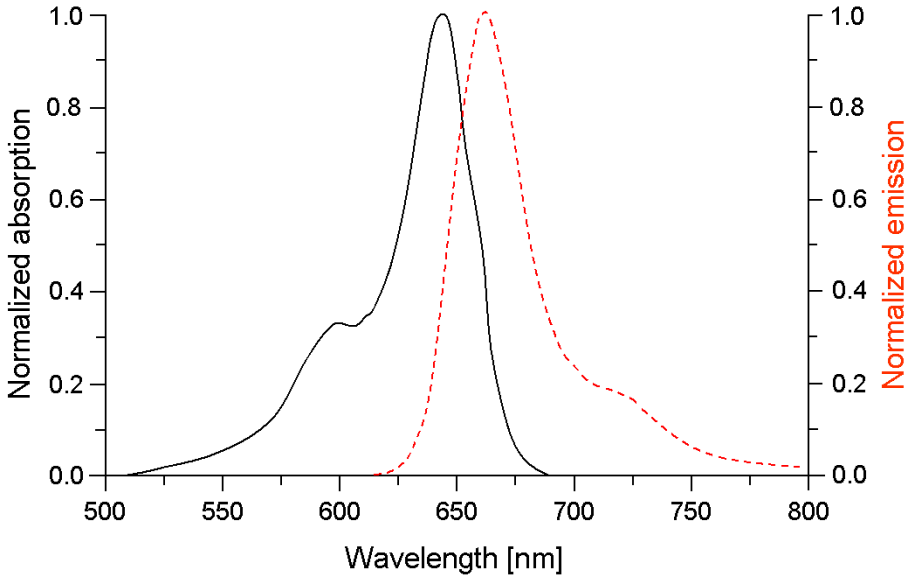

Figure 3.12: Absorption and emission spectra of Cy5 in PBS. Absorption (solid line) of the molecule peaks at 646 nm. The excited state has a lifetime of 1 ns before emitting a fluorescence photon with a quantum efficiency of 0.27. Emission (dashed line) is strongest at 664 nm. Both curves are normalized to their respective maxima. Data taken from literature [Muj93]

3.2.4 Functionalization and regeneration procedures

After one night of thiol incubation, the grating sample was rinsed thoroughly with pure ethanol to remove unbound thiols. The sample was than incorporated in the flow cell (see section 3.3.2) and fixed on the sample holder of the experimental set-up (described in the subsequent section) to allow monitoring of the various following functionalization steps. With the solutions detailed in the previous sections the functionalization continues like this:

- 15' rinsing with PBS buffer
- 20' cycling streptavidin
- 15' rinsing with PBS buffer
- 30' cycling probe strand
- 15' rinsing with PBS buffer

The streptavidin and probe strand cycling steps can be tracked by SPR kinetic studies for diagnostic purposes. After the third and last rinsing step the target sequence can be added.

The sensor surface can be regenerated by destroying the hybridization of probe and target and removing the target again. This leaves the surface ready for another experiment. A very convenient way to do this is by raising the pH slightly for a short time. In the PBS buffer environment, positive counterions screen the negatively charged DNA backbone. An increase

in OH^- concentration will remove these. The unscreened charges will now repel each other. This electrostatic repulsion of the two backbones prevails over the attractive interaction of the hydrogen bonds and causes dissociation of the double strand. The procedure consists of two steps:

- 1' rinsing with 10 mM NaOH
- 30' rinsing with PBS buffer

3.3 Experimental set-up

The experimental set-up built for this work was designed to meet the following requirements:

- Measure the reflectivity of gratings at varying (azimuthal) angles of incidence
- Permit all planes of polarization for the excitation beam
- Measure the fluorescence emission for a relevant range of grating constants as a function of the (azimuthal) emission angle
- Perform all of the above while having access to the surface for functionalization without removing the sample

Figure 3.13 shows the set-up schematically. A HeNe laser (λ=632.8 nm, 5 mW, PL-750P polarized helium-neon laser, Polytec [POL]) was used as the excitation source. The beam was modulated by a chopper wheel (Light copper 197, Perkin Elmer Instruments [PER]) at 1133 Hz to suppress ambient light contributions. The plane of polarization could be set by a Fresnel rhomb (Fresnel rhomb $\lambda/2$, Bernhard Halle Nachfl. [BER]), controlled by a personal computer (AMD Athlon 1800 CPU with GPIB card and RS232 bus for interfacing with the detectors), while keeping the output power constant. The Fresnel rhomb angle is referred to as ρ. Besides the obvious choice of p-polarization ($\rho = 0°$) that is required for surface plasmon excitation, s-polarization ($\rho = 45°$, a Fresnel rhomb angle of ρ rotates the plane of polarization by an amount of 2ρ) could also be used to distinguish direct illumination contributions from those generated by the evanescent field. After the rhomb the intensity was reduced to 10 % by a neutral density filter to prevent rapid unintended bleaching of the fluorophores. For the same reason, a shutter was included to block the beam during non-measurement periods. Next, the beam was reflected on the sample via three mirrors rather than being routed directly. This triple reflection beam steering was chosen to allow the detectors to move to small angles without interrupting the incident laser beam. It was important to reflect off the edge of the last mirror to minimize the blind angle. Additional advice on the optical alignment of the set-up is included in appendix B.

Before finally hitting the sample, the beam passed an iris in order to cancel all the side spots and halos generated on its way. It reached the sample with a remaining power of 0.14 mW.

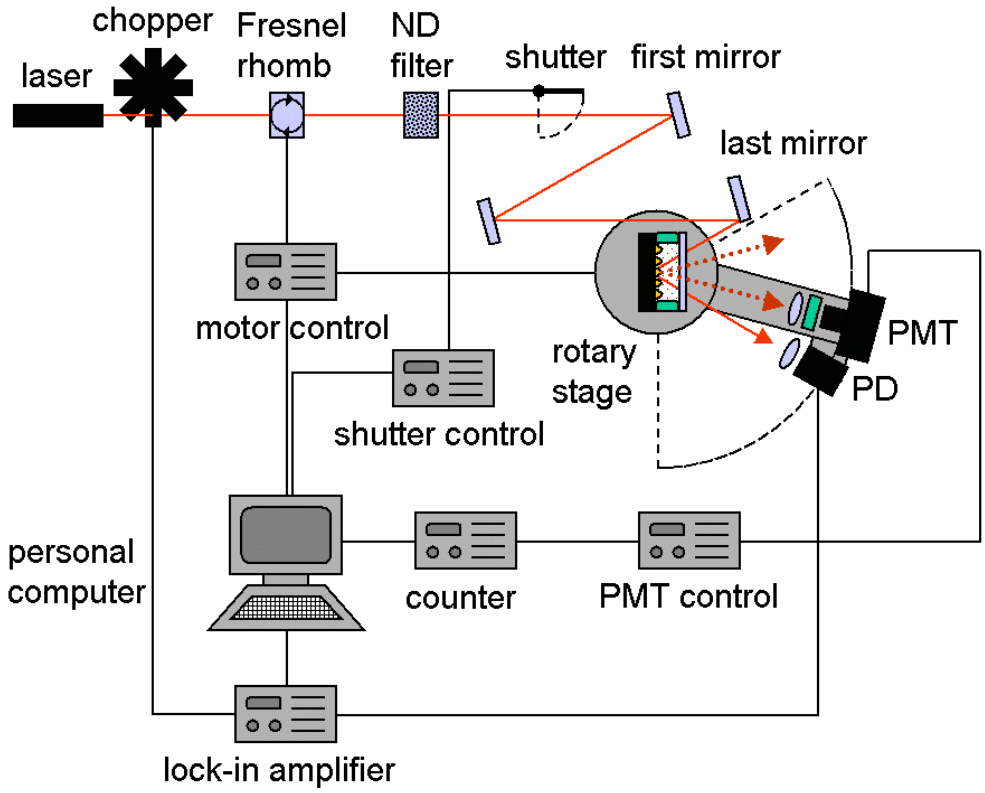

Figure 3.13: The experimental set-up. The sample was mounted in a flow cell on a rotary stage to allow scanning of the angle of incidence. It was illuminated by a chopped HeNe laser for lock-in detection. The polarization was tunable by means of a Fresnel rhomb. The second arm of the rotary stage could move either a photodiode or a photomultiplier tube for measuring the reflected light intensity or the fluorescence intensity respectively. Data acquisition was automated.

The grating was mounted inside a home built flow cell (see section 3.3.2) on one of the arms of two rotary stages (Model 414A00 two circle goniometer with M-BF-810-12 stepper motors, HUBER Diffraktionstechnik [HUB]). By rotating the sample the angle of incidence θ could be changed. The second arm carried the detectors: a photodiode (PD) and a photomultiplier tube (PMT). Both detectors were mounted on the same goniometer arm next to each other with an angle of about 30° between their respective lines of sight. Since both detectors were only used sequentially there was no need for a third arm.

The PD (BPW 34 B silicon photodiode, Siemens [SIE]) measured the photocurrent generated by the light reflected from the grating. It was placed in the focus of a plano-convex lens of focal length f = 40 mm. The current was converted to a voltage and relayed to a lock-in amplifier (7260 digital lock-in amplifier, EG&G, now a division of Ametek [AME]) where the modulated signal was processed. The reference frequency was provided by the chopper. The decoded voltage information was then feed into the personal computer.

The fluorescence detection capability was provided by a PMT (H6240-01 photon counting unit, Hamamatsu [HAM]). It was combined with a computer controlled shutter (Prontor magnetic e/40 100 % ED, Prontor [PRO]) to define the signal integration time. Fluorescence excited

on the grating was imaged on the PMT entry window with a bi-convex lens of f = 50 mm placed in the middle of both with a separation of 2f to each of them.

In order to achieve a high angular resolution for measurements in which the PMT is scanning the angle of emission an iris was placed right in front of the lens. In order to distinguish excitation light from fluorescence two interference filters (both 670FS10-25 interference filters, transmission maximum 67 % at 673 nm, LOT Oriel [LOT]) were placed in front of the PMT entry window. Two filters were used instead of one, because a grating coupling set-up operates essentially in a reflection-type of geometry. Reflection and scattering of laser photons can occur at all the interfaces and edges of the flow cell. These unwanted contributions are more effectively suppressed with an additional filter. As soon as a signal was generated that exceeded the counting logic threshold, the PMT put out a TTL-pulse that was registered by a counter (universal counter 53131A, Agilent [AGI]) integrating over a preset gate time and relaying the counting total to the personal computer. The entire optical pathway of the set-up, including everything from the laser to the two detectors, was placed and operated inside of a black box to block the access of undesired ambient light contributions.

3.3.1 Operational modes

There are four basics modes of operation that were used to perform measurements with the set-up described above:

- $\theta/2\theta$-mode: the $\theta/2\theta$-mode was used to take measurements of reflectivity versus angle of incidence. If the sample is rotated to a given angle of incidence θ, the detector arm has to move by 2θ in order to collect the reflected beam with the PD.

- Fixed/θ-mode: angular fluorescence spectra were measured in this mode. The grating was kept at a fixed angle of incidence to excite surface plasmons. The PMT moved to measure the fluorescence intensity at different emission angles relative to the surface normal of the grating.

- θ/θ-mode: this is the so-called tuning-mode. It was used to find the most efficient excitation condition. The grating was rotated and moved through the resonance while the PMT rotated by the same angle to maintain the same sample perspective.

- Kinetic-mode: in the kinetic-mode the goniometer was at rest with the grating fixed at a convenient excitation angle. This mode was used to study the binding of substances to the sensor surface as a function of time. The nature of the experiment determined which detector was the appropriate one. Hence there were two ways of measuring kinetics. For studies based on reflectivity, the PD was fixed at an angle equal to twice the chosen excitation angle. In experiments where the injected substance of interest was a fluorophore, the PMT was brought to rest over the grating at the peak emission angle using a narrow aperture. Alternatively, for samples with a small grating constant for which the fluorescence emission is expected to be concentrated around the surface normal, the PMT was

kept looking along the surface normal. In this case, no additional aperture restriction was applied. The field of view is hence defined by the diameter of the lens in front of the PMT and therefore maximized.

Additionally, the set-up can be used to determine the grating constant of a sample in a quick polarization-independent way that requires no modelling of any layers properties. In order to do this the diffraction caused by the grating is studied in the Littrow configuration. The diffraction of light of wavelength λ on a corrugated surface with the grating constant Λ is described by the grating equation

$$m\lambda = \Lambda(\sin\theta_{inc} + \sin\theta_{dif}) \tag{3.3.1}$$

where m is the diffraction order, θ_{inc} and θ_{dif} the angle of angle of incidence and the angle of diffraction respectively [Pet80], [Loe97]. The special case in which the diffracted beam of a given diffraction order coincides with the incident beam is called the Littrow configuration. This means

$$\theta_{inc} = \theta_{dif} \equiv \theta_L \tag{3.3.2}$$

with the Littrow angle θ_L. Equation 3.3.1 accordingly simplifies to

$$m\lambda = 2\Lambda\sin\theta_L. \tag{3.3.3}$$

Thus the grating constant can conveniently be measured for $m = 1$ where the diffraction peak is strongest. The sample is rotated and the diffracted beam traced until the angle is found where it travels right back into the laser aperture.

3.3.2 Flow cell

For performing experiments on binding from solution, a flow cell that can easily be attached to functionalized gratings is necessary. It has to provide full optical access to the sensor surface over a broad range of azimuthal angles and to remain sealed for longer than 24 hours. Because of the anticipated fluorescence contribution of unattached fluorophores present in the bulk liquid phase, a fluidics design of thin cell thickness was targeted.

A very practical solution fulfilling these conditions is sketched in figure 3.14. A thin film of poly(dimethylsiloxane) (PDMS) with a hole was placed on the sample with the hole being centered over the grating area. The film was covered by a quartz slide with an inlet and an outlet pipe. A thin metal screen was placed on top of all of this and the whole stack was mounted on a rotatable sample holder with two stationery metal binder clips.

This type of flow cell assembly can easily be self-made. PDMS (Sylgard 184 silicone elastomer kit, Dow Corning [DOW]) was cast into the desired shape with a bathtub shaped teflon mould. The film thickness is limited by how thin one can mill a trough in the teflon block and amounted to 300 μm. The hole was chosen to be of elliptic shape with its principal axes being 4 mm and 8 mm. Fully assembled and under pressure from the binder clamps the cell volume was determined to be approximately 10 μl, which is much less than the volume calculated from the

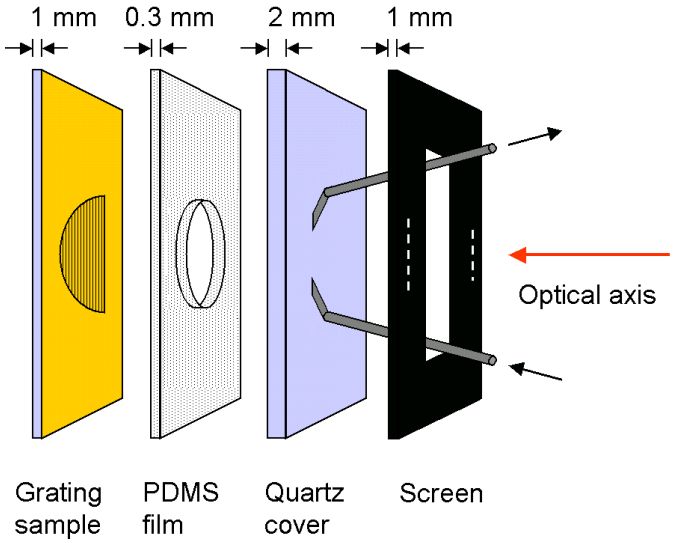

Figure 3.14: The flow cell. The clamps are attached at the dashed positions on the screen. The plane of rotation of the goniometer is normal to the image plane.

hole dimensions in relaxed condition. The PDMS slide was cleaned by sonicating it in ethanol and could be used essentially for an unlimited number of experiments. The quartz cover was required to be of a sturdy thickness to take the force of the binder clips necessary to seal the flow cell. The holes for inlet and outlet were made with a sonic drill at an angle of 45° at a separation of 7 mm between their centers. Two syringe needles were cut and bend to fit into the holes and glued with two component adhesive (UHU plus sofortfest, UHU [UHU]). Because the glue swells in ethanol, cleaning of the quartz cover was done by rinsing and wiping it.

The final layer of the flow cell stack was composed of a thin metal plate machined from aluminum. This plate served two purposes at the same time: first, it distributes the force from the binder clamps evenly on the quartz cover to prevent it from bending and breaking under stress; second, it shields the detectors from some of the light scattered inside of the PDMS film. To reduce reflections from the shiny metal surface itself the outward side was covered with black adhesive tape. A peristaltic pump (Reglo Digital ISM 834A MS-4/8, tubing pump, Ismatec [ISM] was used to pull rather than pump the liquids through flow cell and tubing (Tygon R3607, inner diameter 0.76 mm, wall thickness 0.8 mm, Saint-Gobain [TYG]) at a flow rate of 1.5 ml/min. This method allows to remove any bubbles from the flow cell easily by pressing the inlet tubing closed and releasing it again.

Chapter 4

Sample characterization

Gratings produced by holographic grating manufacture and reactive ion beam etching can show very different efficiencies of coupling incident light to surface plasmons under the resonance condition, because the fabrication of structures at the nanometer level is very sensitive to a multitude of parameters like photoresist inhomogeneities, local variations in the laser beam power, exposure time, etc. that require tight control. For the optical characterization of a the term coupling efficiency is used. The coupling efficiency $\eta := 1 - R_{min}$ is determined for an uncoated substrate (with an evaporated gold layer only) in air without the flow cell. It is an indicator for the quality of a grating. Essentially, every etched grating is an individual specimen that needs to be characterized in terms of resonance angle and coupling efficiency. Within the boundaries of the accessible manufacturing technology, and not as a fundamental theoretical issue, the question needs to be asked what makes a good grating.

Aided by calculations, the characterization of gratings by different experimental means forms the core of this chapter. Atomic force microscopy is the method of choice to examine the surface profile of gratings and complements optical characterization. Since AFM is a locally probing technique, the uniformity limits of the etched structures are specified first. Then samples from a range of coupling efficiencies are surveyed identifying the characteristic topographic features that make for efficient coupling. Traditional SPR reflectivity and diffraction measurements can serve to characterize a grating optically. When working in aqueous environments the presence of a flow cell introduces refraction and reflection effects that are modelled in the subsequent section. After that, sample placement tolerances like lateral and rotational offsets that are relevant to the design of a GC-SPFS device are discussed. Next, results from AFM and SPR are combined for a full mathematical description of the reflection behavior of a grating with different adsorbed layers and dielectric environments. The last section of the chapter presents a comprehensive collection of calculations that cover the influence of both topographic and material parameters on the optical response of gratings and give guidelines for curve fitting.

4.1 Grating profile determination by AFM

In order to simulate reflectivity curves for prism coupling, the material properties like layer thickness and dielectric number are the determining factors. In grating coupling, full knowledge of the grating profile is additionally important for calculations. For this purpose the surface topographies of several gratings were measured by tapping mode AFM (Dimension 3100 Scanning Probe Microscope, Veeco [VEE]). Samples with coupling efficiencies ranging from 0.5 to more than 0.95 have been studied to relate the surface profiles to their optical responses.

Cleaned gratings were examined by AFM before and after gold evaporation. Figure 4.1 shows the topography of a pure glass specimen with $\eta > 0.95$. The profile shape resulting from the grating fabrication process resembles a series of very shallow trapezoids. This is a significant difference to the expected $\sin^2 x$ intensity profile ideally caused by the interference pattern employed in the holographic grating writing step; it is an indication of excessive development times. Nevertheless, this deviation in shape from the sinusoidal form[1] doesn't pose a problem for applications since gratings of very high coupling efficiency can still be manufactured with this profile type.

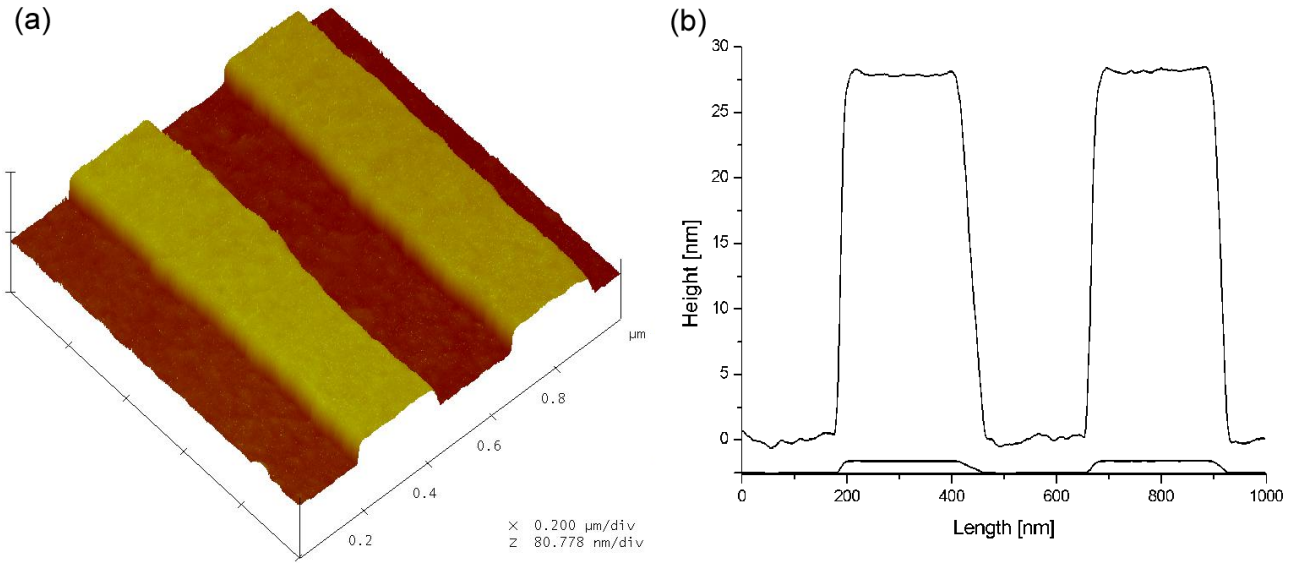

Figure 4.1: Topography of an unmetalized high η grating. (a) The three-dimensional view shows a 1 μm by 1 μm area from the center of the glass sample B104. (b) The section plot is based on averaging over the data of the full area. It yields a trapezoidal type of profile (Λ = 478.5 nm) with an amplitude of 13.9 nm. The smaller curve of the two shows the profile for equally scaled axes and illustrates the shallow character of the corrugation.

After gold evaporation (see figure 4.2, in particular the ridge regions) the roughness of the surface increases significantly. Different quantities are in common use to quantify roughness:

[1]Sinusoidal gratings, if available, are still of high interest. That is mostly because they ease the mathematical modelling of grating coupling. Under treatment with the Rayleigh approximation they can be modelled well with a much smaller expansion order L (refer to section 2.1.8), tremendously facilitating numerical calculations and hence greatly reducing computation time.

the mean roughness increases from 0.41 nm to 1.16 nm. In terms of RMS roughness, gold evaporation raises the value from 0.52 nm to 1.45 nm. For both quantities the increase amounts to a factor of approximately 2.8. Surface roughness alone can permit the coupling of the photon field to plasmons [Sam91], even in the absence of a principal grating profile. This can easily be understood by envisioning roughness as a superposition of a multitude of gratings, each with its own periodicity, with very small amplitudes. The competition between the different coupling orders accessible in the presence of roughness can decrease the coupling efficiency of the principal corrugation.

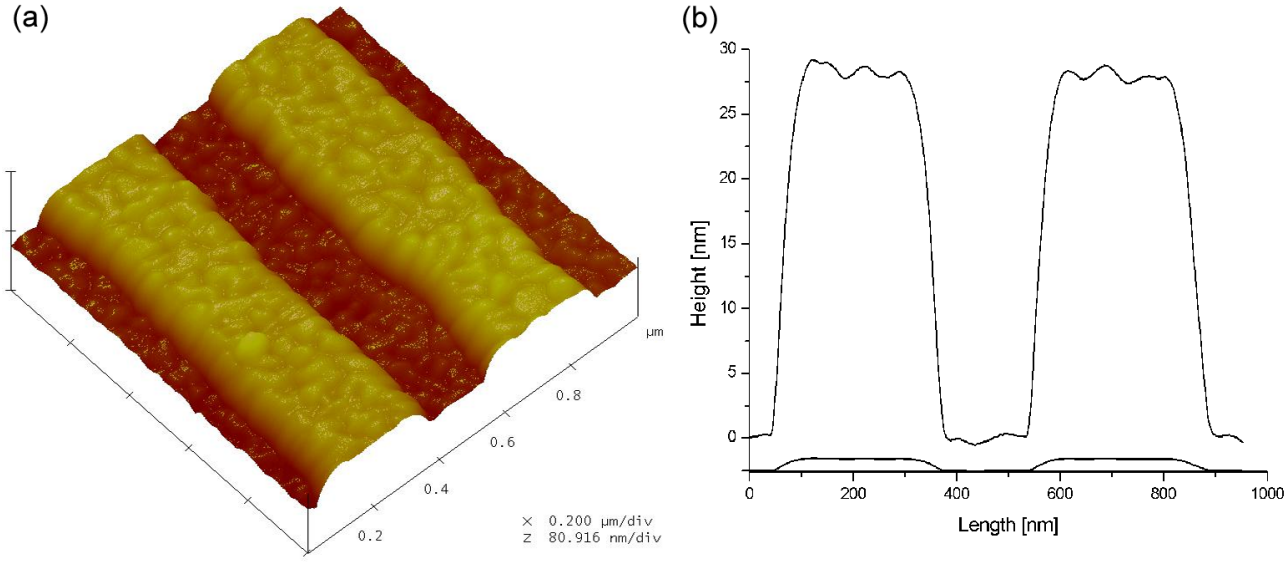

Figure 4.2: Topography of a gold coated high η grating. The granular structure of the metal film after the thermal evaporation of 150 nm of gold is clearly visible. It increases the roughness of grating B104 in both the three-dimensional view (a) as well as in the averaged section analysis (b). The smaller curve of the two sections shows the profile for equally scaled axes.

4.1.1 Locality versus uniformity

To compare the profiles of gratings with different coupling efficiencies, additional parameters are introduced, according to figure 4.3, to describe the trapezoidal profile found. Besides the grating constant Λ and the amplitude a, the land width l and the pit width p are suitable quantities to characterize the profiles. Since AFM is a technique that probes a sample only locally, different spots on the same grating (sample B79 with $\eta > 0.95$) have been studied. The five measurement sites are defined in figure 4.3. All the quantities in question were deduced from the force micrographs by using suitable averaging methods and are given in chart 4.1 for the uncoated sample. The grating constant was determined by averaging over a 10 μm by 10 μm area of 17 to 19 corrugation periods. In order to find the average amplitude a bearing analysis routine was applied to the same region. Both land and pit widths were measured at high resolution by averaging over a 1 μm by 1 μm area. The knowledge of Λ, a, l, and p yields

the aspect ratio Λ/a as well as the mark-to-space ratio p/l. Furthermore, the slope fraction $s := 100(1 - (l + p)/\Lambda)$ is introduced. It is a quantity indicating the percentage of a period occupied neither by land or pit but rather by slopes.

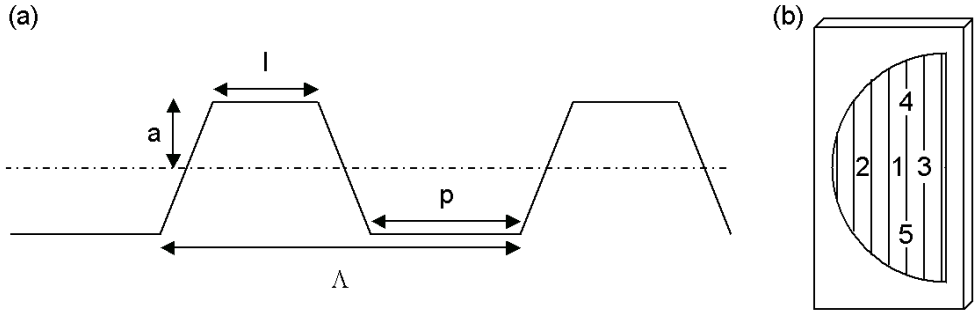

Figure 4.3: Definition of terms used in profile analysis. (a) The four parameters used to describe trapezoidal profiles are: grating constant Λ, grating amplitude a, land width l, pit width p. (b) The definition of the various measurement sites on a grating.

Position on sample B79	Λ [nm]	a [nm]	l [nm]	p [nm]	Λ/a	p/l	s [%]
1	513.2	17	186	213	30.19	1.15	22.25
2	513.2	17.6	264	135	29.16	0.51	22.25
3	512.4	16.4	209	203	31.24	0.97	19.59
4	512.4	16.6	240	145	30.87	0.60	24.86
5	513.5	16	211	193	32.09	0.91	21.32
Mean	512.9	16.7	222	177.8	30.71	0.83	22.06
Abs. std. dev.	0.2	0.7	17.7	14.1	1.35	0.16	0.66
Rel. std. dev. [%]	0.04	4.23	7.96	7.95	4.39	19.65	2.98

Table 4.1: Profile parameters determined from different locations of an uncoated sample

The grating constant is consistent for all measurement sites with very small fluctuations only. This uniformity is expected, because the periodicity is only determined by the monochromatic laser wavelength and the fixed angle picked during the holographic grating writing step. In contrast, the other three parameters are dependent on photoresist film thickness, its chemical homogeneity and changes in the laser beam power distribution. Accordingly, there is more variation in a, l and p. The standard deviation amounts to about 8 to 8.5 % of their respective mean values for all three. Combining p and l to the mark-to-space ratio gives a less coherent picture. There is a sizable range of values. This distribution is most likely an indication of significant global variations in the laser beam power from the ideal interference pattern. On the other hand, the fraction of the period occupied by slopes is consistently within 22 %. This behavior is more strongly related to the etching process rather than to film properties or optical parameters. Fluctuations in the aspect ratio are also small. The good uniformity of the grating constant is also influencing the behavior of this combined quantity, simply for mathematical reasons.

It has been shown that certain grating parameters are subject to significant (but still quantifiable) location dependent variations, despite the care taken to average data over certain sample areas. This must be kept in mind when analyzing AFM data. The absolute variations obtained from this study are assumed to be applicable to all the following AFM measurements for gratings with $\Lambda \approx 513$ nm and they are used to set data into reference. For gratings of different grating constants it is assumed that the relative variations found here can still be adopted to specify meaningful variation ranges.

4.1.2 Profiles for efficient coupling

The next two charts show the grating parameters obtained from force micrographs of gratings with different coupling efficiencies at position 1. Chart 4.2 presents the values from the bare grating structures etched into glass.

Sample	η	Λ [nm]	a [nm]	l [nm]	p [nm]	Λ/a	p/l	s [%]
B70 glass	0.5	512.2	14	131	305	36.55	2.33	14.79
B51 glass	0.8	509.8	19	84	305	26.83	3.63	23.70
B64 glass	0.9	513.7	18.4	125	297	27.92	2.38	17.85
B79 glass	0.95	513.2	17	186	213	30.19	1.15	22.25

Table 4.2: Profile parameters for glass surfaces

The land width found for sample B51 stands out from the values found for the other three samples, affecting p/l and s at the same time. The sample still serves to show that there is an optimal amplitude. Looking at the remaining three gratings, it is clearly visible that a high η specimen favors smaller pits and larger land widths, both approaching approximately 200 nm. Consequently p/l is close to unity. Chart 4.3 gives the data obtained from the same samples after evaporation of 150 nm of gold (including the intermediate 2 nm chromium layer).

Sample	η	Λ [nm]	a [nm]	l [nm]	p [nm]	Λ/a	p/l	s [%]
B70 gold	0.5	512.7	15.6	143	252	32.87	1.76	22.96
B51 gold	0.8	511.1	18.9	104	246	27.04	2.37	31.52
B64 gold	0.9	513.2	18.3	168	197	28.04	1.17	28.88
B79 gold	0.95	513.2	17.2	186	160	29.84	0.86	32.58

Table 4.3: Profile parameters for gold surfaces

Not very surprisingly, no change can be observed in the grating constant. Also, the amplitudes stay virtually the same. Looking at the land and pit widths, a consistent trend can be seen. The land widths increase by about 18 % while at the same time the pit widths decrease by an average 24 % resulting in an overall reduction of the mark-to-space ratio by 34 %. Together with an increase of s by 47 %, the overall profile shape has clearly been changed by the

gold evaporation. Visualization of this deformation is given in figure 4.4. Clearly the gold is accumulating on the sloped areas and especially in the pit corners.

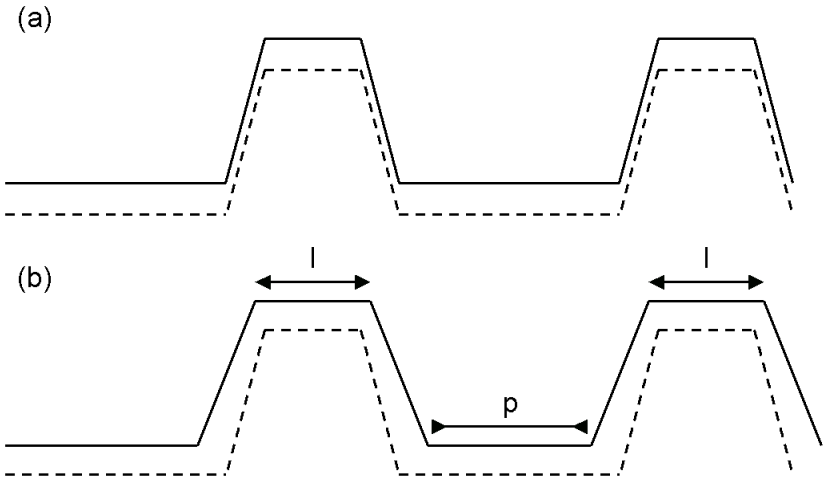

Figure 4.4: How the evaporation process deforms the grating profile. (a) An ideal metal deposition process will maintain the topography given by the underlying glass substrate (dashed profile). (b) The growth of a gold film by thermal evaporation changes the grating parameters - l is expanded and p shrunk. At the same time the horizontal width of the sloped areas is growing.

Besides samples with a grating constant of about 513 nm, substrates with a periodicity of approximately 475 nm were also used. The topography data at position 1 of several uncoated gratings with a particularly high coupling efficiency is given in chart 4.4.

Sample	η	Λ [nm]	a [nm]	l [nm]	p [nm]	Λ/a	p/l	s [%]
B92 glass	0.95	474.1	15.3	182	150	30.99	0.82	29.97
B98 glass	0.95	476.6	16.5	203	168	28.88	0.83	22.16
B104 glass	0.95	478.5	13.9	197	188	34.42	0.95	19.54
Mean	0.95	476.4	15.23	194	169	31.43	0.87	23.89

Table 4.4: Profile parameters of high η gratings

Compared to the parameters determined for grating B79 (chart 4.1), the trend is quite clear. Because of the smaller grating constant, l and p are accordingly reduced. For a high coupling efficiency it is also necessary to have a scaled down amplitude. On the other hand, both the aspect ratio and the mark-to-space ratio are almost preserved. Only the slope fraction has changed a little more than what would seem appropriate. It is impossible to make universal statements from just studying two grating constants, irrespective of the level of scrutiny of the study. However, it can be said that for perodicities in the vicinity of 500 nm the basic profile geometry fabricated and specified here works very well for grating coupling at the HeNe laser line.

Besides the "home made" gratings of trapezoidal shape, a single very different sample was available for study. Our industrial collaboration partner purchased and forwarded to us one specimen form a commercial source (Richardson Gratings, now a division of Spectra-Physics [SPE]) for characterization and experiments. The sample SP42 was also fabricated by holography recorded in a photo resist film. In contrast to the fabrication process explained in section 3.1, the profile was not transferred into the substrate material after development. This results in a fragile corrugation consisting of the photoresist ridges and the metal film only - a sample that is disposable. Unfortunately, this was not indicated and consequently the corrugation was fatally degraded after removing the metal and cleaning the substrate for re-evaporation. Since no other sample was available from the same source, no meaningful fluorescence experiments could be performed with this grating. Nevertheless, the information gained about this type of sample in terms of reflectivity is still useful for future grating coupling applications (especially since the sample showed a coupling efficiency above 0.95) and is thus presented here.

Figure 4.5 presents a force micrograph and a section analysis of sample SP42 coated with gold. The profile is generally of sinusoidal shape[2] indicating a well chosen illumination time during photo resist exposure. It can also be seen that the corrugation is slightly blazed (i. e. the sinusoid is leaning a little to the side and left/right symmetry is broken). When looking at larger areas of the specimen, it becomes clear that the corrugation is afflicted with many irregularities, namely the protruding parts of the profile appear slightly deformed or damaged.

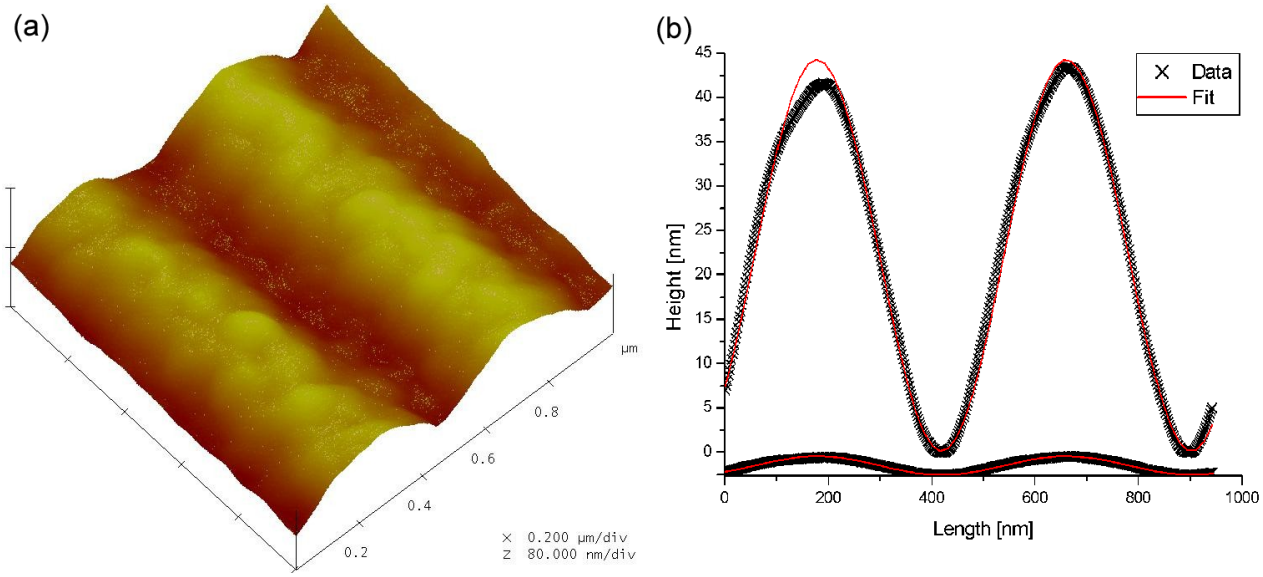

Figure 4.5: Topography of a high η grating from a commercial source. (a) The image shows a central 1 μm by 1 μm region of the metalized sample SP42. (b) The section was obtained by averaging over the same area. It can be fit very well with a sine wave of $\Lambda = 481.5$ nm and $a = 21.3$ nm. Deviations between fit and data are almost exclusively present at the maxima of the curve. Additionally, the corrugation is leaning a little to the right. The smaller set of data and fit shows the profile for equally scaled axes.

[2]The interference pattern of the laser beam during the writing step follows in fact a $\sin^2 x$ intensity distribution. But this dependence can still be expressed as a sine function by re-scaling both axis and shifting the origin along both axis: $\sin^2 x = \frac{1}{2} - \frac{1}{2}\cos 2x = \frac{1}{2} - \frac{1}{2}\sin(90° - 2x)$

4.2 Optical grating characterization

Prism based SPFS utilizes the evanescent field of the surface plasmon mode as an enhanced light source in a localized volume. The fluorescence emission is nearly constant over a range of several degrees[Vas04] in this case and hence precise excitation at the optimal angle is not a primary concern. Reflectivity measurements only serve a diagnostic purpose to monitor the build-up of a given surface functionalization architecture. In contrast to that, the excitation, as well as the fluorescence emission, are grating mediated and therefore restricted to specific angles in grating coupling SPFS. The geometry can only be understood if the grating and the overlying multi-layer system are properly characterized. The reflectivity curve of a grating is a very valuable tool to find the necessary layer properties like thickness and dielectric number and of course the coupling efficiency. Additionally Λ can be found optically by measuring the diffraction of light by the grating in the Littrow configuration (see section 3.3.1). But for a complete elucidation of the profile geometry a complementary method like AFM is necessary. One has to keep in mind the local probing nature of AFM, in comparison with reflectivity or diffraction measurements that integrate over a certain surface area illuminated by the laser spot.

4.2.1 Influence of the flow cell

Most biological reactions take place in an aqueous environment and hence it is necessary to use a flow cell in order to study them. This equates to introducing new dielectric interfaces where different processes like refraction, transmission and reflection take place. In order to understand the system, these effects have to be considered. This is particularly relevant for characterizing the coupling efficiency of a grating immersed in buffer solution because this combination can only be studied using a flow cell.

First, we will focus on refraction. A simple flow cell as illustrated in figure 4.6 consists of a cover glass and a spacer structure that keeps it in place. Additionally, the content of the flow cell has to be considered. The impinging light beam passes the air/glass interface first and than the glass/cell content interface before reaching the grating surface. Refraction takes place at both interfaces. In the case of an empty flow cell, both refractions make up for each other and the beam suffers only a small lateral displacement that can be neglected. But if the flow cell is filled with buffer solution, the angles of incidence at both interfaces are different and have to be distinguished. The light reaches the grating under the angle θ_{real}, also called the inner angle. This is the angle that is referred to by the simulation code. The (outer) angle θ_{meas} is defined at the air/glass interface. This is the quantity recorded in experiments and thus the more convenient one to use. With n_{cell} being the refractive index of the buffer solution filling the cell, both angles are related via:

$$\theta_{meas} = \arcsin\left(n_{cell} \sin \theta_{real}\right). \tag{4.2.1}$$

All graphs based on azimuthal angles in this work are expressed in terms of θ_{meas}. All simulations which assume buffer solution as the dielectric have been corrected accordingly for this

refraction. By the same token, any light emitted from the grating (as in the case of back coupled fluorescence being at the heart of the following chapter) is subject to refraction and one has to distinguish between the apparent and the real angle of emission accordingly.

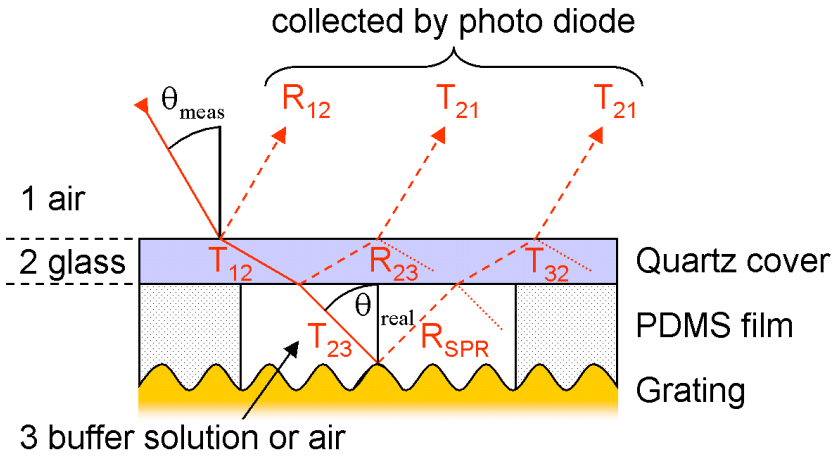

Figure 4.6: Reflection, transmission and refraction at interfaces introduced by the flow cell. The sample is illuminated from the left under the angle θ_{meas}. With absorption being neglected the light can be reflected and transmitted at every interface. The coefficient of the incident power that goes into either one channel for a beam heading from material x to material y is denoted by R_{xy} or T_{xy} respectively. At the grating surface the light forms the angle θ_{real} with the surface normal. The intensity ratio of the reflected light is R_{SPR}. In the first order calculation (in respect to the number of reflections taking place), only the three routes composed of solid and dashed arrows are considered. The three dotted lines are representing the onset of third order reflection processes that are already negligibly small.

Chart 4.5 summarizes the resonance angles for the two grating constants used in the experiments for this work. Numbers are given for the two dielectric environments air and water with the distinction of measured and real angle in the latter case. $\Lambda = 500$ nm is only a theoretical value used in general simulations presented in section 4.2.4. Since the exact position is affected by a great many factors, all angles are approximate and the data serves only as a guideline for quick classification of a sample or identification of the dielectric half-space.

Λ [nm]	θ_r [°] in air	$\theta_{r,meas}$ [°] in water	$\theta_{r,real}$ [°] in water
475	16.5	8	6
500	12.5	10.5	8
515	10.5	15	11

Table 4.5: Summary of typical resonance angles

Secondly, reflection and transmission have to be treated. Even when working in air, there is a difference in the reflectivity curve taken with and without flow cell. For example, the reflectivity minimum appears slightly raised and hence the sample seems to have a smaller coupling efficiency than it really has. Only with an empty cell can the difference easily be assessed. Measurements with buffer solution are impossible without flow cell. On the other

hand, it is desirable to have a method of quantifying the real coupling efficiency of a sample. Because of this, transmission and reflection coefficients for the flow cell have been calculated so their contribution to measurements can be compensated for. The reason for the difference between reflectivity curves taken with and without flow cell lies in the incomplete transmission taking place at the air/glass and glass/cell content interfaces. Since absorption can be neglected for the materials considered, all the non-transmitted power is reflected back into the medium of origin. Because the law of refraction works the same, irrespective of the propagation direction of a light beam, and because of the small height of the flow cell stack, several parallel reflected light contributions make up the total signal measured by the photo diode. Figure 4.6 shows the relevant pathways for a beam that develops into a parallel pencil of rays after reflection and transmission at several dielectric interfaces. The relative magnitude of these contributions can be calculated according to Fresnel's equations (see equation 2.1.14). Theoretically, the full incident intensity has to be accounted for. To achieve this, it is necessary to sum up an infinite number of multiple reflection and transmission processes. It turns out that only the three processes indicated in figure 4.6 have to be considered to model the minimum sufficiently. They are first order contributions in respect to the number of reflection events. The next set of pathways that can hit the photodiode consists of third order events. Their contribution to the total signal is very small since they scale with the third power of reflectivity coefficients that are smaller than 0.05 at air/glass interfaces or smaller than 0.005 at glass/water interfaces respectively.

For a beam of light propagating from medium x to medium y the transmission and reflection coefficient are designated as T_{xy} and R_{xy} respectively. In the case of transmission, the subscript sequence is in accordance with the propagation direction of the beam. The beam stays in the material indicated by the first subscript in the case of reflection. With R_{SPR} denoting the isolated reflection process taking place at the grating surface, the measured total reflectivity can be expressed in the first order approximation as:

$$R_{total} = R_{12} + T_{12}R_{23}T_{21} + T_{12}T_{23}R_{SPR}T_{32}T_{21}. \tag{4.2.2}$$

By using this relationship the influence of the flow cell can be deducted from from reflectivity measurements like shown in figure 4.7. With the flow cell attached, the reflectivity at the minimum is increased and the sample seems to have a lower coupling efficiency than without the cell. The reason for this is the reflection R_{12} at the air/glass interface. For a perfect minimum there is no light returning from the sample. But the photodiode still detects the first reflection and thus records an increased value. The reflectivity value at the minimum can be obtained from the measurement by deducting the flow cell contributions. On the other hand, the Fresnel compensation does not predict the reflectivity correctly at angles far away from the resonance[3]. At these positions the flow cell decreases the reflectivity. For an ideal grating nearly the total light intensity is reflected at these angles, but because of the interfaces between the grating and the detector, some light is reflected away from the detector and only a reduced intensity

[3]Because the sample had to be removed, attached to the flow cell and mounted again in order to measure the different curves discrepancies in measurement and calculation can also arise from working with different locations on the same grating. Influences on sample placement on the reflectivity curve are examined in the following section.

is recorded. Nevertheless, charting of the resonance minimum is the single most important aspect for sample characterization. In air one records a value of R_{min} that is increased by 0.06 in presence of the flow cell. There is a little less difference due to the smaller refractive index contrast in water. According to the value estimated from Fresnel compensated data, the flow cell increases the reflectivity value at the minimum by about 0.04. Since the compensation function is angle dependent due to the Fresnel coefficients, there is also an influence on the position of the observed resonance angle, but this shift is well below 0.1° and can therefore be ignored.

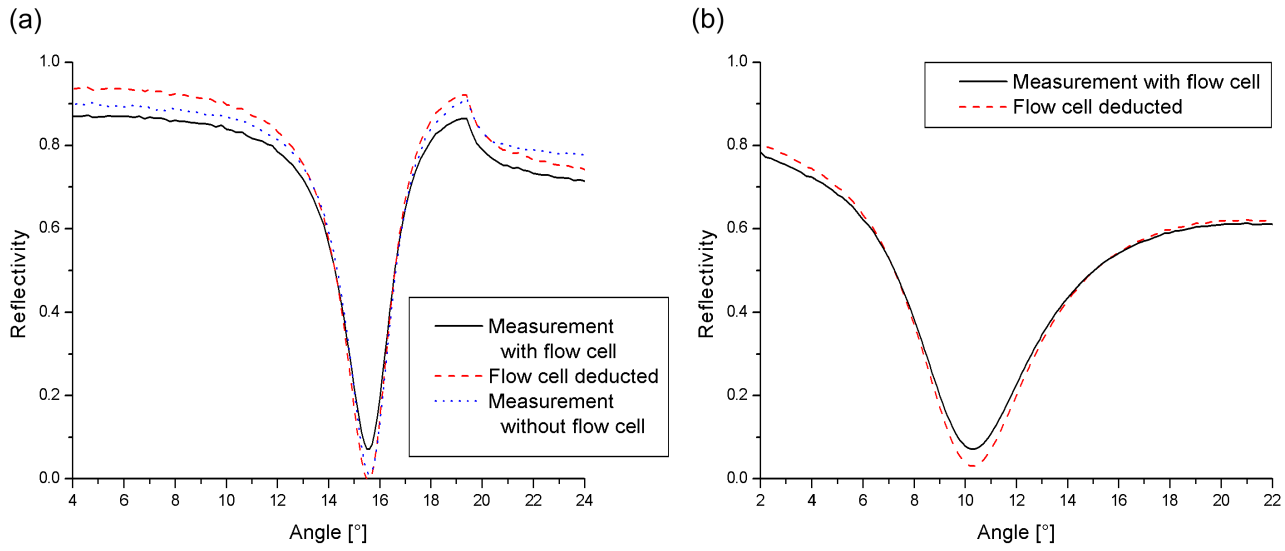

Figure 4.7: Reflectivity alteration due to the flow cell. (a) Measurements of sample B98 with an empty flow cell or without allow a comparison in air. Focussing on the minimum, samples appear worse than they really are. An increased value of R_{min} is detected because of reflection from the cell cover. Deducting this effect and other contributions yields the dashed curve. The Fresnel compensation can trace the minimum and the edge well, but it provides less agreement at other angles. Both experimental curves loose reliability beyond 20° because the flow cell starts to cut off the laser beam from there on. (b) The mathematical deduction of the flow cell is the only way to assess the real coupling efficiency in water.

4.2.2 Sample placement

For designing a device it is important to quantify the tolerances of the constituting elements. A competitive grating coupling SPFS scheme will feature disposable grating slides as the sensor surface. Hence tolerances in sample placement become an issue. Lateral displacement of an ideal grating with a perfect translational symmetry does not affect the performance as long as the laser beam still hits the corrugated functionalized surface. Because of small variations of the laser power distribution during the photoresist exposure, small fluctuations in the grating amplitude over the whole corrugated region are possible. These fluctuations have a small, but measurable, effect on the coupling condition[4]. Figure 4.8 (a) shows reflectivity curves obtained

[4]The relationship between corrugation amplitude and resonance angle is expanded on in section 4.2.4.

from different locations of the corrugated area of the same sample. A difference in the position of the resonance angle is visible for the three measurement sites that amounts to $\pm 0.1°$. Assuming a constant dielectric number for gold at the three measurement sites, one can try to explain the different resonance angles by changes in the grating geometry. Focussing on the grating constant a variation of Λ of $\pm$ 0.5 nm is necessary to explain the observed shift. This value is significantly higher than the variation found in the AFM study in section 4.1.1. Alternatively, the amplitude can also shift θ_r. In order to reproduce the angular range found a variation of $\pm$ 7 nm is needed. This number exceeds the standard deviation specified previously and is not realistic. Even the combination of both, changes in both grating constant and amplitude, is not enough to fully explain the observation. One is forced to consider limits to sample uniformity to be the product of both geometric (grating profile based) and material (dielectric number related) variations, with the latter playing a bigger role. In pure SPR applications with fixed geometries, this effect is of a magnitude that demands consideration. On the other hand, fluorescence based applications are more robust towards small angular fluctuations, depending on the solid angle of the limiting aperture in front of the detector. In this work, two apertures have been used, one to resolve the angular structure of the fluorescence, the other one to integrate the emission over a range of angles ($\pm 7°$). The last method is more suited for a commercial design without a goniometer and is unaffected by small angular shifts introduced by grating inhomogeneities.

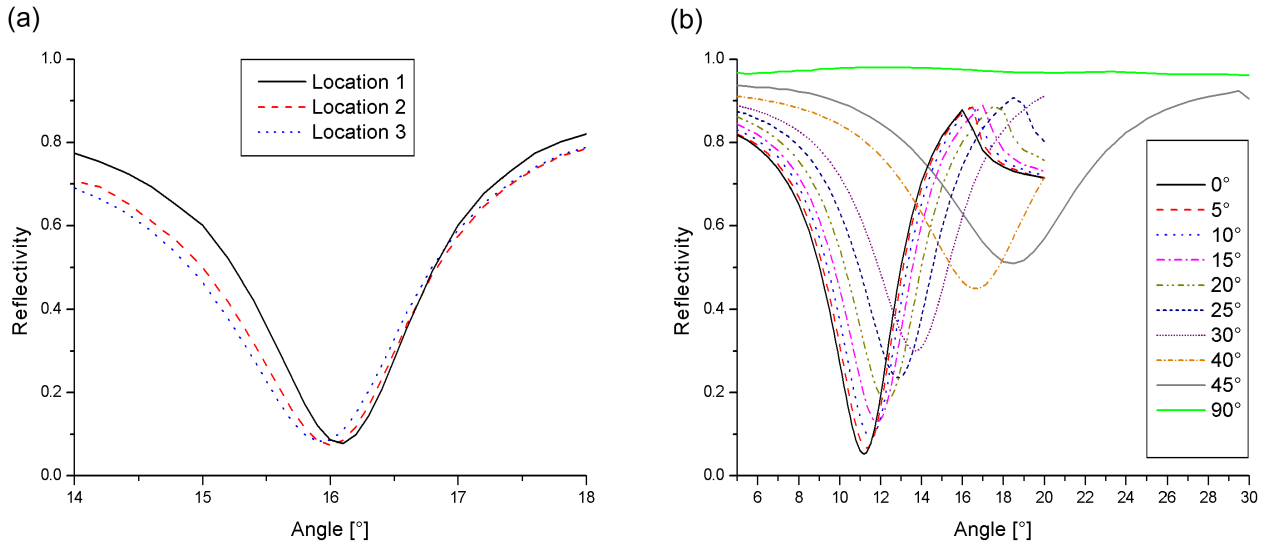

Figure 4.8: Tolerances in grating coupling. Local variations of the corrugation parameters and sample offset (both lateral and angular) of a grating affect the reproducibility of the reflectivity curve. (a) The graph shows reflectivity measurements for three different locations on the same sample B101. The position of the minimum can appear $16° \pm 0.1°$ according to the location of the illuminated spot. (b) Reflectivity curves were measured in air for increasing the skew angle with grating B8. The minimum appears at higher resonance angles for higher values of σ while the magnitude of R at the minimum increases. All measurements taken without flow cell.

Sample tilt constitutes a another possible offset condition and influences the beam geometry for measuring both reflectivity, as well as fluorescence emission. The relevance for measurements of these two quantities is the same as in the case of lateral displacement. However, sample tilt

can easily be identified (by reflecting the laser back in to the aperture of the laser tube) and be compensated for. Sample skew, i. e. placing the grating with its grooves not precisely perpendicular to the p-polarization plane, is more difficult to assess. The effect of inserting a sample with a certain skew angle σ on the reflectivity curve was studied with a rotatable sample holder (see figure 4.8 (b)). For 0° the sample is aligned with the grating vector perfectly parallel to the electric field vector. Increasing σ results in a shift of the minimum towards higher angles. This is due to the rotated grating perceiving a distorted angular axis. At the same time, the magnitude of the reflectivity at the minimum increases because (in the frame of reference of the grating) more and more of the electric field vector is shuffled into the s-polarization direction. This component is essentially fully reflected by the grating. At 90° there is only s-light illumination and no resonance is observed[5].

The geometry, for which the grating vector does not lie in the plane of incidence, is commonly called the conical mount. In order to model the relationships between the skew angle and the resonance angle, or the magnitude of R at the minimum respectively, with the existing program (working in the frame of reference of the grating), a coordinate transformation is necessary. First, angles are converted into wavevectors because it facilitates handling of the geometry. Then their projections on the x-axis (grating vector axis) are calculated. After that, they are converted back to angles. According to this procedure, the following calculations were performed in the frame of reference of the grating:

$\mathbf{k_0}$ is a wavevector oriented along the grating just as in the ordinary case of perfect alignment. Together with the grating it forms the angle θ_0 measured from the surface normal. Both are related via the projection $\mathbf{k}_{xy,0}$ of $\mathbf{k_0}$ onto the xy-plane (the grating surface):

$$\sin\theta_0 = \frac{|\mathbf{k}_{xy,0}|}{|\mathbf{k_0}|}. \tag{4.2.3}$$

The same relation holds true for the respective quantities in case of a grating that is rotated by an angle σ as illustrated in figure 4.9:

$$\sin\theta_\sigma = \frac{|\mathbf{k}_{xy,\sigma}|}{|\mathbf{k}_\sigma|}. \tag{4.2.4}$$

The component of the projection $\mathbf{k}_{xy,\sigma}$ that is parallel to the grating vector amounts to:

$$|\mathbf{k}_{xy,0}| = |\mathbf{k}_{xy,\sigma}|\cos\sigma. \tag{4.2.5}$$

Equation 4.2.4 can be solved for θ_σ and relation 4.2.5 inserted. With the help of equation 4.2.3 we find:

$$\begin{aligned}\theta_\sigma &= \arcsin\left(\frac{|\mathbf{k}_{xy,\sigma}|}{|\mathbf{k}_\sigma|}\right) = \arcsin\left(\frac{|\mathbf{k}_{xy,0}|}{|\mathbf{k}_\sigma|\cos\sigma}\right)\\ &= \arcsin\left(\frac{|\mathbf{k_0}|\sin\theta_0}{|\mathbf{k}_\sigma|\cos\sigma}\right) = \arcsin\left(\frac{\sin\theta_0}{\cos\sigma}\right).\end{aligned} \tag{4.2.6}$$

[5]It is interesting to note that (in the frame of reference of the experimentalist) a rotated grating can convert the polarization of the incident light under surface plasmon excitation conditions [Els91]. The reflection of a p-polarized beam also contains some s-light for $\sigma \neq 0$.

The fact that both full wavevectors originate from the same source ($|\mathbf{k}_\sigma| = |\mathbf{k_0}| = \frac{2\pi}{\lambda}$) yields the coordinate transformation $\theta_0 \mapsto \theta_\sigma$ that converts the abscissa of `Wingitter` data ($\sigma = 0$) to any given mismatch angle:

$$\theta_\sigma = \arcsin\left(\frac{\sin\theta_0}{\cos\sigma}\right) \tag{4.2.7}$$

In addition to the distortion of the angular scale, one has to keep in mind, that (in respect to the grating) the incoming light has p- and s-components, i. e. coupling and non-coupling contributions. Thus the combined reflectivity curve is given by a weighted sum of a reflectivity curve for p-polarization and one for s-polarization with the ratio being determined by the skew angle:

$$R_{total} = R_p \cos^2\sigma + R_s \sin^2\sigma. \tag{4.2.8}$$

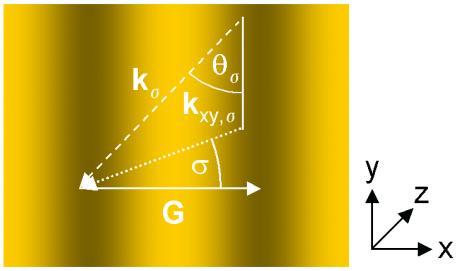

Figure 4.9: Coordinate transformation for rotated gratings. The illustration shows a grating with the grating vector **G** viewed from the top. The projection of an arbitrary wavevector $\mathbf{k}_\sigma$ (dashed arrow) on the xy-plane is called $\mathbf{k}_{xy,\sigma}$ (dotted arrow). The skew angle σ is formed between this projection and **G**. P-light has the **E**-vector oriented along **G**, s-light is perpendicular to that.

The effect of the skew angle on the resonance angle and the magnitude of R at the minimum is shown in detail in figure 4.10. The calculated data points are extracted from individual reflectivity curves transformed according to the described process because there is no analytic expression of the curve shape. The calculations for both the resonance angle, as well as the magnitude of the reflectivity at the minimum, are in good agreement with the data obtained from experiment. For σ beyond $\pm 30°$ the prediction no longer works well in case of the resonance angle. Experimentally, one can find the correct grating orientation ($\sigma = 0$) by first taking a reflectivity curve of a sample that is approximately aligned properly. While running a kinetic measurement at the minimum position, the grating is rotated on the sample holder in order to minimize the magnitude of the reflectivity even further. Since this changes the resonance angle also, ideally an iterative procedure is required. Only a single grating re-orientation step is usually necessary. Typically, the first approximate orientation places the sample better than $\pm 5°$ around the zero degree position where both relationships are rather constant.

4.2.3 Reflectivity curve fitting

The thicknesses and dielectric numbers of a multi-layer system can be derived from reflectivity measurements if the grating profile is known. The exact profile shape has to be determined

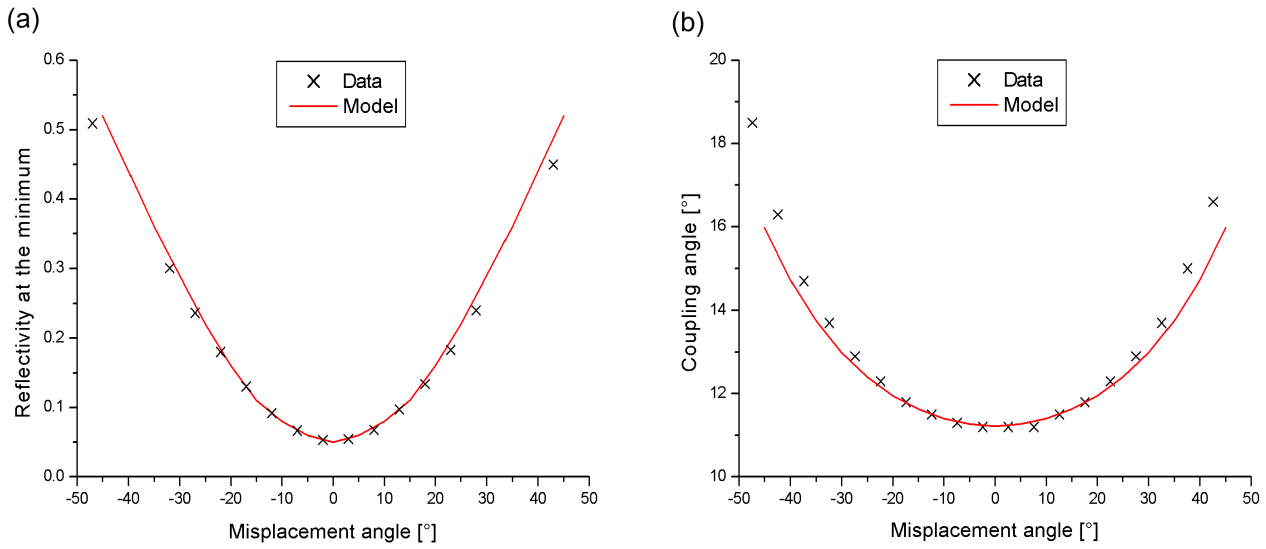

Figure 4.10: Skew effects on R_{min} and θ_r. The effect of a rotational sample offset on the reflectivity minimum can be modelled very well. The coordinate transformation extends the simulation code for the case $\sigma > 0$ and allows to predict (a) the magnitude as well as (b) the shifted position of the reflectivity minimum quite accurately for for a range of approximately ±30°. At higher skew angles the experiment yields slightly higher resonance angles than the calculation.

by AFM as previously shown. The preferred method for finding the grating constant is diffraction. From diffraction in the Littrow configuration (see section 3.3.1) Λ can be assessed easily. Chart 4.6 shows the grating constants found by AFM measurements on glass grating samples and those determined from diffraction.

Sample	B51	B64	B70	B79	B92	B98	SP42
Λ [nm] from AFM	509.8	513.7	512.2	513.2	474.1	474.7	481.5
Λ [nm] from diffraction	510.5	512.8	511.6	512.2	474.0	474.7	481.6
Littrow angle [°]	38.30	38.10	38.20	38.15	41.87	41.80	41.07

Table 4.6: Λ determined by AFM and by diffraction

Both sets of Λ are in very good agreement. On average, they differ by less than 0.5 nm with a standard deviation of 0.48 nm. In the following analysis the values for Λ derived from diffraction are used preferably since they are based on the average response of a laser spot sized area as opposed to the very local probe characterization obtained from AFM.

Figure 4.11 (a) presents the reflectivity curve for sample SP42 in air, after thiol incubation and without flow cell. The curve can be fit by using calculations based on the Rayleigh approximation. The fit is based on the following information:

- The grating profile is of sinusoidal shape with an amplitude of 21.3 nm as determined by AFM

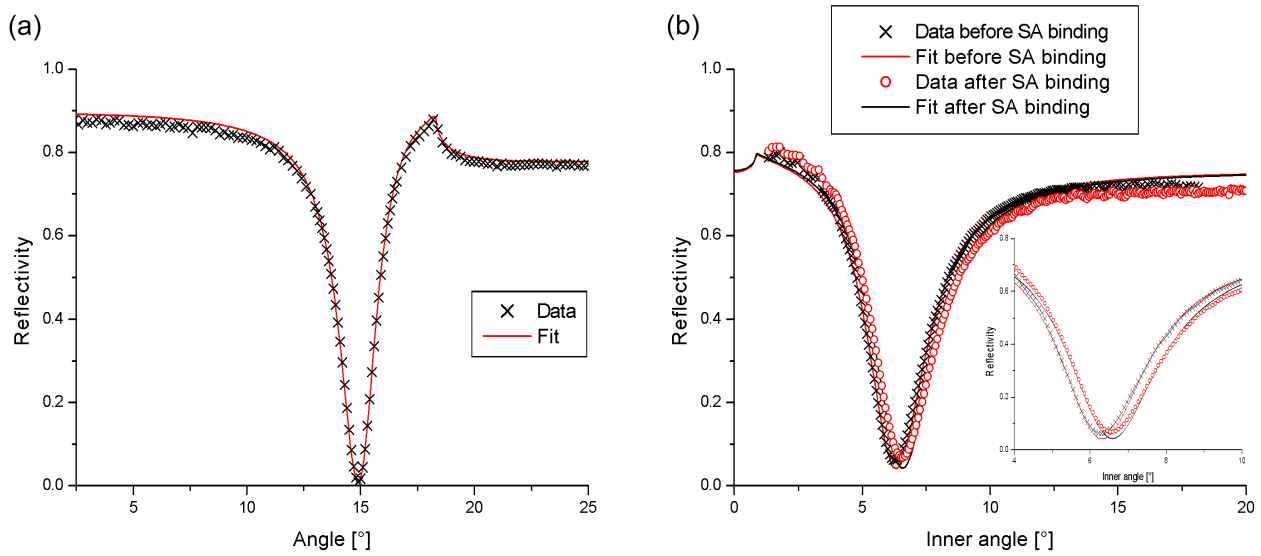

Figure 4.11: Reflectivity curve fitting with and without flow cell. (a) The reflectivity curve of the thiol coated grating SP42 in air without flow cell can be fit well by using the Rayleigh approximation. (b) In buffer solution, the gold has to be modelled by a different dielectric number to obtain a good fit. $\varepsilon_{Au} = -10.5 + i1.6$ was used in air and $\varepsilon_{Au} = -11.5 + i1.7$ in the buffer. Binding streptavidin to the surface shifts the minimum 0.3° to the right (see inset picture). All remaining relevant parameters are given in the main text.

- The grating constant obtained from diffraction in the Littrow configuration amounts to 481.6 nm
- A thiol layer is located on top of the gold with an effective thickness of 1.5 nm and $\varepsilon = 2.25$ [Ulm91], mimicking the underlying corrugation

The dielectric parameters of the infinitely thick gold film are left as fit parameters. A very good agreement between fit and measured data can be achieved by choosing $\varepsilon_{Au} = -10.5 + i1.6$. In order to continue the build-up of the surface functionalization, the flow cell has to be attached to the sample for all immobilization steps following the thiol incubation. Figure 4.11 (b) shows reflectivity measurements in buffer environment before and after streptavidin binding. The influence of the flow cell is compensated for in the experimental data and plotted against inner angles to facilitate the fitting process. The measured curve shape before binding can't be reproduced well by just exchanging the dielectric air half-space ($\varepsilon = 1$) with water ($\varepsilon = 1.78$). Keeping all other quantities constant, one is forced to use different dielectric values to describe the response of the gold layer. To obtain a good fit the numbers chosen are $\varepsilon_{Au} = -11.5 + i1.7$. Three mechanisms are possible for the need to model the gold response differently here: first, removal of the sample, attachment of the flow cell and finally re-mounting of both puts a different spot into the laser beam that can exhibit slightly different properties. Secondly, the Fresnel compensation calculation has already been shown to have limitations. Finally, the roughness of the gold, as specified in section 4.1, means there is a certain thickness range of the film where the buffer solution can enter fissures and both materials are present. Since the

field of the surface plasmon mode is concentrated at the interface on both sides, it is sampling this material blend very strongly, resulting in a different effective dielectric number. By simply adding the additional layer and keeping all other values constant, the same number can be used to fit the reflectivity curve after streptavidin immobilization. The streptavidin layer is modelled with $\varepsilon_{SA} = 2.1025$ and a thickness of 4 nm[6] according to the values commonly used in literature to describe this architecture [Spi93].

Using these numbers, both fits are of similar fidelity. Most importantly, they predict the position of the minimum well, however at slightly lower values of reflectivity. The growth of the streptavidin layer moves the minimum by 0.3° to the right. Discrepancies between measurement and simulation arise far away from the minimum, where the calculations turn out a little lower (at the edge) or higher than the measured data (beyond 15.9°). For small angles this relationship is in line with the deviations inherent to the Fresnel compensation.

The simulation of the reflectivity response of a flat multi-layer system is almost instantaneous with today's personal computers. Performing the same calculations for a corrugated system is numerically much more demanding. This is especially relevant in the presence of grating profiles that require a Fourier expansion of higher orders. These can take tens of minutes to solve. For this reason, an alternative approach has been suggested for data analysis [Kno81]. In this method, grating coupling is compared to an equivalent prism coupling geometry. Grating resonance angles are converted to prism resonance angles relating to the same in-plan component of the wavevector. This method succeeds in reproducing the minimum well in terms of position and half-width, but agreement is rather poor at the edge. This transformation approach is hence appropriate for fast analysis of additional layers. It is not suited for characterization of the grating itself, since good reflectivity curve fits can only be achieved by the use of dielectric numbers for the metal that stray significantly from the values commonly used in SPR [Kre00].

4.2.4 A reference for reflectivity curve fitting

Many parameters like geometrical dimensions of a grating and multi-layer material properties affect the optical response of a system. It is very instructive to have a closer look at the impact of variations to these parameters on the reflectivity curve. This study is focussing on qualitative effects. Since the simulation of grating coupling is numerically elaborate and accordingly very time consuming, reflectivity curve fitting is facilitated by comprehending the trends inherent in changing the parameters. For looking at the role of basic parameters, a sinusoidal grating profile is sufficient most times. This profile shape can be confidently and speedily dealt with. In this work, samples of essentially two types of grating constants have been used: 475 nm and 515 nm. For a compromise we will focus on a sinusoid with a periodicity of 500 nm and an amplitude of 20 nm. The gold thickness amounts to 150 nm with $\varepsilon = -12 + i1.3$. These are the standard values used in all the following calculations unless otherwise noted. Angles are corrected for refraction in the presence of water but, whether the dielectric is air or water, no further flow cell effects are included in the data.

[6] X-ray crystallography measurements of the crystallized protein yield higher values. The thickness used here is an effective optical value that includes the influence of the unoccupied surface fraction.

Figure 4.12 shows how a change of the dielectric half-space affects the reflectivity minimum. In the experiment, the change from air to water appears to shift the minimum from +12.69° to +10.7°. This is not true, since after the injection of water, one observes a minimum different minimum and one will draw the wrong conclusions from this apparent shift about the cause of both magnitude and direction of the shift caused by a refractive index increase. In fact exchanging air with water moves the minimum beyond the origin from about -12.69° to +10.7°. Thus the critical angle appears to have changed to the other side of the minimum, but coupling hasn't changed (m = +1). In case of a left/right symmetric grating profile $\zeta(x)$ (i. e. one can find a suitable origin so the profile satisfies $\zeta(x) = \zeta(-x)$), like for the gratings discussed in this work, there is no difference between positive and negative angles. But for blazed gratings, illumination from a given angle θ is not necessarily the same as for $-\theta$ and one has to distinguish between incidence along the blaze direction and against it. In addition to the position of the reflectivity minimum, the dielectric change also affects the width of the resonance dip. In water, the width of the curve has doubled, because the angular scan line cuts through the dispersion relation at a smaller angle in respect to its slope (this situation can be seen best in figure 2.4). At the same time, the asymptotic reflectivity (R far from the minimum) is always lower in water than in air. Additionally, the magnitude of the reflectivity minimum has changed, since the surface plasmon field samples into the medium and the resonance responds differently to the changed dielectric environment. The coupling efficiency can be improved by optimizing the grating amplitude.

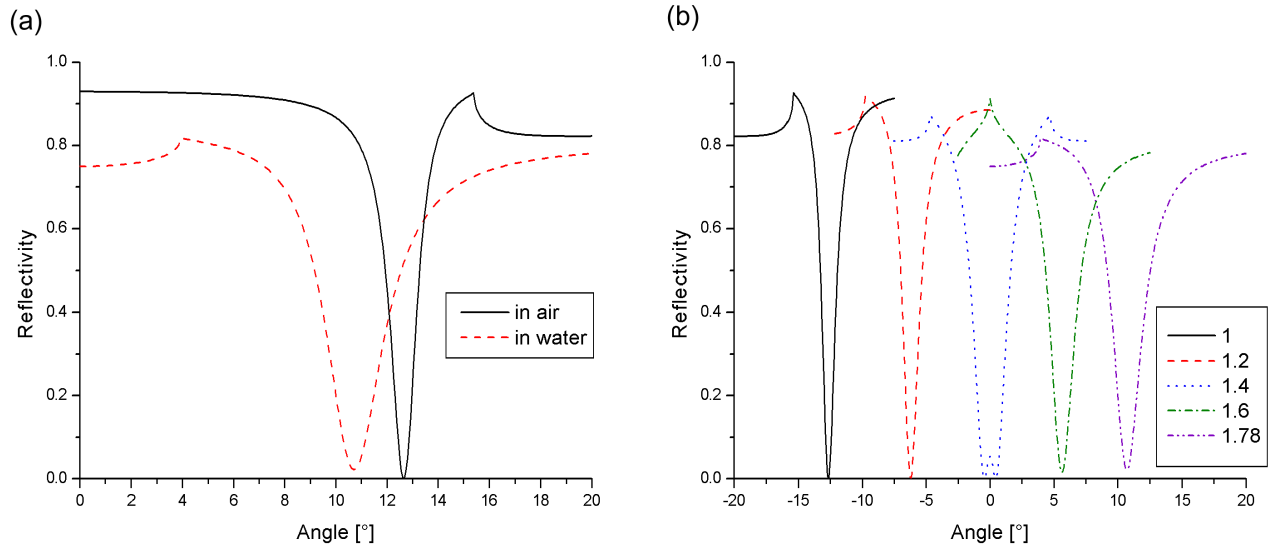

Figure 4.12: Crossing the origin while going from air to water. (a) The reflectivity minimum appears to move only a little in experiments where air ($\epsilon = 1$) is removed with water ($\epsilon = 1.78$), while the edge seems to jump to other side of the minimum. (b) A thought experiment, where one can tune the dielectric number of the medium continuously, reveals the transition of the minimum from the left over the origin to the right. All reflectivity curves are symmetric to the origin in fact, but the mirror images on the other side of the origin have been omitted for clarity.

The grating constant is the main, but not the sole, geometric factor determining the resonance angle, see figure 4.13. By picking the right value it can be used to engineer a convenient working geometry for a set-up. Grating constants in the range from half to twice the wavelength of the light source are suitable. These allow excitation up to ±60° from the surface normal in air or ±30° in water. Special care has to be taken for the case of orthogonal coupling. Profile/material combinations exhibiting band gaps in the dispersion relation can prohibit surface plasmon excitation at 0° if the photon energy $\hbar\omega$ falls into a band gap (see section 2.1.6).

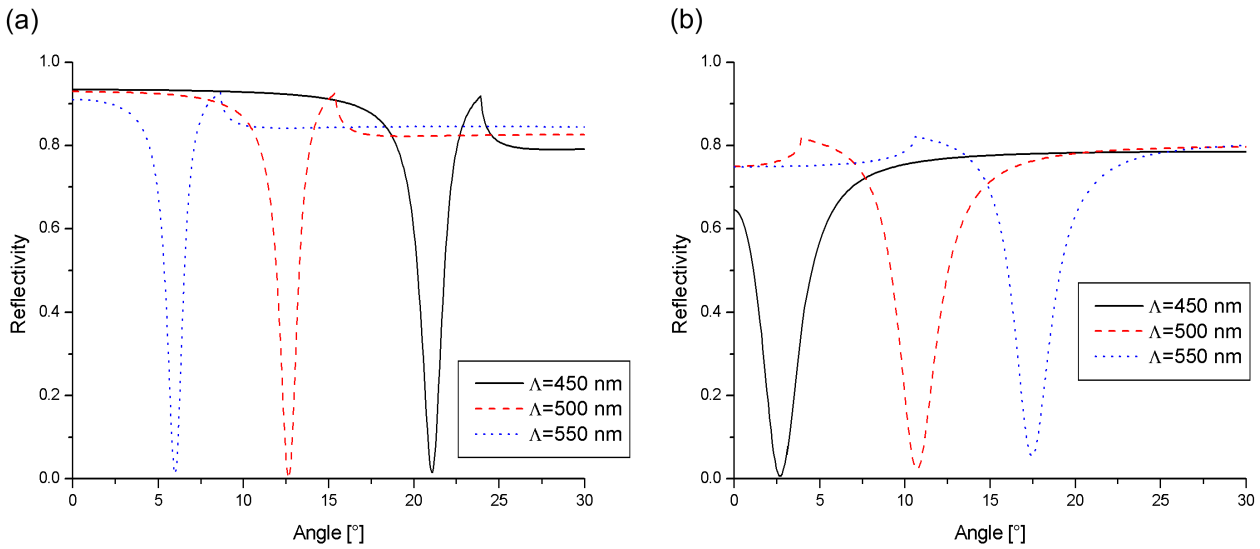

Figure 4.13: How the grating constant affects the resonance angle. For the model system, an increase of the grating constant shifts the resonance angle into the edge→minimum direction. Λ alone only determines the approximate value of θ_r and the precise location depends also on the corrugation shape and amplitude. (a): in air; (b) in water

The exact position for exciting the resonance is also weakly influenced by the amplitude (figure 4.14) and even more strongly by the exact profile shape (figures 4.15 and 4.16) of the corrugation. The impact of these two quantities might appear surprising at the first glance and initially raise questions about the validity of the Rayleigh approximation on which the simulation algorithm is based, especially since in diffraction optics, it is only the dominating Fourier component of the corrugation that determines the geometry of the diffraction pattern. But the interaction between profile geometry and coupling condition is a physical phenomenon. The reflectivity minimum is not a curve feature caused by diffraction only[7]. One has to keep in mind that surface plasmons were only derived as surface bound electromagnetic solutions to Maxwell's equations in section 2.1.4 for a flat interface. Strictly speaking, corrugated interfaces are not covered by this. Treating the corrugation as a small perturbation of the flat surface is synonymous with perturbing the dispersion relation found in the flat surface scenario. Amplitude and shape of a regular perturbation to the surface (i. e. grating profile) will impact

[7]On the other hand the (pseudo-)critical edge is a pure diffraction phenomenon. Its location is fixed and does not vary with changes in amplitude or profile shape.

on the magnitude and nature of the perturbation of the dispersion relation. The dispersion relation, on the other hand, defines the resonance angle. This interaction between corrugation depth and reflectivity response has already been reported in the literature for experiments with symmetric gratings in the infra-red [Lop98] and for blazed gratings in the visible/near infra-red part of the electromagnetic spectrum [Kre02]. Additionally, different dielectric media require different amplitudes to achieve efficient coupling. This relationship can be seen in figure 4.14 as well. An amplitude of 20 nm gives the best coupling in air, whereas 25 nm are necessary in water to achieve the same value of R_{min}. Therefore, gratings have to be optimized for a certain dielectric environment. For grating applications operating in an aqueous environment, the coupling efficiency ideally should be quantified for an immersed grating, but traditionally the coupling efficiency is given for the gold/air interface.

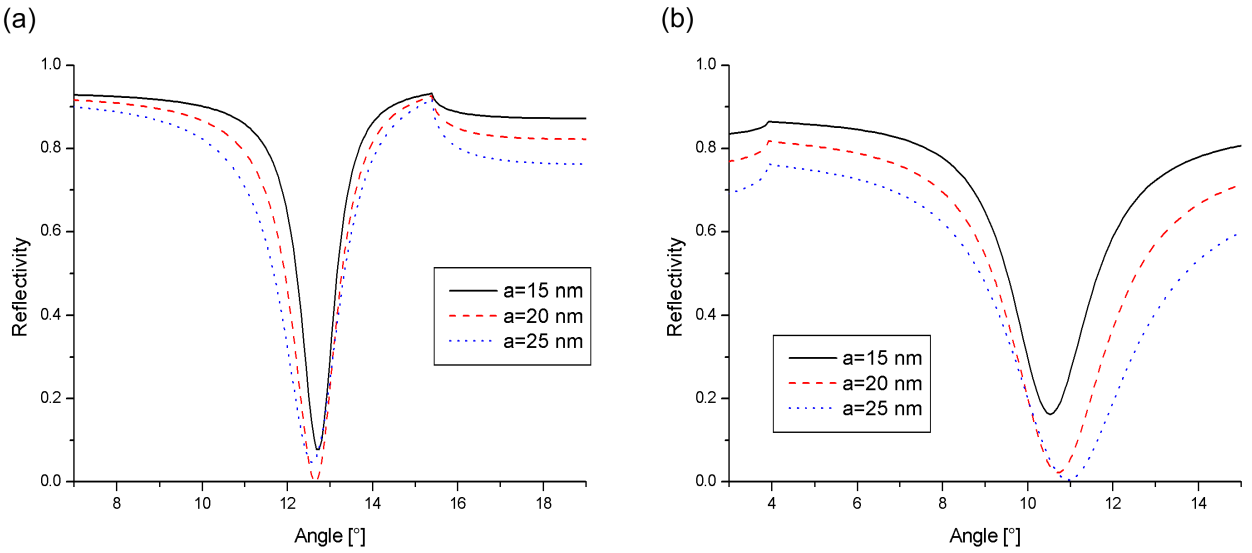

Figure 4.14: Influence of the grating amplitude on the coupling. Both resonance angle as well as coupling efficiency are functions of the profile amplitude. The optimal amplitude depends on the dielectric environment. An amplitude a of 20 nm works best in air (a), but in water (b) an increased amplitude of 25 nm is necessary to reach a very low reflectivity minimum. At the same time, the resonance angle changes its position by some tenths of a degree as a function of the amplitude. Additionally the amplitude influences the half-width of the minimum. The higher the losses, the broader the resonance curve. More efficient coupling, by tuning a for example, equates to increased radiation damping and hence resonance width. Therefore, the curve with the highest η is never the one exhibiting smallest width. Another prominent curve feature related to the amplitude is the height of the plateau, i. e. the magnitude of R beyond the edge. It can serve as a direct feedback about the development time during grating fabrication.

Three different profile types of equal amplitude and periodicity and their impact on the optical response of a grating are presented in figures 4.15 and 4.16. The first curve shape is a pure sinusoid, like the commercially obtained specimen. Profile number three is of trapezoidal shape with sharp corners - similar to the self-made gratings. It is characterized by a mark-to-space ratio of 0.7 and a slope fraction of 32 %. The second one adds a third harmonic component with an amplitude of 3 nm to the fundamental given by the first profile. This is the onset of the Fourier expansion of a square wave and this profile is meant to serve as an intermediate between

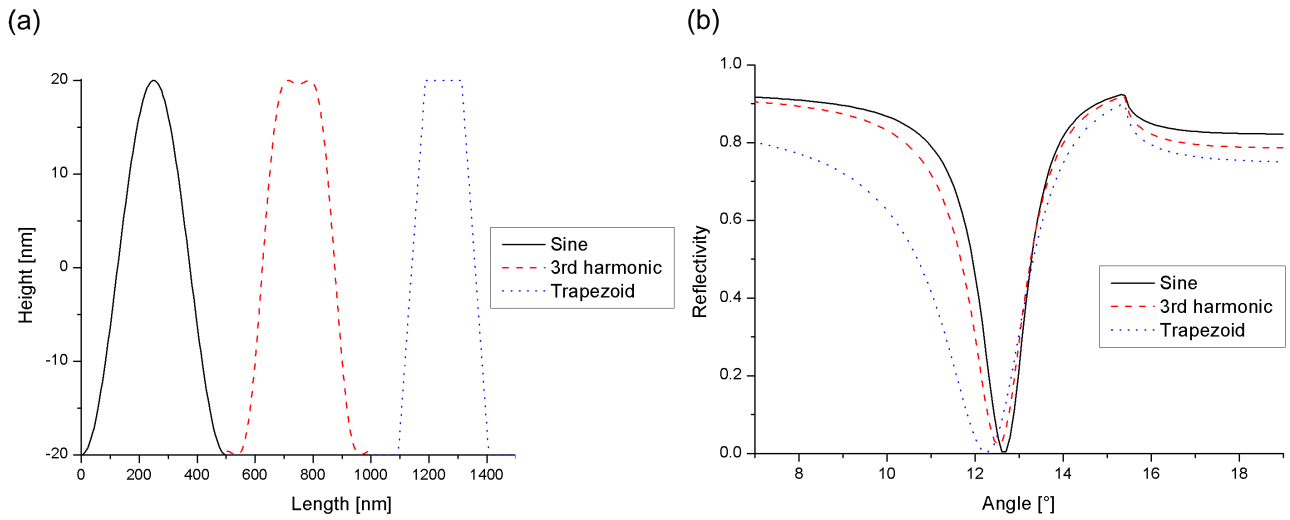

Figure 4.15: Profile shape and optical response in air. Different grating profile shapes result in a different reflectivity curves. (a) Of the three profile types used for the calculations, the first and the third form resemble the corrugations found by AFM, the second type acts as an intermediate. (b) The reflectivity curves of all three grating profiles exhibit different half-widths, resonance angles and efficiencies in air. Only the edge position is universal.

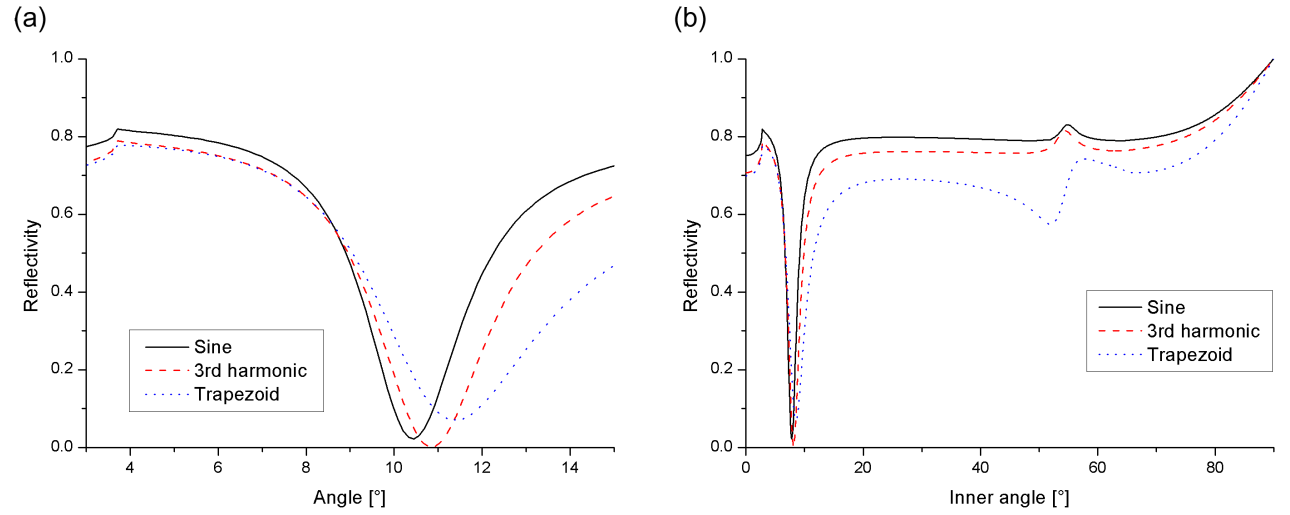

Figure 4.16: Profile shape and optical response in water. The graphs show reflectivity calculations in water for the grating profiles introduced in figure 4.15 (a). (a) Again, the three curves differ in the three key parameters. The half-width of the trapezoidal profile is always the largest because of increased radiation damping due to re-emission mediated by the 250 nm second harmonic component contained in the trapezoidal shape. (b) The second minimum caused by this second grating structure is located at an *inner* angle of approximately 54°. Because of the refraction taking place when working with a flooded flow cell, the second minimum caused by this second grating structure can't be detected directly. For this reason, the graph (b) shows the reflectivity curve as a function of the inner angle as an exception.

the other two shapes. All three profiles show different coupling efficiencies[8], resonance angles and half-widths in air and water with the sine cum third harmonic curve mostly being located between the other two. The curve related to the trapezoidal profile is the broadest of all three. The reason for this lies in its nonvanishing second harmonic Fourier component. Effectively two superposed gratings are present allowing reradiation mediated not only by Λ but also by $\Lambda/2$. The presence of this additional decay channel equates to a larger width because of increased radiation damping. Coupling to this second harmonic grating ($m = -2$) can be seen clearly in the case of water at an *inner* angle of about 54° in figure 4.16 (b). In a real experiment where the grating is immersed in water that is contained by a flow cell, the resulting refraction makes direct observation of the second minimum impossible. In contrast to all this, reflection data for s-polarized light is almost independent of the grating profile since coupling to the corrugation can't take place.

Taking up the trapezoidal profile again, one can vary a single characteristic parameter and study the impact on the reflectivity curve. Figure 4.17 shows calculations for different values of p/l while keeping s constant. S is varied in figure 4.18 for a fixed value of p/l over a similar dynamic range as before. The corresponding grating profiles are shown in figure 4.19. The two parameters have a very different influence on the curve shape. The reflectivity is particularly sensitive to variations in s. The position of the resonance angle, the curve width as well as the coupling efficiency all depend strongly on the magnitude of s in air as well as in water. On the other hand changes to p/l affect half-width and resonance angle only a little. Only in water does η change significantly as a function of p/l for the given numerical range. Concentrating on a high coupling efficiency only the transition from air to water demands an increase in both s and p/l to maintain efficient coupling. For working in an aqueous environment, it is desirable to use fabricate gratings with p/l approaching unity and s exceeding 40 %. In general terms $p/l = 1$ characterizes a symmetry aspect, a corrugated surface equally occupied by lands or pits. A high value of s means the transition from land to pit is smooth and not so abrupt as for a profile of low s. So the general shape is moving away from a square wave or trapezoid and getting a little closer to an approximation of a sine profile.

Besides the geometric attributes of the corrugation, the material properties of the metal also play an important role in the coupling process. Of course, the dielectric constant can't be tuned as easily as for example the grating constant in real life. But for the purpose of curve fitting, it is valuable to have a look at the influence of the real and the imaginary part of ε (i. e. ε' and ε'') on the reflectivity curve. The effect of ε' on R is shown in figure 4.20, now again for a sinusoidal corrugation. This quantity primarily affects the resonance angle. An increase in ε' shifts the reflectivity minimum towards the edge. There is also small influence on the curve width and on the coupling efficiency. The latter is especially pronounced when the dielectric half-space is consists of water. In the case of ε'' (see figure 4.21), there is only a negligible impact on the resonance angle irrespective of the medium. On the other hand, the half-width and the coupling efficiency depend significantly on ε''. The higher its magnitude, the broader the minimum dip of the curve. A fact that suits the expectation, since ε'' is the quantity describing the loss processes in a material. Looking at the coupling efficiency, the

[8]For the same default amplitude of 20 nm. An optimal amplitude can be found for all three to reach R = 0.

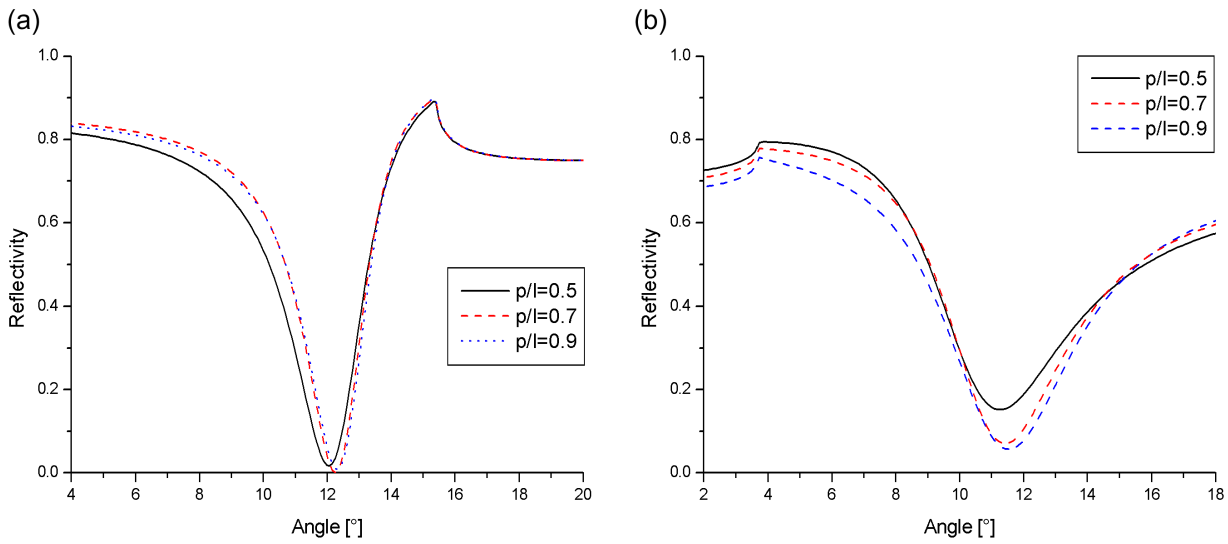

Figure 4.17: How p/l of trapezoidal profiles affects the reflectivity curve. (a) Variations in the mark-to-space ratio of a trapezoidal profile have little effect on the reflectivity curve in air. (b) A bigger impact exists in a water environment, where the coupling efficiency depends significantly on p/l. The slope fraction is maintained constant at 32 % for all curves.

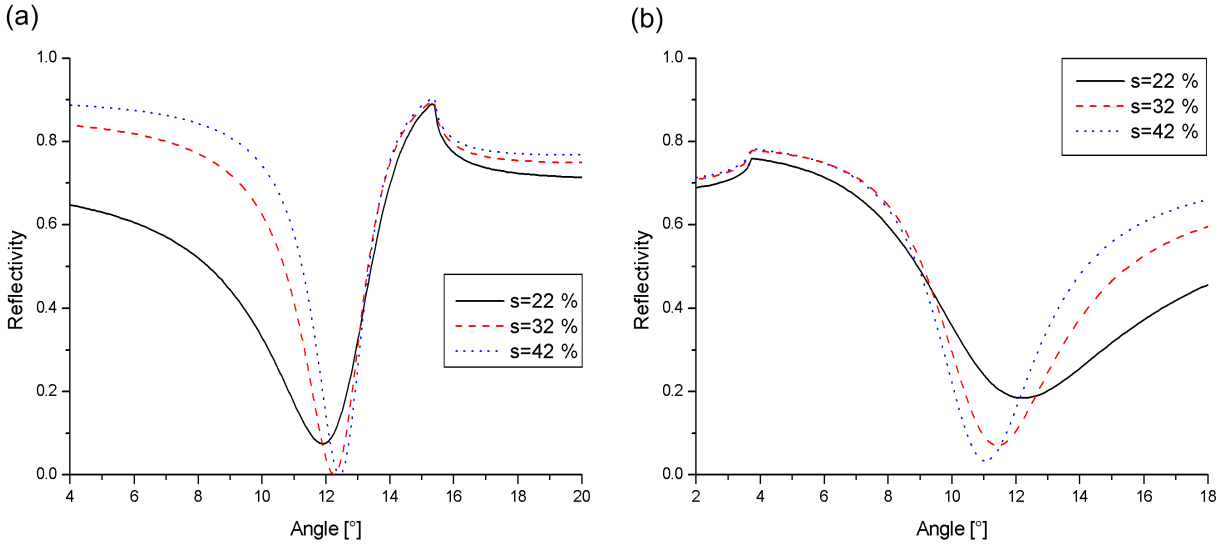

Figure 4.18: How s of trapezoidal profiles affects the reflectivity curve. For a constant p/l of 0.7, the slope fraction has a strong influence on the curve shape. In both media ((a): in air; (b) in water), the resonance angle, the half-width and also the coupling efficiency can be very different according to the s value of the profile.

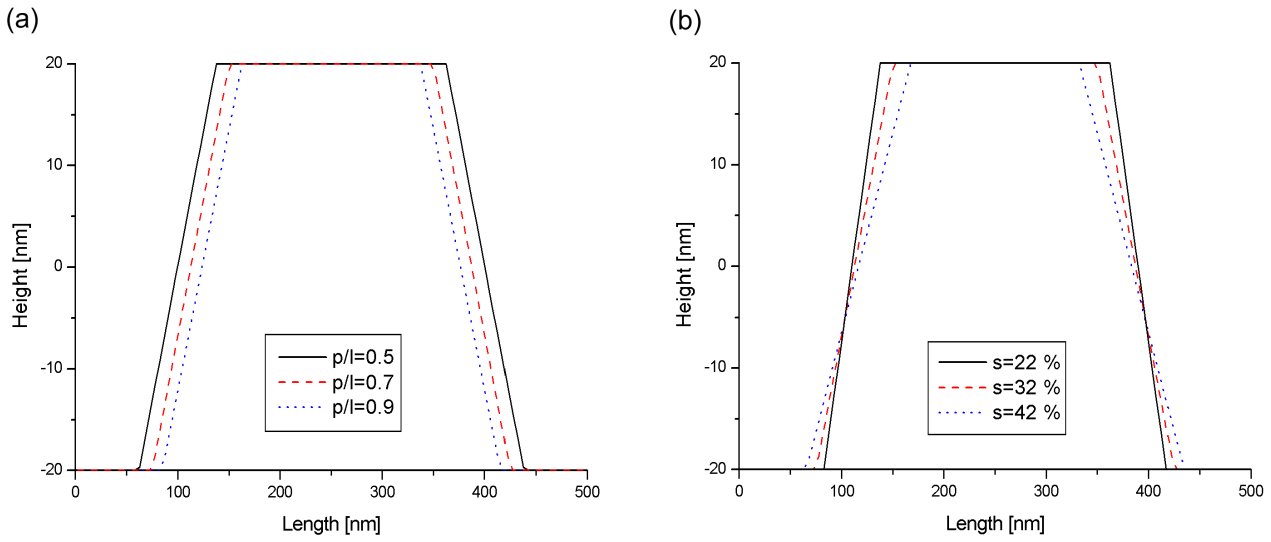

Figure 4.19: Trapezoidal profile shapes for different values of s and p/l. The trapezoids shown are the profiles used in the calculations for figures 4.17 and 4.18. (a) The three profiles all feature $s = 32$ % but are described by different p/l. (b) The profiles have the same p/l of 0.7 in common but differ in s. The length of the abscissa corresponds to Λ.

dependence is not monotone and a value of 1.3 gives a very low η in both air and water.

4.3 Conclusion

Gratings were fabricated by photolithography and RIBE. Their surface profiles were characterized by AFM and found to have a trapezoidal shape. Shallow amplitude profiles of this form are very efficient for coupling light to surface plasmons. The evaporation of gold changes the corrugated surface, not only in terms of roughness but also the topography itself, which has to be taken into account for simulations. Efficient gratings are characterized by structures in glass with an aspect ratio of about 30, a mark-to-space ratio between 0.8 and 0.9 and a slope fraction of less than 25 % in air (40 % in water), with the exact values depending on the grating constant.

Reflections introduced by a flow cell are difficult to model for all angles but can be sufficiently described in the vicinity of θ_r for precise investigations. Lateral as well as rotational offset effects were studied, setting tolerances for device engineering. The former is determined by the uniformity limits inherent to the grating fabrication technique. The latter is governed by geometric relations, that can be easily calculated, and turns out to be a negligible effect for offset angles of up to $\pm 5°$.

GC-SPR was used for thin film characterization in terms of layer thickness and dielectric constant itself. The fitting of grating data with complicated topographies obtained from AFM can be very time consuming. The influences of surface profile parameters and layer properties

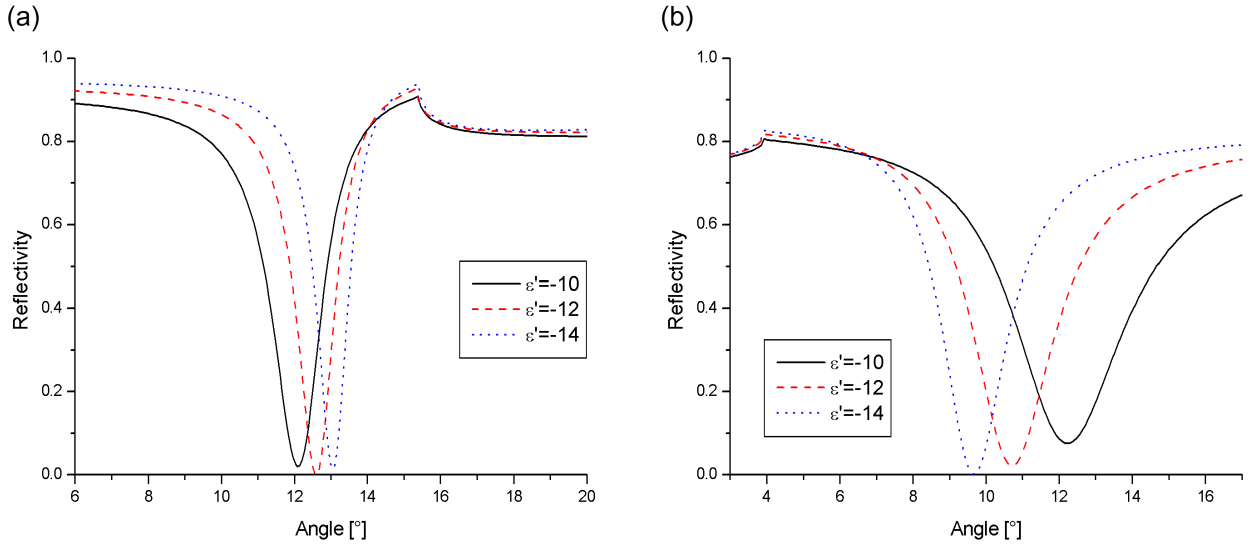

Figure 4.20: How ε' of gold affects the reflectivity curve. Decreasing its magnitude separates the minimum further from the edge. (a) The half-width of the curve and the coupling efficiency are only slightly changing in air for different values of ε'. (b) This relationship is stronger in water (right graph).

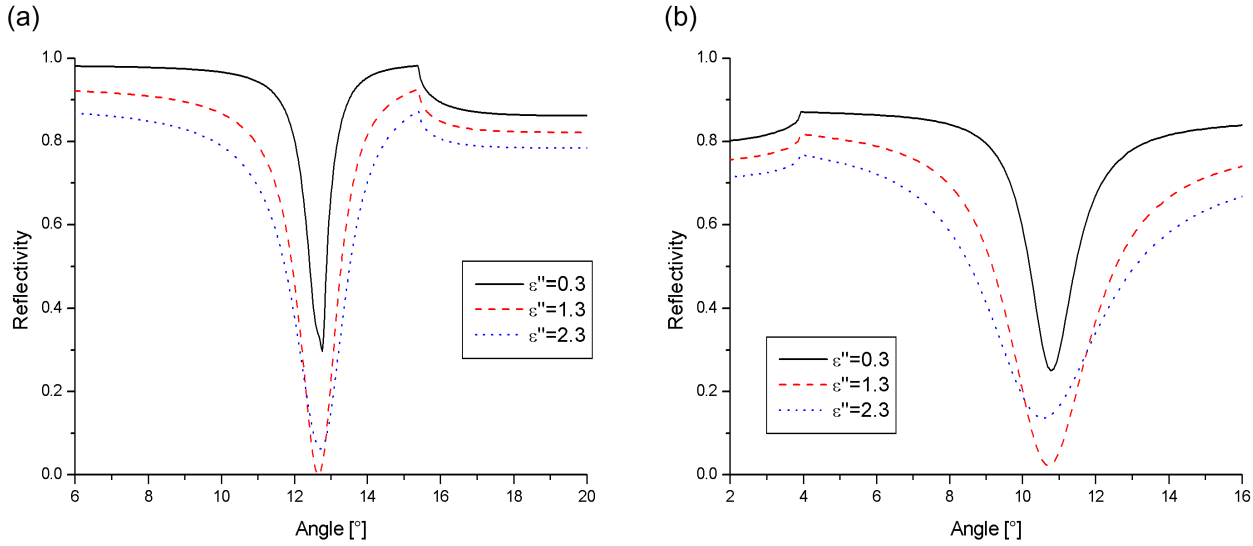

Figure 4.21: How ε'' of gold affects the reflectivity curve. Changes in the imaginary part of ε of the metal strongly affect the half-width and the depth of the minimum. On the other hand the resonance angle is virtually independent of it. (a): in air; (b) in water

on the reflection response of gratings were comprehensively studied and compiled to facilitate this process.

Chapter 5

Back coupling

The first report on the fluorescence emission of dyes placed on a periodically structured metal surface goes almost back a quarter of century [Kno81]. At that time that, it was observed that the emission of the fluorophores is angle dependent. To the author's knowledge only a surprisingly small number of articles (three) have been published since then on this subject. Namely these cover the calculations of the plasmonic fields and enhancement optimization [Kit96], various excitation and emission geometries [Kre01], as well as studies of fluorescence lifetime as a function of the dye/metal separation [And01]. In all of these publications, the fluorophore layer was prepared prior to experiments and the metal under investigation was silver (with one exception). No affinity studies are yet published, that combine the evanescent field of grating coupled surface plasmons with fluorescence detection. With the objective of performing analyte detection from solution, gold was used in this work because of its superior stability in saline buffers. Experiments with this metal in the presence of a different dielectric environment (water instead of air) complement the scarce literature in existence in this field.

Before coming to experimental results, the mechanism behind the back coupling process is explained. The back coupled fluorescence emission from gratings is strongly directional. Depending on the experimental methods used, the symmetry of the back coupled fluorescence emission pattern can be broken and care has to be taken to identify artifacts. This is described in the second section. The strong relation between the location of the emission lobes and the grating constant of a sample is investigated in the following section. Next, the interaction between the fluorescence emission from a grating and the polarization of the illumination is studied. The fifth section focusses on bleaching effects. Tuning measurements of the difference between the minimum of the reflected intensity and the maximum fluorescence excitation position conclude the last experimental section. For the purpose of comparison, selected topics of this chapter are also covered in the context of prism coupling. All experiments described here were performed in the absence of bulk fluorophores. Measurements were only taken after the equilibrium sensor surface coverage of the complementary target strand had been reached and after the flow cell had been rinsed with pure buffer.

5.1 Background on back coupling

SPFS schemes are commonly realized by prism coupling. The two essential processes of the technique are: first, the coupling of the incident beam to surface plasmon modes and second, the energy transfer between the evanescent field of a surface plasmon to a fluorophore. The same mechanisms can take place with time being reversed: an excited fluorophore can transfer its energy into a metal film to launch a surface plasmon, which then decays via radiating a far field photon. This reversed process is called back coupling. Because the re-radiation is now bound to the plasmon/photon coupling condition, the fluorescence emission shows a distinct angle dependence. Back coupling is a doubly resonant process and therefore doubly enhanced. As an additional advantage the geometrical restrictions introduced by the outcoupling condition concentrate the emitted light into a solid angle much narrower than the free emission taking place in conventional SPFS.

The fluorescence back coupling process taking place on a grating surface can be thought of the five sequential steps illustrated in figure 5.1. In the beginning, photons of the incident beam ($\lambda = 633$ nm in this work) have to meet the coupling condition. The angle of incidence where this condition is met is determined by their dispersion relations and the combined energy and momentum conservation (detailed in sections 2.1.5 and 2.1.6 respectively) and appears as the site of the minimum in the reflectivity curve. Under illumination at this angle, surface plasmons are excited. Their evanescent field can excite fluorophores near the metal surface. Internal conversion processes quench the vibrational excitation of the dye nonradiatively. The remaining excited state is purely electronic and hence of lower energy than the original excitation. Due to the proximity of dye and metal, the fluorophore can transfer its energy to the metal film to excite a surface plasmon - just as during dye excitation, only in the reversed order. The Stoke's shift causes the new plasmon mode to be of a red-shifted frequency in respect to the incident beam. Interaction with the surface corrugation allows the surface plasmon mode to reduce its momentum and decay radiatively by emitting a far field photon. This photon is characterized by the fluorescence emission wavelength of the dye (664 nm for Cy5). As in the case of photon-to-plasmon-coupling there is a distinct resonance angle. In the case of plasmon-to-photon-coupling this outcoupling angle θ_o is determined by how the red-shifted plasmon perceives the periodically structured metal/dielectric interface. In other words: simulating the reflectivity response of the corrugated gold at the fluorescence wavelength approximately[1] yields the outcoupling angle under which the photons are emitted from the grating. When working with an interference filter in front of the PMT it has to be kept in mind that the detector sees the product of the broad wavelength spectrum emitted by the dye and the transmission curve characteristic for the filter. This combined function has its maximum at about 670 nm.

Lately, back coupling has been studied in great detail in the context of prism coupling [Vas04]. In principal, the back coupling process in the context of prism coupling consists of the

[1]The two angles are not precisely the same. The fact that a small shift exists between the angle of the reflectivity minimum and the maximum excitation position (where energy transfer is most efficient) is already well known in the context of prism coupling [Lie00b]. In grating coupling this issue is more complex It is taken up again in section 5.6.

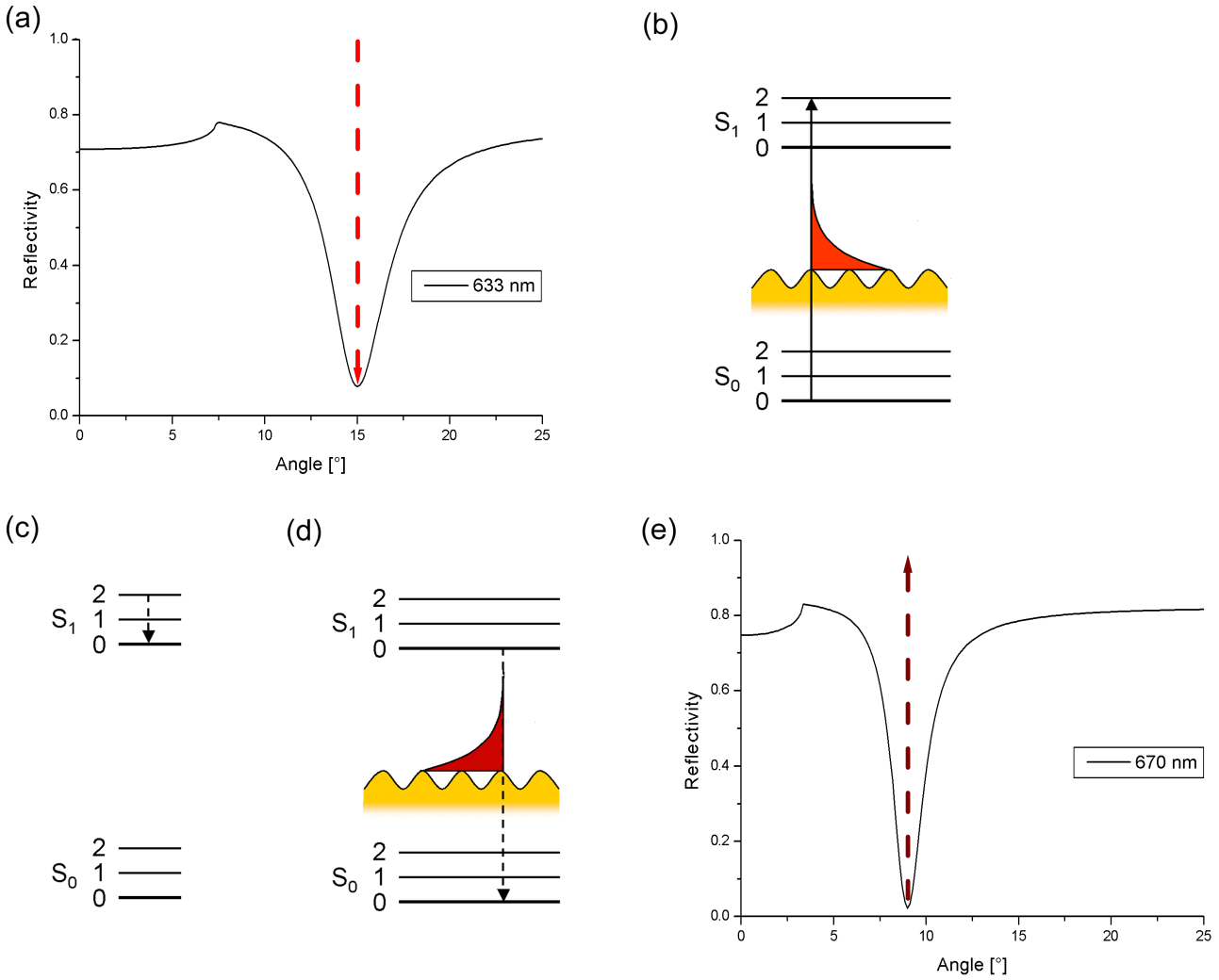

Figure 5.1: The series of events leading to directional emission: (a) light of 633 nm launches a surface plasmon on the metal grating under the angle of minimum reflection (approximately 15° in the example). (b) The evanescent field excites dye molecules in proximity to the surface, symbolized by the Jablonski diagram. (c) Internal conversion in the fluorophore reduces the energy of the excited state. (d) The energy corresponding to the decay to the ground state is transferred into the grating and excites a second plasmon. (e) The second plasmon is red-shifted, because of the energy loss during the vibrational transition of the dye. The grating can reduce the momentum of the plasmon in order to allow conversion into a propagating photon at the new coupling condition given for the peak fluorescence emission wavelength of 664 nm. (This is the same angle one would identify as the resonance angle by measuring the reflectivity of the grating with a light source of this red-shifted wavelength). The presence of an interference filter in front of the detector shifts observation to 670 nm.

same sequence of steps, but there are two important differences. First, the beam geometry is different in respect to the materials and the detector. In prism coupling, detection takes place in the half-space excluding the dye and the light has to pass the metal film twice (see figure 5.2). In a grating coupling set-up, fluorophore, light source and detector are located in the same half-space. The back coupled fluorescence is radiated back into the original half-space of the beam in both cases. The second difference concerns the pattern of the fluorescence emission. Assuming a certain degree of rotational freedom and intrinsic mobility of the "immobilized" dye (an assumption that is justified for the employed DNA assay due to the unhybridized and thus flexible 15-mer spacer sequence of the probe strand and the constantly flowing buffer solution), a dye molecule can reach a different orientation during the 10 ns that typically separate emission from absorption. Ideally the spectrum of dipole orientations is isotropic and any polarization information stemming from the excitation process is lost prior to fluorescence emission. This is equal to offering all possible definitions of the p-plane to the energy transfer from the dye to the metal. Since the metal film in prism coupling features the same continuous rotational symmetry (in respect to the z-axis), the re-radiation is symmetric to rotations around the surface normal, i. e. the emission pattern becomes a ring. In the case of grating coupling, the corrugation breaks this rotational symmetry and concentrates the fluorescence emission into two lobes symmetric to the xz-plane that is easy to harvest. When recording the emission pattern in the azimuthal plane two fluorescence peaks are present at $+\theta_o$ and $-\theta_o$ due to the mirror symmetry of the grating and the isotropy of the dipole orientations.

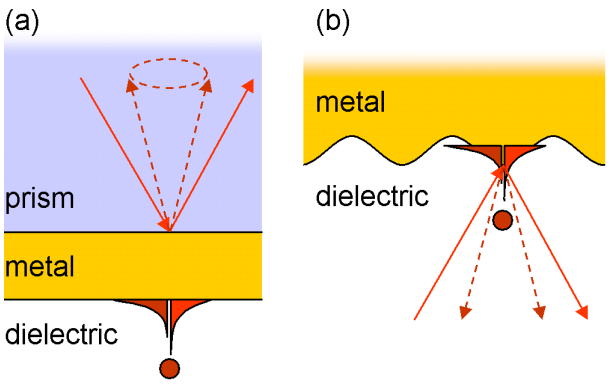

Figure 5.2: Emission patterns for back coupling with prisms and gratings. (a) In prism systems not making use of back coupling, the metal film separates dye and light source as well as dye and detector. Given sufficient rotational freedom of the fluorophores the original definition of the p-polarization plane is lost and fluorescence is emitted in a cone pattern (dashed lines). The cone is contained within the angle formed by the incident beam and its reflection (solid lines) because of the red-shift of the fluorescence wavelength. (b) Light source, detector and dye are all located in the dielectric half-space in the case of grating applications. Since the rotational symmetry of a flat metal surface is broken by the periodic corrugation the emission takes place in the form of a pair of lobes. These lobes are located within incident beam and its reflection.

In prism coupling schemes the fluorescence emission commonly detected stems from dipoles that radiate freely into the dielectric half-space. They don't couple back into the metal film to emit through the prism. This type of fluorescence emission is almost constant in intensity for angles close to the surface normal [Vas04]. That is why in such a system the detector is usually

mounted in a fixed position over the sample. It is favorable to collect photons from a large solid angle in order to increase sensitivity. In a grating set-up, the choice of the grating constant determines where the fluorescence lobes are located. Gratings can therefore be engineered to direct the emission into a solid angle that is conveniently covered by the detection optics.

5.2 Symmetry of the emission pattern

The first thing one notices when looking at a fluorescence intensity versus detection angle curve is the apparent asymmetry of the two emission lobes. Figure 5.3 (a) gives an example of a typical curve obtained from a sample with a grating constant of 511.6 nm. The locations of the back coupled fluorescence emission lobes are symmetric to the origin, corresponding to the orientation of the surface normal of the grating, but they are of different height. It is always the left peak that is higher than the right one. This is an artifact caused by bleaching of the immobilized dye molecules and not a consequence of a grating corrugation asymmetry or another anisotropy effect. For recording angular fluorescence data the PMT was always scanned from the left to the right in respect to the angular scale in all the figures given here. Therefore, the data shown in a plot for higher angles has been measured with a system that contains a certain proportion of bleached fluorophores. On the other hand the data given for lower angles is obtained from a situation where a smaller fraction of bleached molecules is present or none at all. Typically, curves like those in figure 5.3 (a) required a measurement time (and hence exposure to the laser beam) of 5 to 10 minutes, depending on the desired angular coverage. In between measurements the laser beam was blocked by a shutter to prevent additional bleaching.

There are two ways to prove that the difference in peak height is not related to an asymmetry of the corrugation. First, questions of a possible asymmetry can be addressed by flipping the grating and taking a second measurement. A comparison like this is shown in figure 5.3 (a). It is still the left peak, measured first, that is higher. Flipping the grating by 180° doesn't change this. Secondly, one can reduce the exposure time to the illuminating laser by probing only small angular intervals. The time for the PMT to scan the full angular range can last several minutes, depending on resolution. Figure 5.3 (b) presents data taken specifically around the peaks only. Even if there are fluorophores present in the bulk, the result is the same: both peaks have virtually the same height. The left peak is still a little higher in both cases, but the difference is much smaller compared to the data set in figure 5.3 (a) where a much longer exposure time was used in order to record the whole emission pattern. All these results indicate that the apparent asymmetry is only an artifact caused by bleaching.

5.3 Emission angle versus grating constant

The back coupling process features two interactions of the grating structure with the electromagnetic field. One at the excitation wavelength and another one at the emission wavelength. Therefore, samples need to be studied under both wavelengths. The quantity that changes the properties of the grating while going from one wavelength to the other is the dielectric constant

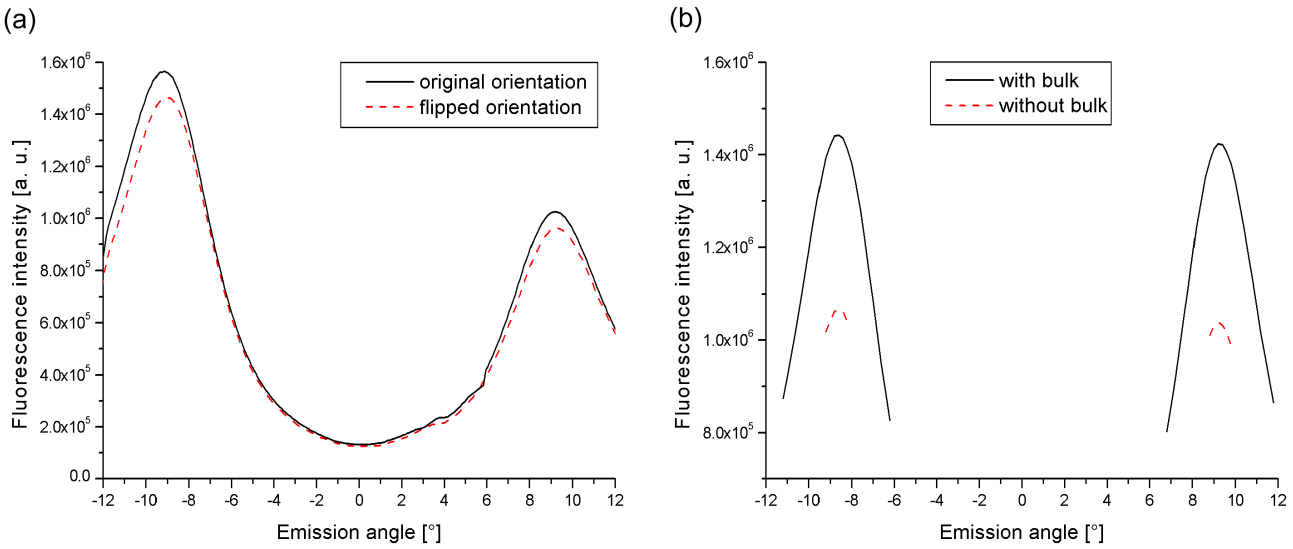

Figure 5.3: Emission asymmetry - a bleaching artifact. The directional fluorescence emission from Cy5-labeled target oligonucleotides immobilized on a grating was measured in the experiments. The curves have been recorded by keeping the sample fixed at the resonance angle and rotating the PMT with a narrow aperture. Both peaks are symmetric to the origin in both position and shape. Their apparent difference in height is an artifact caused by bleaching. (a) Flipping the grating by 180° (sample B63 without bulk) doesn't invert the height relation of the peaks, something that should happen if the effect is related to the profile orientation. (b) By the same token, when the exposure time is minimized, for example by measuring only over a small angular range, the intensities of both peaks are nearly equal (grating B60).

of the gold film. It is straight forward to characterize a sample at the excitation wavelength by recording the reflectivity response. But information about the optical properties of a grating at the emission wavelength are more difficult to come by unless a light source of said wavelength is available. In this case, another reflectivity measurement can be taken with this second source to find the resonance angle and the corresponding coupling efficiency at 670 nm. This method does not require analyte binding and is therefore very reliable. However, even without such a second light source, information about the optical response of a grating at the emission wavelength can be obtained by studying the location of the emission peak.

Figure 5.4 shows the back coupled fluorescence emission pattern for the two grating constants predominantly used in this work. Both lobes are located closer to each other for the sample with the smaller grating constant. At the same time, the width of the peaks is much smaller. By picking the right grating constant the emission angles can be engineered in a way that is convenient for a given device geometry. Unfortunately, the fluorescence intensities generated by both samples can't be compared strictly. Samples with a grating constant of 474.7 nm only became available much later in this work. At that time, certain properties of the experimental set-up, like beam collimation and thus laser power, had been changed.

From recording the emission pattern with at least one of its two maxima, one can derive information about the optical properties of the grating at the fluorescence wavelength. The minimum of the reflectivity curve at 670 nm determines the approximate outcoupling angle

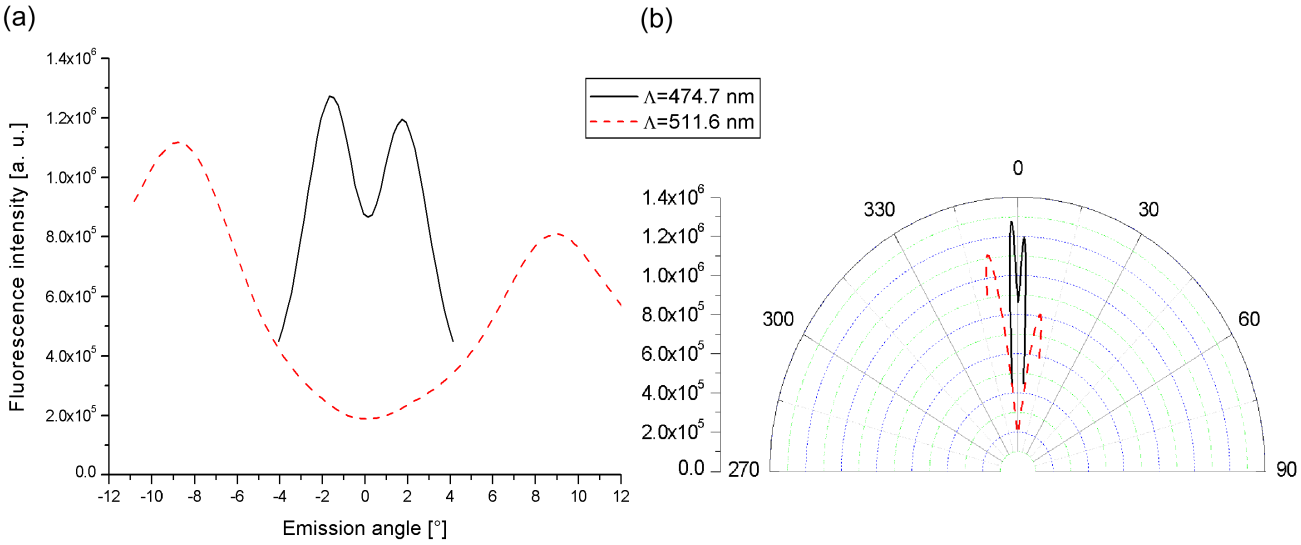

Figure 5.4: Tuning the emission angle by changing the grating constant. (a) Sample B104 has a grating constant of 474.7 nm and a resonance angle of 8.06°. Grating B55 ($\Lambda = 511.6$ nm) is resonantly excited at 15° and shows a larger angular separation between the two fluorescence emission lobes. (b) The emission geometry is more intuitively visualized by the polar plot, which shows the same data.

and vice versa. In principle, the emission pattern can be measured and, if the grating topology is known, curve fits are possible in order to characterize the multi-layer system. Examples of this are given in figure 5.5 for a multi-layer system of water/streptavidin/thiols/gold. The thin, dilute oligonucleotide layer can be neglected. The rigorous fitting of reflectivity curves at 633 nm has already been discussed in section 4.2.3 and the same parameters are used here to describe the organic materials. Force micrographs yielded the surface profile used for the calculations. Only the dielectric constant of the gold film was adapted in order to achieve agreement with the experiments. ε'_{Au} and ε''_{Au} were also the only free parameters for modelling the reflectivity response of the system at the fluorescence wavelength of 670 nm. Essentially matching the peak intensity position with the reflectivity minimum is the only criterion for choosing the dielectric number of gold at 670 nm. For sample B55 the metal was modelled with $\varepsilon_{Au} = -11.3 + i1.2$ at 633 nm and with $\varepsilon_{Au} = -13.9 + i1.5$ at 670 nm. In the case of B104, $\varepsilon_{Au} = -11.9 + i1.3$ was used for the excitation and $\varepsilon_{Au} = -14.1 + i1.4$ for emission.

In figure 5.5, the right half of the emission pattern is superimposed on the reflectivity curves for the two gratings. In both cases, the shape of the resonance minima are very similar to that of the intensity peaks, just inverted. This similarity is indicating the relationship of the two phenomena as already described. The transition from 633 nm to 670 nm affects the reflectivity curves of the two samples very differently. B55 is a grating with η higher than 0.8 for both wavelengths. The curve shape is essentially unchanged while the reflectivity minimum is located at a smaller angle for 670 nm, 8.8° instead of 15°. At 633 nm B104 has a coupling efficiency higher than 0.95 and the minimum is located at 8.06°. The minimum position at the emission wavelength appears also at a smaller angle (1.65°) for sample B104, but the diffraction edge is

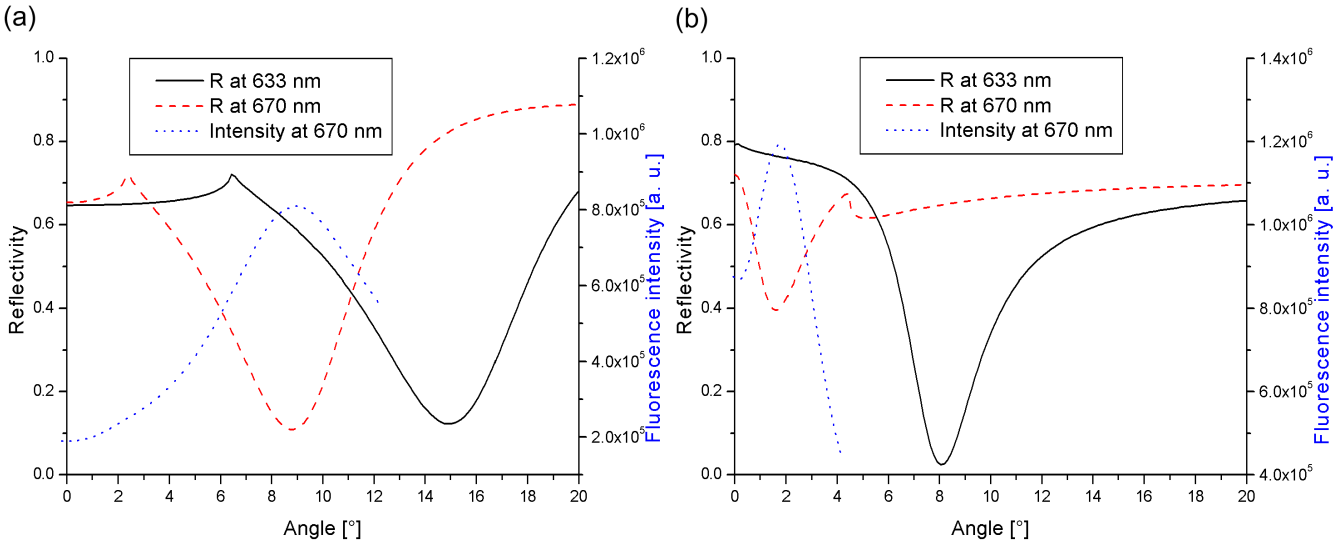

Figure 5.5: Calculations of reflectivity at 633 and 670 nm. Both graphs show calculated reflectivity curves for the multi-layer system water/streptavidin/thiols/gold for grating B55 and B104. Only the dielectric parameters of the metal have been varied to fit the resonance angles at 633 nm or 670 nm. Laid over these are the measured emission patterns already shown in figure 5.4. The widths of reflectivity minima at 670 nm correspond to that of the emission lobes. (a) Grating B55 has a similarly high coupling efficiency at both wavelengths. (b) In contrast to that, B104 has an even higher η at 633 nm, but interacts much weaker at 670 nm. For efficient back coupling the optical response has to be considered at both wavelengths.

now located on the other side of the minimum. This indicates coupling to another branch in the dispersion relation scheme. The coupling efficiency to this branch is about 0.6 and much lower than before. For a grating that is efficient for both enhanced fluorophore excitation, as well as for back coupled emission, the coupling efficiency has to be high for both wavelengths. At a first glance B55 looks like the better suited candidate. But looking at the two reflectivity curves of a sample only does not provide the full picture. Nothing is said about the relative strength of the excitation and emission process taking place on the grating surface. It will be shown in the following sections, that samples of a smaller grating constant like B104 are better in terms of polarization discrimination and bulk rejection.

5.4 Polarization discrimination

One has to be careful of reflections of the laser beam, since even fluorescence detection in grating coupling schemes is essentially taking place in a reflection geometry. One way to cut down on the number of detected laser line photons is to use a second interference filter in front of the PMT. Additionally, it is very helpful for the interpretation of data to be able to switch between p- and s-polarization of the light source. Only p-light can excite surface plasmons. Ideally, any structure seen in the fluorescence under s-light excitation has to stem from reflected and/or diffracted laser spots that are not completely blocked by the interference

filters.

The Fresnel rhomb integrated in the set-up (refer to section 3.3) was used to change the polarization of the illuminating laser beam without altering its power. Figure 5.6 shows the impact of the polarization state on the emission pattern after bulk removal for two different grating constants. Under p-polarization, the enhanced surface plasmon field is utilized and a very strong directional fluorescence emission recorded. Dye excitation by direct illumination is the dominating process under s-light conditions. The fluorescence intensity is much lower in this case. At the left peak position the ratio of the two intensities equals approximately 1:18 (for $\Lambda = 511.6$ nm) or about 1:35 (with $\Lambda = 474.7$ nm) respectively. This discrimination ratio is shifted in favor of p-light excitation for the sample with the smaller grating constant. For this sample, the two fluorescence lobes strongly overlap. Apparently, the overlap not only results in a superposition of the fields (that wouldn't change the discrimination ratio), but has a non-linear effect.

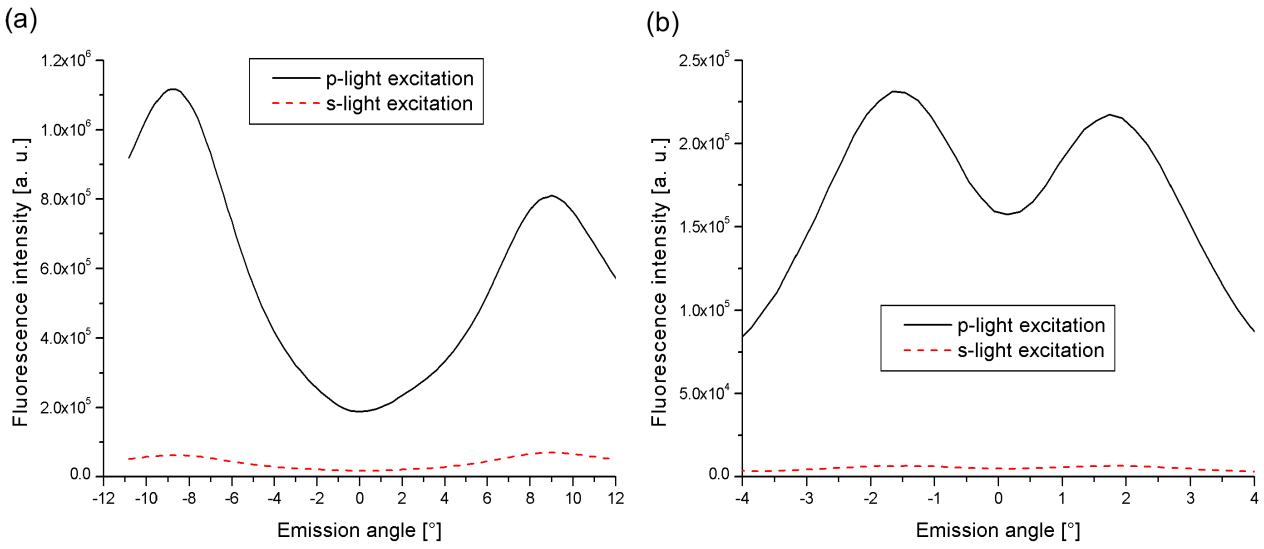

Figure 5.6: Fluorescence emission under p- and s-light excitation. Prior to the measurement, all unimmobilized fluorophores were removed from the flow cell. P-light illumination results in a much stronger fluorescence signal showing the two peaks characteristic for back coupling clearly. Nevertheless the emission under s-polarization is also structured and peaks at the same angles. The samples are (a) B55 and (b) B104 again, as in the previous figures.

The emission pattern generated from s-light illumination features also two peaks at the exact same positions as under p-light conditions. This fact is best visible from the measurements with the higher grating constant. An excited dye molecule can still couple out via the grating (steps (c) to (e) in figure 5.1), even if the excitation occurs under s-polarization. Apparently, there is enough time during the fluorescence cycle and sufficient rotational mobility for the fluorophore to depolarize to a certain degree. The same must hold true for the p-light case, indicating an orientational loss mechanism: a fluorophore with a dipole moment that has a non-vanishing component perpendicular to the grating surface transfers energy most efficiently

to the grating. All molecules of parallel orientation predominantly radiate in the normal fashion without utilizing the resonant enhanced route over the grating. It is therefore advantageous for achieving higher a fluorescence signal to employ an immobilization method that fixes the dye molecules in the desired orientation. The structure in the fluorescence emission generated by s-light could, in principle, also stem from a different alignment of polarizer and grating vector. For this to be the sole reason of the structure and intensity of the emission spectrum, one would be forced to assume a relative alignment error of the two components of about 10° or 13° respectively - an error high enough to be safely excluded.

The discrimination ratio can also be used to quantify the efficiency of the full back coupling process for a given grating. In this view, the s-light excitation gives a background value against which the response to p-polarization is compared. Ideally, s-light is not meant to interact with the grating (apart from diffraction) and should generate a flat angular spectrum for the fluorescence wavelength. A highly efficient grating will generate a much higher fluorescence signal under p-illumination because of the double enhancement. The discrimination ratio contains both fluorescence intensities (λ = 670 nm) weighted against each other. The coupling efficiency (measured at 633 nm) describes only the incoupling process and ideally needs to be complemented by a second value determined at 670 nm.

For comparison to the aforementioned results, figure 5.7 presents fluorescence intensity measurements from a prism coupling experiment. The experimental method employed here is the tuning mode in which the PMT is fixed to the sample while the sample is rotated through the resonance condition. For prism coupling the PMT is placed with its line-of-sight parallel to the surface normal. This method is different to the one used above to study polarization discrimination on gratings and curve shapes can't be compared. Nevertheless, the intensity value at the peak position can still be ascertained and compared. After target immobilization and removal of remaining dye in the bulk, the ratio of the intensities for the two polarizations amounts to 1:86. Polarization discrimination is hence approximately twice as high as in grating coupling in comparison to the Λ = 474.7 nm candidate. The reason for this lies in the experimental geometry. The thin gold film in a prism coupling experiment is acting as a barrier between the laser and the dye molecules. For s-polarization the metal is highly reflective (R= 0.92) and only a very small fraction of the original intensity will be transmitted and can then excite the fluorophores. On the other hand, p-light can pass much more efficiently. If incident under the resonance angle it is resonantly funnelled through the metal to re-appear on the other side as an enhanced, evanescent field. However, even under s-light illumination there is a characteristic structure in figure 5.7 that follows the shape of the curve for p-polarization. Again, an assumed alignment error (which would need to amount to 6°) can be ruled out as the only explanation.

5.5 Bleaching effects

As mentioned before, a significant amount of bleaching takes place during the time necessary to record an emission pattern. For the comparison of measurements on the same specimen that were obtained sequentially it is therefore important to have some appreciation of the

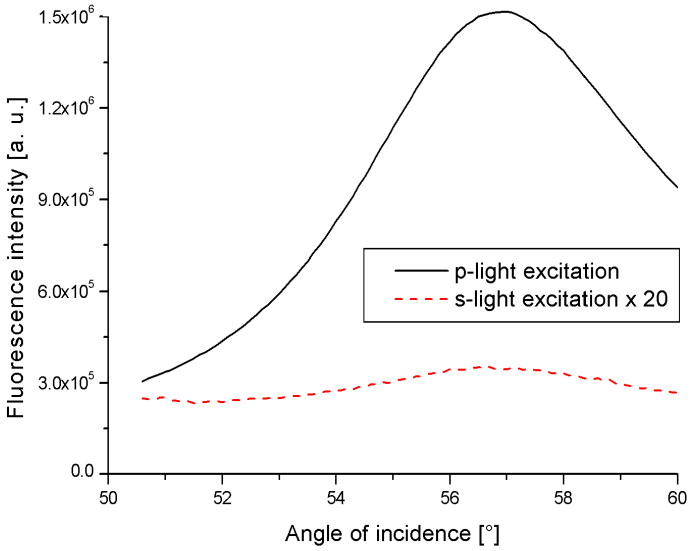

Figure 5.7: P-light and s-light excitation in prism coupling. Both curves feature a maximum at about 57° in this tuning experiment (refer to section 5.6. At this angle, the two curve peaks exhibit an intensity ratio of 1:86. The signal recorded under s-light illumination is magnified by a factor of 20 to show its structure in detail. The sample consisted of LaSFN9 prism, gold film and the usual surface functionalization.

characteristics of the process.

For each polarization, the angular fluorescence emission of the same sample was measured repeatedly and successive curves divided by each other to ascertain the change. Figure 5.8 gives the results for the experiments performed after bulk removal. There is a strong difference in intensity in the case of p-polarization between the first and the second curve. The intensity ratio shows a monotonous decrease for increasing angles. On the other hand, there is virtually no difference between two successive fluorescence measurements under s-light illumination. The intensity drops uniformly by about 5 % only. The spike between 1° and 4° is attributed to a multiple reflection of the laser from the flow cell that finds its way through both filters into the detector. The normal $+\theta/-\theta$ reflection is located at 16° in this case. The spike only appears when a flow cell is mounted and it is already observable before injection of the dye, equally under both polarizations. Diffracted beams can not be responsible for this effect since already the $+1^{st}$ and the -1^{st} diffraction order are prohibited from leaving the flow cell because the corresponding diffraction angles are subject to total internal reflection for the grating constants used in this work. Similar spikes were only observed for gratings in the $\Lambda = 511.6$ nm range for which they were usually located at an angle between 3.5° and 4.5°. Because this spike is not related to fluorescence emission it has to be ignored in figure 5.8.

In the case of p-polarization the intensity decay shows a certain dynamic behavior. The overall emission pattern remains, but the intensity is reduced further and further while the detector moves to higher angles. The movement of the detector from one angle to the next is

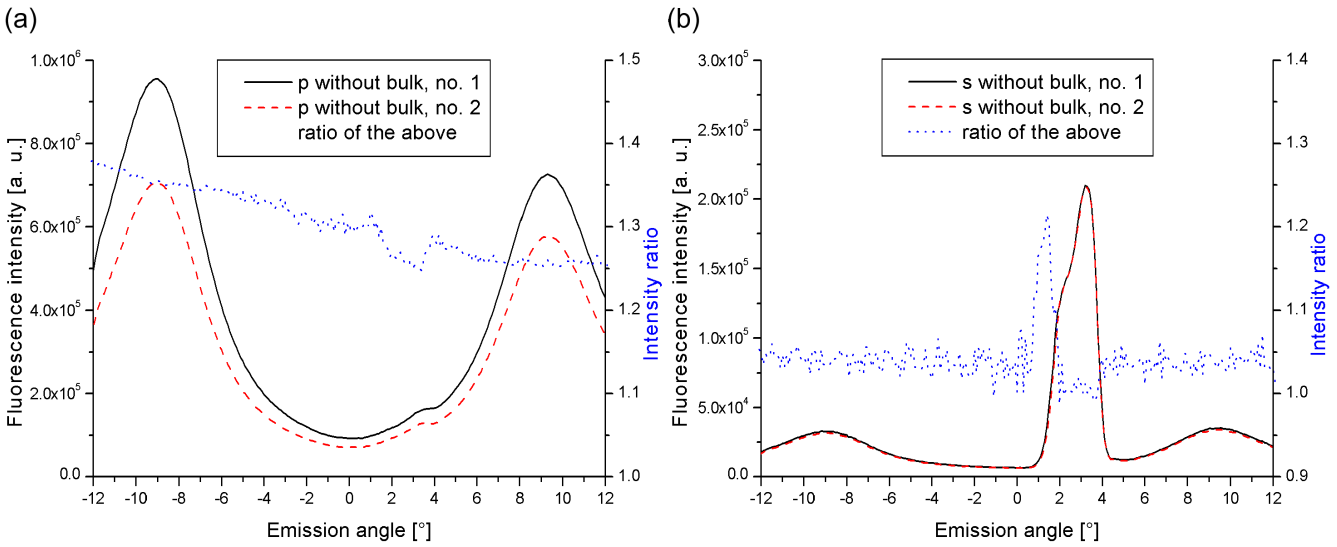

Figure 5.8: Bleaching from successive measurements. The fluorescence intensity emitted from sample B63 (without bulk fluorophores) is dropping from one measurement to another as a consequence of bleaching under laser beam exposure. (a) This effect is much more significant for p-light illumination, where the strong electromagnetic field of the surface plasmon mode is present. (b) Under s-polarization it is the direct illumination of the laser only that causes bleaching resulting in a weaker reduction per renewed measurement. The spike between 1° and 4° present in all curves is a polarization independent artefact presumably resulting from multiple reflections of the laser and is unrelated to fluorescence emission.

equivalent to the uniform passage of time and the abscissa can be re-scaled with knowledge of the effective speed of rotation of the goniometer. The intensity ratios are plotted against this new time scale in figure 5.9, separately for both polarizations. Besides bleaching, it is also possible that the signal strength decreases over time because of desorption of the dye-labeled oligonucleotide target. For comparison, a calculated desorption kinetic describing this process has been included in the figure with the T2/P2 desorption rate constant $k_{off} = 7 \times 10^{-6} s^{-1}$ taken from literature [Lie99]. It can be seen clearly that desorption is not the dominant process in signal reduction. It acts on a much larger time scale and is therefore excluded from this discussion on bleaching. An exponential decay curve characteristic for the bleaching process can be fit quite well to the intensity ratio measured under p-light. The fit yields a much higher rate constant of $k_{bleach,\,p} = (1.85 \pm 0.16) \times 10^{-3} s^{-1}$ compared to the value for mismatch zero desorption. Similarly, an exponential decay can be fit to the data for s-polarization with a three times smaller rate constant. But since there is practically no trend in the very noisy data, this result is not very reliable. The enhanced electric field in the case of resonant p-illumination is responsible for enhanced fluorescence intensities, as well as for enhanced bleaching rates.

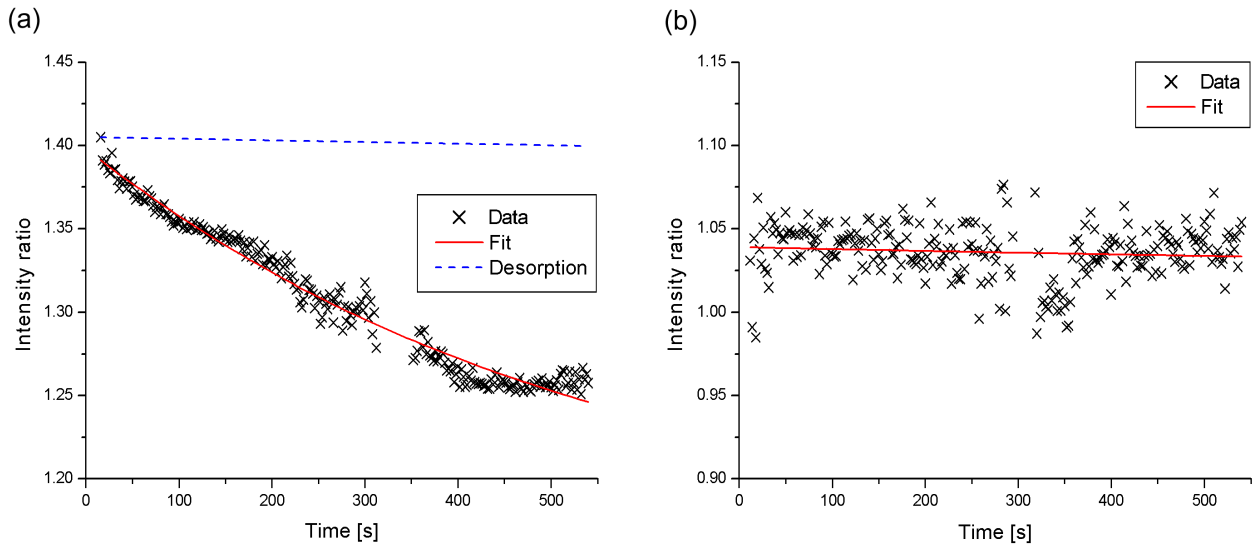

Figure 5.9: Fitting the bleaching dynamics. The intensity ratios of figure 5.8 can be fit by an exponential decay curve typical for a bleaching process. (a) In the case of p-light, the rate constant amounts to $k_{bleach,\,p} = (1.85 \pm 0.16) \times 10^{-3} s^{-1}$. For comparison, a simulated mismatch zero desorption kinetic (dashed curve) is also included in the figure. Desorption is much slower than bleaching and can safely be ignored in this experiment. (s) It is also possible to fit an exponential decay to the data for s-polarization, but there is not much insight in it because of the static nature and the noise level of the data. Data points originating from the reflection spike between 1° and 3° have been omitted.

5.6 Tuning measurements

Fluorescence techniques utilizing surface plasmons for dye excitation make use of the enhanced electromagnetic field that is present at metal/dieletric interfaces, if the coupling condition is met. Reflectivity measurements are commonly performed in order to locate the resonance. Generally speaking, an angle of incidence of the illuminating beam on the sample with a low reflectivity equates to a high intensity of the enhanced field. However, the angle of the minimum of the reflected intensity does not coincide precisely with the position of maximum fluorescence excitation. As already mentioned in sections 2.1.5 and 2.1.6, this phenomenon is common to both excitation types. In this section, results are reported from experiments in which the peak intensity of a fluorescence lobe was recorded, while the grating was rotated through the reflectivity minimum angle.

After target immobilization on functionalized samples with a grating constant of $\Lambda = 511.6$ nm, all bulk fluorophores were rinsed away with buffer. Measurements of reflectivity and angular scans of fluorescence intensity were performed in the same way as in he previous sections (according to the operational procedures described in section 3.3). Additionally, the PMT was fixed to one of the two peak positions, where the emission is at maximum, and operated with a narrow aperture. Grating and detector were rotated in unison by the same amount to cover angles on either side of the reflectivity minimum position. The PMT thus maintained a constant aspect of the sample while the efficiency of the coupling from the laser beam to the surface

plasmons was varied (tuned).

In a series of measurements using half a dozen samples of various coupling efficiencies, very different results have been found. The measurements for the sample B55 in which the highest shift between the angles of R_{min} and I_{max} was found are given in figure 5.10. At an angle of incidence of 15°, the reflected laser intensity drops to a minimum. Recording the emission pattern identifies the two fluorescence emission peaks at almost symmetric emission angles of -8.8° and 9° respectively. Fixing the PMT at 9° relative to the surface normal and rotating both grating and detector from 10° to 25° yielded the first tuning curve. The second curve was taken by maintaining a constant perspective of -8.8° of the sample by the detector. Both tuning measurements give a fluorescence intensity curve that peaks at an angle higher than the R_{min} position. For the right lobe the maximum is located at 16.6°, for the left one it is at 16.4°. Of course some bleaching is taking place during the data acquisition but the repeated appearance of this 0.2 difference is pointing to a small systematic error in the relative alignment of sample holder and PMT. Under this assumption, it doesn't make any difference for the tuning measurement whether the left or the right peak is tracked. On average the sample shows a positive shift of 1.5° between the positions of R_{min} and I_{max}. Comparing the intensities for the right peak measured under excitation at 15° and under 16.6° shows that optimization of the resonance angle can give a 10 % increase in the signal strength. The data shows also nicely that the outcoupling geometry in the frame of reference of the grating is fixed by material properties (grating constant, dielectric number of gold, fluorescence wavelength) and independent of the angle of incidence.

For the six samples studied, the amount of the shift between the reflectivity minimum and the fluorescence intensity maximum varied considerably. They have the same grating constant, but different coupling efficiencies. However, no obvious relationship between the two quantities was observed. Tuning shifts covered the entire range from 0.3° to 1.5°. One sample even exhibited a small negative shift (I_{max} preceding R_{min}). For a given grating constant, different profiles can exist to realize a certain coupling efficiency. Therefore, it is assumed that the topology of the sample surface strongly affects magnitude and direction of the shift. The easiest way to compare various profile shapes and their influence on the shift is simulation. Similarly to the discussion in section 4.2.4, a sine profile and a sine with a small third harmonic component have been used for calculations, in addition to the surface profile obtained by AFM for sample B55. The multi-layer systems were modelled by the same dielectric values already used in section 5.3 with an amplitude of 18.9 nm. In addition to the reflectivity curves, the electric field intensities were calculated at 0.1 nm distance from the streptavidin layer. For the sine profile a shift of 0.27° was found between the angles of R_{min} and I_{max}. In combination with a third harmonic this amount reduces to 0.18°. For the profile taken from force micrographs the shift is pointing to the right again and amounts to 1.08°. This value is much higher than the results for the two theoretical profiles, but it is still clearly smaller than the shift found experimentally. The simulation code based on the Rayleigh approximation works well for reflectivity calculations and comparison with experimental data. Small discrepancies arise between simulation and experiment for intensity calculations, but these are not necessarily an indication of limitations concerning the Rayleigh approximation, because they are also present in prism coupling.

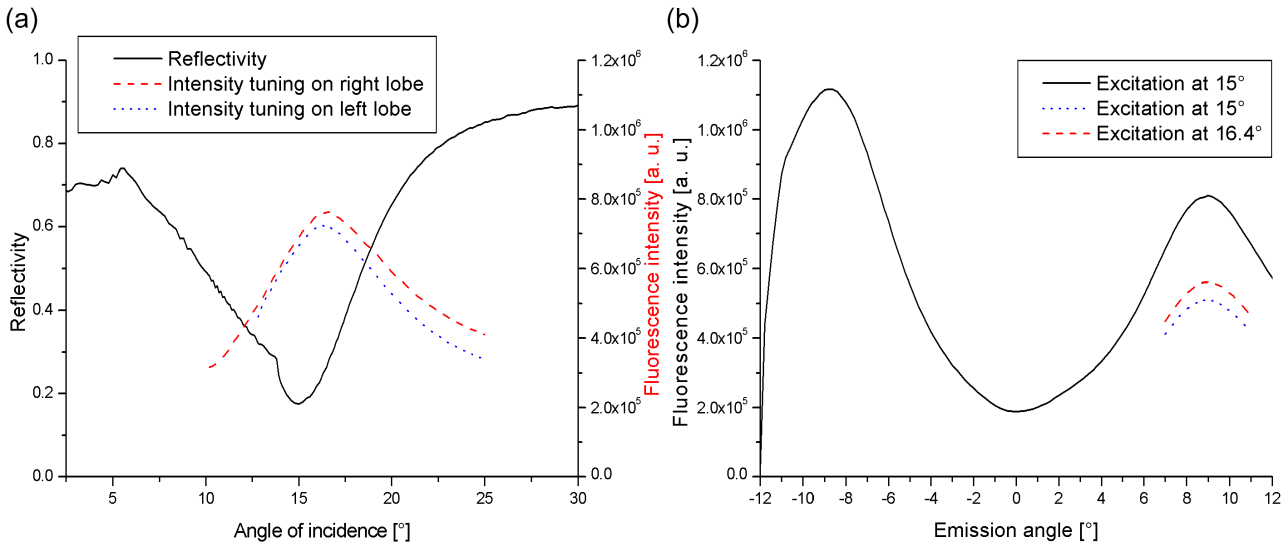

Figure 5.10: Tuning the resonance angle. The condition of maximal fluorescence excitation can be found by slightly varying the resonance angle. (a) Sample B55 shows a particularly large angular shift of 1.5° between the reflectivity minimum and the fluorescence excitation maximum, no matter which of the two intensity peaks is tracked. (b) Illuminating the grating under this optimized resonance angle of 16.4° increases the fluorescence intensity by about 10 % (a comparison of the two curves measured subsequently from 7° and to 11°). All fluorescence radiation exits under the same emission angles relative to the grating normal, irrespective of the angle of incidence.

Compared to grating coupling, the mathematical modelling of prism coupling is much less complicated and therefore more reliable [**?**], using the transfer matrix formalism for example described in section 2.1.7. Figure 5.11 shows data from a tuning experiment with accompanying calculations. The reflectivity curve can be fit very well, and the minimum position is precisely reproduced. Using the values obtained from the fit, the electric field intensity can be calculated as a function of the angel of incidence of the exciting beam. By scaling it appropriately, the curve can be compared to experimental fluorescence intensity data. The agreement between the two curves is not as good as in the case of reflectivity. The model predicts a maximum that is 0.2° closer to the reflectivity minimum than the experimental result. As in the case of grating coupling, the simulated tuning shift is smaller than observed. Strictly speaking, the reason for this lies in the inadequacy of the intensity comparison. Fluorescence intensity (the measured quantity), is similar, but not exactly equal to electric field intensity (the calculated quantity). The difference in orientation of the absorption and the emission dipole of a fluorophore has to be considered, if applicable for a given fluorophore. This difference has an impact on the recorded signal even for an isotropic distribution of the orientation of the dye molecules [Vas04]. In order to predict the shape of the fluorescence curve with higher confidence, the simulation program has to be expanded by this effect in the future.

The direction of the tuning shift is governed by the profile shape. This view is strongly

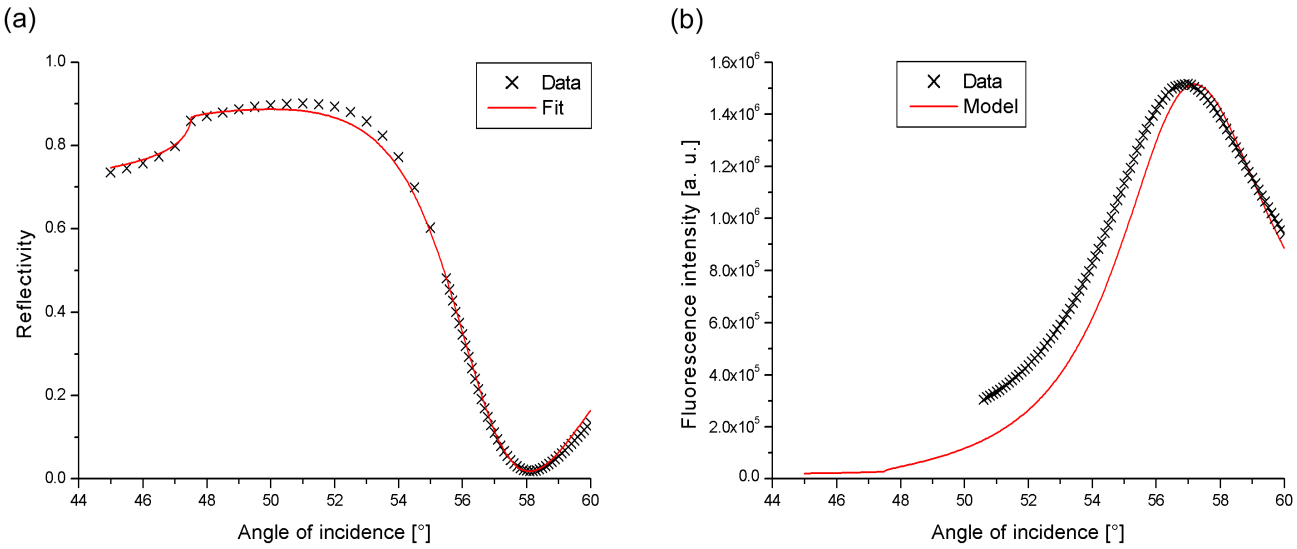

Figure 5.11: Tuning the excitation condition in prism coupling. (a) The reflectivity curve obtained from a sample of 48 nm gold on a LaSFN9 slide in Kretschmann configuration can be fit with high fidelity. (b) The graph shows the fluorescence intensity measured in a tuning experiment. The fluorescence excitation maximum precedes the reflectivity minimum position at 58.1° by 0.9°. Calculating the total electric field intensity at the metal surface yields the model curve (data scaled by a suitable factor to match peak magnitudes). Agreement is significantly worse than in the case of the reflectivity fit. The predicted tuning shift amounts to 1.1°.

supported by the findings made in the context of embossed gratings[2]. For a grating with a given mark-to-space ratio, an ideal embossed replica features exactly the inverted topography and consequently the inverse value of p/l. Most etched gratings examined exhibited a positive shift. However, their embossed replicas show a negative shift direction indicating the strong relationship between tuning shift and profile shape.

Figure 5.12 shows two force micrographs of etched profiles that are responsible for a shift into opposite directions. Grating B55 is the sample discussed previously in detail. It induces a huge positive shift (1.5° measured, 1.08° calculated). The second profile (grating B59), shifts the intensity maximum to the left of the reflectivity minimum . Both profiles clearly have a different shape. In B55 most of the surface area is located on land regions. It has a mark-to-space ratio of 2.37. On the other hand, the surface of B59 is described by $p/l = 0.83$. It is dominated by wide pits and fields a negative shift (-0.27° according to calculation). In terms of the mark-to-space relationship, the two sinusoids are perfectly symmetric. Both feature a small positive shift and define the ideal, undisturbed case. The tuning shift can be increased or reduced and even turned into the opposite direction by altering the symmetry appropriately. Because of this intimate relationship between shift and shape, determining magnitude and direction of the shift can serve to characterize symmetry properties of the corrugation profile.

[2]Refer to chapter 7 for more details on embossed gratings.

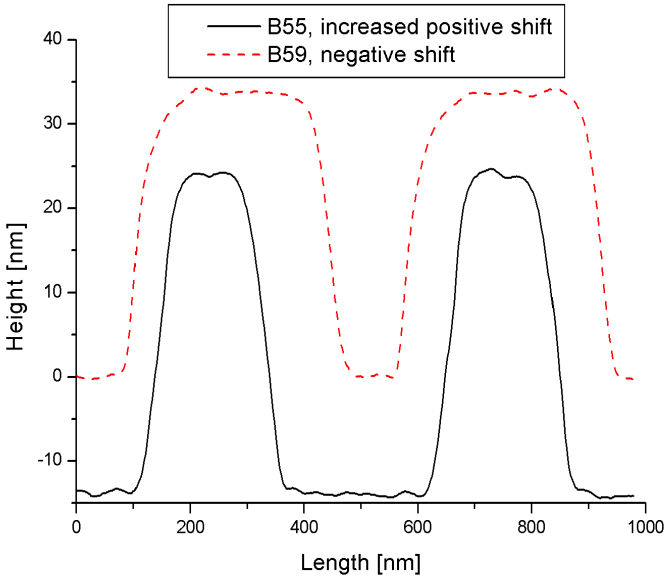

Figure 5.12: Force micrographs of profiles with negative and positive shifts. According to its mark-to-space ratio, a grating can inducing an increased positive or even a negative tuning shift. Sample B55 is described by $p/l = 2.37$ and features a positive shift of 1.5°. Grating B59 ($p/l = 0.83$) was found to cause a small shift in the opposite direction.

5.7 Conclusion and outlook

The back coupled fluorescence emission from dye coated gratings was studied. The emission pattern consists of two lobes of equal intensity arranged symmetrically in respect to the grating normal. It was shown that results in which this is not the case are subject to experimental artifacts, caused for example by bleaching. The position of the outcoupling lobes is mainly determined by the grating constant. The effect of Λ on the separation of the two lobes was demonstrated. It was suggested to characterize gratings also at the fluorescence wavelength by additional reflectivity measurements.

Engineering a close proximity of the lobes is favorable for detection schemes meant to easily integrate the full directional emission. But even in narrow aperture experiments (designed to resolve the angular structure of the fluorescence emission) samples with smaller outcoupling angles showed superior polarization discrimination. A small separation of the lobes allows overlap between the two resonances, which makes the back coupling more efficient. It was shown how the corrugation profile shape affects the difference between the reflectivity minimum position and the angle of maximum fluorescence excitation. Tuning experiments revealed that the mark-to-space ratio of a profile determines direction and magnitude of the angular shift.

The enhancement caused by the evanescent field results in high electric field intensities that can cause rapid bleaching of the fluorophores. Another experimental method is desired to record the fluorescence emission pattern of a grating at much shorter exposure times and at

simultaneous illumination. This situation has motivated experiments with an imaging set-up that drastically reduces the bleaching problem (see chapter 8).

Chapter 6

Bulk fluorescence emission

It is surprising to find that there is no literature yet on studies of analyte binding kinetics performed with grating coupled SPFS, especially given the fact that prism based SPFS is already well established [Lie00b], the enhanced field of grating coupled surface plasmons has been used to excite fluorophores already more than two decades ago [Kno81] and grating SPR systems are commercially available [HTS]. GC-SPFS bears the potential for competitive clinical applications because of its easier, and hence cheaper, production of consumable components. Presumably, GC-SPFS has not been utilized in the academic or commercial context because of the bulk fluorescence contribution. The illuminating light needs to first pass the flow cell before it reaches the grating. On its way, the light beam can excite dye molecules in the buffer volume directly, without involving surface plasmon excitation. Additionally, the tail of the evanescent field reaches out into the flow cell, beyond the layer of immobilized fluorophores on the sensor surface, and can also excite unimmobilized dyes. This second bulk effect is also present in prism coupling.

Fluorescence emission from the bulk constitutes a background that contributes to the total signal. This contribution is unwanted and can lead to incorrect data interpretation, especially in the case of analyte molecules that are incompatible to the surface functionalization. The material contained in this chapter addresses this question of how the presence of bulk fluorophores affects the performance of a GC-SPFS sensor. Before addressing the bulk emission, a brief explanation is given for comparison about how kinetic measurements are performed by conventional SPR. This is followed by DNA/DNA hybridization studies, demonstrating the capability of GC-SPFS to perform affinity measurements. At the same time the signal-to-noise ratio (SNR) of the technique is quantified. From this, the lower limit of detection of the method is derived. The bulk emission at high concentration is studied as a function of the emission angle for samples of different grating constants in the subsequent section and the results are compared to prism coupling. Next, bulk fluorescence is examined as a function of different excitation and detecting polarizations. Based on these findings, polarization sensitive detection is discussed as a method to identify and reduce bulk fluorescence emission.

6.1 Kinetics by SPR

SPR systems based on grating coupling can be used to measure the affinity of a binding reaction by monitoring the change in reflectivity of the surface in the same way as prism SPR can. Figure 6.1 gives an example of the two immobilization steps (streptavidin and probe oligomer) that are part of building the surface functionalization of the DNA assay. The sample is illuminated an angle (8° in this case) that corresponds to a point of inflection of the reflectivity curve. At such a location, sensitivity is largest, because $\frac{\partial R}{\partial \theta}$ is maximized. Additionally, the reflectivity curve can be approximated well by a straight line at a point of inflection to give a linear relationship between reflectivity change and (optical) thickness. The photodiode is placed in the reflected beam and records its intensity as a function of time. If the adsorption of a molecule with a dielectric number different from the medium takes place, the reflectivity curve shifts gradually and the resonance minimum moves. Since the PD still monitors the reflected intensity of the laser beam at the same position, a change in the photocurrent is recorded constituting the signal in SPR kinetics.

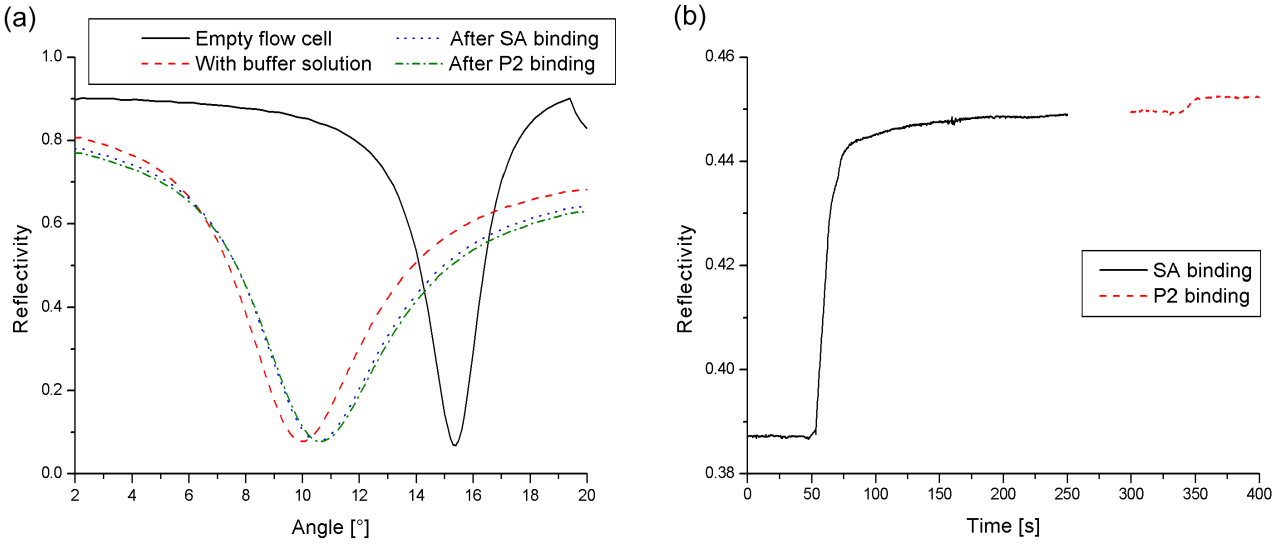

Figure 6.1: Binding kinetics monitored by SPR. (a) The graph shows angular scans of reflectivity for a grating with $\Lambda = 474.7$ nm (B98) before and after the binding of streptavidin and the oligomer P2. (b) Kinetic curves were recorded by monitoring the light reflected from the sample under an illumination of 8°. Both kinetic curves proceed towards an asymptotic value in only a couple of seconds since analyte binding at high concentration (SA: 1 μM, P2: 500 nM) reaches the equilibrium surface coverage rapidly.

6.2 Affinity measurements with SPFS

In order to study the impact of bulk fluorescence on kinetic measurements, a DNA titration experiment was performed. The concentration of the analyte MM0 (refer to section 3.2.3) was changed three times by a factor of ten to map the effect over a wide concentration range. A

highly efficient grating (B98, $\eta > 0.95$) of $\Lambda = 474.7$ nm was chosen for a strong excitation. The same was illuminated with p-light under the resonance angle of 10.6°, the minimum of the reflectivity curve. Because of the small grating constant, the back coupling emission lobes are in close proximity to each other. By opening the aperture next to the lens (diameter 22.4 mm), halfway between sample and PMT (each distance 2f = 100 mm), emission angles within ±6.08° of the grating normal were covered, integrating both fluorescence lobes at the same time in order to maximize the signal. This arrangement resulted in very high intensity levels exceeding the input limit for the PMT and the laser intensity had to be further reduced by a second neutral density filter of T = 10 % to allow for safe operation. To prevent bleaching over the anticipated great length of the experiment, illumination by the laser beam was controlled and blocked by an automatic shutter (open for 5 s, closed for 300 s).

Before injecting the complementary strand, background and bulk signal intensities were measured while pumping PBS through the flow cell. The first column in figure 6.2 (a) was recorded before the injection of the fluorescently labeled inert oligomer MM15. Its height gives the background signal level for an empty flow cell (in terms of fluorophores) at an average of 2169 counts of the PMT. It is composed of mainly two contributions: electronic noise and illumination crosstalk. The electronic noise is always present, even when the shutter is closed (visible in the three gaps between the last four columns), and amounts to a mean value of 266 counts. It is mainly caused by the dark current of the PMT. Assuming the electronic noise to be independent of PMT illumination, the remaining 1903 counts that appear upon opening the aperture are caused by laser line photons scattered into the detector, despite the two interference filters. The background value corresponding to an empty flow cell (indicated by the dashed line in figure 6.2 (a)) was deducted from the average height of all other columns in order to quantify the pure bulk fluorescence contribution.

Following the injection of a MM15 solution at a concentration of 3 pM, the second column was recorded. Its height is only slightly higher than that of the first one. It appears more noisy since the data acquisition rate of the PMT had been increased at this point. The following columns correspond to MM15 concentrations of 30 pM, 300 pM and 3 nM. After deduction of the "empty" background level, the remaining counts correspond to the pure bulk fluorescence emission. These intensities are plotted in figure 6.2 (b) against concentration. The intensity is expected to scale linearly with the concentration. For that reason the data is fit with a line through the origin. More emphasis is placed on the intersection of the line fit with the origin (i. e. no fluorescence in the absence of fluorophores) than on the optimal coverage of all data points.

Strictly speaking, this simple approach doesn't give the intensity of the pure bulk fluorescence correctly. The precision is limited because the total background is not made up by separate contributions that don't interact. Without dye molecules, the PMT counts laser line photons. If it is present, some of these photons are now responsible for the fluorophore excitation and are thus absorbed before reaching the detector. The simplification is still made, because it is valid in the low concentration regime, which is of particular interest here.

The flow cell was thoroughly rinsed and the regeneration protocol applied to ensure full removal of all MM15 oligomers. After that, the MM0 titration experiment started with the

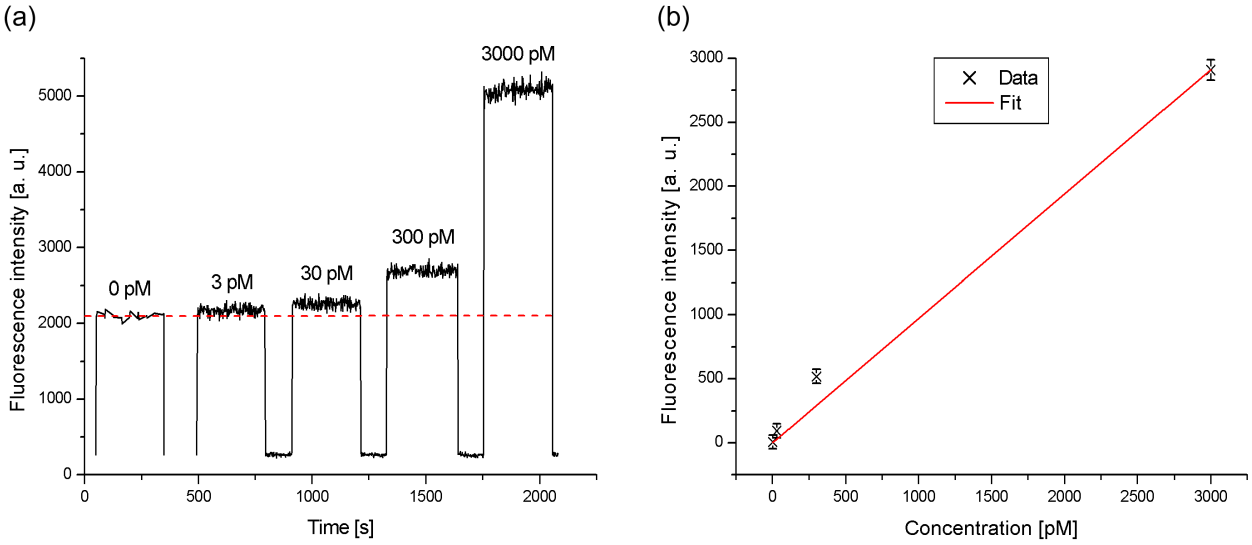

Figure 6.2: Background in GC-SPFS. Bulk fluorescence emission is only one of several mechanisms contributing to the signal background. (a) The graph shows background measurements for different concentrations of the fluorescently labeled inert sequence MM15. The intensity emitted from the bulk is concentration dependent and rides on a constant level of electronic noise and illumination crosstalk (dashed line). (b) The pure bulk contribution scales linearly with the dye concentration (the error bars are determined by the RMS value of the PMT signal).

injection of 3 pM solution. The hybridization of this complementary strand was monitored for more than 11 hours before the solution was exchanged with pure buffer and the flow cell continuously rinsed for about 5 hours. Similarly, titration was continued with the adsorption from solutions of 30 pM, 300 pM and 3000 pM concentration and subsequent rinsing steps (see figure 6.3). Adsorption was permitted until the curve shape started to approximate the equilibrium region. Assuming the validity of the Langmuir model for this immobilization reaction, the four adsorption and the four desorption curves were fit one by one in order to find k_{on} and k_{off}. Both rate constants and the fluorescence intensities for the different concentrations are given in chart 6.1.

I_{max} gives the maximum fluorescence signal detected for a given MM0 adsorption phase. I_{bulk} indicates the pure bulk fluorescence emission previously measured. It can be seen clearly that the maximum intensities measured for each MM0 concentration always exceed the corresponding MM15 signal levels by several orders of magnitude. The bulk emission can be considered irrelevant in this concentration range and was therefore neglected in the quantitative analysis.

Values for k_{on} can be found by analyzing the four adsorption phases 1, 3, 5 and 7 (see chart 6.1). They are very similar, in particular the numbers for the three highest concentrations are almost equal. All eight phases can be used to find k_{off}. Pure desorption fits from the even numbered phases are to be trusted more, since the absence of k_{on} means there is one fit parameter less, reducing uncertainty. There is some variation in the values, but generally the numbers are in the range of a few 10^{-5} s^{-1}. The values for the last three desorption phases are

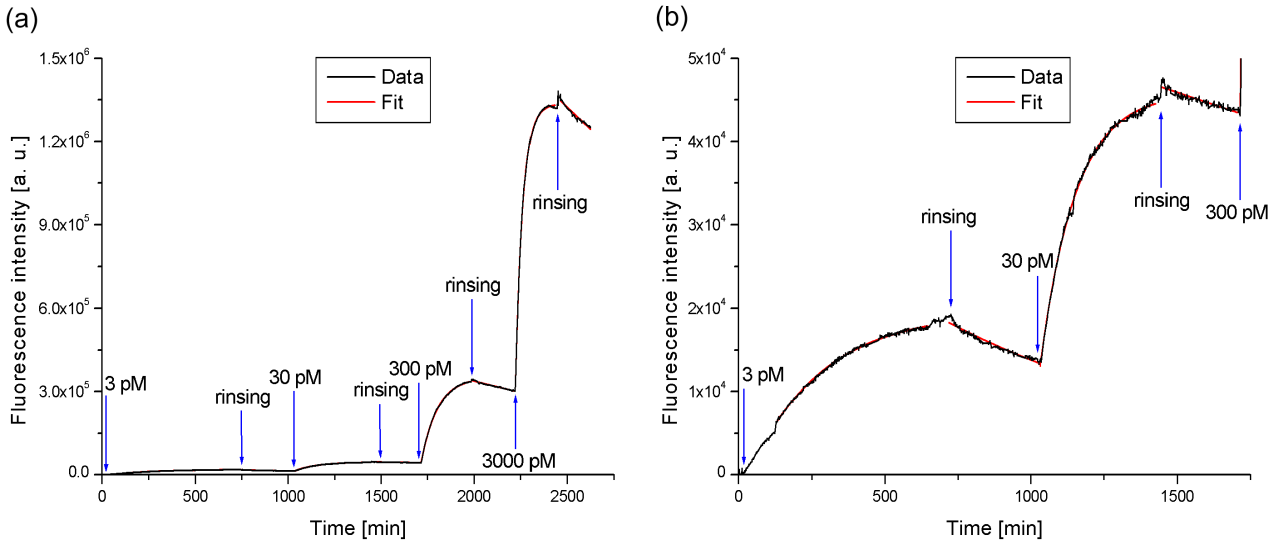

Figure 6.3: A titration experiment with the target strand MM0. (a) The target concentration was increased logarithmically from 3 pM to 30pM, 300 pM and 3000 pM. The flow cell was rinsed with pure buffer before each increase in target concentration. The resulting adsorption and desorption kinetics can be fit well with the Langmuir model, using the rate constants given in chart 6.1. Each injection or rinsing step defines the beginning of new adsorption or desorption phase respectively. (b) A closer look at the adsorption and desorption curves for the two lowest concentrations of the series.

in very good agreement, but using them for fitting the adsorption curves does not produce good fits. Because of this incompatibility, the affinity constant was only calculated from k_{on} and k_{off} derived from the same adsorption phase. The four K_a values for the different concentrations can be divided into two groups of two numbers (phase 1 + 7 and phase 3 + 5) that are almost equal. All the parameters found for fitting phases 3 and 5 are in very good agreement. However, plotting I_{max} as a function of the concentration can not be fit well with a Langmuir isotherm based on $K_a = 1.13 \times 10^9$ M^{-1}. In order to cover the data point for I_{max} at 3 nM also, a higher affinity constant has to be used. Taking the value 4.55×10^9 M^{-1} from the second group gives the Langmuir isotherm shown in figure 6.4 (a). The curve fits three of the four data points well. The data point for c = 300 pM was recorded before the fluorescence intensity was close enough to the equilibrium value. In conclusion, the kinetic parameters derived from the seventh phase are considered to be the most accurate.

The hybridization reaction of the very same pair of probe and target oligomer has been studied in the literature before by prism coupling SPFS [Lie00a]. From a single concentration kinetic ($c = 10^{-6}$ M) k_{on} was found to be 3.7×10^4 $M^{-1}s^{-1}$ and $k_{off} = 7 \times 10^{-6}$ s^{-1}. Both values are roughly a factor of four smaller than the numbers found in the titration experiment. Combined to form K_a, these factors cancel of course and the published value of 5.3×10^9 M^{-1} comes very close to the preferred affinity constant of 4.55×10^9 M^{-1}. It is not clear where the common factor of ten for both kinetic parameters comes from. The reason is more likely to be found in the nature of the published experiment (only a single concentration kinetic versus a titration series) than in the difference of the excitation schemes (prism versus grating

Phase	c [pM]	k_{on} [$M^{-1}s^{-1}$]	k_{off} [s^{-1}]	K_a [M^{-1}]	I_{max} [a. u.]	I_{bulk} [a. u.]
1	3	3.06×10^5	7×10^{-5}	4.37×10^9	1.77×10^4	6
2	0	-	2×10^{-5}	-	-	-
3	30	1.47×10^5	13×10^{-5}	1.13×10^9	4.32×10^4	94
4	0	-	0.9×10^{-5}	-	-	-
5	300	1.57×10^5	14×10^{-5}	1.12×10^9	33.46×10^4	519
6	0	-	0.9×10^{-5}	-	-	-
7	3000	1.36×10^5	3×10^{-5}	4.55×10^9	133.07×10^4	2909
8	0	-	0.8×10^{-5}	-	-	-

Table 6.1: Hybridization rate constants of the target strand MM0

coupling). Additionally, sample to sample variations do exist already for the kinetic parameters obtained from the flat gold film substrates used in prism coupling, even for identical preparation procedures. These can be as high as ±50 % of the quantity in question [Kam01].

The bulk emission and the equilibrium coverage of the surface are both functions of the analyte concentration. The former can be modelled by a linear relationship, the latter is predicted by the Langmuir isotherm. A high SNR is generally desired in an experiment. The intensity ratio of the equilibrium fluorescence divided by the full background (electronic noise + illumination crosstalk + bulk emission) is plotted in figure 6.4 (b). The curve exhibits a pronounced maximum at around 250 pM. The range from 10 pM to 30 nM is best suited for high SNR operations with a ratio of approximately 100. Distinction between the background and the equilibrium signal from binding is still possible if both are equally strong and their ratio equals one. This criterion yields a theoretical lower limit of detection (LOD) for c = 40 fM for this DNA assay[1]. At the same time, there is an upper LOD of 1.5 μM, since increasing the concentration even further increases practically only the background when operating in the plateau region of the Langmuir isotherm. Recent publications on prism based SPFS report attomolar sensitivity [Yu04]. Clearly, GC-SPFS is not suited for operation at such ultra-low concentrations.

At dye concentrations below 1.5 μM, emission from the bulk is always weaker than the equilibrium fluorescence signal. The lower LOD is mainly determined by the background caused from illumination crosstalk in this direct DNA assay. It can be reduced even further by reducing the reflection of all involved surfaces, for example by using anti-reflection coated flow cell cover. Additionally, better wavelength selectivity can be achieved by using a notch filter optimized for blocking the laser wavelength in front of the PMT instead of the two interference filters employed in these experiments chosen for their transmission properties. Other protocols will feature different LODs, not only because of different materials and surface densities, but also by design. In particular sandwich assays, in which the dye concentration is independent of the analyte concentration, will be characterized by other SNR curves.

[1]One must keep in mind it takes about 35 hours to reach 95 % of the equilibrium value at this concentration, which may not be practical for many applications.

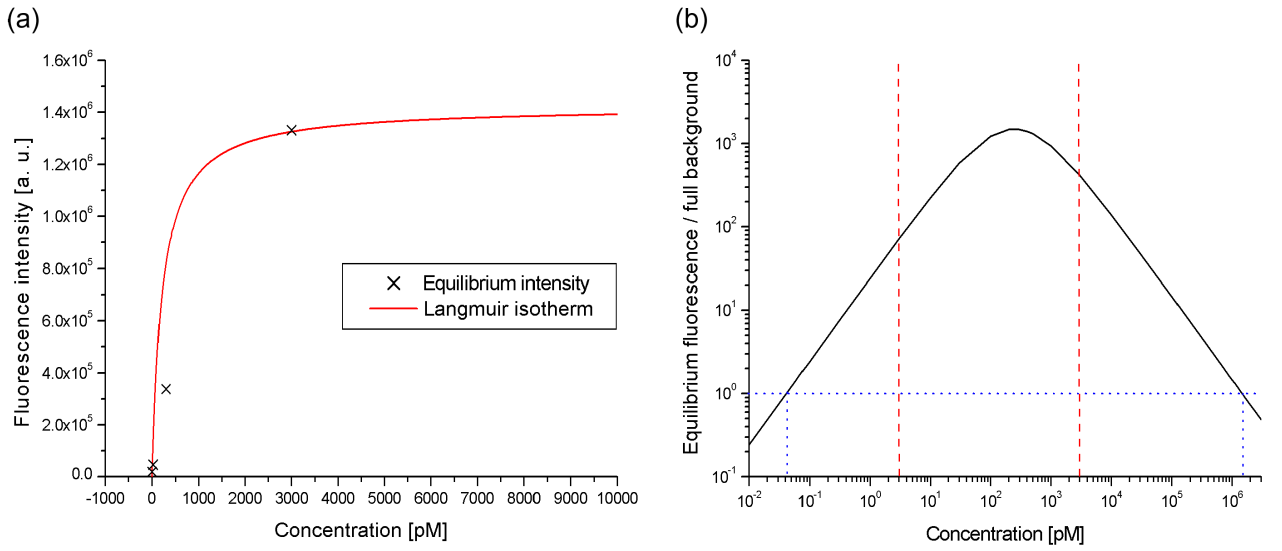

Figure 6.4: Langmuir isotherm and signal-to-noise ratio. (a) The equilibrium fluorescence intensity values from the titration experiment can be fit by a Langmuir isotherm using the affinity constant found for a concentration of 3 nM. The third data point was recorded before reaching equilibrium. (b) Dividing the Langmuir isotherm by the total background function specifies the signal-to-noise ratio of the technique. This ratio is plotted semi-logarithmically in the figure as a function of analyte concentration. The curve peaks at 250 pM and drops to smaller values for both smaller and higher concentrations. The upper and lower limit of detection are given by the concentrations where the ratio is one (dotted lines). They amount to 40 fM and 1.5 μ M respectively. The two dashed lines indicate the concentration range spanned by the experiment.

6.3 Measurements at high bulk concentrations

The previous experiments took place on the low concentration flank of the SNR peak. This regime is relevant for clinical scenarios in which only a scarce amount of an analyte is available. Experiments in this section have been performed at a much higher concentration of 500 nM that puts them on the opposite side of the SNR peak. The effect of the corresponding strong bulk emission was studied as a function of the emission angle.

The fluorescence emission of samples with different grating constants was recorded as a function of the emission angle. Measurements were taken directly after having reached the surface saturation (with bulk) and also after rinsing the flow cell with buffer (without bulk) for both polarizations. The fluorescent probe was present in the bulk at a concentration of 500 nM. The results for a grating of $\Lambda = 511.6$ nm are presented in figure 6.5. Focussing on the peak intensities under p-illumination the presence of bulk fluorescence almost doubles the intensity observed. The difference between the two curves with and without bulk is a rather flat but not fully featureless curve. However, if compared to the peak heights of these two curves, the bulk fluorescence contribution appears almost isotropic. As an indicator to quantify the "flatness" of curve over a given interval, the fraction of the standard deviation over the mean of the curve can be used. It amounts to 0.18 for this curve. For s-light the intensity drops dramatically after bulk removal. Bulk fluorescence, if present, dominates the total signal (ignoring the

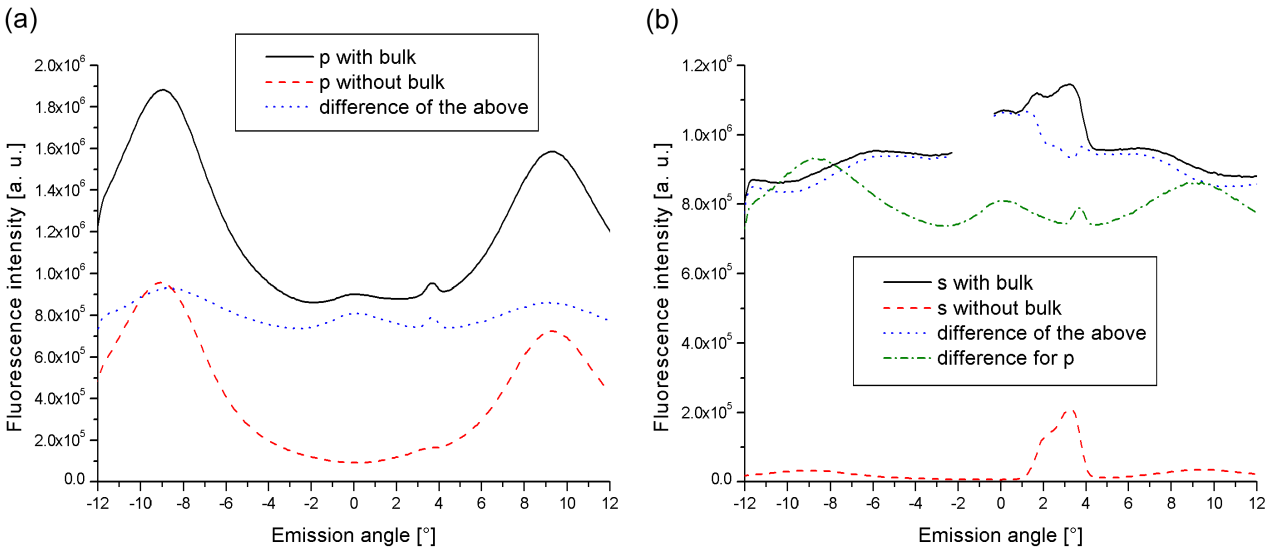

Figure 6.5: Bulk signal contribution to the total signal for $\Lambda = 511.6$ nm. (a) For p-polarization, the bulk contribution makes up as much as 50 % of the maximal signal generated on sample B63 and is rather flat. (b) Nearly all the signal stems from bulk emission under s-illumination. Comparing the two contributions, the bulk is excited more intensely by s-light. Data between -2° and 0° is missing for two curves because of a brief detector overload.

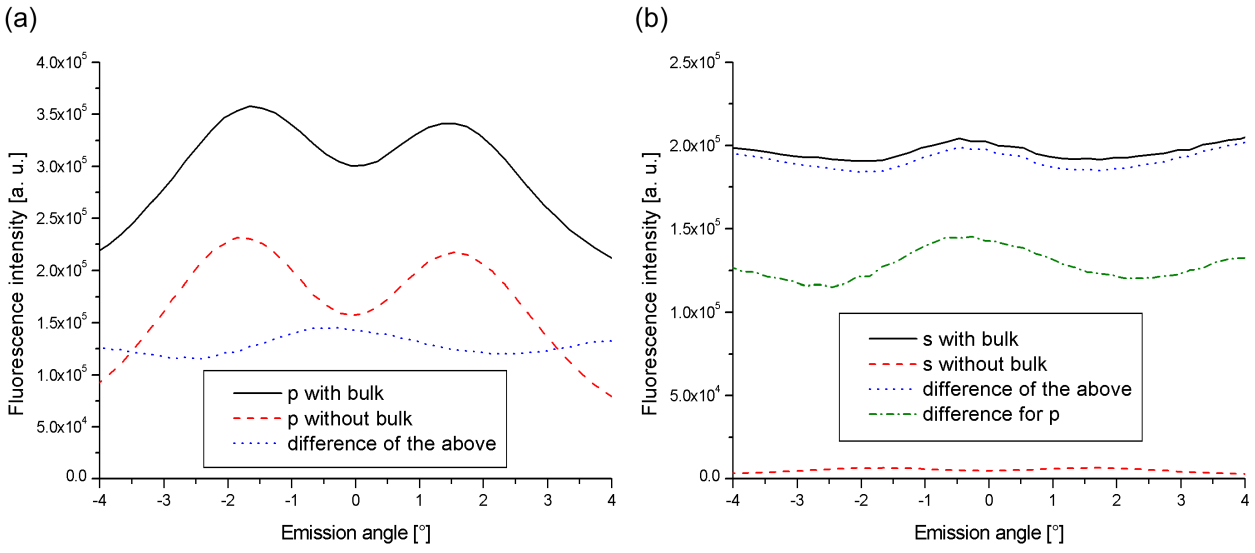

Figure 6.6: Bulk signal contribution to the total signal for $\Lambda = 474.7$ nm. (a) P-light measurements show that the emission of unimmobilized dyes is still an important contribution for bulk experiments. But for this sample (B104) the close location of the two outcoupling angles has the peaks overlap, giving the immobilized fluorophores a higher weight in the total signal. (b) For s-polarization, almost all the photons detected in the presence of bulk do not originate from the sensor surface. Shown very clearly by this sample, bulk emission plays a bigger role in s-light experiments than in measurements under p-illumination.

multiple reflection spike between 1° and 4°) and makes up 97 % of it. In comparison, the bulk contribution for p-light is lower than the difference curve for s-polarization over nearly the entire angular range. Qualitatively, this result is to be expected. For an ideal grating, s-light is fully reflected and hence passes through the flow cell twice, whereas p-light penetrates the flow cell once, to be fully absorbed by the grating. On the other hand, both curves have a similar shape. Both feature maxima at the outcoupling angles. These appear because of the evanescent tail of the surface mode that reaches out into the bulk and excites unimmobilized fluorophores.

Data for measurements with a sample of $\Lambda = 474.7$ are shown in figure 6.6. For the p-polarization case the bulk emission is again a sizable part of the total signal and almost flat. The ratio of standard deviation over mean equals 0.07 in this case, less than half the value found for the previous sample. The intensity generated by immobilized fluorophores is now larger than the bulk contribution for this smaller grating constant. This is presumably due to the proximity of the two back coupling lobes and their resulting overlap. In the presence of bulk fluorophores and under s-illumination, the total fluorescence signal is almost exclusively generated by unimmobilized dyes, as in the case of the sample studied previously. Comparing the bulk fluorescence contributions for the two polarizations. It is again for s-light, where bulk emission plays the more important role, constituting 97 % of the total signal on the average. For this grating constant, the difference curve for s-polarization is distinctly higher than the bulk contribution for p-light. The magnitudes of the two curves relate to about 2:3 over the entire range and they exhibit a very similar shape.

It is interesting to compare the role of bulk signal contributions in gratings with their impact on prism coupling. Results of a tuning experiment with a functionalized LaSFN9/gold sample are given in figure 6.7. For p-light one finds the intensity maximum always at the same angle, no matter whether fluorophores are present in the bulk or not. If unimmobilized dye molecules are populating the flow cell, their excitation by the evanescent tail of the surface plasmon mode makes up as much as 20 % of the total recorded intensity. This is less than the 50 % or 1/3 contribution respectively, observed for grating samples where the illuminating beam passes through the flow cell before reaching the metal layer. The bulk excitation is mainly caused by the evanescent tail of the surface plasmon mode reaching out in the bulk and also by laser line photons which are scattered by the roughness of the substrate. This contribution drops linearly with the concentration and can be neglected for lower target concentrations. Similarly to gratings, fluorescence intensities excited by s-polarized light depend strongly on the bulk fluorophore concentration. In prism coupling, the signal contribution due to a dye concentration of 500 nM amounts to about 76 % of the total intensity under s-light excitation. This value is lower than the 97 % specified above for gratings with Λ being 474.7 nm or 511.6 nm.

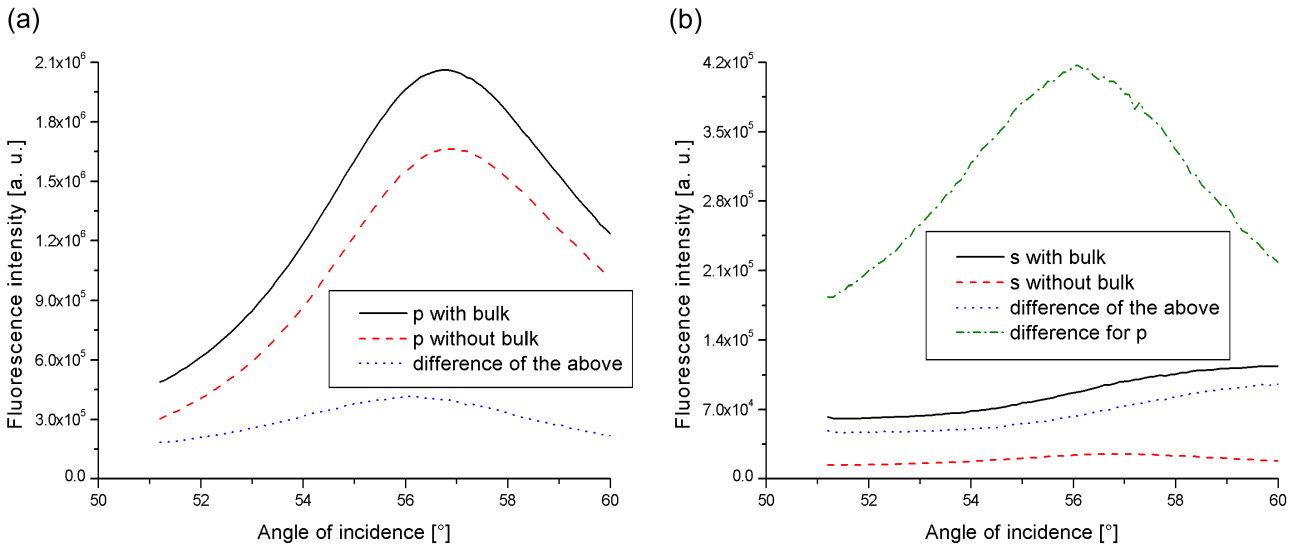

Figure 6.7: Bulk signal contribution for prism coupling. (a) Under p-light illumination, the evanescent tail of the surface plasmon mode reaches out in the bulk and can excite unimmobilized dyes. This contribution makes up one fifth of the total signal at a target concentration of 500 nM. (b) Even s-polarized light samples the bulk to an almost equal extend. When comparing the bulk contributions for the two polarizations, clearly many more fluorescence photons are generated by p-light, proving the high polarization discrimination inherent to prims coupling.

6.4 Polarization sensitive detection

As the results of the previous section have shown, fluorescence emission from the bulk can make up a sizable portion of the total signal at high concentrations. Since the back coupling process sends out fluorescence photons that have to fulfill the coupling condition to the grating, their polarization is determined by the grating orientation. As with the incident light, that must be p-polarized in order to excite surface plasmons, the back coupled fluorescence emission is also p-polarized. In contrast to this, the bulk is an isotropic medium that doesn't favor a specific excitation polarization. The experiments in this section are concerning the question if polarization sensitive detection (PSD) can help to discriminate between the fluorescence emission of immobilized and unimmobilized dye molecules.

The fluorescence measurements in all previous sections of this work were performed in a polarization insensitive way, by recording the total intensity without discrimination between p- and s-polarized fluorescence. In the following experiments, a polarizer was mounted right in front of the PMT. It was used in either p- or s-orientation. The polarization of the illuminating beam was controlled by the orientation of the Fresnel rhomb, just in the previously described experiments. Therefore, four combinations of polarizations are possible: excitation by p or s and detection by p or s. These combinations were studied under different conditions with a grating of high coupling efficiency (B98, $\Lambda = 474.7$ nm, $\eta > 95$ %). They are abbreviated in the form a/b from here on, where a is the polarization of the incident light and b is the polarization state interrogated by the PMT.

The first series of experiments used only the fluorescently labeled inert sequence MM15 at a concentration of 500 nM. These pure bulk experiments were performed under resonance excitation and detection geometry, as well as far off the reflectivity minimum angle and besides the emission lobes to exclude interactions with the grating as much as possible. The incident angles and the detection angles for these two situations are explained in figure 6.8. The sample was rotated to 10.6° (the reflectivity minimum angle) for resonance excitation. Detection took place at the peak emission angle of 3.1°. In the experiments out of resonance the sample was illuminated under 4°, well beyond the dip at a location that is characterized by a relatively high reflectivity for p-polarized light. The detector was moved to 8° in order to be far away from the right intensity hump as well as from the laser reflection peak at 4° (figure 6.8 (b) shows the onset of the reflection peak with its maximum at 10.6° and not at 4°, because the curve was obtained from a measurement under the resonance condition where θ_r equals (-)10.6°). This configuration essentially mimics a flat metal surface. Measurements consisted of 60 seconds of continuous data acquisition to find reliable mean values of the noisy signals.

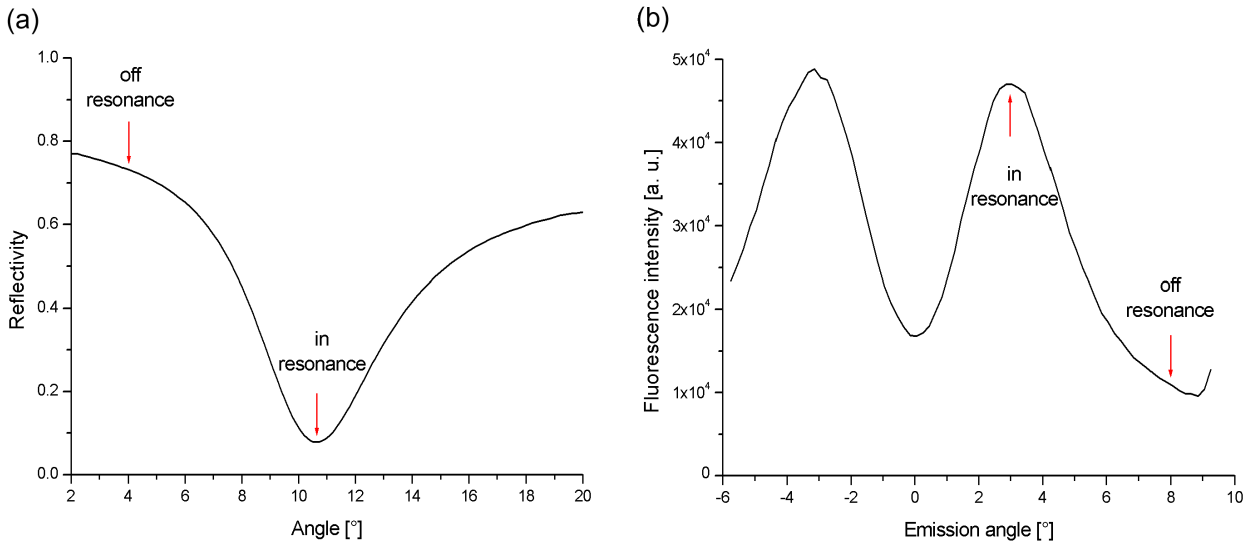

Figure 6.8: Excitation and detection angles used in the experiments. (a) For the MM15 measurements in resonance, the sample was illuminated under 10.6°. (b) The detector was placed at an emission angle of 3.1°. The sample was rotated to 4° and the detector to 8° for experiments out of resonance.

Figure 6.9 shows the data for the first experimental series. Out of the resonance, the polarization of the incident light plays almost no role. The light penetrates the bulk, is reflected at the sample surface and passes the bulk again, exciting bulk fluorophores during both passages. The total response for both illumination polarizations is nearly equal. In the three curve pairs in the figure (total response pair on the top, equal and crossed polarization pairs in the middle and bottom respectively), it is always the p-illumination curve of a pair that is the lower one. This hierarchy results from the fact that even at the angle of incidence of 4° the reflectivity of the grating for p-light is a little smaller than for s-light. Therefore, the reflected p-polarized beam is a little weaker than its s-light counterpart and causes less fluorescence excitation on

its way out of the flow cell. On average, this results in intensities that are 8 % lower than those excited by s-polarized light. Both incidence polarizations suffer equally from depolarization, for example due to molecular collisions, which can be seen by comparing p/p to p/s data and s/s to s/p data respectively. The intensity total is split into one part in the original polarization (63 %) and another part in the perpendicular state (37 %). This distribution is the same for both p- and s-excitation in the out-of-resonance scenario.

This symmetry is broken under the resonance condition and the detection polarizations have to be distinguished carefully. The s/s component has the same intensity in both excitation geometries, because it doesn't couple with the grating at all, neither at 633 nor at 670 nm. On the other hand, the s/p configuration drops to 63 %, compared to the previous value obtained without outside of the resonance condition. Some of the p-polarized fluorescence that is excited by s-light in the bulk couples to the grating and is practically absorbed. While the total s-polarization response was divided into 63 % of s/s and 37 % of s/p before, the distribution changes in the resonance case to 73 % and 27 % respectively. The total response to p-illumination (p/p + p/s) is much weaker compared to the full intensity excited by s-light (s/p + s/s). Under the resonance condition, p/p + p/s amounts to almost half of the intensity measured outside of the resonance, where the sample surface essentially acted as a mirror. In an idealized situation, the grating acts as a perfect absorber for p-polarized light. Neglecting excitation of the fluorophores in the bulk by the evanescent tail[2], the fluorescence emission is indeed expected to drop by 50 %, because the bulk is only penetrated once. However, the two constituents p/s and p/p interact differently with the grating. Compared to the counterpart values (p/s and p/p in the out-of-resonance scenario), they amount to only 63 % and 44 % respectively. The p/p component is reduced disproportionately more, because p-polarized fluorescence can interact with the grating, whereas s-polarized fluorescence can't.

The second series of experiments employed the fluorescently labeled complementary strand MM0. Measurements were performed after the equilibrium surface coverage of the sensor was reached, with and without bulk fluorophores, but always with resonant excitation. The analyte concentration was always 500 nM. Since, in practical terms, bleaching is an irreversible process for the immobilized fluorophores, the laser beam exposure time was reduced to two seconds in MM0 experiments. This is possible because the much higher fluorescence signal from bound dyes overpowers the intensity fluctuations that were relevant in pure bulk measurements with MM0.

The intensities recorded without bulk are shown in figure 6.10 (a). Generally speaking, all intensities related to s-light excitation or detection are very weak. The p/p combination is dominating the emission. For p-illumination, 97 % of the emitted intensity maintains the same polarization state during re-radiation. Even for s-light incidence the emission is strongly p-polarized (91 %), but at a much lower intensity. The fact that the fluorescence polarizations is strongly shifted towards p-polarization indicates that back coupling is a very efficient energy transfer channel for the relaxation of excited fluorophores. But it has to be emphasized that the vast majority of all s-polarized photons are reflected from the grating and not responsible

[2]Fluorescence excitation of bulk fluorophores by the evanescent tail can be neglected, if the flow cell is much thicker than the penetration length of the evanescent field.

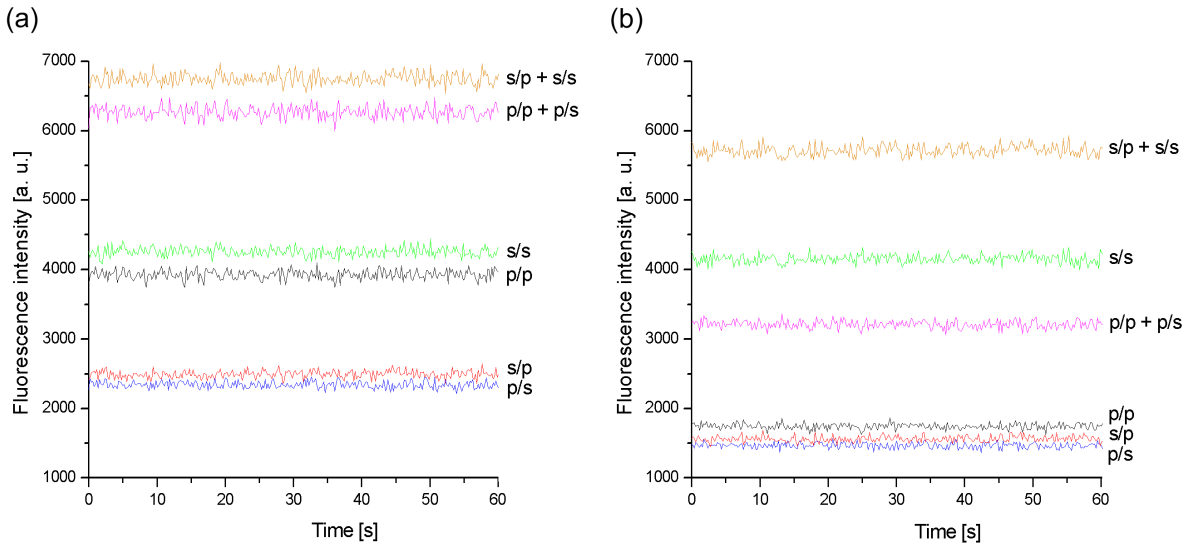

Figure 6.9: PSD measurements of bulk emission. (a) Outside of the resonance, the bulk fluorescence responds almost equally to p- or s-light excitation. Depolarization is observed and 37 % of the intensity of each of the two polarizations is emitted in the perpendicular state. (b) The individual intensities obtained in the resonance geometry. The previous symmetry is broken, because the individual polarization combinations interact differently with the grating. Processes involving p-polarization are reduced in intensity due to grating coupling (sample B98, fluorophore concentration 500 nM).

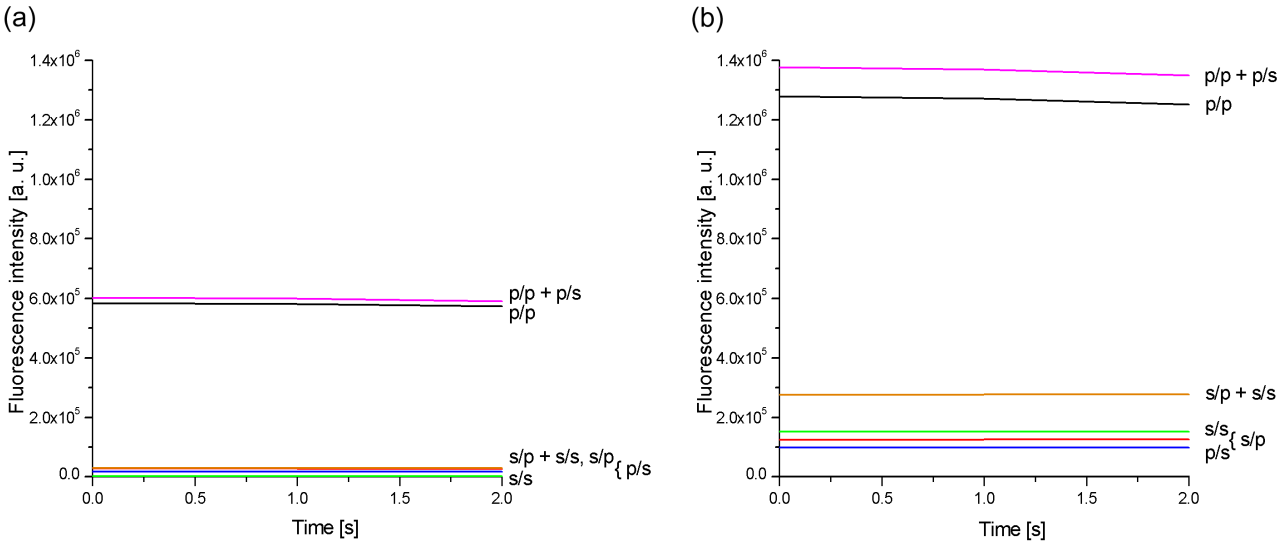

Figure 6.10: PSD measurements of combined bulk and surface emission. Both figures show data obtained after saturation of the sensor surface with resonant excitation. (a) The combination of p-polarized excitation and p-light emission is the strongest single component of the spectrum in the absence of bulk fluorophores. (b) With bulk fluorophores, all polarization combinations feature higher intensities. Combinations involving s-polarized emission increase in particular, because of the double penetration of the bulk phase.

for fluorescence excitation at all. The emission of p-light at s-excitation can be possible due to direct excitation of fluorophores that re-radiate via the grating. It is also possible, that a small misalignment of Fresnel rhomb and grating vector causes the presence of a non-vanishing p-polarized light component.

In the presence of bulk (see figure 6.10 (b)), all intensity components are increased, because additional fluorophores are present that are readily excited. It is still the p/p combination that causes the strongest signal. P-light incidence results mostly in p-polarized emission (91 %), but it contains a large percentage of photons emitted from the bulk that can not be distinguished from those originating from the sensor surface. S-polarized fluorescence emission increases due to the double passage of the beam through the bulk phase, where it can excite dye molecules. However, with a contribution of 55 %, the majority of the intensity caused by s-illumination is still emitted in p-polarization. Besides the mechanisms already discussed for bulk free measurements that can cause a change from s- to p-polarization, there is now also a contribution due to depolarized emission of p-polarized fluorescence from the bulk.

The fact that depolarization takes place for the Cy5-labeled 15-mer target complicates the interpretation of data considerably, but it could be studied in the MM15 experiments without too many other factors interfering. With the aim of suppressing the contribution of bulk fluorescence to the total signal, the presence of depolarization is actually a positive aspect. As experiments showed, the emission of s-polarized fluorescence by bound molecules under p-illumination is negligibly small. In the presence of bulk fluorophores, the p/s intensity is increased by depolarized emission from the bulk. It can be rejected safely by PSD without loosing binding related information from the surface. However, nothing can be done about the bulk fluorescence that stays p-polarized with this method. PSD will also not reduce the lower LOD for GC-SPFS discussed in section 6.2, since the factor dominating the SNR ratio was found to be illumination crosstalk and not bulk fluorescence for the employed assay type. For other biomolecular detection schemes, this outcome can be different.

6.5 Conclusion and outlook

With the aim of demonstrating grating coupling as a viable biosensing scheme, the in-situ fluorescence detection of analyte immobilization was demonstrated. Bulk fluorescence emission, commonly thought to be a fundamental obstruction for the technique, was found to not hamper the ability of GC-SPFS to measure the kinetic parameters of DNA hybridization. It was also found, that the lower LOD of 40 fM is not caused by bulk effects, but rather by illumination crosstalk, a contribution that still leaves space for optimization with skillful engineering. Illumination crosstalk can be reduced significantly by two-photon excitation of the fluorophores, in which a near infra-red laser is used [**?**]. Two (evanescent) photons from this source provide the energy for dye excitation together. Thus excitation wavelength and fluorescence wavelength are separated further apart in the spectrum and can be discriminated more effectively by an interference filter.

The impact of bulk fluorescence on the overall emission from a grating was shown to be

smaller in samples with overlapping emission lobes. However, even the best grating can not prevent the excitation of bulk fluorophores by the incident light on its way into the flow cell. It was shown to what extend PSD can be used to reject fluorescence originating from this interaction. PSD does not reduce the lower LOD of experiments with the employed DNA hybridization assay, because it is not a method designed to reduce illumination crosstalk. Nevertheless, PSD promises to lower the LOD in experiments with sandwich assays, in which the dye concentration is typically much higher than that of the analyte.

As a word of caution about generalization of these results, it is necessary to say, that all quantitative statements contained in this chapter were obtained from measurements with the direct DNA assay and are not necessarily transferable to other assay types. For example, the magnitude of depolarization has to be specified for a given assay. The higher the intensity ratio of p/s to p/p, the better PSD will be able to suppress bulk fluorescence emission. This ratio can be manipulated by choosing a fluorophore with a particularly high fluorescence lifetime, a low molecular mass and a high collisional cross section. The flow rate of the bulk phase is also expected to affect depolarization, since it affects the energy and momentum of molecules colliding with surfaces from the flow cell or grating.

Chapter 7

Embossed gratings

Highly efficient gratings for surface plasmon excitation can be fabricated by holographic photolithography in photoresist films. To make the structures more durable and allow for multiple use of a sample the corrugation can be transferred into the underlying glass substrate by ion milling. These etched samples make up the lion's share of all samples studied in this work and they are fine for experimental work. Unfortunately, their production is quite time consuming. Even after having mastered the technique, not all gratings are the same, especially in terms of coupling efficiency. For a commercial application this fabrication method is clearly too expensive and will not yield a narrow tolerance output. In order to offer a competitive device the grating samples have to be disposable and cheap.

The fast, high throughput and high fidelity reproduction of structures in the nanometer scale has already been realized in the CD/DVD industry by injection molding of thermoplast polymer substrates using a structured mould. Characteristic dimensions of the pits on a CD are: a minimum length of 830 nm (400 nm for a DVD), widths of 600 nm and depths of 110 nm (320 nm and 120 nm in the case of DVDs respectively). Successor technologies are aiming at even smaller pit dimensions by using read-out lasers of shorter wavelengths and optics of higher numerical apertures. Essentially, the same replication method can be applied to grating production. The method can be changed to an embossing process that is much easier to realize in a laboratory environment. Embossed grating structures are suitable for fluorescence based biosensing and their utilization is demonstrated in this chapter as a proof of principle. Additionally, working with replicas offer insight into the tuning shift phenomenon (see section 5.6), since they display a corrugation that is essentially the inversion of the master profile.

7.1 Hot embossing of gratings

The digital information stored on a CD or DVD is expressed in pit and land structures on a polycarbonate disc. Their height difference is detected by interferometry. The structured surface is coated with a reflective aluminum layer and sealed with another layer of polycarbonate to seal and protect the data layer. The pit and land structures are replicated on the industrial scale by injection moulding. A master structure ("stamper") is formed in a process that bears

many similarities with the grating fabrication method described in section 3.1: first, a land and pit pattern is written into a photoresist layer spin coated onto a glass substrate. After the writing step, a developing step is conducted, in which all the unexposed pit areas are washed away. The resulting topography is coated with silver that can be connected to a cathode and serve as the negative terminal in an electroforming step. Nickel is deposited from an electrolyte solution on the silver layer to form a thick, robust film. The nickel is separated from the glass, cut into a stamper and inserted in the mold. During disc production hot, molten polycarbonate is injected into the mould at cycle times of only about four to five seconds. Pressures in the range of several tens of kN are applied to make the polymer faithfully and quickly fill the holes in the stamper.

Certain aspects of the industrial production format are not easily realized in the laboratory, namely the injection of hot polymer melts and the high pressures involved. Therefore, a new method has been derived in our group to replicate the corrugations of etched glass masters into polymer substrates by hot embossing. Hot embossing was originally developed to study the glass transition temperature (T_g) and viscoelastic properties of a polymer material at and near its surface [Ham00]. In such an experiment, the corrugation pattern imprinted into the polymer substrate serves as a diffraction grating for an incident laser beam. The diffracted intensity is recorded while the sample is heated above T_g. As soon as the polymer starts to melt, surface tension will eventually destroy the grating structures resulting in a drop in the intensity of the diffracted beam. The dynamics of this decay can be monitored to examine properties of the polymer surface [Pet02].

Suitable master structures were chosen from glass gratings fabricated by the usual photolithography and etching procedures to serve as stamps. As a simplification of the original hot embossing protocol in order to achieve much shorter cycle times, unheated bulk polymer slides were used as substrates (as opposed to spin-cast polymer films of 1 μm thickness, also heated above T_g). Plates of industrial poly(methylmethacrylate) (extruded PMMA, see figure 7.1 (a), thickness 2 mm, Hecker Kunststofftechnik [HEC]) were cut into substrate chips. Substrates were cleaned by wiping them with ethanol. Long exposure to ethanol, e. g. during sonication, has to be avoided since extruded PMMA will develop cracks and break into pieces. In order to facilitate separation of master and substrate after contact, an anti-adhesion coating was applied to the master. A SAM of a chloro-silane (dimethyldichlorosilane, refer to figure 7.1 (b), ABCR [ABC]) was formed on the glass surface from the gas phase in an Argon atmosphere and cured at 110° C for 10 minutes. This hydrophobization of the glass surface increases the contact angle from 80° to more than 100°.

The master structure was embossed into the substrate with the self-built set-up sketched in figure 7.2. Substrates were mounted on the bolt by clamps and screws and a master was fixed on the stage. Care was taken to ensure good thermal contact of the master to the heatable stage. Before embossing the stage was heated to 160° C (T_g + 40° C). The bolt was lowered until contact between master and substrate was achieved. A good measure of force was applied to the lever and it was held in the contact position for a short time. After the separation of master and replica, the next substrate can be mounted. Embossing can continue as soon as the master has reached its operating temperature again. The first replica imprinted by a newly

coated master was always discarded because of the transfer of surplus silane from the master to the substrate.

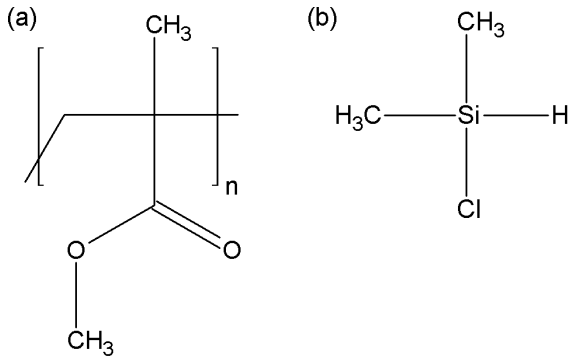

Figure 7.1: Poly(methylmethacrylate) and dimethyldichlorosilane. (a) Gratings were fabricated by hot embossing of the thermoplast PMMA. The polar side chains of the polymer cause an unwanted attraction of the substrate to the master because of the hydroxylic groups at the glass surface. During separation of the two after the embossing, strong adhesion can lead to damage of the master. (b) Dimethyldichlorosilane was self-assembled on the master grating to reduces the hydrophilic properties of the glass surface.

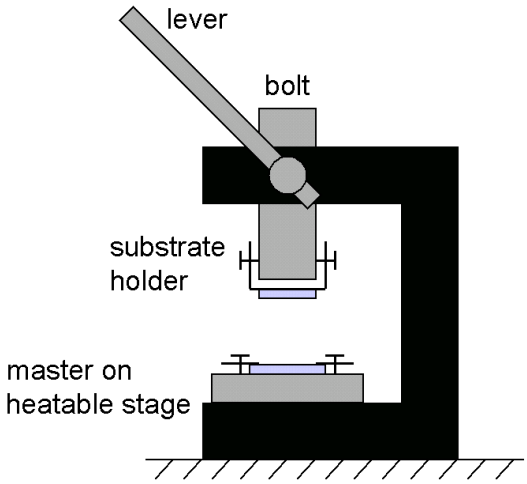

Figure 7.2: The set-up for hot embossing. A glass grating master was mounted on the stage, which was heated above the glass transition temperature of the polymer. Substrates were attached to the bolt and pressed unto the master to obtain a corrugated surface.

7.2 Quality of embossed gratings

Replicas from hot embossing have distinct corrugated and, sometimes flat, defect regions that can easily be distinguished with the naked eye. Reasons for incomplete transfer of the master topography are thought to be caused by dust particles, roughness and curvature of the substrates, all of which prevent the stamp from making full contact with all locations on the

substrate surface. The lack of iridescence (the play of colors due to the dispersion of white ambient light by the diffraction grating into its constituting colors), indicates that curvature is responsible for the gradual decline of the corrugation that is visible for many samples at the grating borders. The trapping of air bubbles between master and substrate acts as another defect mechanism. Areas where transfer is incomplete can be as large as the corrugated ones. On the lab scale, with a flexible experimental set-up, it is acceptable to focus on the well corrugated regions only. For more demanding applications, a preparational polishing treatment of the substrate can rule these factors out and increase uniformity of the grating replicas.

Etched gratings already show a certain, but small, variation in uniformity. Recording the reflectivity on different areas of the grating will yield slightly different results. Sample tolerances of this type can result from local deviations of the surface profile as well as the dielectric number of the metal layer, as already discussed in section 4.2.2 in the context of lateral sample offsets. Clearly the embossing process introduces additional parameters that affect uniformity of the imprinted grating structure. In other words, a replica won't be more uniform than the master. Figure 7.3 (a) shows measurements quantifying the uniformity that can be achieved with hot embossing. By recording the reflectivity on different regions on an *etched* grating sample, deviations of the resonance angle of $\pm 0.1^\circ$ were found while the value of R_{min} remained constant (refer to section 4.2.2). In the case of *embossed* gratings, the same angular deviation of $\pm 0.1^\circ$ was encountered, but R_{min} was found to be location-dependent and in the range of 0.051 ± 0.023. As mentioned before, only corrugated areas are useful for study, but the mere existence of uncorrugated regions is already a sure sign of local changes of the profile. In order to explain the different values of R_{min}, it is most reasonable to attribute them to amplitude variations. Hence, depending on the exact location under scrutiny, a replica related to one of the graphs shown in figure 7.3 (a) falls into the $\eta > 0.95$ (excellent) or $\eta > 0.90$ (very good) category.

Different replicas have been examined to judge the reproducibility of the hot embossing method. When comparing their reflectivity curves it has to be kept in mind, that every single measurement of an individual replica is only a spot survey and within the single sample uniformity limits just detailed. Figure 7.3 (b) gives a selection of reflectivity curves from a series of half a dozen of samples. They show the two extreme cases found and a third curve which is a representative of the mean case. Deviations in R_{min} and θ_r are larger from sample to sample than in the single sample case. Resonance angles were found within a range of 0.4°. That is only two times the range for single samples. R_{min} is not straying much more from replica to replica than before. The set of samples chosen exhibited a slightly higher mean value of 0.069 but a nearly identical deviation of ± 0.024 that still qualifies two out of these three replicas as very good and one as excellent.

Small changes in optical response are more pronounced when comparing different samples. Good uniformity is achieved over the corrugated surface of single samples, but not in the flat regions. The insertion process of new samples and the manual embossing action itself are responsible for these higher variations. Automatization and skilled engineering can further decrease the small tolerances of a small scale lab production with a tentative system. In terms of grating parameters, sample to sample variations are higher due to geometric factors

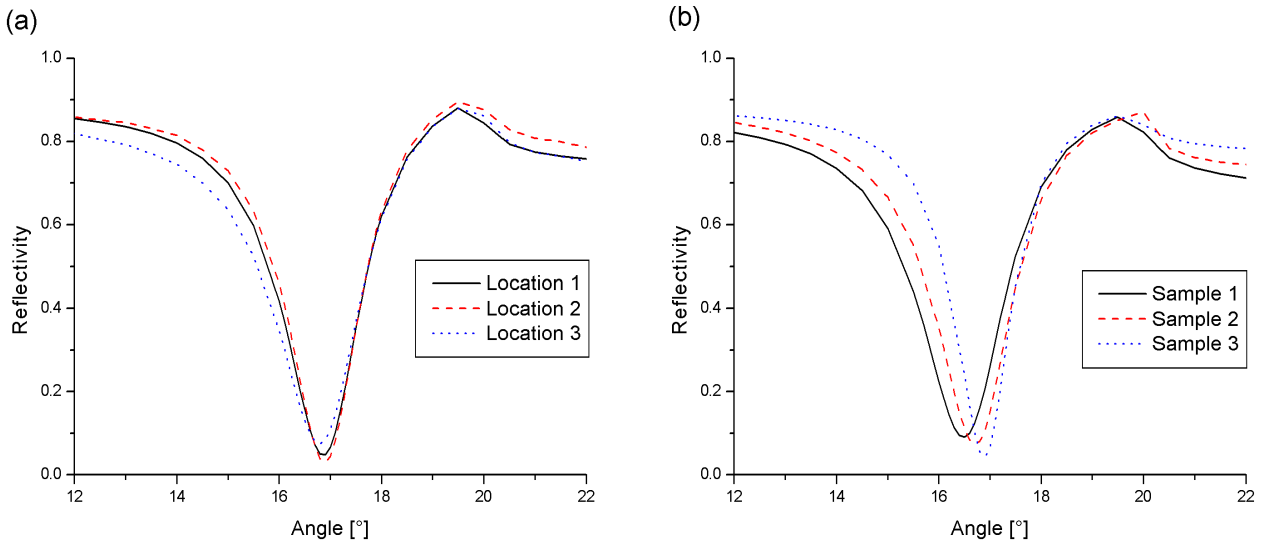

Figure 7.3: Uniformity over a single substrate and reproducibility of the replication. (a) Comparing different corrugated regions of the same replica shows a single sample uniformity that is comparable to that of etched gratings. (b) Larger variations exist between different samples, indicating tolerances in the machinery and the embossing cycle, like the way samples are placed and the actual force exerted during contact. All samples belong to the same evaporation batch to assure identical preparation.

like profile amplitude and even profile shape (for example, when the master is only partially pressed into a substrate region). A strong indication for the presence of different amplitudes is the strong change in the height of the plateau. The value of R beyond the minimum ($\theta > 20°$) is particularly sensitive to the profile amplitude (compare to figure 4.14). In order to further increase the reproducibility of hot embossing, it is necessary to start with flat surfaces free of any dust particles that can act as spacers. The rigid, strictly parallel, mounting of master and substrate has to be ensured to allow only one angle of attack for the contact between glass and polymer.

7.3 Tuning shift inversion

The surface of gold evaporated gratings made by hot embossing can be functionalized in the way described in section 3.2 in order to perform the same type of fluorescence measurements described before. Because they are direct imprints, they display essentially the inverse profile of the master and are additionally interesting for studying tuning shifts.

The angles of reflectivity minimum and most efficient fluorescence excitation don't necessarily coincide in grating coupling. A tuning shift with a distinct orientation has been described in section 5.6 where the direction of the shift was related to the mark-to-space ratio of the corrugation profile. This view is supported by measurements with embossed gratings. Embossing a

desired master structure directly into a soft substrate material (without going over an intermediate nickel stamp like in the CD/DVD industry) will invert the original topography. Strictly speaking a surface corrugation can only be faithfully replicated by direct embossing techniques if the function $\zeta(x)$ describing the surface profile is point symmetric in a general sense. Since the definition of the mathematical origin is arbitrary for this purpose any function that can be translated along the x-axis in a way to fulfill the condition $\zeta(-x) = -\zeta(x)$ is considered here[1]. For functions of this type the integral $\int_0^\Lambda \zeta(x)\,dx$ vanishes. Pending orientation, master and replica of point symmetric profiles have identical corrugations.

Force micrographs of etched gratings have shown their trapezoidal shape. Their surface profiles are not generally point symmetric. Describing them in terms of land and pit widths, mark-to-space ratios a little below one are common for glass gratings of high coupling efficiency. For less efficient gratings p/l is clearly larger than one. In the case of point symmetric profiles, the ratio equals one. Direct embossing will yield a replica in which the magnitude of the fraction p/l is inverted. This shape inversion will not necessarily result in an inverted shift direction. Simulations with sinusoids predict a general shift of I_{max} to the right of R_{min}. Alterations to the profile need to compensate for this before the direction of the shift is inverted. This is the situation in figure 7.4, recorded after bulk removal. Replicas of the master grating B82 ($\eta > 0.95$) exhibited a strong negative shift with I_{max} preceding R_{min}.

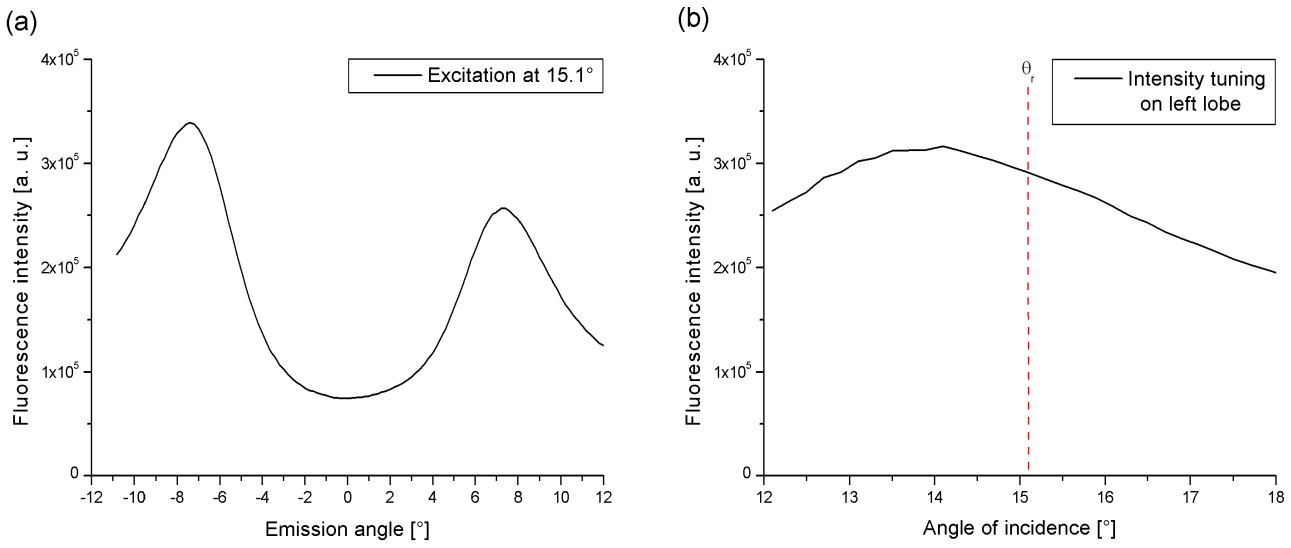

Figure 7.4: Inversion of the tuning shift in embossed gratings. Ideally, embossing creates a surface profile that is complementary to the master corrugation. The mark-to-space ratio of the original profile is inverted, which can lead to a reversal of the R_{min} and I_{max} sequence. (a) The directional emission of fluorescence emitted from an embossed grating, a replica of the etched sample B82. Excitation took place at the resonance angle of 15.1°. (b) Tuning the angle of incidence for the same specimen. The optimal fluorescence excitation angle (the maximum in the curve) is preceding the reflectivity minimum position by 1° (dashed line) for this embossed grating.

[1] A good example is the cosine function. It is not point symmetric per se, but can be shifted by a quarter period to yield a sinusoid that is.

7.4 Conclusion and outlook

It has been demonstrated, that hot embossing is a feasible method for the reproduction of highly efficient gratings in a thermoplast. Proving the principle of cheap, disposable gratings is one of the key requirements for realizing competitive grating coupling based SPFS sensing. The method was applied "by hand" and has some room for improvement. A detailed study of the role of the parameters involved in the embossing process (force load, master temperature, contact time) is going to be published in a forthcoming dissertation from our group [Kas06]. Combining this knowledge with a device engineered for automated production will increase reproducibility even further.

While indirect embossing (forming an intermediate nickel stamp from a glass or photoresist master first and finally shaping the polymer replica) can be thought of introducing more parameters affecting the outcome, like nickel grain size for example, this step is absolutely necessary in the long run. Fabricating nickel masters by electroformation will yield more robust and durable stamps. Glass masters have an unappreciably short life that is terminated by forceful master/replica separation or even the embossing action itself. Additionally, indirect embossing generates real surface replicas and not inverted corrugations. The latter are interesting for basic scientific studies, but the former are more convenient for master selection and prototyping.

Chapter 8

Solid angle imaging

This chapter discusses experiments in which fluorescence detection was performed with a sensitive CCD camera instead of a photomultiplier. With such a set-up, images of the fluorescence emission of a sample within a certain solid angle can be recorded with a single snapshot. There is no need to scan a detector around the sample, which takes time and is associated with bleaching effects during the course of each measurement, like those described in chapter 5. All pixels of the chip record intensities that result from laser exposure of the sample at the same time and for the same duration. This is especially relevant if the emission pattern is going to be recorded in two (angular) dimensions. In fact, the main motivation for changing the existing set-up to solid angle imaging (SAI) was to measure both azimuthal (θ) and polar (ψ) angles simultaneously. Recording images of the fluorescence emission within a certain solid angle conveniently covers both angles. These images are rather two-dimensional angular spectra (a position on the CCD image relates to the angle under which the ray has left from the object) than images in the strict sense (a position in the object plane corresponds to a position in the image plane).

A secondary motivation for this study on SAI originates from potential applications with array chips. Imaging optics and detection have already been combined with SPR under the name of surface plasmon microscopy (SPM [Rot88]) and also with prism coupled SPFS [Lie99]. The interest in resolving an area, as opposed to integrating over it, stems from the potential to perform topological multiplexing. Different spots arrayed on the substrate can be functionalized differently. An injected analyte can interact with several spots of an array at the same time and the information from all interaction sites is read out simultaneously. Lately, biologically functionalized quantum dots became readily available from commercial sources [Cha98]. These provide new opportunities for color multiplexing: a set of quantum dots, which differ in size or chemical composition, can be excited by a given single laser line and will emit at several well defined and separated wavelengths [Zho03]. Experimental set-ups suitable for working with assays like this require a monochromator to distinguish the different colors and the corresponding target/probe interactions, adding significantly to the cost of the system. Incorporating grating coupling in such a detection scheme can eliminate the need for a monochromator and hence reduce the cost of the device. Fluorescence emission taking place on the grating surface is predominately back coupled and therefore strongly directional. Different wavelengths experience different dielectric numbers of the gold and couple out under distinct angles. Thus, the signal

recorded by an appropriately positioned detector is already color specific.

The changes necessary to enable the previously described set-up to image the solid angle of the back coupled fluorescence emission are described in the first section of this chapter. The resulting images, their characteristics and their limitations due to spherical aberration are discussed in the following section. Next, the impact of bleaching on the SAI technique is quantified. As an application of the method, angular spectra of polarization sensitive detection (PSD) experiments are given. PSD studies were previously only possible under restricted circumstances in rotating PMT experiments.

8.1 Changes to the experimental set-up

The set-up was identical to what was described in section 3.3, except for fluorescence detection. The PMT is removed and replaced with a cooled CCD camera (CoolSNAP$_{HQ}$ Monochrome, Photometrics [PHO]). During operation, the camera is always positioned in such a way that its optical axis is oriented parallel to the surface normal of the grating. A simple paraxial series of three bi-convex spherical lenses between sample and camera illustrated in figure 8.1 collects the light and projects it on the sensitive chip. Many components limit the design and usage of the set-up, namely the position of the last mirror can be in conflict with the direction of the outcoupling fluorescence lobes. Location and size of the lens array can also turn out to restrict operation. The choice of focal length and diameter of the first lens defines the angular coverage of the system. The set-up that was found most useful is described here. It is optimized for samples with a grating constant of 474.7 nm. Because of this inherent inflexibility and the need to study other grating constants, the solid angle imaging method serves only as a complementary technique to the experiments performed in this work with a movable PMT set-up.

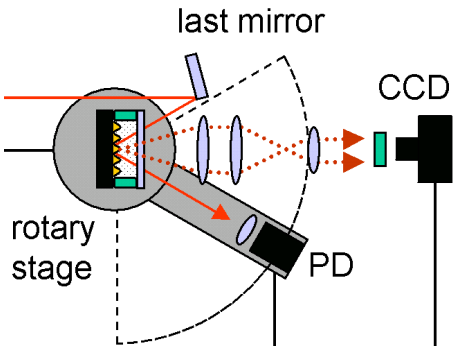

Figure 8.1: The set-up for solid angle imaging. The fluorescence emission is turned into a parallel pencil of rays first and then shrunk by a Kepler beam expander. The resulting beam diameter fits on the sensitive chip of a cooled CCD camera that is mounted along the surface normal of the grating.

The first lens (f_1 = 105 mm) has the grating at its focal point and shapes the fluorescence emission from the sample into a parallel pencil of rays. According to trigonometry, its free

diameter of 22.4 mm sets the angular coverage of the whole imaging system to ±6.09°, relative to the surface normal for both azimuthal and polar axis. The second and the third lens (f_2 = 80 mm and f_3 = 25 mm) are set apart by a distance equal to $f_2 + f_3$ to form a Kepler beam expander. The expander shrinks the diameter of the parallel pencil with its reduction of 3.2 to a size that is well covered by the active chip area (8.77 mm x 6.6 mm constituted by 1392 x 1040 pixels) of the CCD camera. Like in the original set-up, the light has to pass through two interference filters matched to the fluorescence wavelength before it reaches the detector. All images taken by the camera are relayed to the personal computer where they can be stored and analyzed.

8.2 Shape of the fluorescence lobes

SAI can map the full shape of the fluorescence lobes as shown in figure 8.2 (a). In respect to this type of measurement, the previously presented plots of fluorescence intensity versus polar angle (for example those in chapter 5) are horizontal line scans through the center of the solid angle image. Both lobes are almost of equal intensity. The minute difference between the two peaks visible in the figure is attributed to small imperfections in the optical alignment.

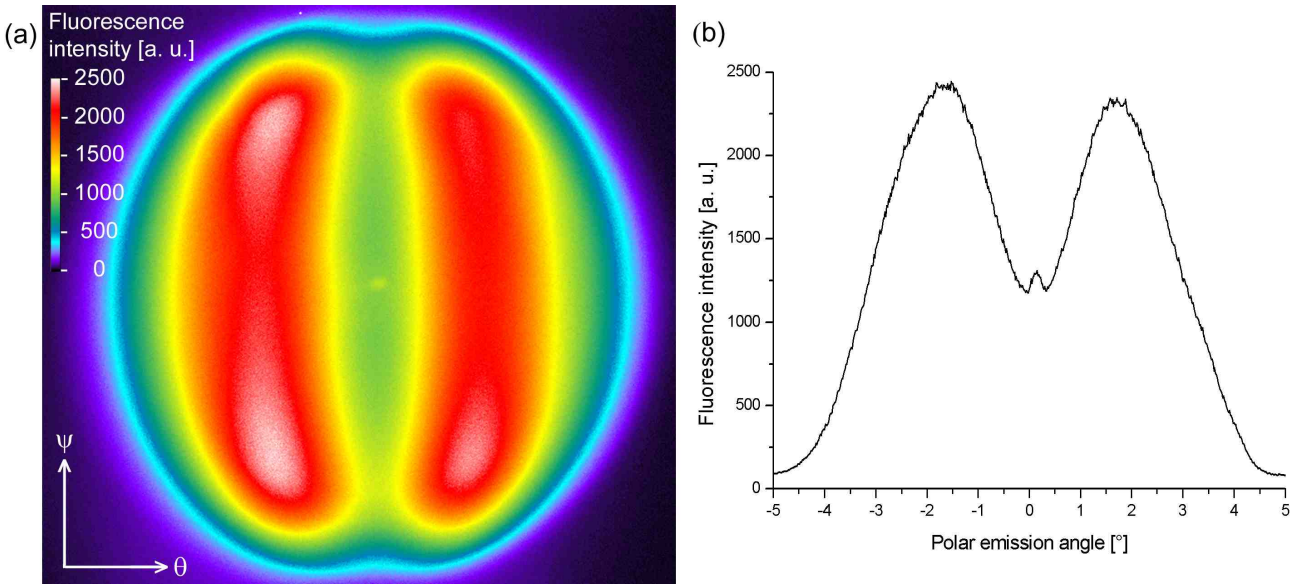

Figure 8.2: Imaging the fluorescence lobes. (a) Imaging the solid angle of the fluorescence emission shows the two high intensity lobes emitted from sample B95 under resonant excitation at 8.45°. The curvature of the two areas for ψ approaching the circular boundary is an artifact caused by spherical aberration. (b) A horizontal (polar plane) line scan through the center of the image. The data is almost perfectly symmetric around the center of the image. Close to the center, a little multiple reflection spike appears like those already discussed in chapter 5. The abscissa in the figure is converted from pixel positions on the chip to polar angles in degrees by using results from previous experiments in the conventional format in which the fluorescence maxima were located at ±1.75°.

Two prominent characteristics of the the solid angle image in figure 8.2 (a) are the two kidney-shaped bright regions and the circular boundary encompassing them. It is understood

that these two features of the image are the results of spherical aberration of the three paraxial lenses and not physical properties of the fluorescence emission distribution. The Gaussian theory of optics is based on the approximation

$$\sin\varphi \approx \varphi \tag{8.2.1}$$

and works well for small angles of incidence φ [Hec01]. The full Taylor expansion of the sine function

$$\sin\varphi = \varphi - \frac{\varphi^3}{3!} + \frac{\varphi^5}{5!} - \frac{\varphi^7}{7!} + \dots \tag{8.2.2}$$

indicates, that higher order terms become relevant as φ increases. Gaussian theory breaks down for higher angles and several types of blurring effects can appear in images. Higher angles of incidence equate to rays that pass the first lens far away from the optical axis. Those rays result from fluorescence light leaving the grating under higher emission angles. If the sample is in the focus of the lens, spherical aberration causes the rays emitted under higher emission angles to be out of focus (see figure 8.3). By doing so, spherical aberration reduces the angular coverage of the imaging optics below the theoretical limit of ±6.09° given by simple trigonometry. This additional reduction is the reason why the intensity line scan in figure 8.2 (b) drops so quickly at angles beyond ±3° compared to previous measurements with a rotating PMT (for example as the one shown in figure 6.8). This behavior is even more pronounced in the curves for s-polarized fluorescence emission in figure 8.7 (b).

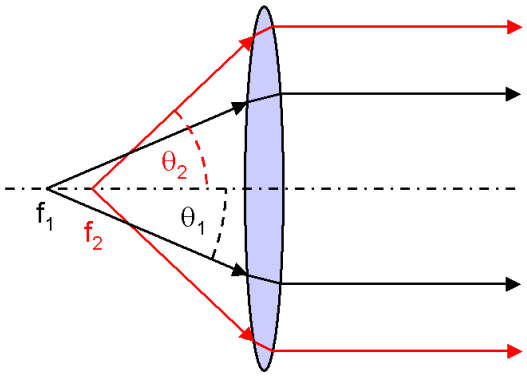

Figure 8.3: Spherical aberration of a lens. A lens that is separated from a grating by its focal length f_1 turns all rays emitted from the sample with small angles of emission within the range $\pm\theta_1$ into a parallel pencil. Spherical aberration creates a different focus f_2 closer to the lens for light emitted under higher angles of emission $\pm\theta_2$. Those rays will be out of focus.

The full aperture is used also by the second lens in the series, which is part of the beam expander. Hence the aberration increases as rays pass through the lenses. Only small sections of the full emission geometry can be studied without the beam expander. It is nevertheless instructive to look at such images of reduced spherical aberration. Figure 8.4 gives two such images. The first one shows the central area between the two bright regions. They are running parallel and without curvature. The second picture is taken after translating the camera in order to image the polar end of an emission lobe. Both lobes maintain the same separation and

are parallel and straight until the end, where the intensity increases slightly. The intensity also drops rapidly for higher polar angles, as in the images taken with the beam expander.

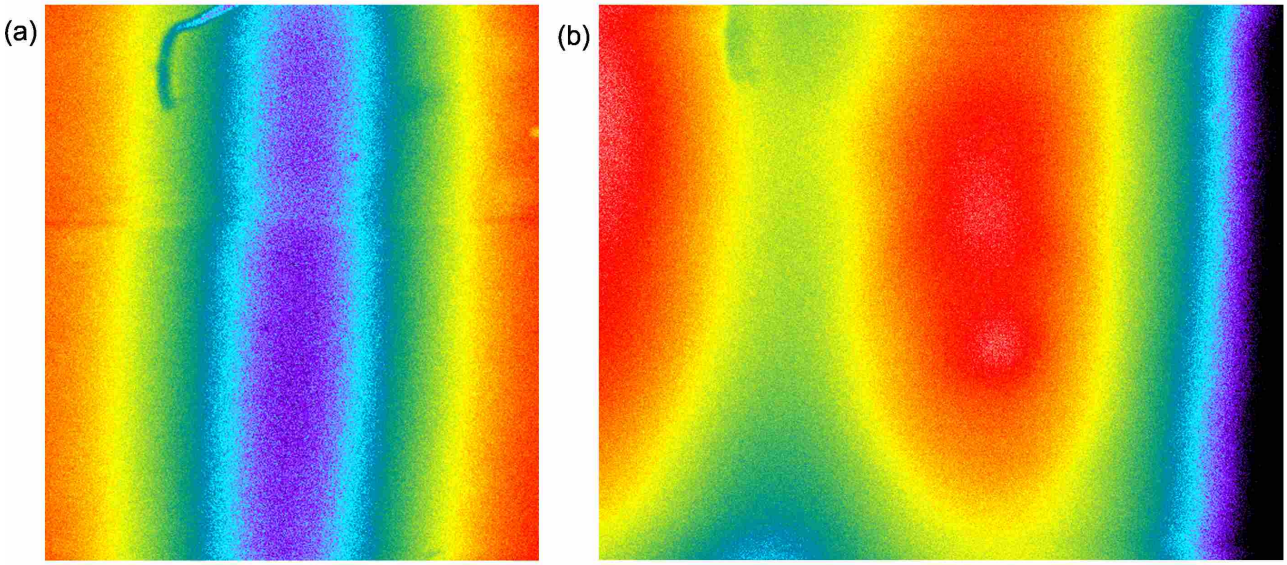

Figure 8.4: Images without a beam expander. (a) A central region located between the two fluorescence lobes. (b) An image of the lobe end in the polar plane. Both pictures show that the lobes are straight and not curved.

The image shape is determined by the geometrical restrictions inherent to the back coupling process. Momentum matching, as discussed in chapter 2, is dictating the angles under which fluorescence emission can take place. The extension of the parallel laser beam incident on the sample doesn't influence the shape of the image. Increasing or decreasing the laser spot diameter merely augments or reduces the intensity of the image uniformly. Its shape can only be changed by altering the grating properties or the dielectric profile of the multi-layer system.

This direct approach to SAI can only image very small sections of the full emission pattern. A beam expander is necessary to adapt its size to the sensitive area on the CCD chip. It is still advantageous to incorporate the beam expander in the set-up, because it collects more photons, thus increasing the signal-to-(electronic)-noise ratio of the data by the reduction factor of 3.2. If high imaging fidelity is required, the spherical aberration can be reduced by using aspherical optics or doublet lenses.

8.3 Bleaching effects

SAI experiments were partially motivated by the requirement to record the emission pattern with much lower bleaching. Successive images of the directional emission from sample B95 were taken under 15 s of p-light excitation. The measurements were performed with a saturated sensor surface, but without bulk fluorophores. Azimuthal line scans through the center of the images are given in figure 8.5. There is only a negligibly small difference in intensity between

the two curves. The intensity ratio of the two, which is also included in the figure, is constant in the range of -3.5° to 3.5° and gives an intensity loss due to bleaching that amounts to only 1.4 %. This value is an improvement compared with the rotating PMT experiments of chapter 5 in which reductions around 30 % were found.

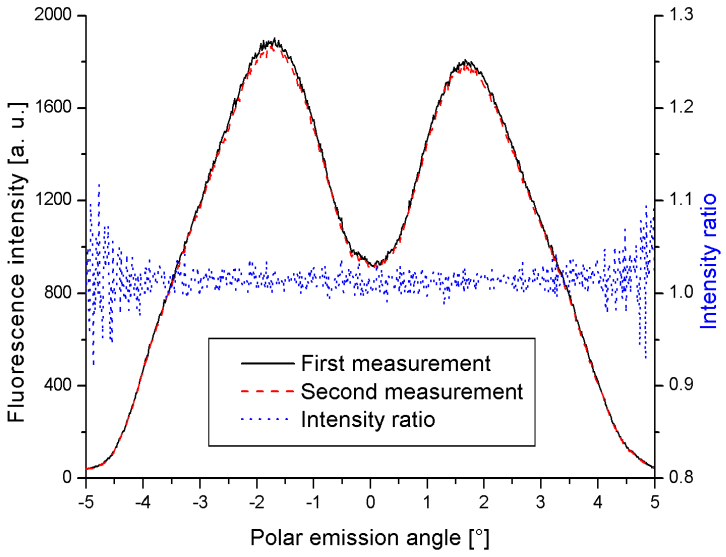

Figure 8.5: Bleaching in SAI. Bleaching is negligible in SAI due to the short exposure times required. Both fluorescence intensity profiles were taken successively with an exposure time of 15 s. Virtually no intensity is lost between the first and the second experiment, as indicated by the flat intensity ratio approaching unity. The persistent difference in intensity between the two peaks is attributed to small imperfections in the alignment of the detection optics.

SAI is very effective for reducing the sample exposure time. Its capability of simultaneous measurements for a range of angles eliminates the problem of progressive bleaching during detector movement, which was encountered in chapter 5. The curves contained in that chapter are smoother than the data in this chapter, because CCD detection features an decreased electronic signal-to-noise ratio compared to the much more sensitive PMT technology. However, this poses no problem in experiments shown here, because of the high fluorescence intensities. The question, which detection method is the most suitable one, has therefore to be answered in the context of the experimental goals. The long integration times of CCD chips necessary to achieve a good signal-to-noise ration (e. g. 15 s were required to record the data shown in figure 8.5) are disadvantageous for real time measurements monitoring the binding of an analyte.

8.4 Polarization sensitive detection

Bleaching is a problem in experimental set-ups with rotating PMTs, due to the long duration of measurements and the related exposure of the fluorophores to the laser beam, as well as to

surface plasmon fields. In theory, the rates for bleaching can be determined and the intensity reduction of the data over time can be compensated mathematically. Polarization sensitive detection studies use several combinations of excitation and detection polarization, which are changed during the experiment and which are described by individual bleaching rates, complicating compensation significantly. SAI is the more practical method for recording the angular structure of the emission in PSD experiments, since bleaching can be neglected.

In accordance with the experiments described in chapter 6, a polarizer was mounted in front of the PMT aperture to detect only p-polarized or s-polarized fluorescence emission. The polarization of the laser beam was changed with the Fresnel rhomb. Solid angle images obtained by this method are presented in figure 8.6. They show the emission from the saturated surface of sample B95 without bulk contributions. Azimuthal plane line scans through the center of these images are compiled in figure 8.7. The p/p combination results in the highest intensity for the full imaged range of angles. Excitation and emission both utilize the grating and are therefore enhanced. The configuration s/s results in the lowest signal, because of the lack of interaction with the grating. For the two mixed states, their relative intensity depends on the emission angle. The combination p/s describes the emission from a small fraction of fluorophores that are excited by the evanescent field, but their orientation changes before fluorescence emission can take place and they radiate freely without coupling to the grating. By the same token, dye molecules excited by s-light can depolarize and emit in the perpendicular polarization state. Because of the enhanced emission via the grating, this s/p combination is even stronger in intensity than s/s. Concentrating on the outcoupling angle of 1.75°, the intensities of the four combinations appear in the same sequence as given in chapter 6 for fixed angle experiments at this position.

8.5 Conclusion and outlook

Solid angle imaging was introduced as a method to record the fluorescence emission of a grating simultaneously over a range of azimuthal angles, as well as in the polar plane. According to the demanded angular coverage, SAI can be limited by spherical aberration since it requires large apertures optics. Imaging fidelity can be increased by utilizing aberration corrected doublets or aspherical lenses. Their incorporation into the set-up is the next logical step.

SAI was shown to reduce bleaching effects during individual measurements to a negligible level. Because of this property, the method is better suited for mapping directional emission than rotating PMT schemes. Particularly PSD experiments are facilitated by the technique and examples of such a study were given as a demonstration of SAI.

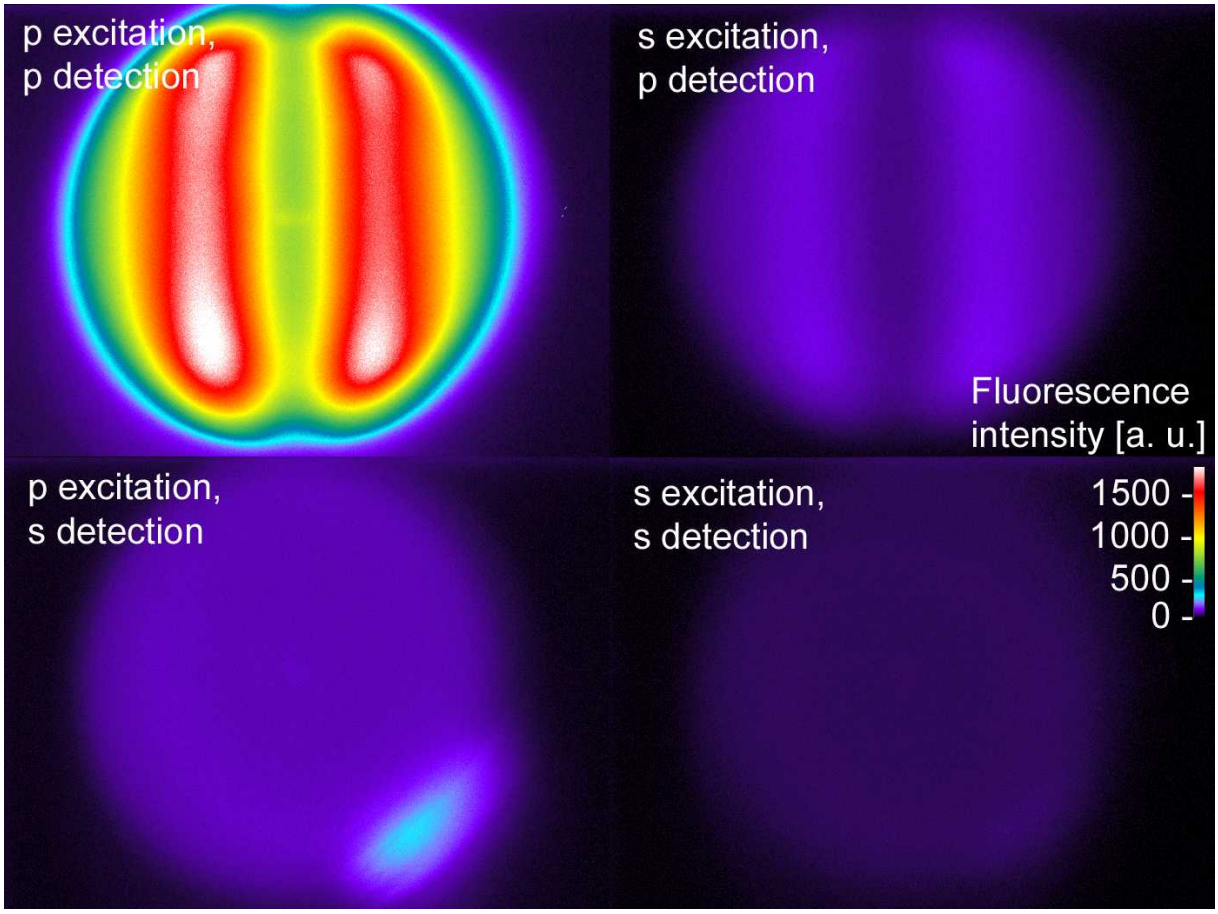

Figure 8.6: Solid angle images of polarization sensitive detection. The sample surface (B95) was saturated first and bulk fluorophores removed before the images were taken. The directional character of the p-polarized fluorescence emission is clearly visible under p-light excitation. The two emission lobes are also visible if the illumination is s-polarized, but at much lower intensities. The intensity spectra recorded for the two combinations of crossed excitation and detection polarization (p/s and s/s) are almost isotropic. The blurred spot in the lower right corner of the p/s image was caused by a dust particle.

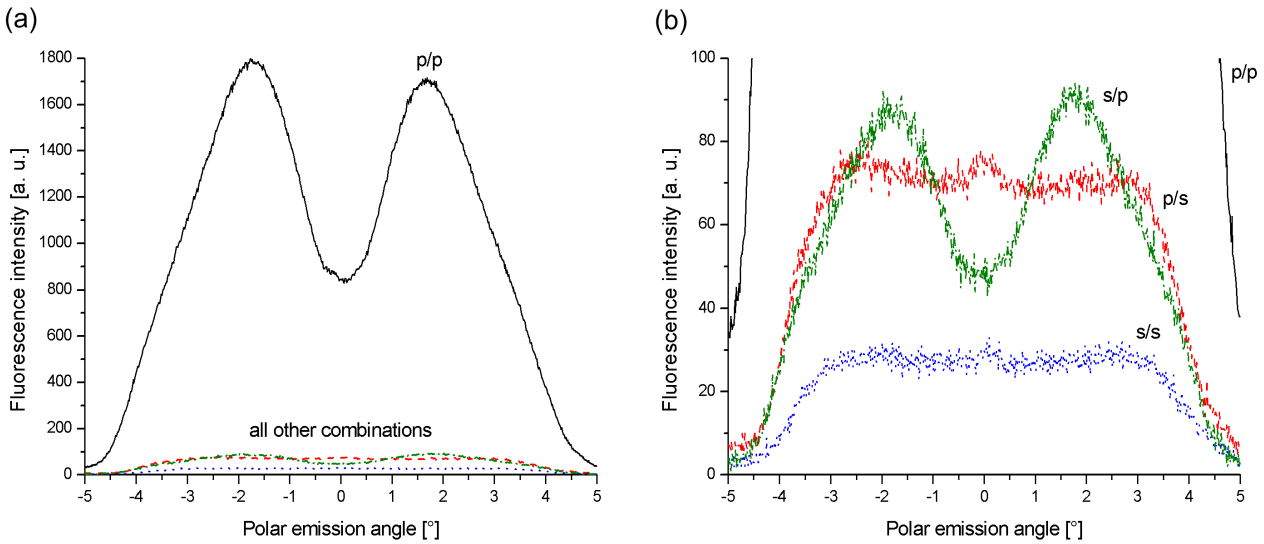

Figure 8.7: Line scans of polarization sensitive detection. All four curves represent horizontal line scans through the center of the images shown in figure 8.6. (a) All four combinations of excitation and emission are given in the graph, with p/p exhibiting the strongest intensity. (b) The graph shows the same data in more detail, focussing on the three weaker combinations. Independent from the excitation polarization, the emission of p-polarized fluorescence is always directional and hence predominantly grating coupled. In contrast to that, s-polarized emission is almost isotropic within the field of view of the system. The spectra of the combinations s/s and p/s indicate a cut-off angle of about 3° caused by spherical aberration of the imaging optics.

Chapter 9

Elliptical polarization modulation

The fluorescence emission from bulk fluorophores adds to the background intensity in GC-SPFS measurements. This is of particular concern for experiments at high dye concentrations. The bulk contribution was identified in chapter 6 as a factor that does not determine the limit of detection in experiments with direct assays. This situation is different for other protocols, for example sandwich assays, in which high fluorophore concentrations are desired for reasons of rapid detection. Elliptical polarization modulation (EPM) is suggested and successfully demonstrated in this chapter as a novel detection method to cancel the background fluorescence originating from the bulk.

The underlying concept of EPM is explained first. The method is based on modulating the intensity of the incident beam in intensity as well as polarization and requires additions to the previously described GC-SPFS set-up. Supporting experiments are detailed in the following two sections. These concern the reflectivity response of a grating with incident light of arbitrary linear polarization and the relationship between the bulk fluorophore concentration and the mixing angle, a new control parameter peculiar to EPM. DNA hybridization experiments at high concentration are covered in the subsequent section, demonstrating the capability of EPM to remove bulk fluorescence. Next, a sandwich assay is studied to apply the technique to measurements at low analyte concentration, while keeping the bulk fluorophore concentration high. The chapter concludes with a discussion of certain technical aspects of the system contributing to noise and how the limit of detection can be lowered by electro-optical implementations of the EPM concept.

9.1 The concept behind elliptical polarization modulation

In terms of intensity, the two orthogonal polarization states p and s interact differently with the bulk. The reflectivity of an ideal grating in resonance is zero for p-light and one for s-light. In a pure bulk scenario, fluorescence is excited by the processes illustrated in figure 9.1: s-polarized light is fully reflected by the grating and passes the flow cell twice, exciting bulk

fluorophores during each passage. P-polarized light is completely absorbed by the grating. It passes the bulk only once, but additional fluorophores can be excited by the evanescent tail of the surface plasmon mode reaching out into the bulk. For a flow cell much thicker than the decay length of the evanescent field and for equal incident intensities, the fluorescence intensity excited by s-light illumination will always exceed the intensity caused by p-light, up to a maximum factor of two.

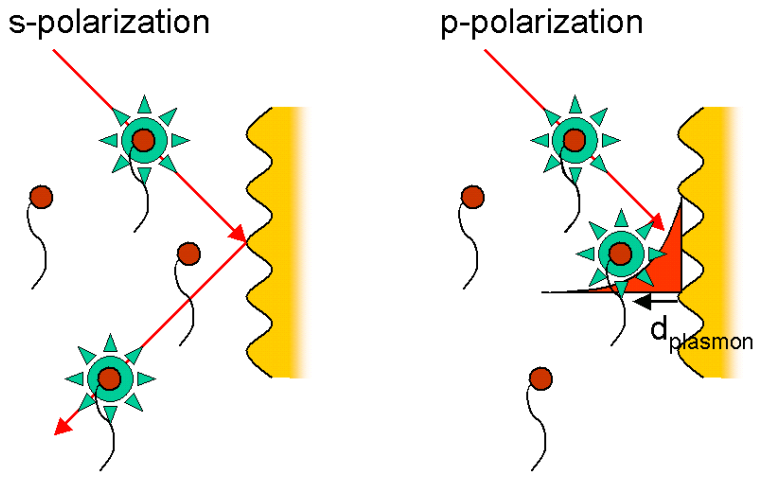

Figure 9.1: Bulk emission in respect to polarization. The intensity of the bulk emission is different for the two fundamental illuminating beam polarizations. No binding (and thus accumulation at the sensor surface) takes place for an inert analyte. The signal contribution that remains is emission from the bulk. S-polarized light is completely reflected by an ideal grating. It penetrates the bulk twice and can excite fluorophores on its way in and out of the flow cell. On the other hand, p-polarized light is fully absorbed in the resonance condition and there is no reflected beam. Bulk excitation is caused by the incident beam and by the evanescent tails of surfaces plasmons. For macroscopically thick flow cells, the fluorescence intensity generated by bulk emission is always higher for a s-polarized incident beam.

The difference in bulk fluorescence intensity response by the two fundamental polarizations can be compensated by changing the relative strengths of the two polarizations: reducing the incident intensity of s-light, while increasing the incident intensity of p-light at the same time until both fluorescence intensities are the same. This condition can be achieved by rotating the Fresnel rhomb to a suitable angle. This angle is called the mixing angle ρ_m. The resulting polarization of the beam can than be decomposed into a p-component and a s-component that each cause a bulk fluorescence signal of equal intensity. If the intensities are scaled in this way, one can't tell the polarization of the beam by measuring the fluorescence intensity from a pure bulk experiment alone. However, if the complementary strand MM0 is injected and binding takes place, p-light illumination will cause a higher fluorescence signal due to the additional emission from bound strands accumulating at the sensor surface where the enhanced electromagnetic field is located.

This additional intensity from binding is the relevant signal that needs to be separated from the bulk emission. This deduction can be performed by lock-in detection. If the relative strength of p and s is equalized in the described way and the system switches constantly between the two states at a fixed frequency, the constant bulk baseline can be deducted from the

total signal to give the binding kinetics. In the frequency domain, the total signal consists of the DC bulk contribution and the AC binding signal that is frequency-encoded at the modulation frequency of the polarization switching, since the immobilized fluorophores are almost exclusively responding to p-polarized illumination. The AC component can be extracted by a lock-in detector.

Rather than switching between to discrete states, the polarization was continuously changed in the experiments described here by constantly rotating a polarizer. This method requires a non-linear polarization state, since there shouldn't be a polarizer position for which the transmitted light becomes extinct. Elliptical polarization, the most general condition of polarized light, was hence used (for examples, see textbooks like [Gol03]). If the rotating polarizer revolves much slower than the electric field vector of the elliptical polarized beam (5 Hz $<<$ 10^{12} Hz)[1], the full ellipse is present at every orientation of the rotating polarizer. The polarizer selects only one linear polarization from the full spectrum of electric field vectors forming the ellipse. Thus the resulting beam is modulated in polarization as well as in intensity. The method is hence called elliptical polarization modulation.

9.2 Changes to the experimental set-up

Changes to the existing system detailed in section 3.3 took place in the fields of optics, fluorescence detection and detection electronics. These are illustrated in figure 9.2. A $\lambda/4$-plate was inserted after the Fresnel rhomb with its slow axis in the direction of p-polarization, followed by a polarizer. The polarizer orientation was controlled by a motor and it could be rotated continuously at frequencies up to 5 Hz. The digital photon-counting PMT used in all previous experiments was replaced by an analog PMT (H8249-101, Hamamatsu [HAM]) that could produce a continuous output in order to be compatible with lock-in detection. The PMT signal was fed into a lock-in detector together with the reference frequency from the motor control attached to the rotating polarizer. The chopper present in the set-up (f $>$ 1 kHz) is only used for reflectivity measurements with the photodiode and totally unrelated to the operation of this second lock-in detector. Due to mechanical constraints of the rotating polarizer assembly, 5 Hz was the highest frequency that could be stably maintained with this system over a long time. This is still high enough to allow work with time constant settings of the lock-in detector suitable to monitor DNA hybridization at high concentrations.

The processing of the original laser beam in order to achieve the desired polarization and intensity consists of three steps that are illustrated in figure 9.3: the laser emits a linearly polarized beam. The plane of polarization is rotated by the Fresnel rhomb[2], set to the mixing angle, while the Fresnel rhomb maintains the total intensity of the beam, the distribution of this total intensity into the two perpendicular polarization states has changed. The beam reaches the $\lambda/4$-plate, which causes a phase-shift of 45° between the two polarization directions,

[1] The whole concept of elliptical polarization modulation breaks down if this condition is not met.

[2] Confusion has to be avoided when talking about rotating the plane of polarization by a certain angle. For a given Fresnel rhomb angle ρ, the polarization of the beam is rotated by 2ρ.

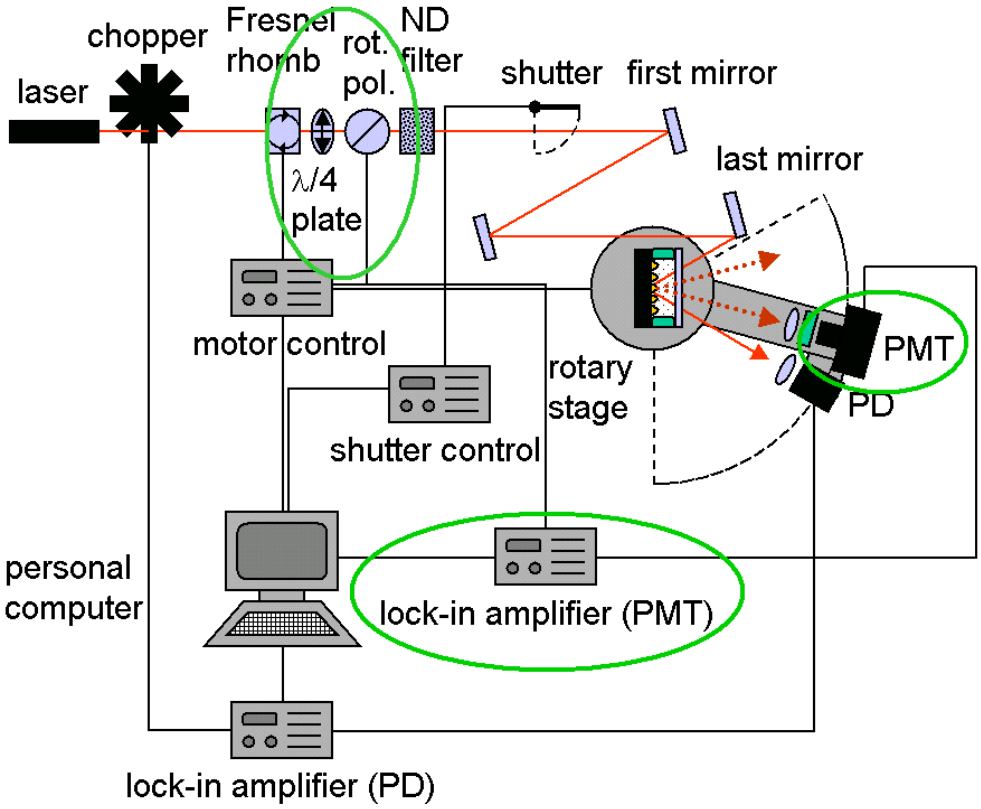

Figure 9.2: The set-up for elliptical polarization modulation. A $\lambda/4$-plate and a rotating polarizer are added to shape polarization and intensity of the beam in the desired way. The modulated fluorescence signal is detected by an analog PMT. A lock-in detector extracts the frequency-encoded binding signal component from the PMT output. The frequency reference is obtained from the motor control unit.

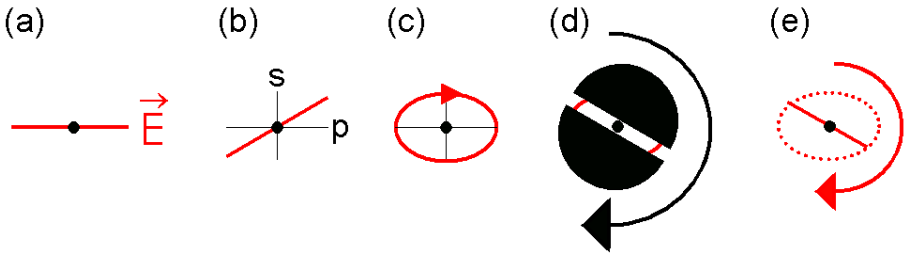

Figure 9.3: Shaping modulated elliptical polarization. The sketches show the electric field vector, viewed along the optical axis. (a) The laser beam is originally linearly polarized. (b) Its plane of polarization is rotated by the Fresnel rhomb. (c) The anisotropic phase-shift introduced by the $\lambda/4$-plate rotates the linear polarization of the beam into elliptical polarization. (d) The beam passes through the rotating polarizer that eliminates vectors perpendicular to its orientation. (e) The emerging beam can be described as a polarization and intensity modulated condition. The electric field vector is slowly rotating, with the modulation frequency given by the rotating polarizer.

forming elliptically polarized light. Since the retardation plane is oriented parallel to the p-axis, the ellipse is not tilted, i. e. the main axes of the ellipse are either parallel or perpendicular to the p-axis. The ellipse falls onto the rotating polarizer, which allows only the component parallel to its orientation to pass. The resulting beam consists of an electric field vector that rotates with the frequency of the rotating polarizer (much smaller than the THz range of optical frequencies). Its magnitude also changes and is determined by the shape of the ellipse. Additional information on procedures for performing EPM-experiments is given in appendix C.

9.3 Mixed polarization response

In all previously described experiments, the incident laser beam was either p-polarized or s-polarized. EPM employs all intermediated polarizations. These can be expressed as linear combinations of the two fundamental polarization states p and s. The application of the superposition principle is trivial for the far field illumination. It is also expected to be valid for the optical response of a grating, expressed in terms of reflectivity, but it has to be measured to exclude unexpected electromagnetic interactions.

The reflectivity curves of a grating were recorded as a function of the Fresnel rhomb angle ρ. Sample B8 was studied without flow cell to facilitate data analysis. The reflectivity spectra obtained from these measurements are shown in figure 9.4 (a). The curve for $\rho = 0°$ has the smallest value of R at $\theta = 11.1°$. For the given grating, the reflectivity doesn't exactly reach zero and a constant background reflectivity was found. As ρ increases, the value of R_{min} also increases also, but the position doesn't change. The resonance minimum disappears under s-polarized illumination ($\rho = 45°$).

The value of R_{min} was extracted from each curve and plotted as a function of 2ρ, which is the angle by that the plane of polarization is rotated. The reflectivity axis was normalized with $R_{min}(\rho = 0°)$ defined as zero and $R_{min}(\rho = 45°)$ set to one. The former definition compensates the constant background reflectivity, the latter cancels bulk absorption by the gold. The resulting data can be fit very well with a $\cos^2$ function as shown in figure 9.4 (b). The good agreement between the data and the fit proves the validity of the assumption. Superposition is also the appropriate description of the optical response of a grating to arbitrarily polarized illumination.

9.4 Mixing angle versus bulk concentration

For full compensation of the bulk fluorescence emission in EPM experiments, the mixing angle needs to be accurately determined. Using a different angle will not necessarily prevent the detection of a binding reaction, but the observed magnitude of the fluorescence signal will be wrong.

The relationship between the ρ_m and the bulk fluorophore concentration was studied for MM15 with a fully functionalized grating. The concentration of the inert strand was varied

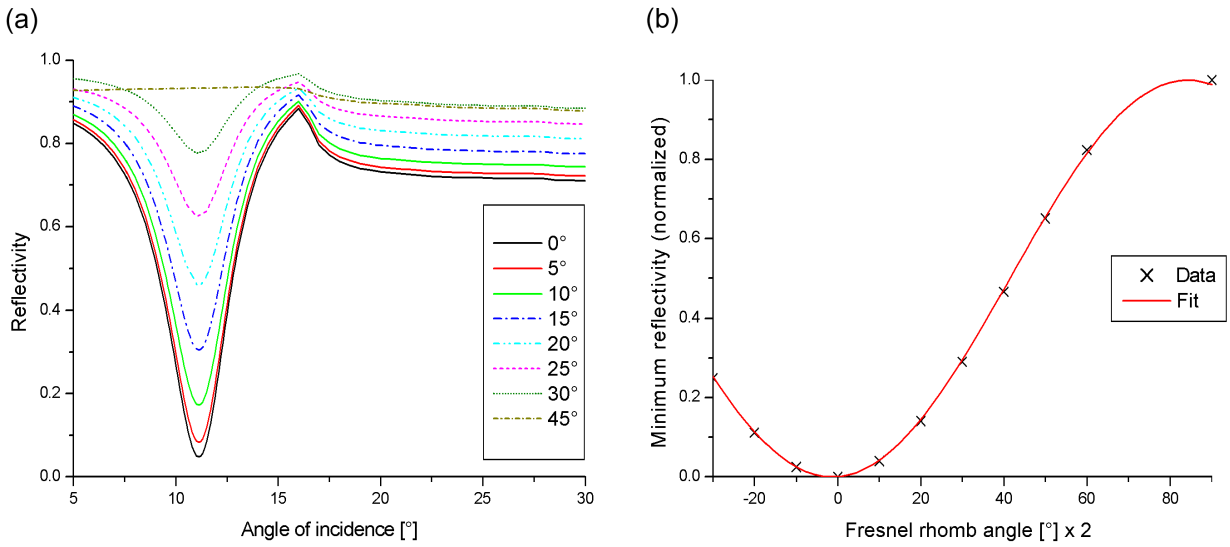

Figure 9.4: Reflectivity curves for mixed polarization. The reflectivity response of a grating to an incident beam of mixed polarization can be determined by the linear combination of the curves for the two fundamental polarizations s and p. (a) Reflectivity curves of a grating as a function of the Fresnel rhomb angle ρ. The curve for p-polarized light features a pronounced resonance dip, whereas the s-light curve remains flat. (b) The magnitude of the minimum reflectivity (R at $\theta = 11.1°$) versus ρ times two. The data is in very good agreement with a $\cos^2$ fit, indicating the validity of the superposition principle.

over several orders of magnitude and the mixing angle identified for each concentration. Since the resolution of the Fresnel rhomb angle was limited to 0.5° by the stepper motor rotating the rhomb, the data was interpolated. A parabola was fit to the intensity of each apparent mixing angle and the two neighboring intensities, separated by ±0.5°. The angle of the minimum position of each parabola was recorded as the mixing angle.

The interpolated mixing angle is plotted as a function of MM15 concentration in figure 9.5. ρ_m increases with higher concentrations only to reach a saturation value. The relationship of the two quantities is only understood qualitatively. Bulk absorption effects can't be neglected and these affect s-polarized light stronger than its counterpart. The full fluorescence intensity caused by a s-polarized light is generated by absorption of the beam as it passes into and also out of the flow cell. The laser intensity is therefore getting exponentially weaker and weaker on its way. A p-polarized beam is subject to bulk absorption only once and therefore less affected by higher fluorophore concentrations. To compensate for this, a higher incident intensity was chosen for s-polarized light during the adjustment of the mixing angle, resulting in an increased value of ρ_m for higher concentrations. The relative strength of the intensities caused by p-polarized or s-polarized illumination respectively depends on the Fresnel rhomb angle in the following way:

$$\frac{I_p}{I_s} = \frac{1}{\tan^2 2\rho}. \tag{9.4.1}$$

The relationship between mixing angle and dye concentration can be described well by a line fit, if the concentration is plotted on a logarithmic scale. This corresponds to a power

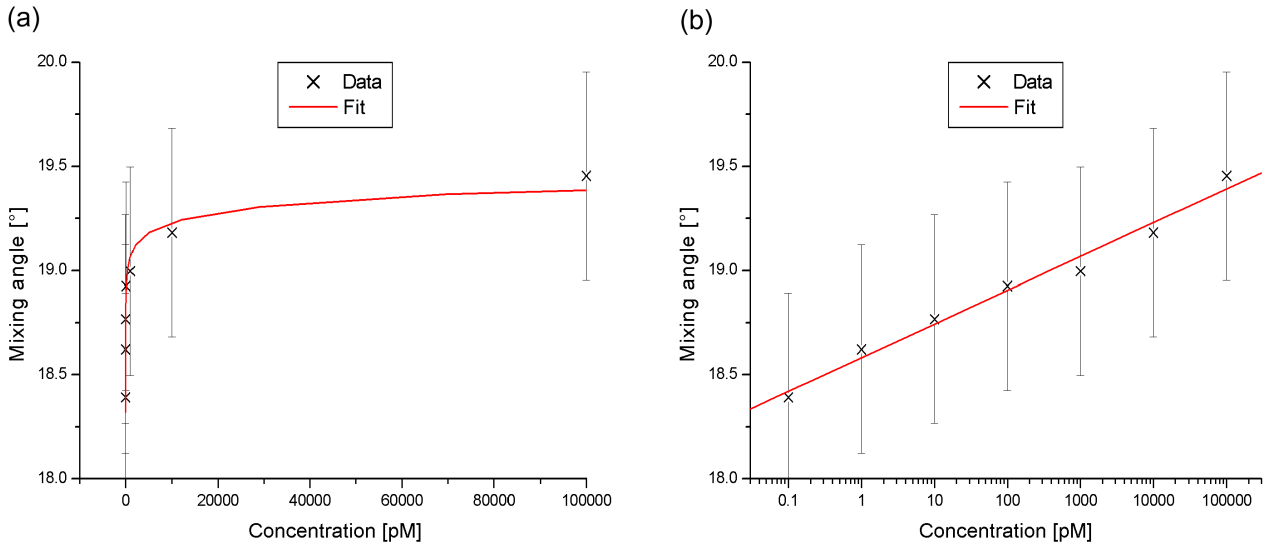

Figure 9.5: The mixing angle as a function of MM15 concentration. The mixing angle is not independent of the bulk fluorophore concentration, because the two fundamental polarizations interact with the bulk to a different extend. Since s-polarization experiences bulk absorption stronger, a higher incident intensity is necessary when adjusting ρ_m, resulting in higher angles for an increase in MM15 concentration. The exact relationship between the two quantities still requires a successful theoretical description. (a) Plotted on a logarithmic scale, a linear curve shape is proposed. (b) The same data and fit curve shown on a linear scale.

law relationship on a linear scale in which the mixing angle scales approximately with $\rho^{1/6}$. This result is purely empirical. An explanation of the curve shape has still to be found which is derived from a thorough theoretical analysis. Simple considerations based on the Lambert-Beer law [Atk02], equating absorption of the bulk medium with fluorescence emission for the two polarizations with their respective bulk penetration lengths, are not sufficient.

For an ideal grating that resonantly absorbs p-light completely and reflects s-light fully and if bulk absorption as well as excitation by the evanescent tail (in the case of p-polarized light) could be ignored, the bulk fluorescence intensity ratio p versus s would equal 1:2. This would correspond to a mixing angle of 17.63°. A real grating of high coupling efficiency, for example the one studied in figure 9.4, has a non-vanishing reflectivity of about 0.05 for p-light and reflects s-polarized light with R = 0.02. Using these values ($\frac{I_p}{I_s} = \frac{1+0.05}{1+0.92}$), equation 9.4.1 predicts a mixing angle of 18.24° for the case of zero bulk fluorophore concentration. This number is approached well by the intersection of the line fit with the ordinate in figure 9.5 (b).

9.5 Experiments with a direct assay

Binding kinetics of DNA hybridization were measured with and without EPM to show the advantages of the technique. The concentration of the oligomer solutions of MM15 and MM0 was always 500 nM to guarantee a strong bulk fluorescence emission. Sensor surface saturation was quickly reached at this concentration and the binding kinetics had to be measured with

continuous illumination, instead of using an automated shutter for the laser beam as in the affinity studies described in chapter 6. For this reason, there is a reduction of the fluorescence intensity over time, caused by bleaching of immobilized dye molecules, but this effect does not interfere with the intended comparison.

Sample B62 ($\eta > 0.96$) was used for experiments in the conventional format. Surface plasmons were excited under the optimal angle of 16.1° to cause maximum fluorescence intensity. The PMT was placed on the peak of the left emission lobe at -8.8° and operated with a narrow aperture. The hybridization kinetics of the complementary strand MM0 measured with this grating are shown in figure 9.6 (a). They were measured not only under p-polarized illumination, but with s-light as well. In both cases, the hybridization was observed for about 60 seconds upon injection of the analyte, followed by a dark period to reduce bleaching and a second period of illumination and fluorescence detection. Altogether, the sensor surface was exposed to the analyte for a duration of three minutes, enough for reaching full surface coverage. After this, the flow cell was rinsed with PBS buffer for approximately one minute, again without exposure to the beam. The shutter was opened and a third measurement taken at this point.

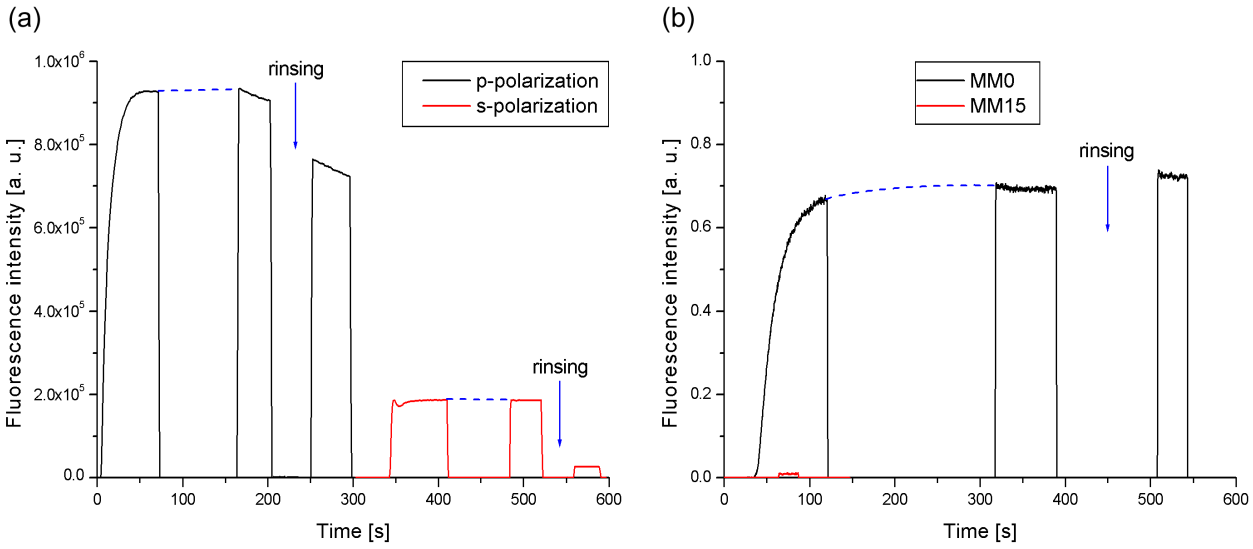

Figure 9.6: Cancelling the bulk jump with EPM. (a) In conventional kinetic experiments, rinsing of the flow cell after saturation of the sensor surface reduces the fluorescence intensity. Hybridization continued during the off-times of the laser, as indicated by the dotted lines added by the author. (b) Rinsing did not decrease the signal in the corresponding measurement using EPM, because the bulk fluorescence contribution is not detected by this technique. Instead the intensity increased a little, since the immobilized fluorophores experienced the full incident laser intensity after rinsing. The small step of the MM15 curve around 75 s shows the remaining, almost vanishing, magnitude from the initial minimization process for finding ρ_m for comparison. The ordinates of the two graphs are differently scaled due to the different experimental formats - photon counting for the conventional method versus voltage measurement in EPM.

The main aspect of focus in this experiment is the change of intensity due to rinsing. This phenomenon is also known as the bulk jump. Rinsing removes all bulk fluorophores and their contribution to the total observed fluorescence intensity and only immobilized fluorophores

remain in the flow cell. The bulk jump amounts to 1.41×10^5 intensity units (a decrease by 15.4 %) in the case of p-polarized incident light. For s-polarization, the reduction equals 1.59×10^5 intensity units (a drop in signal by 85.5 %). The intensity change is smaller for p-polarization, because the resonant coupling to the grating is a more efficient excitation process than exciting bulk fluorophores directly. Emission from the bulk plays a much higher role for s-light excitation. The majority, but not all, of the total fluorescence intensity is caused by emission from the bulk and can be removed by rinsing. The small remaining signal stems from direct excitation of the hybridized target strand by the laser (refer to sections 5.4 and 8.4). The time-dependent intensity measured for p-polarized illumination decays, with and without bulk being present, whereas the signal excited by s-light stays virtually constant. The signal decay for p-polarization is attributed to bleaching of the immobilized fluorophores in the enhanced surface plasmon field, a finding that is discussed in more detail in section 5.5.

Rinsing the flow cell has a very different consequence for measurements employing elliptical polarization modulation. Data from the same type of experiment performed with EPM is given in figure 9.6 (b). Grating B101 ($\eta > 0.96$) was illuminated under the resonance angle of 8.75° and the fluorescence intensity was measured with an analog PMT placed in the center of the right emission lobe, located at 2.75°, using a narrow aperture. Before injection of the MM0 strand, the mixing angle was identified at about 17.5°. ρ_m could not be adjusted with a higher precision due to the finite step size of the Fresnel rhomb motor of 0.5°. For that reason, the bulk emission intensity was almost completely, but not fully cancelled in this experiment (MM15 curve). Its magnitude is also included in the figure for comparison. It equals $1/70^{th}$ of the intensity generated by the MM0 saturated surface.

After reaching the equilibrium surface coverage the flow cell was rinsed. In contrast to the previous experiments, the fluorescence intensity did not drop but instead increased slightly. Since EPM can distinguish between emission originating from the sensor surface or from the bulk, there is no signal reduction upon rinsing - the bulk contribution is already cancelled from the beginning. However, the method is not insensitive to all interactions of the bulk fluorophores with the laser beam. The small increase in intensity after rinsing can be attributed to the bulk fluorophores screening the sensor surface. Fluorophores present in the bulk absorb a portion of the laser beam and the grating experiences a reduced incident intensity. If the screening dyes are removed, the immobilized fluorophores are exposed to the unattenuated laser power, causing a higher fluorescence emission.

Bleaching takes place in the EPM experiment also, but the decay rate is very small, since the sample is exposed to a much lower illumination intensity compared to the experiment with a purely p-polarized or s-polarized beam. The polarization processing of the beam in EPM distributes the total power of the linearly polarized laser among the elliptical trajectory of the electric field vector (compare to 9.3). The rotating polarized discards all field components that are not parallel to its orientation, resulting in an incident beam of reduced power.

9.6 Experiments with a sandwich assay

Another assay was used for EPM experiments, which was provided by our industrial collaboration partner DPC. Only a general overview is given here about the design of this other functionalization protocol. Figure 9.7 illustrates the composition of the assay: a layer of biotinylated bovine serum albumin (BSA) is formed unspecifically on the gold film by hydrophobic interaction. Streptavidin is immobilized on the biotin groups protruding from the BSA. A biotinylated antibody binds to remaining binding pockets of the streptavidin layer, concluding the sensor surface functionalization. The protocol is designed to immobilize a specific antigen that is not fluorescently labeled. The dye (Alexa Fluor 647, excitation maximum 650 nm, emission maximum 668 nm, Molecular Probes [MOL]) is carried by a secondary antibody (concentration 0.2 μg/ml) which also binds to the targeted antigen.

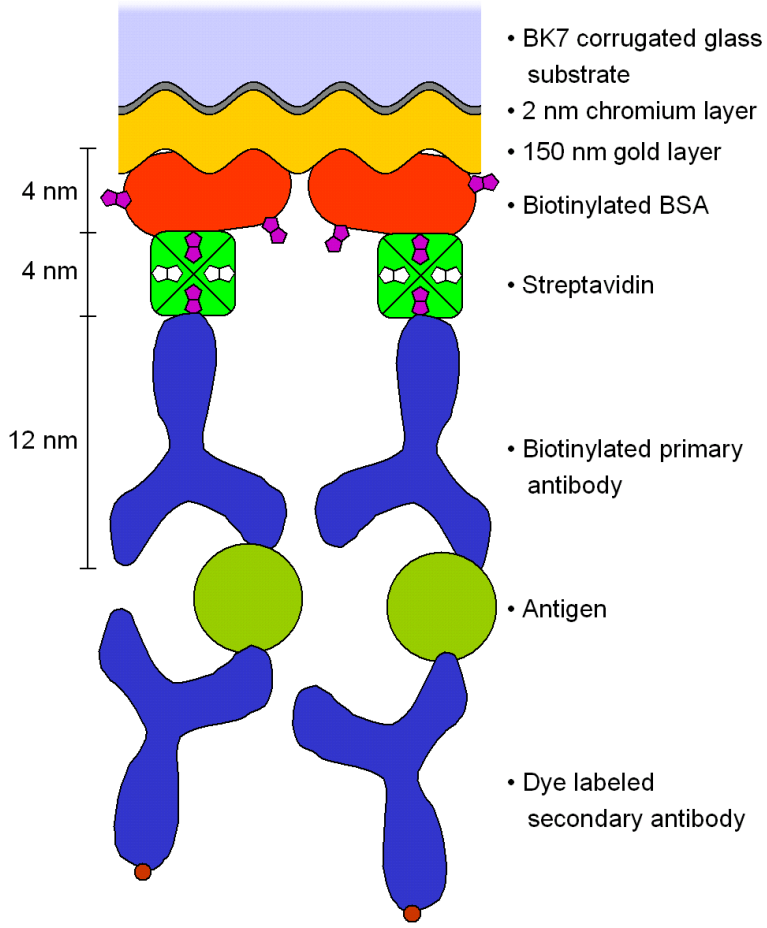

Figure 9.7: Sandwich assay surface functionalization. The unlabeled antigen is the analyte in this recognition scheme. A fluorescence signal is only generated if a fluorescently labeled secondary antibody binds to the immobilized antigen in a second reaction. The drawing is not to scale; molecular dimensions are indicated, but considerable uncertainty exists in the dye/metal separation, resulting from freedom of the geometry.

The advantage of this method is that no coupling chemistry has to be applied to label the

antigen with a fluorophore, which is particularly practical in a clinical context. The disadvantage is that two binding interactions have to take place until a fluorophore is immobilized: antigen to primary antibody and secondary antibody to antigen. This situation is not suitable for affinity studies, but perfectly capable of detecting the presence or absence of an analyte. In the laboratory, the last two molecules can be brought to interact already prior to experiments to save time. A high concentration of the fluorescently labeled antibody is desired in a clinical scenario for the same reason. This is potentially a drawback for a combination with GC-SPFS detection technology, since there is always a high concentration of bulk fluorophores present. EPM is used to address this issue. Typically, the concentration of the labeled antibody is a fixed quantity and the antigen concentration is varied in experiments as well as in clinical examinations. This arrangement is advantageous in the context of EPM measurements, since titration experiments can be performed without changing the mixing angle. No inert analyte derivative is necessary to find ρ_m. Cycling the secondary antibody solution without the antigen simulates the pure bulk case.

The separation of the label from the analyte is the fundamental difference to the DNA assay used in all other experiments described in this thesis. While the dye concentration equals that of the analyte for the DNA assay, both can be different for the sandwich assay. This situation changes some observations described before, for example statements on the relative intensity of fluorescence emission from the bulk and from the surface. In particular, findings about the limit of detection derived from DNA experiments can't be applied to this sandwich assay.

A titration study was undertaken in which the antigen concentration was increased. Grating B95 ($\eta > 0.95$) was used as the sample and excited under the resonance condition at $\theta_r = 8.65°$. The PMT was operated with a wide aperture, integrating both fluorescence emission lobes of the grating to increase gain as well as the signal to noise ratio. A mixing angle of 19° was found for this sandwich assay in experiments that excluded the antigen. The titration of the pre-mixed antigen/secondary antibody solution started with antigen concentrations in the pM range (see figure 9.8). Since the experiment was intended to find the limit of detection for recognition at quick response times, every concentration was observed for about 100 seconds before increasing the concentration. Binding was first observed as a constant increase in the fluorescence intensity at a concentration of 720 pM.

Every titration step was interrupted before equilibrium was reached. Nevertheless, it can still be seen that the fluorescence intensity increase during 100 seconds of exposure is higher than the noise and binding can be clearly recognized as such. A lower limit of detection can be realized by allowing longer interaction times. Aside from this, no affinity parameters are known about the recognition reaction to estimate the equilibrium fluorescence signal, necessary to extrapolate the physical limit of detection for $t \to \infty$.

The basic technical aspects that determine the LOD in GC-SPFS have been discussed in chapter 6, namely illumination crosstalk. EPM introduces additional noise contributions that can affect detection. One source for fluctuations in the signal was the rotating polarizer assembly. If the optical axis and the axis of rotation don't coincide, the laser beam passes through different parts of the crystal as the polarizer rotates. These parts will be slightly different in terms of transmission. An additional problem occurs, when dust particles located on the

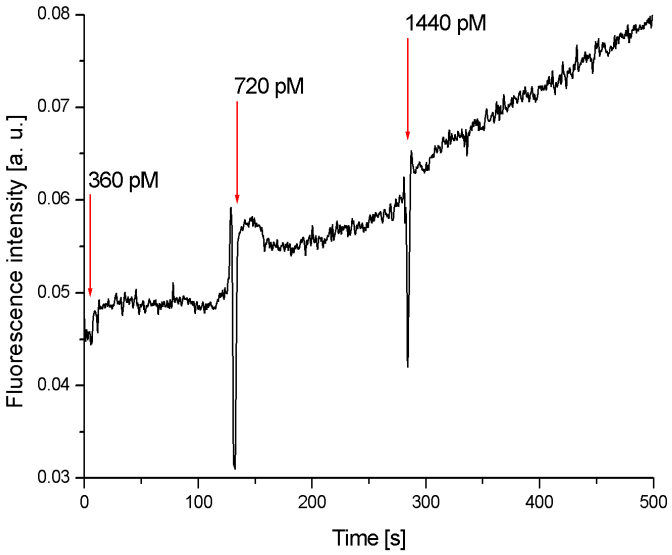

Figure 9.8: A titration experiment with the sandwich assay. The arrows mark the injection of a antigen/secondary antibody solution with the specified antigen concentration. The fluorescence intensity stayed constant for an antigen concentration of 360 pM. Binding was observed after increasing the concentration to 720 pM.

surface of the polarizer rotate in and out of the beam. Noise generated by this off-axis effect is automatically encoded at the modulation frequency and therefore picked up by the lock-in detector. Precession of the axis of rotation was identified as another aspect of this mechanical solution of rotating the polarization, that is open for optimization. Precession of the crystal causes angles of incidence of the laser beam that vary from 90°. Refraction takes place, which affects the direction of the beam. In combination with the apertures present in the set-up, like irises for beam collimation, a moving beam equates to changes in the incident intensity on the sample, because parts of the beam cross section can be temporarily obstructed.

9.7 Conclusion and outlook

Elliptical polarization modulation was introduced as an experimental technique to eliminate the bulk jump. EPM is a hardware based method of subtracting the unwanted intensity contribution by bulk fluorophore emission, which is unrelated to surface recognition. Several forms of technical realization of the EPM concept are imaginable. The version demonstrated in this work utilized traditional optical ($\lambda/4$-plate) and moving mechanical components (rotating polarizer). The beam is shaped into a form that is modulated in both intensity and polarization. It was shown, that the reflectivity response of a grating under illumination of arbitrary linear polarization can be represented by a linear combination of the s-polarized and the p-polarized case. The interactions of the two fundamental polarizations with the bulk fluorophores depend

differently on the dye concentration, which is why the mixing angle changes as a function of the bulk fluorophore concentration in the described way.

EPM was first demonstrated in measurements with the DNA assay at high bulk concentrations. The bulk jump effect was successfully eliminated in these experiments. Additionally, studies on a sandwich assay were performed in which the bulk fluorophore concentration is independent of the analyte concentration and gives a constant, strong bulk jump. The limit of detection with this biochemical system was found to be at about 720 pM in quick response experiments. A lower LOD can be reached for longer detection times and reduced noise.

Noise contributions introduced by processes specific to EPM were identified as being related to the combined mechanical and optical realization of the concept. Precession and off-axis rotation of the polarizer crystal are responsible for intensity fluctuations in the signal. Additionally, the rotating polarizer assembly was restricted to a maximum modulation frequency of 5 Hz because of overheating. It is therefore suggested that electro-optical components be used in future experiments, which will eliminated these limitations. Liquid crystal cells can be used to modulate polarization and intensity of an electromagnetic wave in the required way. Alternatively, a Pockel's cell can be employed for discreet switching of the polarization.

Chapter 10

Summary and outlook

The enhanced electromagnetic field of surface plasmons, excited optically by grating coupling, has been used in this work to detect the immobilization of fluorescently labeled analyte molecules. Fundamental properties of the interaction between the grating and the emitted fluorescence light have been studied, as well as aspects relevant to commercial applications of this detection scheme.

Gratings with periodic surface modulations in the nanometer scale have been fabricated holographically and showed high coupling efficiencies. The corrugation shape of samples exhibiting particularly high coupling efficiencies has been characterized by AFM and was found to be a symmetric trapezoidal pattern. Shallow modulations with an aspect ratio of approximately 1:30 proved most efficient. The coupling of light to surface plasmons via these gratings could be simulated well within the Rayleigh approximation. Reflection and refraction related effects introduced by a flow cell were modelled with sufficient agreement. The uniformity limits of etched samples were found to be small enough to be ignored in GC-SPFS. Similarly, rotational offsets caused by skew angles of several degrees were found to pose no problem as well. Sinusoidal corrugations were also studied. They offer the advantage of significantly simplified and hence faster calculations. They are of continued interest for applications that demand a more precise agreement between experiment and simulation, like SPR sensors.

The fluorescence emitted from a dye coated grating was found to be strongly directional. The emission geometry resembled a double hump symmetric to the surface normal of the sample and could be manipulated by varying the grating constant. It was shown, that this shape is the result of the excited fluorophores, relaxing via intermediate red-shifted surface plasmons, which decay radiatively over the grating. It was suggested to complement sample characterization in the future by additional reflectivity measurements at the fluorescence wavelength, allowing to obtain information about the outcoupling process without the need to contaminate the sensor surface. Experiments on the difference between the reflectivity minimum position and the angle of maximum fluorescence excitation indicated the effect of the profile shape on direction and magnitude of the separation between the angle of the reflectivity minimum and the position of maximum fluorescence excitation. The computer code used for simulations proved insufficient to predict this relation well, even in the case of prism coupling. An expansion of the program

to take geometric factors (like detection geometry and orientation of the dipole moments) into account is the next logical step.

The in-situ fluorescence detection of analyte immobilization using GC-SPFS was demonstrated. It was found that bulk fluorescence is not a crucial factor for the limit of detection when working with direct assays, but rather illumination crosstalk. A lower limit of detection of 40 fM was extrapolated by analyzing the different noise contributions present in the system, a value that could be reduced even further by anti-reflection coating of the flow cell and interference filters featuring increased discrimination. Furthermore, two-photon excitation of the fluorophores was also suggested as a method to reduce illumination crosstalk.

Experiments with gratings with overlapping emission lobes were found to be less affected by bulk emission. Additionally, polarization sensitive detection was suggested and evaluated for reducing the bulk fluorescence contribution in measurements with sandwich assays. The degree to which this can be achieved can be manipulated by changing properties of the dye molecule, like fluorescence lifetime, molecular mass and collisional cross section, giving opportunity for further experiments.

The replication of gratings by hot embossing was described. The cheap and faithful mass production of disposable samples from a given master grating is one of the key requirements for the commercial feasibility of GC-SPFS. It was demonstrated that good reproducibility can already be achieved with simple means, using glass gratings as stamps. For prolonged production, the transfer of the corrugation into a robust nickel specimen is desirable and will allow to optimize the processing parameters involved in embossing. Experiments performed with embossed gratings, featuring the inverse structure of the master grating, have provided additional results concerning the relation between tuning shift and profile shape.

Bleaching effects turned out to be sizable and obstructive in experiments with a rotating photomultiplier, resulting in distorted spectra. Solid angle imaging was introduced and demonstrated as a suitable method to minimize the amount of bleaching during a measurement to a negligible amount, maintaining the shape of the fluorescence emission pattern. Particularly polarization sensitive detection experiments were improved by the combination with solid angle imaging. A future set-up will see aberration corrected optics to improve the imaging qualities of the system and increase angular coverage in both dimensions.

Elliptical polarization modulation was suggested as a hardware based technique capable of eliminating the bulk jump. The concept was demonstrated successfully in DNA hybridization experiments at particularly high bulk concentrations. Additional measurements were performed with a sandwich assay for which a limit of detection of about 720 pM was found in a quick response scenario, a value that could be reduced with longer interaction times. The technique was realized in a set-up with moving mechanical components introducing noise by precession and off-axis rotation of the polarizer. Future implementations of elliptical polarization modulation will feature an improved sensitivity and reduced response times by utilizing electro-optical components.

GC-SPFS has been evaluated in this fundamental study in the context of analyte detection for the first time. The method meets the key requirements for turning it into a feasible

commercial system and is ready go into a subsequent engineering phase:

- The technique features high sensitivity.
- GC-SPFS is capable of affinity measurements.
- Highly efficient gratings can be cheaply reproduced, reducing operating cost.
- Distinction of the bulk signal from the bound analyte contribution is possible by elliptical polarization modulation or polarization sensitive detection. For certain assays even, the bulk emission constitutes no significant background contribution at all.

Appendix A

Grating data summary

The following chart comprises the relevant information of all glass grating samples employed in the described experiments for reference purposes. The coupling efficiencies (η = 1 - R_{min}) were measured in air. Gratings are sorted into groups of minimum coupling efficiencies in η increments of 0.05 for convenience. A sample with $\eta = 0.95$ has in fact a coupling efficiency of at least 0.95 or more.

The grating constants are specified in two ways for most samples: first, the value targeted during fabrication; second, the value found by measuring diffraction of the grating in the Littrow configuration (with an error of approximately ±1 nm). No manufacturing information was available for the first and the last specimen on the list, which stem from external sources.

Sample	η	Λ_{fab} [nm]	Λ_{diff} [nm]
B8	0.95	-	493.8
B51	0.8	511.6	510.5
B55	0.8	511.6	-
B60	0.95	511.6	512.8
B62	0.95	511.6	-
B63	0.95	511.6	-
B64	0.9	511.6	512.8
B70	0.5	511.6	511.6
B79	0.95	511.6	512.2
B82	0.95	511.6	-
B92	0.95	474.7	474.0
B95	0.95	474.7	474.7
B98	0.95	474.7	474.7
B101	0.95	474.7	475.1
B104	0.95	474.7	-
SP42	0.95	-	481.6

Table A.1: Grating data summary

Appendix B

Alignment guidelines

The multitude of mirrors present in the set-up made it susceptible to accidents (bumping into them, most likely the last one) resulting into misalignment of the system. To achieve good alignment is therefore a task that the experimenter encounters not only during construction of the system but perhaps also during regular operation. Some advice and procedures are given here that were found useful.

If the beam steering is misaligned, the beam is not passing over the center of rotation of the goniometer. First one should check for mirror tilt. Place some kind of screen (e. g. a closed iris with its central hole as a well defined reference point) on a movable stand at the height of the reflected beam as observed in the vicinity of the last mirror. Move it far away and check for a difference in height of the spot on the screen. Tilt mirror accordingly to compensate and to achieve a beam parallel to the table surface.

To find the center of rotation, mount a long optical rail on the goniometer, pointing away from the last mirror with an orientation approximately parallel to the beam. Place two irises on the rail on rods with their central holes at beam height. Fix one directly above the estimated center of rotation, the other one on the far end of the rail. Make sure both apertures are located above the center line of the rail and are oriented perpendicular to the beam. Rotate the mirror to an angle from which the reflected beam hits the central aperture. Rotate the rail/goniometer to the angle where the beam spots also hits the center of the second iris. Most probably, this will not happen simultaneously for both irises at the beginning of the process. If that is the case, rotate the mirror a little and try to hit the center of both iris. In order to achieve this, it will be necessary to rotate the goniometer also a little. Repeat both steps successively until the beam and the center line of the rail, defined by the two apertures, coincide. The beam will now cross the axis of rotation. This method of employing a double aperture, with two points defining a line in space, is most useful for the collinear alignment of components, for example any type of detector.

For every sample, the angle of normal incidence (defining the 0° position) has to be found anew. For samples of varying thicknesses, it is also necessary to confirm that the sample is placed with its surface directly over the center of rotation every time. Mount the sample in a position where the sample surface approximately grazes the axis of rotation. Rotate the

goniometer accordingly to achieve back reflection of the beam into itself. Observe the back reflected spot at the first mirror (the longer the distance the higher the angular resolution) and compensate sample holder tilt and angular offset. This defines 0° on the angular scale. Move to the smallest angle[1] where the reflected beam clears the last mirror. Mount a marked screen/closed iris for observation on the detector arm. Have the detector arm rotate to the position where the reflected beam hits the mark/hole. Rotate the sample to a much higher angle and the detector arm to twice that angle (for example to 30° and to 60° respectively) to collect the reflection spot. If the spot has left the target, move the sample holder on its rail forward or backward in order to have the beam hit the aperture again. If target and laser spot coincide, rotate both arms back to 0° and check for the location of the back reflection again.

The correct alignment of both detectors can be found with the double aperture method described above. Before starting an experiment it is important to find the minimum safe angle for operation, which is the smallest angle accessible by the detector closest to the last mirror before collision.

In contrast to prism coupling SPFS, where only fluorescence information matters and reflectivity measurements just serve as a diagnostic tool, reflectivity data is still essential in grating coupling to characterize gratings that can have slightly changing properties like grating constant and amplitude. Since the power of gas lasers is slowly changing, the reference voltage for reflectivity measurements with the photodiode has to be found on every given day in the lab. The “1” on the reflectivity scale is given by a clean shot of the laser on the PD without the sample interfering. Bring the detector arm to the position where the PD is directly opposite the last mirror. Calibrate the PD by finding the voltage for the unattenuated laser power and set it as the reference value.

[1]This amounts to below 3° in the set-up built. The described procedure works best for angles as close to 0° as possible. If such an angle is not accessible due to the size of the last mirror the same approach can still be used if the sample is tilted temporarily in a way to over shoot the mirror and the aperture is temporarily aligned at the appropriate height.

Appendix C

Operational procedures for EPM

The inert sequence MM15 can be used to study the bulk fluorescence emission in isolation and is needed to find the mixing angle. There are several ways of how to find ρ_m while a solution of MM15 is cycled through the flow cell. The method described here has the advantage of being fast and providing feedback about the successful conversion of the set-up from the conventional DC mode (which is needed for angular measurements of the emission spectrum of a sample) to EPM.

The $\lambda/4$-plate and the rotating polarizer have to be installed. The Fresnel rhomb is set to a mixing angle of $\rho = 22.5°$ as a starting value. In this position, the plane of polarization of the p-polarized incident beam is rotated by 45° and the incident intensity of p-light is equal to that of s-light. Fluorescence detection can be performed with a digital PMT as well as with an analog PMT. Both methods are described here because the comparison between them is instructive for understanding the principle of data acquisition in EPM.

Let's consider the case of a digital PMT serving as the fluorescence detector. First, ρ_m has to be found. The polarization of the incident beam can be controlled by inserting a polarizer, but the faster method is to use the rotating polarizer and to revolve it continuously. The fluorescence signal is then oscillating like the example given in figure C.1 (a). The oscillation is due to the different fluorescence response of the bulk to the two polarizations. The angle of the Fresnel rhomb has to be decreased until the oscillation amplitude is minimized - this position marks ρ_m.

Lock-in detection is used in photodiode reflectivity measurements as well as in fluorescence detection performed under with the EPM technique. Since such measurements are done sequentially, one such expensive device is enough. The moment after ρ_m has been determined is a good time to convert the set-up to EPM operations by changing the lock-in detector wiring and settings and, if necessary, replace the digital PMT with its analog counterpart. The oscillations, that were observed previously, are detected in terms of their amplitudes when using EPM. This situation is illustrated in figure C.1 (b). Finding the mixing angle meant minimizing the amplitude before. In EPM, ρ_m is found as soon as the signal magnitude is minimized. This means the bulk fluorescence emission is fully cancelled. Before continuing with the experiment, it is recommended to move the Fresnel rhomb temporarily to an angle where the signal amplitude

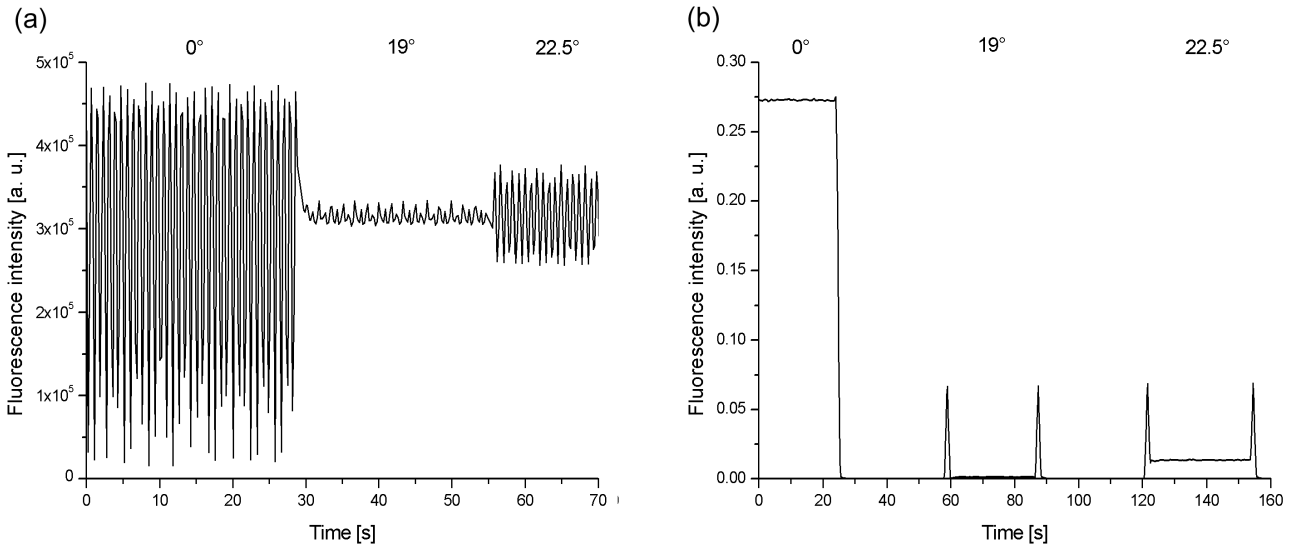

Figure C.1: PMT output in the two experimental formats. (a) Finding the mixing angle means minimizing the oscillation amplitude in the conventional type of experiment. Three examples are shown in the graph for different values of ρ. A Fresnel rhomb angle of 0° corresponds to pure p-polarized incident light, 22.5° to an equal mixture of p and s. In this example, ρ_m was found to be 19°[2]. (b) The EPM technique deletes all DC components of the signal and extracts only those contributions that are encoded by the modulation frequency. The bulk signal is well cancelled at $\rho = 19°$. It can only be recognized in the graph by the two flanking transients, artifacts due to start and cessation of the measurement. The ordinates of the graphs are different in scale, because the two PMTs provide a very different type of output signal: either photon counts (for the digital PMT) or a voltage (for the analog PMT used in EPM).

is different from zero, because a vanishing signal can also result from many other unintended factors. After having ruled out such factors, the flow cell can be rinsed and the complimentary sequence injected for kinetic measurements.

Abbreviations

A	Adenine
a	Grating amplitude
AC	Alternating current (in a more general sense: a signal that has one or more frequency components at f $\neq$ 0)
AFM	Atomic force microscopy
ATR	Attenuated total reflection
a. u.	Arbitrary units
B	Magnetic field vector
BK7	A boron-crown glass with n = 1.515 at λ = 632.8 nm
BSA	Bovine serum albumin
C	Cytosine
c	Speed of light
CCD	Charge-coupled device
CD	Compact disc
D	Electric displacement vector
DC	Direct current (in a more general sense: a signal that has only a single frequency component at f = 0)
DNA	Deoxyribonucleic acid
DVD	Digital versatile disc
E	Electric field vector
e	Electron charge
EPM	Elliptical polarization modulation
f	Focal length
FRAP	Fluorescence recovery after photo bleaching
FRET	Fluorescence resonant energy transfer
G	Guanine
G	Grating vector
GC-SPFS	Grating coupling surface plasmon fluorescence spectroscopy

GFP	Green fluorescent protein
H	Magnetic field strength vector
HeCd	Helium-cadmium (laser)
HeNe	Helium-neon (laser)
I_i	Impinging intensity
I_{max}	Fluorescence intensity maximum
I_r	Reflected intensity
I_t	Transmitted intensity
i	Imaginary unit
k	Wavevector
K_a	Association or affinity constant
K_d	Dissociation constant
kN	Kilo Newton
k_{off}	Desorption rate constant
k_{on}	Adsorption rate constant
$\mathbf{k}_x$	In-plane wavevector
L	Rayleigh expansion order
l	Land width
LaSFN9	A high refractive index glass with n = 1.845 at λ = 632.8 nm
LOD	Limit of detection
m	Diffraction order
m_e	Effective electron mass
M_g	Molecular weight
MM0	Mismatch 0
MM15	Mismatch 15
n	Refractive index
ND	Neutral density (filter)
n_e	Electron density
p	Pit width
p	P-polarization (also known as TM-polarization)
P2	DNA probe strand 2
PBS	Phosphate-buffered saline (buffer solution)
PD	Photodiode
PDMS	Poly(dimethylsiloxane)

PMMA	poly(methylmethacrylate)
PMT	Photomultiplier tube
PSD	Polarization sensitive detection
R	Reflectivity
r	A point in space
RIBE	reactive ion beam etching
R_{min}	Magnitude of the reflectivity at the resonance angle
RMS	Root mean square
rpm	rounds per minute
s	Slope fraction
s	S-polarization (also known as TE-polarization)
SA	Streptavidin
SAI	Solid angle imaging
SAM	Self-assembled monolayer
SNR	Signal-to-noise ratio
SPFS	Surface plasmon fluorescence spectroscopy
SPM	Surface plasmon microscopy
SPR	Surface plasmon resonance
T	Thymine
t	Time
T2	DNA target strand 2
TE	Transverse electric polarization (also known as s-polarization)
T_g	Glass transition temperature
TIR	Total internal reflection
TM	Transverse magnetic polarization (also known as p-polarization)
TTL	Transistor-transistor logic

α_i	Angle of incidence
α_r	Angle of reflection
α_t	Angle of transmission
ε	Dielectric number
ε_0	Electric permittivity of free space
ε'	Real part of ε
ε''	Imaginary part of ε
ε_d	Dielectric number of a dielectric

ε_m	Dielectric number of a metal
ζ	Surface profile
η	Coupling efficiency (1 - R_{min} in air)
Θ	Surface coverage
θ	Azimuthal angle
θ_L	Littrow angle
θ_o	Outcoupling angle
θ_r	Resonance angle
Λ	Grating constant
λ	Wavelength
μ	Relative permeability
μ_0	Magnetic permeability of free space
ρ	Fresnel rhomb angle (i. e. plane of polarization)
ρ_m	Mixing angle
σ	Skew angle
τ	Collision time
ψ	Polar angle
ω	Angular frequency
ω_p	Plasma frequency

Bibliography

[ABC] www.abcr.de

[AGI] www.agilent.com

[Agr82] V. M. Agranovitch and D. L. Mills (editors), *Surface Polaritons*, North-Holland, 1982

[Alb02] B. Alberts, A. Johnson, J. Lewis, M. Raff, K. Roberts and Peter Walker, *Molecular Biology of the Cell*, Garland Science, 2002

[AME] www.signalrecovery.com

[And01] P. Andrew and W. L. Barnes, *Molecular fluorescence above metallic gratings*, Physical Review B, 64: 125405.1-125405.11, 2001

[Ash76] N. W. Ashcroft and N. D. Mermin, *Solid State Physics*, International Thomson Publishing, 1976

[Atk02] P. Atkins and J. de Paula, *Physical Chemistry*, Oxford University Press, 2002

[Att91] J. W. Attridge, P. B. Daniels, J. K. Deacon, G. A. Robinson and G. P. Davidson, *Sensitivity Enhancement of Optical Immunosensors by the Use of a Surface Plasmon Resonance Fluoroimmunoassay*, Biosensors & Bioelectronics, 6: 201-214, 1991

[Bai89a] C. D. Bain, E. B. Throughton, Y.-T. Tao, J. Evall, G. M. Whitesides and R. G. Nuzzo, *Formation of Monolayer Films by the Spontaneous Assembly of Organic Thiols from Solution onto Gold*, Journal of the American Chemical Society, 111 (1): 321-335, 1989

[Bai89b] C. D. Bain, J. Evall and G. M. Whitesides, *Formation of Monolayers by the Coabsorption of Thiols on Gold: Variations in the Head Group, Tail Group and Solvent*, Journal of the American Chemical Society, 111, 7155-7164, 1989

[Bai89c] C. D. Bain and G. M. Whitesides, *Formation of Monolayers by the Coadsorption of Thiols on Gold: Variation in the Length of the Alkyl Chain*, Journal of the American Chemical Society, 111: 7164-7175, 1989

[Ban95] C. N. Banwell and E. M. McCash, *Fundamentals of Molecular Spectroscopy*, McGraw-Hill, 1995

[Bar96] W. L. Barnes, T. W. Priest, S. C. Kitson and J. R. Sambles, *Physical Origin of Photonic Energy Gaps in the Propagation of Surface Plasmons on Gratings*, Physical Review B, 54: 6227-6244, 1996

[Bar98] W. L. Barnes, *Fluorescence near Interfaces: the Role of Photonic Mode Density*, Journal of Modern Optics,45 (4): 661-699, 1998

[Bec63] P. Beckmann and A. Spizzichino, *The Scattering of Electromagnetic Waves from Rough Surfaces*, Pergamon Press, 1963

[BER] www.b-halle.de

[BIA] www.biacore.com

[Bin86] G. Binnig, C. F. Quate and C. Gerber, *Atomic Force Microscope*, Physical Review Letters, 56: 930-933, 1986

[Boa82] A. D. Boardman (editor), *Electromagnetic Surface Modes*, Wiley, 1982

[BOC] www.bocedwards.com

[Boh97] P. W. Bohn, *Localized Optical Phenomena and the Characterization of Materials Interfaces*, Annual Review of Materials Science, 27: 469-498, 1997

[Bor99] M. Born and E. Wolf, *Principles of Optics*, Cambridge University Press, 1999

[Bun92] K. J. Bunch, W. N. Cain and R. W. Grow, *Use of Extrapolation on Wave Expansions to Force the Satisfaction of the Rayleigh Hypothesis*, Journal of the Optical Society of America, 9: 755-764, 1992

[Cel88] V. Celli, P. Tran, A. A. Maradudin and D. L. Mills, k*Gaps for Surface Polaritons on Gratings*, Physical Review B, 37: 9089-9092, 1988

[Cha82] J. Chandezon, M. T. Dupuis, G. Cornet and D. Maystre, *Multicoated Gratings: a Differential Formalism Applicable in the Entire Optical Region*, Journal of the Optical Society of America, 72 (7): 839-846, 1982

[Cha98] W. C. W. Chan and S. Nie, *Quantum Dot Bioconjugates for Ultrasensitive Nonisotopic Detection*, Science, 281 (5385): 2016-2018, 1998

[Chi90] C. E. D. Chidsey, D. N. Loiacono, 1990, *Chemical Functionality in Self-assembled Monolayers: Structural and Electrochemical Properties*, Langmuir, 6: 682-691, 1990

[DOW] www.dowcorning.com

[Dru00] P. Drude, *Zur Elektronentheorie der Metalle*, Annalen der Physik, 1: 566-613 and 3: 369-402, 1900

[Ebe90] R. C. Ebersole, J. A. Miller, J. R. Moran, M. D. Ward, *Spontaneously Formed Functionally Active Avidin Monolayers on Metal Surfaces: a Strategy for Immobilizing Biological Reagents and Design of Piezoelectric Biosensors*, Journal of the American Chemical Society, 112: 3239-3241, 1990

[Els91] S. J. Elston, G. P. Bryan-Brown and J. R. Sambles, *Polarization Conversion from Diffraction Gratings*, Physical Review B, 44: 6393-6400, 1991

[Fan41] U. Fano, *The Theory of Anomalous Diffraction Gratings and of Quasi-stationary Waves on Metallic Surfaces (Sommerfeld's Waves)*, Journal of the Optical Society of America, 31: 213-222, 1941

[FIS] www.fishersci.com

[Fis94] B. Fischer, T. M. Fischer and W. Knoll, *Dispersion of Surface Plasmons in Rectangular, Sinusoidal, and Incoherent Silver Gratings*, Journal of Applied Physics, 75: 1577-1581, 1994

[Fre97] S. Freitag, I. Le Trong, L. Klumb, P. S. Stayton, R. E. Stenkamp, *Structural Studies of the Streptavidin Binding Loop*, Protein Science, 6: 1157-1166, 1997

[Fru98] A. G. Frutos and R. M. Corn, *Surface Plasmon Resonance of Ultrathin Organic Films*, Analytical Chemistry, 70: 449A-455A, 1998

[Giv01] A. L. Given, *Flow Cytometry: First Principles*, John Wiley and Sons, 2001

[Gol03] D. Goldstein, *Polarized Light*, Marcel Dekker, 2003

[Gor80] J. G. Gordon and S. Ernst, *Surface Plasmons as a Probe of the Electrochemical Interface*, Surface Science, 101: 499-506, 1980

[Gre75] N. M. Green, *Avidin*, Advanced Protein Chemistry, 29: 85-133, 1975

[HAM] www.hamamatsu.com

[Ham00] M. Hamdorf and D. Johannsmann, *Surface-rheological Measurements on Glass Forming Polymers Based on the Surface Tension Driven Decay of Imprinted Corrugation Gratings*, Journal of Chemical Physics, 112 (9): 4262-4270, 2000

[Hal89] P. Halevi and O. Mata-Méndez, *Electromagnetic Modes of Corrugated Thin Films and Surfaces with a Transition Layer*, Physical Review B, 39: 5694-5705, 1989

[Har95] F. E. Harris (editor), *Handbook of Optical Constants of Solids*, Academic Press, 1995

[HEC] www.plexiglas-hecker.de

[Hec01] E. Hecht, *Optics*, Pearson Addison Wesley, 2001

[Hei87] D. Heitmann, N. Kroo, C. Schulz and Z. Szentirmany, *Dispersion Anomalies of Surface Plasmons on Corrugated Metal-Insulator Interfaces*, Physical Review B, 35: 2660-2666, 1987

[HEL] www.hellma-worldwide.de

[Hen89] W. A. Hendrickson, A. Pähler, J. L. Smith, Y. Satow, E. A. Merritt, R. P. Phizackerley, *Crystal Structure of Core Streptavidin Determined from Multiwavelength Anomalous Diffraction of Synchrotron Radiation*, Proceedings of the National Academy of Sciences of the United States of America, 86: 2190-2194, 1989

[Hes02] S. T. Hess, S. Huang, A. A. Heikal and W. W. Webb, *Biological and Chemical Applications of Fluorescence Correlation Spectroscopy: a Review*, Biochemistry, 41 (3): 697-705, 2002

[Hom99] J. Homola, S. S. Yee and G. Gauglitz, *Surface Plasmon Resonance Sensors: Review*, Sensors and Actuators B, 54 (1): 3-15, 1999

[HTS] www.htsbiosystems.com

[HUB] www.xhuber.com

[ISM] www.ismatec.com

[Jac98] J. D. Jackson, *Classical Electrodynamics*, Wiley, 1998

[Joh96] M. E. Johnson, D. A. Berk, D. Blankschtein, D. E. Golan, R. K. Jain and R. S. Langer, *Lateral Diffusion of Small Compounds in Human Stratum Corneum and Model Lipid Bilayer Systems*, Biophysical Journal, 71: 2656-2668, 1996

[JOM94] *A Special Issue on Photonic Band Structures*, Journal of Modern Optics, 41 (2), 1994

[JOS93] *A Special Issue on Photonic Band Gaps*, Journal of the Optical Society of America, 10 (2), 1993

[Kam01] D. Kambhampati, P. E. Nielsen and W. Knoll, *Investigating the Kinetics of DNA-DNA and PNA-DNA Interactions using Surface Plasmon Resonance-enhanced Fluorescence Spectroscopy*, Biosensors & Bioelectronics, 16: 1109-1118, 2001

[Kas06] A. Kasry, *title to be announced*, forthcoming Ph. D. thesis, University of Mainz, 2006

[Kit96] S. C. Kitson, W. L. Barnes, J. R. Sambles and N. P. K. Cotter, *Excitation of Molecular Fluorescence via Surface Plasmon Polaritons*, Journal of Modern Optics, 43 (3): 573-582, 1996

[Kno81] W. Knoll, M. R. Philpott, J. D. Swalen and A. Girlando, *Emission of Light from Ag Metal Gratings Coated with Dye Monolayer Assemblies*, Journal of Chemical Physics, 75 (10): 4795-4799, 1981

[Kre68] E. Kretschmann and H. Raether, *Radiative Decay of Non-radiative Surface Plasmons Excited by Light*, Zeitschrift für Naturforschung, 23A: 2135-2136, 1968

[Kre00] M. Kreiter, *Surface Plasmon-related Resonances on Metallic Diffraction Gratings*, Ph. D. thesis, University of Mainz, 2000

[Kre01] M. Kreiter, T. Neumann, S. Mittler, W. Knoll and J. R. Sambles, *Fluorescent Dyes as a Probe for the Localized Field of Coupled Surface Plasmon-related Resonances*, Physical Review B, 64: 075406.1-075406.11, 2001

[Kre02] M. Kreiter, S. Mittler, W. Knoll and J. R. Sambles, *Surface Plasmon-related Resonances on Deep and Asymmetric Gold Gratings*, Physical Review B, 65: 125415.1-125415.13, 2002

[Kuh70] H. Kuhn, *Classical Aspects of Energy Transfer in Molecular Systems*, Journal of Chemical Physics, 53: 101-108, 1970

[Lak99] J. R. Lakowicz, *Principles of Fluorescence Spectroscopy*, Plenum Publishing, 1999

[Lan18] I. Langmuir, *The Adsorption of Gases on Plane Surfaces of Glass, Mica and Platinum*, Journal of the American Chemical Society, 40: 1361-1403, 1918

[LEY] www.leyboldoptics.com

[Lie83] B. Liedberg, C. Nylander and I. Lundström, *Surface plasmon resonance for gas detection and biosensing*, Sensors and Actuators, 4: 299-304, 1983

[Lie94] M. A. Lieberman and A. J. Lichtenberg, *Principles of Plasma Discharges and Materials Processing*, Wiley, 1994

[Lie99] T. Liebermann, *Oberflächenplasmonen-Fluoreszenzspektroskopie zur Detektion molekularer Erkennungsreaktionen (Surface Plasmon Fluorescence Spectroscopy for the Detection of Molecular Recognition)*, Ph. D. thesis, University of Mainz, 1999

[Lie00a] T. Liebermann, W. Knoll, P. Sluka and R. Herrmann, *Complement Hybridization from Solution to Surface-attached Probe-Oligonucleotides observed by Surface-Plasmon-Field-enhanced Fluorescence Spectroscopy*, Colloids and Surfaces A, 169: 337-350, 2000

[Lie00b] T. Liebermann and W. Knoll, *Surface-Plasmon Field-enhanced Fluorescence Spectroscopy*, Colloids and Surfaces A, 171 (1): 115-130, 2000

[Lin97] M. Lin and K. Nielsen, *Binding of the* Brucella Abortus *Lipopolysaccharide O-chain Fragment to a Monoclonal Antibody*, Journal of Biological Chemistry, 272 (5): 2821-2827, 1997

[Lod04] H. Lodish, A. Berk, P. Matsudaira, C. A. Kaiser, M. Krieger, M. P. Scott, S. L. Zipursky and J. Darnell, *Molecular Cell Biology*, W.H. Freeman and Company, 2004

[Loe97] E. G. Loewen and Evgeny Popov, *Diffraction Gratings and Applications*, Marcel Dekker, 1997

[Lop98] T. López-Rios, D. Mendoza, F. J. García-Viadal, J. Sánchez-Dehesa and B. Pannetier, *Surface Shape Resonances in Lamellar Metallic Gratings*, Physical Review Letters, 81: 665-668, 1998

[LOT] www.lot-oriel.com

[Mai85] X. Mai, R. Moshrefzadeh, U. J. Gibson, G. I. Stegeman and C. T. Seaton, *Simple Versatile Method for Fabricating Guided-Wave Gratings*, Applied Optics, 24 (19): 3155-3161, 1995

[Mar82] in [Agr82], chapter 5

[McG78] A. R. McGregor, J. O. Crookall-Greening, J. Landon, D. S. Smith, *Polarisation Fluoroimmunoassay of phenytoin*, Clinica Chimica Acta 83 (1-2): 161-166, 1978

[MEL] www.mellesgriot.com

[MEN] www.menzel.de

[MIC] www.microresist.de

[MIL] www.millipore.com

[Mit95] S. Mittler-Neher, J. Spinke, M. Liley, G. Nelles, M. Weisser, R. Back, G. Weber and W. Knoll, *Spectroscopic and Surface-analytical Characterization of Self-assembled Layers on Au*, Biosensors & Bioelectronics, 10: 903-916, 1995

[MOL] www.probes.com

[Muj93] R. B. Mujumdar, L. A. Ernst, S. R. Mujumdar, C. J. Lewis and A. S. Waggoner, *Cyanine Dye Labeling Reagents: sulfoindocyanine succinimidyl esters*, Bioconjugate Chemistry, 4 (2): 105-111, 1993

[MWG] www.mwg-biotech.com

[Nag00] K. Nagata and H. Handa, *Real-Time Analysis of Biomolecular Interactions*, Springer, 2000

[Nyl82] C. Nylander, B. Liedberg and T. Lind, *Gas Detection by Means of Surface Plasmon Resonance*, Sensors and Actuators, 3 (1): 79-88, 1982

[Ott68] A. Otto, *Excitation of Nonradiative Surface Plasma Waves in Silver by the Method of Frustrated Total Reflection*, Zeitschrift für Physik, 216 (4): 398-410, 1968

[Pal02] C. Palmer, *The Diffraction Grating Handbook*, Richardson Grating Laboratory, Thermo RGL, 2002

[Pau90] T. C. Paulick, *Applicability of the Rayleigh Hypothesis to Real Materials*, Physical Review Letters B, 42: 2801-2824, 1990

[PER] las.perkinelmer.com

[Pet66] R. Petit and M. Cadilhac, *Sur la diffraction d'une onde plane par un réseau infiniment conducteur*, Comptes Rendus de l'Academie des Sciences B, 262: 468-471, 1966

[Pet80] R. Petit (editor), *Electromagnetic Theory of Gratings*, Springer, 1980

[Pet02] K. Petersen and D. Johannsmann, *Measurements on the Surface Glass Transition of PMMA from the Decay of Imprinted Surface Corrugation gratings: the influence of molecular weight*, Journal of Non-crystaline Solids, 307-310: 532-537, 2002

[PHO] www.photomet.com

[Pis95] D. Piscevic, *Molekulare Erkennungsreaktionen an funktionalisierten, selbstorganisierten Adsorptionsschichten (Molecular Recognition Reactions on Functionalized SAMs)*, Ph. D. thesis, University of Mainz, 1995

[Pla97] T. Plakhotnik, E. A. Donley and U. P. Wild, *Single-Molecule Spectroscopy*, Annual Review of Physical Chemistry, 48: 181-212, 1997

[Poc78] I. Pockrand, J. D. Swalen, J. G. Gordon and M. R. Philpott, *Surface Plasmon Spectroscopy of Organic Monolayer Assemblies*, Surface Science, 74: 237-244, 1978

[Poc80] I. Pockrand and A. Brillante, *Nonradiative Decay of Excited Molecules near a Metal Surface*, Chemical Physics Letters, 69: 499-504, 1980

[POL] www.polytec.com

[Pop89] E. Popov, *Plasmon interactions in metallic gratings: ω- and* k*-minigaps and their connection with poles and zeros*, Surface Science, 222 (2-3): 517-529, 1989

[Por87] M. D. Porter, T. B. Bright, D. L. Allara, C. E. D. Chidsey, *Spontaneously Organized Molecular Assemblies. IV. Structural Characterization of n-alkyl thiol Monolayers on Gold by Optical Ellipsometry, Infrared Spectroscopy and Electrochemistry*, Journal of the American Chemical Society, 109: 3559-3568, 1987

[Pow59] C. J. Powell and J. B. Swan, *Origin of the Characteristic Electron Energy Losses in Aluminum*, Physical Review, 115: 869-875, 1959

[PRO] www.prontor-werk.de

[Rae88] H. Raether, *Surface Plasmons on Smooth and Rough Surfaces and on Gratings*, Springer, 1988

[Rit57] R. H. Ritchie, *Plasma Losses by Fast Electrons in Thin Films*, Physical Review, 106: 874-881, 1957

[ROC] www.roche-diagnostics.com

[ROH] www.electronicmaterials.rohmhaas.com

[Ron91] S. Ronggui and G. C. Righini, *Characterization of Reactive Ion Etching of Glass and its Applications in Integrated Optics*, Journal of Vacuum Science and Technology, 9 (5): 2709-2712, 1991

[ROT] www.roth-rau.de

[Rot88] B. Rothenhäusler and W. Knoll, *Surface-Plasmon Microscopy*, Nature, 332: 615-617, 1988

[Rud70] D. Rudolph and G. Schmahl, *High Precision Gratings Produced Holographically by means of Reconstructed Identical Wave Fronts*, Optik, 30 (6): 606-609, 1970

[Sam91] J. R. Sambles, G. W. Bradbery and F. Z. Yang, *Optical Excitation of Surface Plasmons: an Introduction*, Contemporary Physics, 32 (3): 173-183, 1991

[Sar82] D. Sarid, R. T. Deck, A. E. Craig, R. K. Hickernell, R. S. Jamerson and Joseph J. Fasano, *Optical Field Enhancement by Long-Range Surface-Plasma Waves*, Applied Optics, 21 (22): 3993-3996, 1982

[Sar91] D. Sarid, *Scanning Force Microscopy*, Oxford University Press, 1991

[Sch97] P. Schuck, *Use of Surface Plasmon Resonance to Probe the Equilibrium and Dynamic Aspects of Interactions between Biological Macromolecules*, Annual Review of Biophysics and Biomolecular Structure, 26: 541-566, 1997

[Sch00] U. Schröter, *Oberflächenplasmonen auf modulierten Silberfilmen (Surface Plasmons on Modulated Silver Films)*, Shaker Verlag, Ph. D. thesis, University of Hamburg, 2000

[SIE] www.siemens.de

[SIG] www.sigmaaldrich.com

[Smi77] D. S. Smith, *Enhancement Fluoroimmunoassay of thyroxine*, FEBS Letters, 77 (1): 25-27, 1977

[SPE] www.spectra-physics.com/gratings

[Spi93] J. Spinke, M. Liley, H.-J. Guder, L. Angermaier and W. Knoll, *Molecular Recognition at Self-assembled Monolayers: the Construction of Multicomponent Multilayers*, Langmuir, 9: 1821-1825, 1993

[Str88] L. Strong, G. M. Whitesides, *Structures of Self-assembled Monolayer Films of Organosulfur Compounds adsorbed on Gold Single Crystals: Electron Diffraction Studies*, Langmuir, 4: 546-558, 1988

[Sug98] M. Sugawara (editor), *Plasma Etching Fundamentals and Applications*, Oxford University Press, 1998

[Tio77] F. Tiogo, A. Marvin, V. Celli and N. R. Hills, *Optical properties of Rough Surfaces: General Theory and the small Roughness Limit*, Physical Review Letters B, 15: 5618-5626, 1977

[Tsi98] R. Y. Tsien, *The Green Fluorescent Protein*, Annual Review of Biochemistry, 67: 509-544, 1998

[TYG] www.tygon.com

[UHU] www.uhu.de

[Ull76] E. F. Ullman, M. Schwarzberg and K. E. Rubenstein, *Fluorescent Excitation Transfer Immunoassay. A General Method for Determination of Antigens*, Journal of Biological Chemistry, 251: 4172-4178, 1976

[Ulm91] A. Ulman, *An Introduction to Ultrathin Organic Films*, Academic Press, 1991

[Vas04] K. Vasilev, W. Knoll and M. Kreiter, *Fluorescence Intensities of Chromophores in Front of a Thin Metal Film*, Journal of Chemical Physics, 120: 3439-3445, 2004

[VEE] www.veeco.com

[Wan96] X. F. Wang and B. Herman, *Fluorescence Imaging Spectroscopy and Microscopy*, John Wiley and Sons, 1996

[Web89] P. C. Weber, D. H. Ohlendorf, J. J. Wendoloski, F. R. Salemme, *Structural Origins of High-Affinity Biotin Binding to Streptavidin*, Science, 243: 85-88, 1989

[Wid91] C. A. Widrig, C. A. Alves, M. D. Porter, *Scanning Tunneling Microscopy of Ethanethiolate and n-octadecanethiolate Monolayers Spontaneously adsorbed at Gold Surfaces*, Journal of the American Chemical Society, 113 (8): 2805-2810, 1991

[Wie94] R. Wiesendanger, *Scanning Probe Microscopy and Spectroscopy*, Cambridge University Press, 1994

[Wil90] M. Wilchek, E. A. Bayer, *Avidin-Biotin Technology*, Academic Press, 1990

[Wit94] P. Wittung, P. E. Nielsen, O. Buchardt, M. Egholm and B. Norden, *DNA-like Double Helix formed by Peptide Nucleic Acid*, Nature, 368: 561-563, 1994

[Woo02] R. W. Wood, *On a Remarkable Case of Uneven Distribution of Light in a Diffraction Grating Spectrum*, Proceedings of the Physical Society of London, 18: 269-275, 1902

[WOR] J. Worm, worm@mpip-mainz.mpg.de

[Yu04] F. Yu, B. Persson, S. Löfås and W. Knoll, , *Attomolar Sensitivity in Bioassays based on Surface Plasmon Fluorescence Spectroscopy*, Journal of the American Chemical Society, 126: 8902-8903, 2004

[Xie98] X. S. Xie and J. K. Trautman, *Optical Studies of Single Molecules at Room Temperature*, Annual Review of Physical Chemistry, 49: 441-480, 1998

[Zai91] S. H. Zaidi, M. Yousef and S. R. J. Brueck, *Grating Coupling to Surface Plasma Waves. II. Interactions between First- and Second-Order Coupling*, Journal of the Optical Society of America, 8 (6): 1348-1359, 1991

[Zho03] X. Zhong, M. Han, Z. Dong, T. J. White and W. Knoll, *Composition-tunable Zn x Cd Se Nanocrystals with High Luminescence and Stability*, Journal of the American Chemical Society, 125 (28): 8589-8594, 2003